

学位論文

Chemo-thermal evolution of collapsing gas
clouds and the formation of metal-poor stars

(収縮ガス雲の熱化学進化と低金属量星の形成過程)

平成27年12月 博士（理学）申請

東京大学大学院理学系研究科
物理学専攻

千秋 元

Abstract

The first metal-free stars (Population III or Pop III star) are considered to be massive (10–1000 M_{\odot}). On the other hand, the typical mass of the present-day stars is small ($\lesssim 1 M_{\odot}$). Recently, the low-mass but very primitive stars are observed in the halo. Their peculiar abundance pattern suggests that they are the very second-generation stars born in the cloud enriched by metal-free massive stars (Pop III stars). Since the metallicity of the parent cloud is sufficiently small, the lack of cooling agents leads the gas to contract without fragmentation. The monolithic collapse should serve as the massive single object. In this sense, the origin of the extremely metal poor (EMP) stars surviving until now is still unknown.

In this Thesis, we aim to reveal the origin of the low-mass EMP stars. It is considered that the additional cooling by dust thermal emission promotes the gas fragmentation into low-mass clumps during cloud collapse. Therefore, we should care about the properties of dust which is crucially important to induce the gas fragmentation. In this field, the present-day dust model is often used. In solar neighborhood, all refractory elements such as Mg, Si, and Fe are locked into grains. However, this is not the case in the early Universe. Since the formation path of early grains is limited to Pop III supernovae, the Pop II star-hosting cloud is considered to be pre-enriched by metal and dust released by the supernovae. In the supernova ejecta, the grains have also partly been destroyed by the reverse shocks. The second-generation stars are formed in such a dust-deficient environments. In such the case, the accretion of gas-phase metal onto grains (grain growth) might be important.

First, we investigate the effect of the early dust models and grain growth in metal-deficient clouds pre-enriched by Pop III supernovae. We employ the semi-analytic one-zone model of chemo-thermal cloud evolution. During the collapse, we for the first time solve the process of grain growth in the self-consistent manner. The initial metal and dust properties are given by a variety of Pop III models, in which nucleosynthesis and dust formation/destruction are solved. We then follow the evolution of clouds with various metallicities to define the critical metallicity Z_{cr} above which dust cooling is efficient for each Pop III model. In some cases, grain growth occurs efficiently before the gas becomes optically thick. The dust cooling efficiency is enhanced, and consequently Z_{cr} becomes smaller. This can be seen especially in the models with small initial fractions $f_{\text{dep},0}$ of metal depleted onto grains (depletion factor). While Z_{cr} depends on f_{dep} reciprocally as $Z_{\text{cr}}^{(\text{ng})} = 2.3 \times 10^{-8} f_{\text{dep},0}^{-1}$ without grain growth, the dependency is mitigated into $(Z_{\text{cr}}^{(\text{gg})}/10^{-5.5} Z_{\odot}) = (f_{\text{dep},0}/0.18)^{-0.44}$. We can conclude that the grain growth is necessary process to determine the fragmentation condition for low-mass star formation. Although the critical metallicity has the slight dependency on the Pop III model, it is

estimated to be on average $\sim 10^{-5} Z_{\odot}$.

Then, we perform three-dimensional simulations for low-metallicity cloud collapse. We for the first time self-consistently solve grain growth, non-equilibrium chemical reactions, metal molecular cooling, chemical heating owing to hydrogen molecular formation. The mass resolution is refined by our state-of-the-art particle splitting technique based on the Voronoi diagram down to $\sim 10^{-5} M_{\odot}$ (10 Earth masses). In this Thesis, we follow the thermal evolution of four gas clouds: one with the uniform density as a controlled simulation, and three primordial clouds retrieved from a recent cosmological simulation. We investigate the wide range of metallicity 10^{-6} – $10^{-3} Z_{\odot}$ to define the critical condition for the cloud fragmentation.

As a result, we find that there are two fragmentation modes. With $Z \gtrsim 10^{-5} Z_{\odot}$, dust cooling induces the instabilities of cloud elongation. A filamentary structure is formed, and eventually fragments into several protostellar cores. Even with $< 10^{-5} Z_{\odot}$, where dust cooling is not effective, the spiral arms on the accretion disk fragments into tiny blobs. We call these two modes as *filament fragmentation* and *disk fragmentation*, respectively.

We also find that the cloud fragmentation occurs only one out of four clouds, contrary to the accepted notion that clouds would be likely to fragment above the metallicity where dust cooling is efficient. We here focus on the case with filament fragmentation. In the cases where the filament fragmentation fails, H_2 formation heating stabilizes the gas to make the cloud rounder. Even though dust cooling is efficient at higher densities, the timescale for the cloud elongation and fragmentation becomes longer than the dynamical timescales for most of clouds with $Z > 10^{-5} Z_{\odot}$. Meanwhile, in some cases with fragmentation, the heating mechanism does not work, or compensated by OH/ H_2O line cooling. We for the first time find that the diversity of the thermal evolution stems from the collapse timescale t_{col} of the clouds, which varies among the clouds. In a slowly collapsing cloud, the gas temperature becomes lower throughout the collapse due to the less efficient gas compressional heating. For different thermal paths, the clouds enter the regime where the different cooling/heating processes are dominant.

Acknowledgment

I would like to express the deepest appreciation to my academic advisor, Naoki Yoshida, who introduced to me such a interesting research topic in my Ph.D. course. His deep insight in the various fields of astrophysics, fluid dynamics, cosmology, and numerical simulation helps me to attack the problems in conducting the researches. I am deeply grateful to my main collaborators, Takaya Nozawa, Raffaella Schneider, Kazuyuki Omukai, and Shingo Hirano for their sophisticated knowledge and invaluable discussion, which helps me to obtain great results. I can finish this work by the help of the other collaborators: Stefania Marassi, Marco Limongi, and Alessandro Chieffi. I am also grateful to Kohji Yoshikawa, Takayuki Saitoh, Takashi Hosokawa, Hajime Susa, Nozomu Tominaga, Kohei Inayoshi, Takashi J. Moriya, Thierry Sousbie, John H. Wise, Andrea Ferrara, Simon C. O. Glover, Ke-Jung (Ken) Chen, Anastasia Fialkov, Shu-ichiro Inutsuka, Toru Tsuribe, Tomoaki Matsumoto, and Kengo Tomida for fruitful discussion and helpful comments. I would like to thank the examiner, Noriko Yamasaki (chief), Synge Todo, Takao Nakagawa, Fujihiro Hamba, and Kazuhiro Nakazawa for their indications which improve the quality of my Thesis.

During my six-year life of Ph.D. course, I spend the first one year in Hongo Campus in the University of Tokyo, next one year in the Kavli Institute for Physics and Mathematics of Universe (K-IPMU) in Kashiwa Campus, and finally in the University of Tokyo Theoretical Astrophysics (UTAP) in Hongo Campus. I would like to thank to all the members and staffs in the laboratories. I have led a very fun life with the laboratory members. The experiences have kept encouraging me to solve the daily problems in pursuing the researches. I also deeply thank to Daiki Shibata, Kotaro Otomura, and Daigo Umemoto who have cheered me up in writing the Thesis.

Finally, I am deeply grateful to my family, who continue to support for my life.

The numerical simulations are carried out on Cray XC30 at Center for Computational Astrophysics, National Astronomical Observatory of Japan, and on COMA at Center for Computational Sciences in University of Tsukuba. This work is supported by Research Fellowships of the Japan Society for the Promotion of Science (JSPS) for Young Scientists.

Contents

1	Introduction	1
1.1	Formation of the first low-mass stars	1
1.1.1	Origin of the most primitive stars	1
1.1.2	Transition of the typical stellar mass	2
1.2	Basics of star formation	4
1.2.1	From interstellar medium to stars	4
1.2.2	Cloud fragmentation	7
1.3	Fragmentation criteria	10
1.3.1	Chemo-thermal evolution of collapsing cloud	10
1.3.2	Metal cooling	10
1.3.3	Dust cooling	11
1.3.4	Three-dimensional simulations	21
1.4	Aims of the thesis	23
1.4.1	Grain growth and the Pop III supernova models	23
1.4.2	Three-dimensional simulations	24
1.5	Structure of thesis	26
2	Chemical reactions and cooling rates	27
2.1	Cooling and heating processes	27
2.1.1	Radiative cooling	27
2.1.2	Chemical heating and cooling	36
2.1.3	Dust thermal emission	37
2.2	Chemical reactions	38
2.2.1	Gas-phase chemistry	39
2.2.2	Grain growth	45
3	Grain growth and its effect on cloud fragmentation	47
3.1	Overview	47
3.2	Dust models in the early Universe	48
3.2.1	Pop III supernova model	48
3.2.2	Difference of two models	51
3.2.3	Dust property	53
3.2.4	Setup	54
3.3	Overall thermal evolution of clouds	54
3.3.1	Important chemical and thermal processes	54
3.3.2	Effect of grain growth	58
3.4	Conditions for cloud fragmentation	59
3.4.1	Critical dust-to-gas mass ratio without grain growth	59

3.4.2	Critical metallicity	60
3.5	Implication for the observed primitive stars	63
3.6	Chapter summary	65
4	Zoom-in simulation scheme based on the Voronoi diagrams	67
4.1	Overview	67
4.2	Basics of the particle splitting	68
4.3	Strategy	69
4.3.1	Algorithm of Voronoi tessellation	71
4.3.2	Distribution of daughters	71
4.4	Bodenheimer test	81
4.4.1	Setup	81
4.4.2	Results	81
4.5	Collapse simulations of primordial gas cloud	84
4.5.1	Setup	84
4.5.2	Resulting density structures	85
4.6	Discussion	88
4.6.1	Implication for the gas fragmentation	88
4.6.2	Computational time	89
4.6.3	Resolution test	89
4.7	Chapter summary	90
5	Fragmentation properties of metal deficient clouds	93
5.1	Overview	93
5.2	Numerical method	94
5.2.1	Hydrodynamics and particle splitting	94
5.2.2	Chemistry and cooling in collapse phase	95
5.2.3	Accretion phase	95
5.2.4	Initial conditions	96
5.3	Evolution of uniform clouds	102
5.4	Cloud fragmentation	104
5.4.1	Overall features	104
5.4.2	Filament fragmentation	106
5.4.3	Disk fragmentation	125
5.5	Gas accretion onto protostars	125
5.5.1	Overall features	125
5.5.2	Detail cloud evolution	126
5.6	Discussion	130
5.7	Chapter Summary	132

6 Conclusion	135
6.1 Summary	135
6.2 Concluding remarks	139
Bibliography	141

Contents

1.1	Formation of the first low-mass stars	1
1.1.1	Origin of the most primitive stars	1
1.1.2	Transition of the typical stellar mass	2
1.2	Basics of star formation	4
1.2.1	From interstellar medium to stars	4
1.2.2	Cloud fragmentation	7
1.3	Fragmentation criteria	10
1.3.1	Chemo-thermal evolution of collapsing cloud	10
1.3.2	Metal cooling	10
1.3.3	Dust cooling	11
1.3.4	Three-dimensional simulations	21
1.4	Aims of the thesis	23
1.4.1	Grain growth and the Pop III supernova models	23
1.4.2	Three-dimensional simulations	24
1.5	Structure of thesis	26

1.1 Formation of the first low-mass stars

1.1.1 Origin of the most primitive stars

The recent observations of the extremely metal-poor (EMP) stars with ~ 10 Gyr lifetimes in the Galactic halo direct the questions on their origin. For example, SDSS J102915 + 172927 (hereafter, SDSS J1029 + 1729) is the most primitive star ever observed (Caffau et al. 2011). The metallicity of the star is very low $< 4.5 \times 10^{-5} Z_{\odot}$. By their long lifetime and small metal content, these stars are the second or very early-generation of stars after the first-generation metal-free (Population III, or Pop III) stars, born in an interstellar medium polluted by the Pop III supernovae (Audouze and Silk 1995) as indicated in

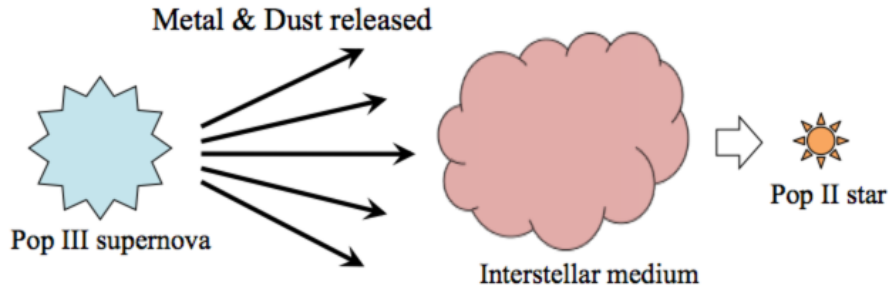


Figure 1.1: Conceptual image of the metal pollution of an interstellar cloud from Pop III supernovae.

Figure 1.1. The mass of SDSS J1029 + 1729 is estimated as $0.8 M_{\odot}$. Also, the most iron-poor star SMSS J031300.36 – 670839.3 ($[\text{Fe}/\text{H}] < -7.1$; hereafter SMSS J0313 – 6708) is low-mass (Keller et al. 2014).

The origin of such low-mass EMP stars is still unknown. The abundance patterns of observed primitive stars indicates that there exist the very massive first-generation stars because of the enhancement of carbon relative to iron (see below). The transition point from the massive Pop III stars to the low mass Pop II/I stars is important in the cosmological and astrophysical contexts. The early massive stars have been considered to cast the first light in the Universe, triggering the first cosmic reionization in the intergalactic medium (Haiman and Loeb 1997; Ferrara 1998). Whereas, the low-mass stars are responsible to emit the far infrared, inducing the dissociation of the hydrogen molecules, which are important coolant in star formation (Haiman et al. 1997; Omukai 2001). The stellar mass plays the crucial roles in determining the history of the global star and galaxy formation. Also, the massive stars can release metal and dust by their supernova explosion. The mass function of the stars significantly affect the evolution of the chemical abundances in the early Universe. The transition of stellar mass scale is thus important to determine the metal enrichment process and the stellar mass function in the early Universe.

1.1.2 Transition of the typical stellar mass

It has been considered that the typical stellar mass reduces in the course of metal enrichment in interstellar media. Recent observations begin to restrict the metallicity which triggers the stellar mass transition. It might be indirectly shown the first stars are predominantly massive. Most of the EMP stars have the C-excess feature (Christlieb et al. 2004; Beers and Christlieb 2005; Norris et al. 2007; Frebel et al. 2008; Keller et al. 2014). Especially, the star SMSS J0313 – 6708, most iron-poor star with $[\text{Fe}/\text{H}] \simeq -7.1$, shows the significant carbon-excess $[\text{C}/\text{Fe}] \gtrsim 4.5$. The progenitor star with intermediate masses of $10\text{--}70 M_{\odot}$ is favored as the polluter of the formation site of the star. To explain the

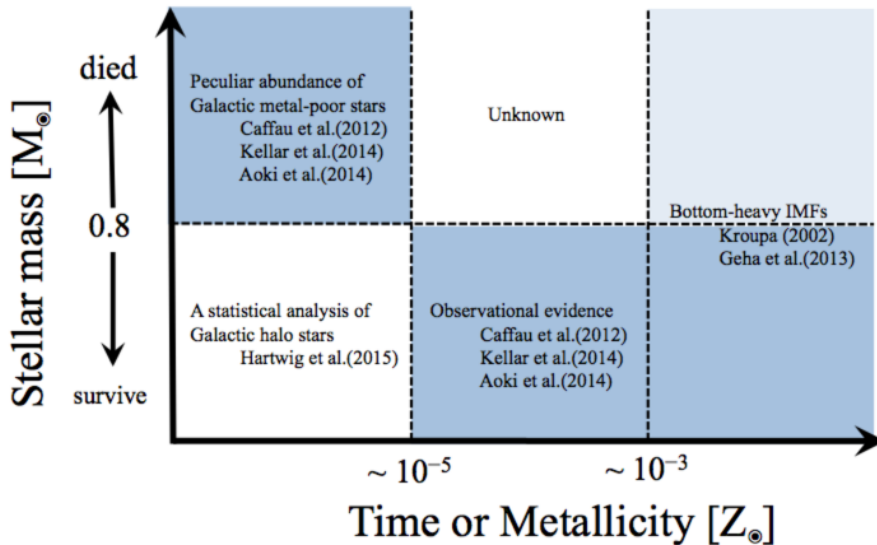


Figure 1.2: Schematic illustration of the mass transition in the early Universe (metal-poor regimes). In the darker colored region, the fraction of the stars is larger.

significant enhancement of carbon relative to iron, the mixing-fall back scenario is suggested (Joggerst et al. 2009; Umeda and Nomoto 2003). In the model, the inner region rich with the heavier elements such as iron is fallen back into the supernova remnant by the mixing effect by the Rayleigh-Taylor instability.

We also comment that Pop III stars would have the wide range of mass. The star SDSS J1029 + 1729, which shows the moderate α -element enhancement, has the abundance similar to the progenitor Pop III star with 20–50 M_{\odot} (Schneider et al. 2012b). The peculiar abundance feature is shown in most recently discovered halo star SDSS J001820.5 – 093939.2 ($[\text{Fe}/\text{H}] = -2.5$) in the following three points. First, the star have the very small abundance of light elements such as C and Mg relative to Fe ($[\text{C}/\text{Fe}] = -0.84$ and $[\text{Mg}/\text{Fe}] = -0.52$), which suggest the violent nucleosynthesis by a very massive star. Second, the ratio of elements with adjacent even and odd atomic number is very large (e.g. $[\text{Co}/\text{Ni}] = -0.77$). Third, even the upper limits of the neutron-capture elements such as Sr and Ba are small. The intermediate mass Pop III star model (25 M_{\odot}) can be well fitted with the overall feature of the stellar abundance, but the large ratio of even- and odd-elements can not be explained. The pair-instability supernova (PISN) model for more massive star even with 1000 M_{\odot} can simultaneously explain the low abundance of lighter elements and the large even/odd ratio.

While we have seen the traces of the high-mass primordial stars even indirectly, there are almost no sign of the existence of the low-mass primordial stars. Hartwig et al. (2015) perform the semi-analytic calculations to follow the history of the surviving primordial stars from their formation in less-massive dark matter halos. This hosting halos undergo the merger and are eventually accreted into the Milky Way-like halo. They estimate the

fraction of the primordial star avoiding the metal pollution during the merger history. For a given minimal mass of the Pop III star, the fraction is determined. If the stars have the mass less than $0.8 M_{\odot}$ (Raiteri et al. 1996), these stars can be observed in the Galactic halo. Despite the energetic observational campaign by Hamburg/European Southern Observatory (ESO) survey for $\sim 4 \times 10^6$ Galactic halo stars, any metal-free stars have not been discovered. From this fact, they can draw the minimal mass of Pop III stars. The hypothesis that the lower limit of the Pop III stellar mass is less than $0.8 M_{\odot}$ can be ruled out at the 68% confidence level by the observations so far.

This would suggest that the first star is considered to be predominantly massive. The numerical studies also support the statement (Bromm et al. 1999, 2002; Abel et al. 2000, 2002; Yoshida et al. 2003). They start their simulations from the cosmological structure formation, and then pick up the primordial minihalo to follow the collapse of the hosted cloud. The primordial gas does not contain heavy elements. Due to the large gas temperature for the lack of efficient coolant but hydrogen molecules, they monolithically contracts without fragmentation. When the gas becomes optically thick, a protostar with the mass of $\sim 0.1 M_{\odot}$ is formed at the central region. Since the ambient gas remains Jeans unstable, the protostar undergoes the mass accretion. The mass accretion phase is followed by Hosokawa et al. (2011) and Hirano et al. (2014) until the gas infall is halted by the ultraviolet emission from the central embryo star. The mass spectrum obtained by the ~ 100 Pop III star spread widely from several tens to thousands solar masses.

We here return to the observed metal-deficient stars (Population II stars). Their own masses are very small: $0.8 M_{\odot}$ for SDSS J1029 + 1729 (Caffau et al. 2012) and $0.5 M_{\odot}$ for SDSS J0018 – 0939 (Aoki et al. 2014). Besides, the massive stars are very rare objects among the present day metal-rich stars (Population I stars) whose initial mass spectrum has the spectral index of -2.35 (Salpeter 1955). The peak mass of the member stars in the nearby clusters are $\sim 0.1 M_{\odot}$ (Kroupa 2002). Such bottom-heavy stellar mass function is also seen in the ultra-faint dwarf galaxies. The spectral index is 1.2–1.3 for these galaxies with metallicity $[\text{Fe}/\text{H}] = -2.5$ – -2.4 (Geha et al. 2013). Although the fraction of the massive stars in the extremely low metallicity 10^{-5} – $10^{-3} Z_{\odot}$, we can expect that the transition of the typical stellar mass might be occur within the metallicity range from massive to low-mass with increasing metallicity. The above discussion is summarized in Figure 1.2.

1.2 Basics of star formation

1.2.1 From interstellar medium to stars

1.2.1.1 Run-away collapse phase

We in this section briefly discuss the basic physical process of the star formation. Figure 1.3 shows the schematic image of the star formation process. Stars are formed when an interstellar gas is attracted by its self-gravity. The gas temperature is nearly isothermal at

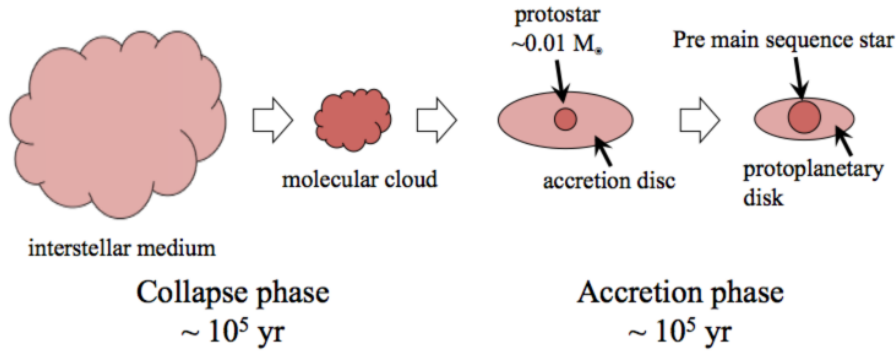


Figure 1.3: Process of the star formation from an interstellar medium to a star.

~ 10 K in the present-day, which is determined by the photoelectric heating by irradiated grains and the line cooling (e.g. Spitzer 1978). In the primordial gas, the temperature is ~ 1000 K by the balance between the adiabatic compressional heating and H_2 molecular line cooling (e.g. Yoneyama 1972). Since the gas contracts by the balance between the pressure gradient force and the gravity, the density profile becomes rather inhomogeneous. The inhomogeneity leads a part of the gas to be attracted to the central region. As the collapse proceeds, i.e. as the central density increases, the core size and the mass become smaller. This means that, in the coordinate comoving with the fluid, the core shrinks in the course of time. In other words, in the frame of the core, the gas in the outer region is seen to go outward. Therefore, such a form of the collapse is called the *run-away collapse* (Larson 1969).

It is known that the physical quantities of the collapsing cloud have the self-similar solution. We obtain the solution based on the procedure of Hanawa and Matsumoto (2000). The basic equations are

$$\frac{\partial \rho}{\partial t} + \nabla \cdot (\rho \mathbf{v}) = 0, \quad (1.1)$$

$$\frac{\partial(\rho \mathbf{v})}{\partial t} + \nabla \cdot (\rho \mathbf{v} \otimes \mathbf{v}) + \nabla p + \rho \nabla \phi = 0, \quad (1.2)$$

$$\Delta \phi = 4\pi G \rho, \quad (1.3)$$

where ρ , \mathbf{v} , p , ϕ are the density, velocity, pressure, and gravitational potential, respectively. In the isothermal gas, the equation of state is written as $p = \rho c_T^2$, where c_T is the isothermal sound speed. We here introduce the zoom-in coordinate as

$$\boldsymbol{\xi} = \frac{\mathbf{r}}{c_T(t_0 - t)}, \quad (1.4)$$

$$\tau = -\ln(1 - t/t_0), \quad (1.5)$$

where t_0 is the time where the density of the cloud center diverges. We introduce the

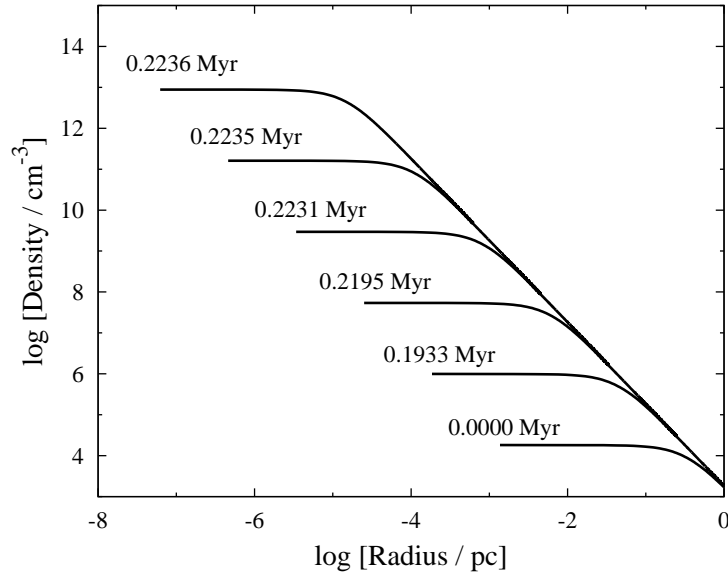


Figure 1.4: Density profile of the cloud in the run-away collapse phase. The calculation is started when the central density is 10^4 cm^{-3} . The number attached to each curve is the elapsed time.

dimensionless variables as

$$D = 4\pi G\rho(t_0 - t)^2, \quad (1.6)$$

$$\mathbf{V} = \frac{\mathbf{v}}{c_0} + \frac{\mathbf{r}}{c_0(t_0 - t)}. \quad (1.7)$$

$$\Phi = \frac{\phi}{c_T^2}. \quad (1.8)$$

By imposing the spherical symmetry, we obtain the equations for the dimensionless quantities as

$$\frac{\partial V}{\partial \xi} + \frac{V}{D} \frac{\partial D}{\partial \xi} = 1 - \frac{2V}{\xi}, \quad (1.9)$$

$$V \frac{\partial V}{\partial \xi} + \frac{1}{D} \frac{dp}{dD} \frac{\partial D}{\partial \xi} + \frac{\partial \Phi}{\partial \xi} = V, \quad (1.10)$$

$$\frac{\partial \Phi}{\partial \xi} = \frac{1}{\xi^2} \int_0^\xi D(\xi') \xi'^2 d\xi' = DV. \quad (1.11)$$

We numerically solve these equations to obtain the dimensionless variables D and V as a function of ξ with the temperature 10 K. Figure 1.4 shows the dimensional form of the density profiles in a course of time from bottom to top. We find that the time intervals becomes shorter as the central density increases. The dynamical time of the cloud is limited to the central density $n_{\text{H,cen}}$ as $\propto n_{\text{H,cen}}^{-1/2}$. We also notice that the core region, which we define as the central flat region, shrinks as discussed above.

1.2.1.2 Accretion phase

After the central core region becomes optically thick, the gas turns to be evolve adiabatically. The gas becomes opaque at $n_{\text{H}} \sim 10^{12} \text{ cm}^{-3}$ due to the grain absorption in the solar neighborhood, or at $\sim 10^{16} \text{ cm}^{-3}$ in the primordial gas (Omukai 2000). In the optically thick regime, since the further collapse is almost halted due to the large pressure gradient, a hydrostatic core, so-called the *first core*, is formed (Larson 1969; Masunaga and Inutsuka 2000). The gas around the core still has the infall velocity, and is accreted onto the core. This secondary phase in the star formation process is called *accretion phase*. Since the gas accretion is determined by the balance between the thermal pressure and the gravity, the rate of the mass accretion depends on the gas temperature as $\sim c_{\text{T}}^3/G$ in the ambient gas and G is the gravitational constant (Shu 1977; Shu et al. 1987).

In the first core, the gas density further increase because of the gas accretion. The temperature also increases adiabatically. When the temperature reaches $\sim 2000 \text{ K}$, the H_2 begins to be dissociated. The most of the thermal energy is converted into the binding energy of the molecule (4.48 eV for each molecule), the specific heat ratio $\gamma = d \ln T / d \ln \rho + 1$ is again below the critical value $4/3$. The gas again begins to contract, and the phase is called *second collapse phase*. This lasts until the almost all hydrogen molecules are depleted, and then the core defined by an accretion shock (*second core*, or *protostar*) is formed. After the temperature of the protostar becomes above the threshold value for the nucleosynthesis, a star eventually forms. The typical lifetime of the protostar is considered to be $\sim 10^5 \text{ yr}$.

1.2.2 Cloud fragmentation

So far we have seen the basic physical process of the star formation. The discussion gives us the implication that the stellar mass is determined by the gas accretion rate onto protostars. Since the rate is proportional to $T^{1.5}$, the mass of the eventually formed stars would be smaller in the cooler cloud if the accretion timescales are not significantly changed. The gas cooling efficiency increases with increasing metal because of its larger cooling efficiency than the primordial species, and thus it can explain the stellar mass transition as the metallicity increases in the early Universe.

The more drastic reduction of the stellar mass is expected if the cloud fragmentation occurs. We here focus on the no-turbulence case for simplicity. The fragmentation occurs only by the thermal process. The gas fragmentation is considered to occur through sheet or filament formation (e.g. Inutsuka and Miyama 1992). The linear analysis of the growth rate of the bar-mode perturbations on a spherical cloud is performed by Hanawa and Matsumoto (2000) and Lai (2000). The cooling/heating efficiency is parametrized by the specific heat ratio γ , and the perturbation amplitude is expressed by the cloud ellipticity $\mathcal{E} = a/b - 1$, where a and b are the major- and minor-axes of the cloud. The growth rate of the perturbation can be translated into the dependence of the cloud ellipticity \mathcal{E} on the density with the power-law index n as $\mathcal{E} \propto \rho^n$. The positive n means the growth

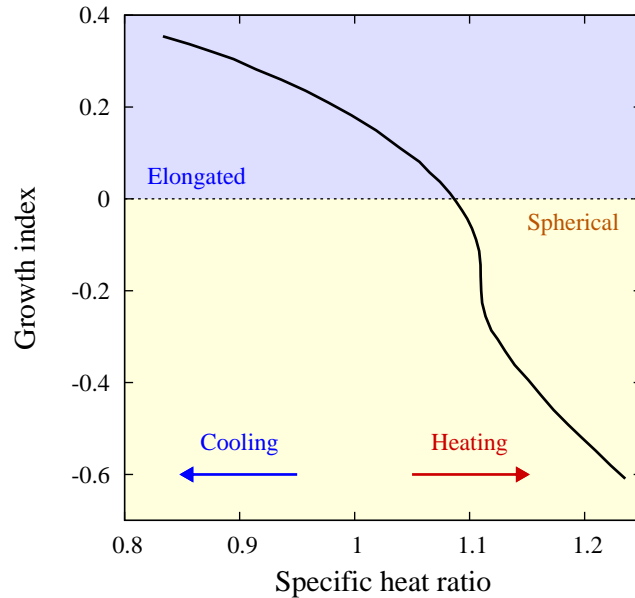


Figure 1.5: Growth index n as a function of the gas specific heat ratio γ . The cloud becomes elongated by the gas cooling $\gamma \lesssim 1$ in the blue-shaded region. That is, the cloud ellipticity increases as $\mathcal{E} \propto \rho^n$ with positive n . The cloud becomes rounder by the gas heating $\gamma \gtrsim 1$ with negative n .

of the bar-mode perturbation, while the negative n means the stabilization. When n keeps positive for a sufficiently long time, the cloud becomes thin filament or disk. When n keeps negative for a sufficiently long time, the cloud shape becomes round. Figure 1.5 shows the dependency of the growth index n on the specific heat ratio γ . As easily expected, the cloud elongation is promoted with the efficient cooling ($\gamma < 1$) while the cloud is likely to be spherical with the heating ($\gamma > 1$).

From the above discussion, we can draw a scenario of the cooling-induced fragmentation as follows and as shown in Figure 1.6. First, when the rapid cooling occurs, the gas elongation is promoted to form disk or filamentary structures. After the cloud further collapses, and the density of the perturbations becomes above the quantity where the cooling becomes inefficient, each density clump begins to contract in a spherical manner. The important point is that the mass scale of the fragments is comparable to the Jeans mass at the density and temperature when the cooling ceases as indicated by orange star in Figure 1.6.

The fragmentation on a filament is numerically confirmed by [Tsuribe and Omukai \(2006\)](#). In their simulation, the gas has initially negative specific ratio, mimicking the radiative cooling effect, and then the specific heat ratio is switched to positive. The fragmentation occurs on the filament kicked in by the gas cooling. We should note that the fragmentation is promoted only when the cloud ellipticity becomes above a critical

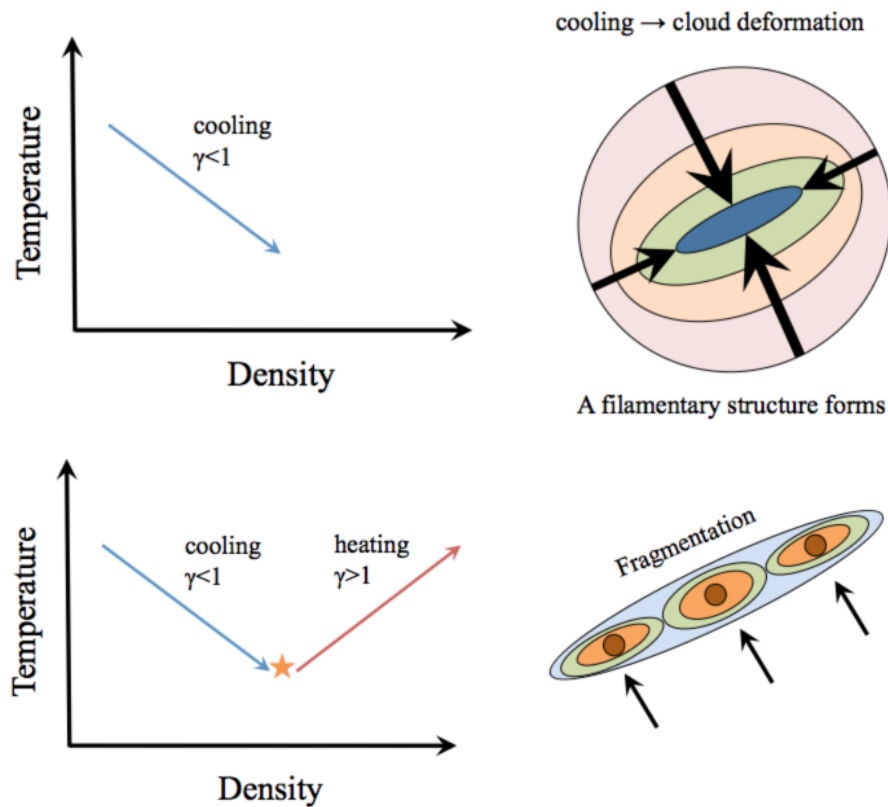


Figure 1.6: Schematic view of the fragmentation scenario. *Top*: the bar-mode perturbation on an originally spherical cloud grows at the time (density) where the cooling efficiency dominates over the heating process. The gas eventually becomes in the form of sheet or filament. *Bottom*: when the density of the perturbation on the filament enters the regimes where the cooling efficiency is reduced, the perturbations are stabilized to become rounder separately. That is the fragmentation due to the thermal processes.

value, 30, until the cooling becomes ineffective. This means that radiative cooling should last for sufficiently long time to induce the fragmentation.

1.3 Fragmentation criteria

1.3.1 Chemo-thermal evolution of collapsing cloud

In this section, we see the important cooling/heating mechanism which enhance/suppress the cloud elongation and fragmentation. Even a trace of metal plays an important role as an additional cooling channel in collapsing cloud. The kinetic energy is converted to the radiative energy by the line transition of C⁺ ions, C and O atoms, and CO, OH, and H₂O molecules (e.g. [Bromm and Loeb 2003](#)). Dust thermal emission is the another important cooling mechanism, which becomes effective even with the extremely small metallicity $\sim 10^{-5} Z_{\odot}$ (e.g. [Omukai 2000](#)). In more detail, such gas cooling deforms the gas by inducing aspherical perturbations on the cloud surface. The gas cooling can be parametrized by the specific heat ratio.

The mass scale of the fragments are determined as the Jeans mass

$$M_J = \frac{\pi^{5/2} c_T^3}{6G^{3/2} \rho^{1/2}}, \quad (1.12)$$

at the density and temperature where the cooling ceases. The physical reasons why the cooling efficiency becomes smaller is different among coolants. H₂, HD, C I, C II, and O I line cooling becomes ineffective because the line population becomes the local thermal equilibrium (LTE) one. CO, OH, and H₂O rotational lines becomes optically thick before their populations reaches LTE. The dust thermal emission becomes weakened because the heat exchange between cold grains and hot gas particles are completed at a density just before the continuum emission becomes optically thick. We will revisit the cooling mechanisms in more detailed manner in Chapter 2. We emphasize that the different cooling mechanisms will yield the cloud fragmentation with different mass scales.

1.3.2 Metal cooling

Some researchers have considered that the metal line cooling trigger the gas cooling ([Bromm and Loeb 2003](#); [Frebel et al. 2005](#); [Santoro and Shull 2006](#); [Maio et al. 2007](#)). In gas clouds, cooling due to C II and O I becomes important for $Z \gtrsim 10^{-3.5} Z_{\odot}$. Such the idea gives the simple formula to the critical condition where the low-mass and low-metallicity stars are formed. [Frebel et al. \(2007\)](#) present the critical discriminant by assuming that the cloud have the similar abundance pattern to the present-day. The critical condition will be given by the balance between the gas compressional heating Γ_{aid} and C II and O I cooling as

$$\Lambda_{\text{C II}} + \Lambda_{\text{O I}} > \Gamma_{\text{adi}}. \quad (1.13)$$

Gas compressional heating per unit volume is given as

$$\Gamma_{\text{adi}} = \rho p \frac{d}{dt} \left(\frac{1}{\rho} \right) \sim \frac{p}{t_{\text{ff}}} = 2 \times 10^{-23} \text{ erg cm}^{-3} \text{ s}^{-1} \quad (1.14)$$

at the characteristic density $n_{\text{H}} = 1 \times 10^4 \text{ cm}^{-3}$, temperature $T = 300 \text{ K}$, and the mean molecular weight $\mu = 1.2$. At the state, the cooling rates of C II and O I are

$$\Lambda_{\text{C II}} = 6 \times 10^{-20} \frac{A_{\text{O}}}{A_{\text{O},\odot}} \text{ erg cm}^{-3} \text{ s}^{-1}, \quad (1.15)$$

$$\Lambda_{\text{O I}} = 2 \times 10^{-20} \frac{A_{\text{C}}}{A_{\text{C},\odot}} \text{ erg cm}^{-3} \text{ s}^{-1}. \quad (1.16)$$

Given the abundances of C and O, the condition of Equation (1.13) can be rewritten as

$$D_{\text{trans}} \equiv 10^{[\text{C}/\text{H}]} + 0.3 \times 10^{[\text{O}/\text{H}]} > 10^{-3.5}. \quad (1.17)$$

Here, they introduce the *transition discriminant* D_{trans} . This simple discriminant can explain the formation of the low-mass stars in the Galactic halo (Ji et al. 2014). For the most iron-poor star SMSS J0313 – 6708, $D_{\text{trans}} = 10^{-2.4}$ for the abundances fitted by the three-dimensional atmospheric model. Although we should note that the oxygen abundance here is the upper limit, the abundance of the even very primitive star satisfies the critical condition for which the carbon and oxygen cooling is effective. That is because the majority of such primitive star have the carbon-enhanced feature relative to the solar abundances. Equation (1.17) seems to well explain the origin of the second-generation metal-poor stars.

1.3.3 Dust cooling

However, C II and O I cooling becomes effective even at small density 10^4 cm^{-3} where the Jeans mass is very large $\sim 10^4 M_{\odot}$ (see Chapter 2). The stellar mass would finally reduced by the succeeding run-away collapse, it is difficult to describe the formation of low-mass stars which survives until the present-day. Also, carbon ions are recombined at the density $\sim 1 \text{ cm}^{-3}$ soon after an interstellar medium begins to collapse gravitationally. As another important cooling channel, several authors focus on the dust thermal emission. The cooling becomes effective at higher density $n_{\text{H}} \sim 10^{12}\text{--}10^{15} \text{ cm}^{-3}$, where the Jeans mass is $\sim 0.1 M_{\odot}$. Therefore, the dust is to be taken into consideration although their properties (abundances and size distribution) is still unclear especially in the early Universe as well as in the present-day.

1.3.3.1 Basic idea

Omukai (2000) present that the metal cooling becomes ineffective at $n_{\text{H}} \sim 10^4 \text{ cm}^{-3}$. The population reaches the local thermal equilibrium (LTE). They also indicate that

the carbon ion is depleted into carbon atoms by chemical reactions. During the gas collapse, the complex chemical reaction and radiative cooling of relevant chemical species are important in the gas. To save the computational cost, we can focus on these processes only in the core region (within the Jeans scale) in the run-away collapse era, when the central region shrinks and envelope is left to fall. In other words, the gas has the outfall velocity on the comoving frame of the core. Such an idea is presented first by [Hayashi and Nakano \(1965\)](#) for a primordial cloud. They follow the evolution of the equilibrium temperature as a function of density. There, the core density is the indicator of the elapsed time because it in general monotonically increases during the collapse.

However, the timescale of the chemical reactions are comparable to the dynamical timescales of collapsing clouds. We should take care of the non-equilibrium chemistry. [Omukai \(2000\)](#) refine the model by including the non-equilibrium chemical reaction networks and cooling rates relevant to the cloud collapse with a wide range of metallicities 0–1 Z_{\odot} . In the central region, the density increases with the order of the free-fall timescale $\sim t_{\text{ff}}$. At each given density, the temperature is solved by integrating the cooling and heating rate. The cooling and heating rates are obtained as the function of the density, temperature, and the abundance of the corresponding species in the self-consistent manner.

Strictly speaking, the timescale of the collapse

$$t_{\text{col}} = \frac{\rho}{d\rho/dt} \quad (1.18)$$

is the function of the cooling and heating efficiency. When the heating is dominant over the cooling, the collapse becomes slower because of the increasing pressure gradient more rapidly than the gravitational force inward the cloud center. Since the net cooling efficiency can be parametrized by the specific heat ratio

$$\gamma = \frac{d \ln T}{d \ln \rho} + 1, \quad (1.19)$$

t_{col} can be written as the functional form of γ . By [Larson \(1969\)](#), the ratio $f_{\nabla p}$ of the pressure gradient to the gravitational force is given as 0.6 in the isothermally collapsing cloud ($\gamma = 1$). From the self-similar solutions for clouds with various γ , the functional form of f is given as

$$f_{\nabla p} = \begin{cases} 0 & (\gamma < 0.83) \\ 0.6 + 2.5(\gamma - 1) - 6.0(\gamma - 1)^2 & (0.83 < \gamma < 1) \\ 1.0 + 0.2(\gamma - 4/3) - 2.9(\gamma - 4/3)^2 & (\gamma > 1) \end{cases} \quad (1.20)$$

The collapse time is proportional to $1/\sqrt{1 - f_{\nabla p}}$ ([Larson 1969](#)). Then, [Omukai et al. \(2005\)](#) estimate the ratio of the collapse timescale to the free-fall timescale as

$$t_{\text{col}} = \frac{1}{\sqrt{1 - f_{\nabla p}}} t_{\text{ff}}. \quad (1.21)$$

Table 1.1: Properties of grains

Species	$f_{\text{dep},i,0}$ [%]
Iron	1.265
Forsterite	12.550
Enstatite	3.665
Carbon	4.897
Troilite	2.845
Total	25.222

Note — Initial depletion factor $f_{\text{dep},i,0}$ of grain species i relative to total mass of heavy elements. We do not include ices and organics, and assume that carbon nuclei are all depleted into amorphous carbon grains.

We will revisit to check the validity of the model in Chapter 5.

Again, the abundances of heavy elements, condensation efficiency of the metal into grains, abundances of grain species, and dust size distribution are highly unknown although they critically determine the cooling efficiency of the gas. Omukai (2000) assume the present-day dust, where the refractory elements such as silicon, magnesium, and iron are all depleted into grains according to the dust model of Pollack et al. (1994). It should be noted that the metal and dust properties in the early star-forming clouds are different from those in the present-day. If the metal abundances are imprinted by a Pop III supernova, which is the first metal polluter, the abundances of lighter elements such as C and O relative to Fe are greater than in the Solar system. The depletion efficiencies of heavy elements onto grains are smaller as demonstrated by the observations of high-redshift damped Lyman α systems (Schady et al. 2010; Zafar et al. 2011). Table 1.1 shows the grain species which we consider here and their mass fraction relative to heavy elements.

Here, we calculate the thermal evolution of clouds with various metallicities $0-1 Z_{\odot}$, employing the present-day metal and dust model according to the recipe presented by Omukai (2000). The number fraction of carbon and oxygen nuclei relative to hydrogen are 2.015×10^{-4} and 4.956×10^{-4} , respectively. If neglecting ices and organics, which are sublimated in warm metal-poor clouds, 25% of oxygen are depleted into grains. We assume that 54% of carbon nuclei is condensed into amorphous carbon grains, whereas a fraction of carbon nuclei are locked into organics in the original calculations by Omukai et al. (2010). Further, we do not include dust sublimation. These modifications from the original calculations do not have significant effects on the thermal evolution of the clouds.

Figure 1.7 shows the results of the calculations with metallicities 0, and 10^{-6} to $1 Z_{\odot}$ every 1 dex from top to bottom. The temperature in the cloud cores tend to decrease with increasing metallicities. Each evolutionary tracks passes the regimes where the different cooling/heating processes are important. We can predict that the gas fragmentation occurs at the density where the temperature dip appears. In a quantitative manner, the

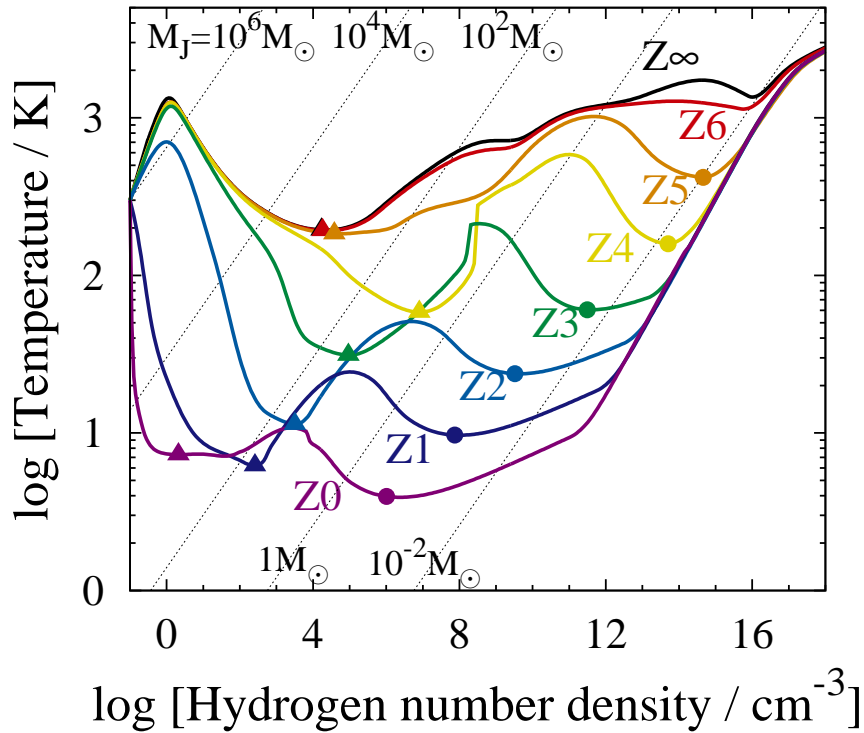


Figure 1.7: Temporal evolution of temperature in a cloud center in the primordial case (black; labeled “ Z_∞ ”), and with metallicities $Z = 10^{-6} - 1 Z_\odot$ (“ $Z_6 - Z_0$ ”) from top to bottom. The thin black dotted lines indicate the Jeans masses at corresponding densities and temperatures. The triangles and circles are plotted at the density and temperature where the condition for the cloud fragmentation into massive ($> 0.8 M_\odot$) and low-mass ($< 0.8 M_\odot$) cores, respectively, is satisfied.

gas fragmentation occurs under the condition as

- the specific heat ratio γ is less than 0.8 for the core to be elongated, and
- γ becomes conservatively 0.97 after the gas cooling

as presented by [Schneider and Omukai \(2010\)](#). The critical values of γ (0.8 and 0.97) in the above criterion is determined from the several three-dimensional simulations for the gases with the various specific heat ratios ([Li et al. 2003](#); [Tsuribe and Omukai 2006](#)). Each evolutionary track undergoes the temperature dip at most at two densities as indicated by triangles and circles. The triangles (circles) depict the density and temperature where the gas is expected to fragment into clumps with the mass larger (smaller) than $0.8 M_{\odot}$. If the mass of stars which eventually form is less than $0.8 M_{\odot}$, the stars can survive for more than the Hubble time ([Raiteri et al. 1996](#)).

With 0, 10^{-6} and $10^{-5} Z_{\odot}$, the temperature dip appears at the density $\sim 10^4 \text{ cm}^{-3}$, where H_2 line cooling is effective although the abundance of H_2 molecule is still $y(\text{H}_2) \sim 10^{-4}$. At the density, the gas fragmentation is expected to occur. We indicate the Jeans mass, and the density and temperature where the temperature dip appears corresponds to $\sim 10^3 M_{\odot}$. This suggests that the clump of $\sim 10^3 M_{\odot}$ is formed and, if the most of the gas eventually fall into the central protostars, massive stars are expected to form. This scenario can be demonstrated by several three-dimensional simulations (e.g. [Abel et al. 2002](#); [Bromm et al. 2002](#); [Yoshida et al. 2003](#)).

With $Z > 10^{-4} Z_{\odot}$, the transition line cooling by metal ions, atoms, and molecules create the temperature dip at densities $n_{\text{H}} \sim 1\text{--}10^6 \text{ cm}^{-3}$ varying with the metallicities. Although the line cooling have been considered to be the crucial to the low-mass gas fragmentation (e.g. [Bromm and Loeb 2003](#)), the cooling efficiencies rapidly become insufficient because the line populations reach LTE or because the lines become optically thick. If the stars eventually formed have the mass comparable to the mass of the fragments, the model predicts the stellar mass of at least $\sim 10 M_{\odot}$ with metallicity $10^{-4} Z_{\odot}$. Such massive stars could not be observed in the Galactic halo.

At higher densities, corresponding to the Jeans mass of $0.01\text{--}0.1 M_{\odot}$, another temperature dip can be seen with metallicities $Z > 10^{-5} Z_{\odot}$. This is due to the dust thermal emission. Dust grains are thermally coupled with gas particles only at the large densities. This can straightforwardly explain the formation of the low-mass cores (even stars) with extremely low metallicities. The dust cooling continues to be effective until the thermal coupling between gas and dust is completed at the densities and temperatures indicated by the circles in Figure 1.7.

From the discussions above, we can define the condition for gas fragmentation into low-mass cores as

$$Z \gtrsim 10^{-5} Z_{\odot} \quad (1.22)$$

in the realm of the model where the gas fragmentation is induced by radiative cooling. Below $10^{-6} Z_{\odot}$, H_2 line cooling is efficient to induce fragmentation at $n_{\text{H}} \sim 10^3 \text{ cm}^{-3}$. In this regime, fragments of mass $\sim 10^3 M_{\odot}$ will be formed. Even with the slight

metallicity ($10^{-6} Z_{\odot}$), the cloud is in the same regime as in the Pop III cloud without metal or dust by definition. Above $10^{-5} Z_{\odot}$, transition line cooling is effective to induce fragmentation but the mass scale of fragments is still large so that the formed stars can not survive until the present-day. Yet, the gas enters the second fragmentation regime at the higher densities. We can expect that the cloud further fragment into low-mass cores with $\sim 0.1 M_{\odot}$.

1.3.3.2 Pop III supernova model

The model in the previous section can simply predict the condition for the stellar mass transition by imposing the assumption that the dust amount is simply proportional to the metal abundance (about half the metal content). However, the assumption is not in the case in the early Universe as revealed by the observations of the low-metallicity DLAs at high redshifts. First, the condensation efficiency of the metal into dust grains in the early Universe is smaller than in the present-day. Further, the diversity of the dust-to-gas mass ratio among the DLAs is significant even with similar metallicities. This implies that the star-forming clouds in the low-metallicity environment have the various dust content, or dust cooling efficiency.

The theoretical model also predict the smaller and diverse condensation efficiencies in the formation site of second-generation stars. The early dust is considered to be mainly supplied by supernovae while the present-day dust is condensed by the various channels such as supernovae, stellar wind from the low-mass asymptotic giant branch (AGB) stars, and grain growth in molecular clouds. This is because the progenitors of the supernovae has large masses ($> 8 M_{\odot}$), or short lifetimes. These massive stars die, releasing metal and dust to the ambient interstellar medium for the sufficiently short timescales relative to the formation epoch of the observed low-metallicity stars in the Galactic halo. A semi-analytic calculations predict that the AGB stars, whose hosts are less-massive, can become to release the dust 500 Myr after the pollution by the supernovae (Dwek et al. 2007). Further, the stellar wind hardly blows from the surfaces of the stars with extremely low-metallicities because the dust grains, which has the large opacities to drive the wind by the radiation pressure from beneath the atmosphere, is not abundant (Ventura et al. 2014).

Especially in the formation site of the very second-generation stars which we here focus on, the gas should be polluted with metal and dust by the supernova of the first stars. In order to consider the stellar mass transition, or the formation of the first low-mass star, it is required to employ the model of metal and dust supplied by Pop III supernovae. Fortunately, we can directly access the metal abundance of the primitive stars by the recent observations of the low-metallicity stars in the Galactic halo (Beers and Christlieb 2005; Frebel et al. 2005; Caffau et al. 2011; Keller et al. 2014; Aoki et al. 2014). These peculiar abundance relative to the solar one can be successfully reconstructed by the nucleosynthetic models of the stellar evolutions and the supernova explosion of parent Pop III stars (Umeda and Nomoto 2002; Limongi and Chieffi 2012; Tominaga et al. 2014).

The remaining uncertainties are the condensation efficiency of metals onto grains, abundance of grain species, and dust size distributions in the parent gas clouds of the low-metallicity stars. These dust properties in the collapsing clouds are significantly important to determine the dust cooling efficiency and the cloud fragmentation properties. The one of the clues is the dust contents in the high-redshift DLA systems. The semi-analytic models predict that the $\sim 1 M_{\odot}$ dust is required per supernova event to explain the dust-to-gas mass ratio in these objects (Dwek et al. 2007). From a more microscopic view, the metal condensation efficiency, dust abundances, and size distributions can be obtained by the models of the evolution of blast waves from an individual supernova (Todini and Ferrara 2001; Nozawa et al. 2003; Bianchi and Schneider 2007; Marassi et al. 2014). These models well predict the production of grains of $\sim 1 M_{\odot}$. We briefly review the dust formation and destruction processes in the supernova shocks as follows.

The efficiency of the condensation of the heavy elements into dust grains is determined by the density, temperature, and chemical composition in their formation sites. The condensation occurs in supernova ejecta rich with the heavy elements. According to the expansion of the ejecta, the temperature decreases adiabatically until $\sim 10^3$ yr after the explosion. After the temperature decreases down to an order of the sublimation temperature of a grain species, the condensation of the species begins typically several hundred years after the explosion. The process soon becomes inefficient because the almost all of refractory elements are locked into the grains. Then, the grain destruction becomes efficient at $\sim 10^4$ yr after the explosion. When the ejecta sweeps up the ambient gas with the same mass, the reverse shock is generated. The shock starts to move backward and penetrate into the ejecta which the grains have been formed. In the downstream of the reverse shock, the temperature is very high (10^7 – 10^8 K). If the grains enter the region, high-energy ions hit the grains to strip the atoms on the surfaces. The sputtering reduces the dust-to-gas mass ratio in the ejecta with a fraction of nuclei again released into the gas-phase. Consequently, both the gas-phase metal and dust are dispersed into the interstellar medium (Nozawa et al. 2007; Bianchi and Schneider 2007).

Schneider et al. (2012a) perform the same one-zone calculations as Omukai (2000, see Section 1.3.3.1) but include the metal and dust model consistently calculated with the stellar evolution of Pop III stars and hydrodynamic evolution of their supernova ejecta. They compute the metal abundances with various Pop III stellar masses M_{pr} . The three parameters of the explosion energy E_{SN} , the mass cut M_{cut} , and the mass $M(^{56}\text{Ni})$ of nickel 56 are determined so that the resulting metal abundance pattern is consistent with that of the recently discovered star SDSS J1029 + 1729. They also compute the dust formation in the expanding ejecta with a simple model mimicking the hydrodynamic evolution of the ejecta. The destruction efficiency of dust is determined by the ambient gas density ρ_{amb} . With larger ρ_{amb} , the resulting dust-to-gas mass ratio becomes smaller. They consider the four cases: without destruction (“norev”), and $\rho_{\text{amb}} = 10^{-25}$ (“rev1”), 10^{-24} (“rev2”), and $10^{-23} \text{ g cm}^{-3}$ (“rev3”).

As a result, they find that the critical metallicity above which low-mass fragmentation is induced are dependent not solely by metallicity but by the depletion factor of metal

onto grains. If the depletion factor is small, the dust cooling efficiency is also small so that the fragmentation criterion in Section 1.3.3.1 is not satisfied even with $Z \gtrsim 10^{-5} Z_{\odot}$. They conclude that not the metallicity but the initial dust-to-gas mass ratio \mathcal{D} is the direct indicator of the cooling efficiency and important to determine the fragmentation property. The critical condition can be analytically driven by the balance between the adiabatic heating rate and the dust cooling rate as

$$\Gamma_{\text{adi}} = \Lambda_{\text{d}}, \quad (1.23)$$

where Λ_{d} is the dust cooling rate per unit volume of the fluid. The properties of the dust is characterized by the geometrical cross-section S per unit dust mass. This indicates the frequency of the collision between gas and dust, and typically take the value of $\sim 10^5 \text{ cm}^2 \text{ g}^{-1}$ with a variation among the progenitor mass M_{pr} and the ambient gas density ρ_{amb} . From Equation (1.23), we obtain

$$S\mathcal{D} > 1.4 \times 10^{-3} \text{ cm}^2 \text{ g}^{-1} \left(\frac{n_{\text{H}}}{10^{12} \text{ cm}^{-3}} \right)^{-1/2} \left(\frac{T}{10^3 \text{ K}} \right)^{-1/2}. \quad (1.24)$$

Since the value S is $[2.22\text{--}5.37] \times 10^5 \text{ cm}^2 \text{ g}^{-1}$ in their dust models, the cloud fragmentation condition can be written as

$$\mathcal{D} > [2.6 - 6.3] \times 10^{-9} \left(\frac{n_{\text{H}}}{10^{12} \text{ cm}^{-3}} \right)^{-1/2} \left(\frac{T}{10^3 \text{ K}} \right)^{-1/2}. \quad (1.25)$$

Schneider et al. (2012b) further apply their model to the formation condition of the most primitive star SDSS J1029 + 1729 ever observed. They prepare the two progenitor mass models with $M_{\text{pr}} = 20$ and $35 M_{\odot}$, and four dust destruction models (norev and rev1–3) for each M_{pr} . They find that the fragmentation condition is satisfied for four out of eight models. For rev3 with $M_{\text{pr}} = 20 M_{\odot}$ and rev1–3 with $35 M_{\odot}$, the dust destruction efficiency is so large that the weak dust cooling can not induce the cloud fragmentation. Nevertheless, their model can partly explain the formation of the primitive star. We can say that dust cooling is crucial to the formation of the low-mass stars in the low-metallicity environment.

1.3.3.3 Grain growth

These authors impose the strong assumption that the dust-to-metal mass ratio, or the condensation efficiency of metal onto grains, is constant during the cloud collapse. However, it would increase while the gas density increases and the collision rate of gas-phase molecules with dust grains. The grains would capture the gas-phase species to grow. This accretion phenomenon is called *grain growth*. In the neighbor dense molecular cloud cores, the evidences of the grain growth are discovered by the recent observations (e.g. Chapman et al. 2009; Steinacker et al. 2010). The mid-infrared observations by the *Spitzer* telescope reveal that the scattered light by micron-size grains are detected in the

cloud core. This can be the evidence of the growth of dust grains whose size is usually sub-micron in the interstellar medium. Also in the early Universe, it is expected that the grains, which has been partly destroyed by the effect of the reverse shock when they are released from Pop III supernovae, again accrete the gas-phase metal during the succeeding cloud collapse as the gas density increases so that the timescale of the growth is smaller than the dynamical time of the gas even with the small dust-to-gas mass ratio.

Nozawa et al. (2012) estimate the effect of the growth of the dust grains of metallic iron and silicon on the low-metal gas. They integrate the depletion rate in the gas whose density increases with the free-fall timescale and whose temperature is fixed 1000 K. They study in the case where the dust size is uniform with initially $0.01 \mu\text{m}$. The initial depletion efficiency of metal is set for 0.001–0.1. Both the values are consistent with the grain properties created in the supernova ejecta (Nozawa et al. 2003). As a result, they find that the grain growth indeed occurs so that the gas-phase materials are totally depleted in the cloud even with the extremely low metallicities $\gtrsim 10^{-5} Z_{\odot}$ although the initial depletion factor is too small 0.001. This study indicates that the grain growth occurs well before the dust cooling becomes efficient. However, the gas temperature is fixed to be 1000 K in this study. Since the temperature evolution is crucial to determine the fragmentation condition, the temperature evolution, which interacts with the grain growth rate, should be required to be solved.

In our previous work, Chiaki et al. (2013) solve the gas temperature evolution and the grain growth for the first time in the context of the low-metal star formation. We employ the semi-analytical model based on Omukai (2000) and explicitly solve the growth rate of the grains which depends on the gas density, temperature, and chemical composition. While Nozawa et al. (2012) consider the metallic iron and silicon grains, which have less efficient cooling rate (photon absorption cross-section), we include the enstatite (MgSiO_3) grains, one of the most important species in the early Universe and present-day. The abundances of silicon and magnesium are the scaled solar abundances as $A_{\text{Mg}} = 3.47 \times 10^{-5}$ and $A_{\text{Si}} = 3.31 \times 10^{-5}$ for $Z = Z_{\odot}$ (Lodders et al. 2009). Figure 1.8 shows the dust depletion efficiency $f_{\text{MgSiO}_3, \text{Si}}(t)$, radius r_{MgSiO_3} and gas temperature. With $10^{-5} Z_{\odot}$, the fragmentation condition is satisfied only with grain growth. The gas fragmentation is favored even with the low initial depletion factor $f_{\text{dep},0}$ of 0.001 in the extremely metal-poor regime $\gtrsim 10^{-5} Z_{\odot}$. This indicates that the critical metallicity above which the dust cooling is effective is *insensitive* to the initial depletion factor. For a wide range of $f_{\text{dep},0}$, the gas-phase silicon is efficiently depleted onto the grains until exhausted well before the dust cooling becomes effective at $n_{\text{H}} \sim 10^{12}\text{--}10^{14} \text{ cm}^{-3}$. This model elegantly shows that a parameter of the dust property hardly affects the gas fragmentation properties.

In this model, however, there are several limitations to be considered. First, we assume a single component of dust, MgSiO_3 . The Pop III supernova model predicts the rather small amount of silicates (MgSiO_3 and Mg_2SiO_4) as shown in Nozawa et al. (2007). These grains had efficiently been destroyed by the reverse shocks before they are dispersed into the interstellar medium (see Chapter 3 in more detail). Although the carbon grains are another important coolant because of their large amount and large emissivity, we can

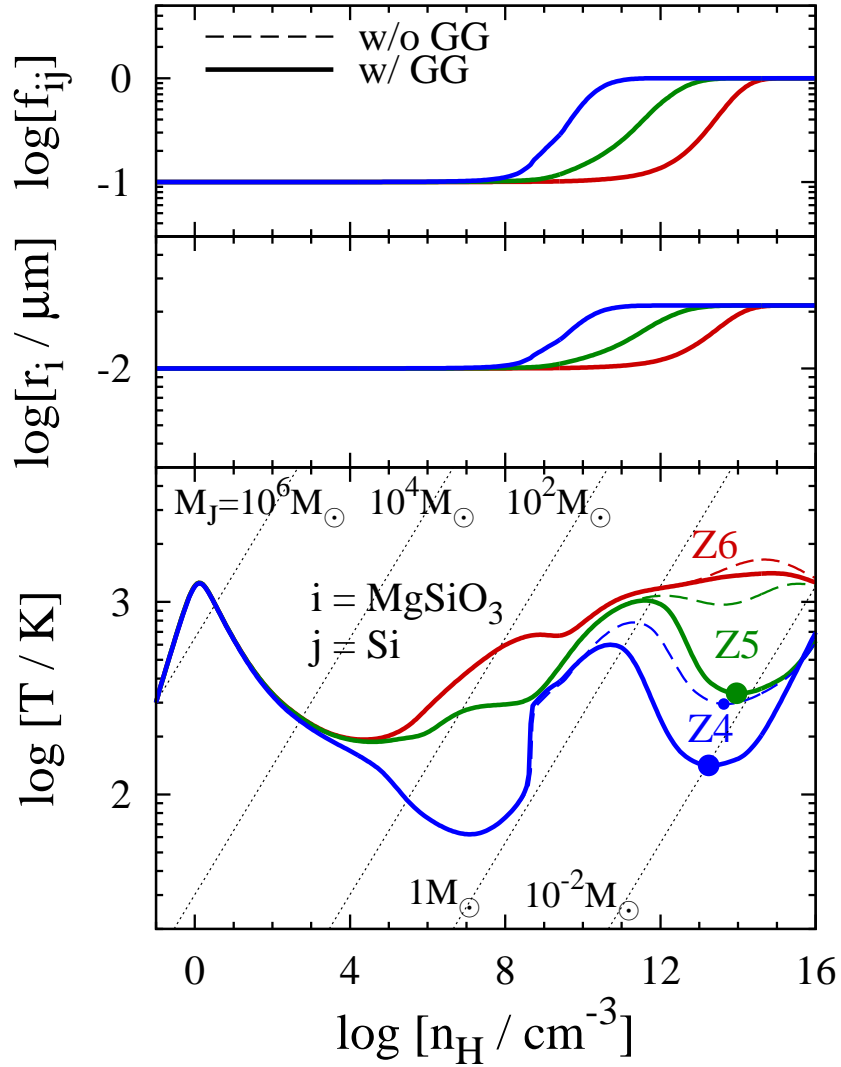


Figure 1.8: The dust depletion efficiency (top), radius (middle), and temperature (bottom) as a function of the central density of the cloud without (thin dashed) and with (thick solid) grain growth (GG) with metallicities 10^{-6} (red), 10^{-5} (green), and 10^{-4} (blue).

expect that they do not grow because the free carbon atoms available to be accreted onto grains are depleted into CO molecules more rapidly than grain growth as in the expanding supernova ejecta (Bianchi and Schneider 2007). Further, we see in Chiaki et al. (2013) the slight dependence of the critical metallicity on the grain size. For the grain sizes less than $0.01 \mu\text{m}$, the critical metallicity is between 10^{-6} and $10^{-5} Z_{\odot}$ while, for $> 0.1 \mu\text{m}$, between 10^{-5} and $10^{-4} Z_{\odot}$ with a fixed initial depletion factor $f_{\text{dep},0} = 0.1$. This is because the total cross-section of the grains is reciprocally proportional to the grain size. The cross-section determines the gas cooling efficiency owing to the collision with the cold grains. Therefore, we should consider the abundance of grain species and the size distribution realistic in the early Universe.

1.3.4 Three-dimensional simulations

The analytic approaches and the one-zone calculations presented above are the powerful tools to study the thermal properties of the collapsing clouds in a simple manner. In the previous section, the transition line cooling and/or dust thermal emission is considered to immediately indicate the cloud fragmentation. However, it is worth noting that we should investigate carefully how the thermal evolution has effects on the cloud fragmentation. Since it is difficult to directly observe star-forming clouds in the low-metallicity clouds at high redshifts, hydrodynamic simulations are useful to see the non-linearity of the cloud fragmentation. Several authors have performed the three-dimensional simulations to investigate the nature of the low-mass star formation in the extremely metal-poor environment.

Dopcke et al. (2011) perform the simulations for a turbulent gas with metallicities 10^{-5} and $10^{-4} Z_{\odot}$. They include the cooling effect of dust whose properties are the same as in the present-day case (Section 1.3.3.1). As the density in the cloud center increases, the dynamical time of the gas becomes very small as $\propto \rho^{-1/2}$. To satisfy the Courant condition, the computational timestep becomes extremely tiny. To save the computational cost, the sink particle technique is often used. After the gas density becomes above $n_{\text{H}} \gtrsim 10^{15} \text{ cm}^{-3}$, where the gas becomes optically thick, and the gas dynamical time becomes several years, they replace the fluid elements with a Lagrangian test particle. The particles gravitationally interact with each other. The gas particles approaching within a radius $r_{\text{acc}} = 1 \text{ AU}$ are accreted onto the sink particle. The formation of the multiple sink particles can be interpreted as the cloud fragmentation. They see that the overlapping filamentary structures are formed and several tens of sink particles are created in the dens clumps. The typical mass of the sinks is $\sim 0.1 M_{\odot}$, which explicitly shows that the low-mass fragmentation is triggered by dust cooling. This occurs in the both of the cases with 10^{-5} and $10^{-4} Z_{\odot}$. Therefore, the critical metallicity should be below $10^{-5} Z_{\odot}$. They extend their simulations for the wider range of metallicities $0-10^{-4} Z_{\odot}$ (Dopcke et al. 2013). Although the fragmentation is confirmed even with the cases with $Z = 0$ and $10^{-6} Z_{\odot}$, the mass function of the sink particles changes from flat, top-heavy types to the peaky, bottom-heavy types with the increasing metallicity. The transition of the

mass function occurs between 10^{-6} and $10^{-5} Z_{\odot}$. They therefore conclude that there exists the metallicity critically dividing the different mass function regimes, and its value is below $10^{-5} Z_{\odot}$.

[Safranek-Shrader et al. \(2014a\)](#) consider the star formation in the star-forming region in the atomic cooling halo with metallicities 10^{-4} – $10^{-2} Z_{\odot}$. In order to see the effect of fine-structure cooling, they replace the gas with the sink particles at somewhat large density $\sim 10^7 \text{ cm}^{-3}$. The line cooling induces the gas fragmentation only with $\geq 10^{-3} Z_{\odot}$, where transition line cooling becomes effective. Only a sink is formed with $10^{-4} Z_{\odot}$ sounded by a circumstellar disk. The typical mass of the central most massive sinks reaches $\sim 100 M_{\odot}$ after the accretion process for several Myr. This result shows that the low-mass fragmentation would be triggered by dust cooling at higher densities. [Safranek-Shrader et al. \(2014b\)](#) extend one of their simulations with $10^{-2} Z_{\odot}$ until the central density reaches 10^{13} cm^{-3} before sink particles are put. The cloud eventually fragment via the multiple filamentary structures into the sub-solar mass clumps. They also confirm that dust cooling can induce the second-step of fragmentation. In addition, the spectral index $\alpha = 1.3$ of the mass function of the sinks are similar to the one in the ultra-faint dwarf galaxies ([Geha et al. 2013](#)).

Above the two authors put the metal by hand uniformly in the turbulent clouds ([Dopcke et al. 2011, 2013](#)) or the first galaxy-forming halo ([Safranek-Shrader et al. 2014a,b](#)). Most recently, [Smith et al. \(2015\)](#) explicitly follow the entire process of the metal enrichment by the expanding blast waves from a Pop III supernova. They first perform the cosmological simulations and put a stellar particle in a primordial minihalo. After that, they follow the propagation of the supernova shock and derive the metal distributions around the minihalo. They find the collapsing neighboring halo enriched with $\simeq 2 \times 10^{-5} Z_{\odot}$. In the turbulent cloud, multilayered filamentary structures appear and the low-mass sink particles are formed. They confirm that the dust cooling can enhance the fragmentation by their controlled simulation without the cooling effect by dust grains.

These simulations explicitly shows that the dust cooling can induce the low-mass star formation. However, there remain rooms for us to elaborate the simulations. First, the present-day metal and dust model is used in these earlier studies. As we have seen in Section 1.3.3.2, the different metal abundance and dust condensation efficiency in the early Universe from in the local Universe can modify the thermal evolution of the clouds. Related to this, the effect of several metal molecular cooling has been overlooked. In the earlier studies, line cooling by CO, OH, and H_2O molecules is ignored. Although this has been justified only in the case with the present-day metal abundance ([Omukai 2000](#)), such cooling would become more effective in the Pop III metal yield model, which predicts O-excess ([Umeda and Nomoto 2002; Limongi and Chieffi 2012](#)). Further, they often ignore the effect of the chemical heating by the H_2 molecular formation. The H_2 molecules are formed via the exothermic reactions. The three-body reactions are efficient and the abundant binding energy is converted into the gas thermal energy at $n_{\text{H}} \sim 10^8 \text{ cm}^{-3}$ (see the yellow line in Figure 1.7). This rapid gas heating might stabilize the gas against the elongation. [Tsuribe and Omukai \(2008\)](#) present that H_2 formation heating significantly

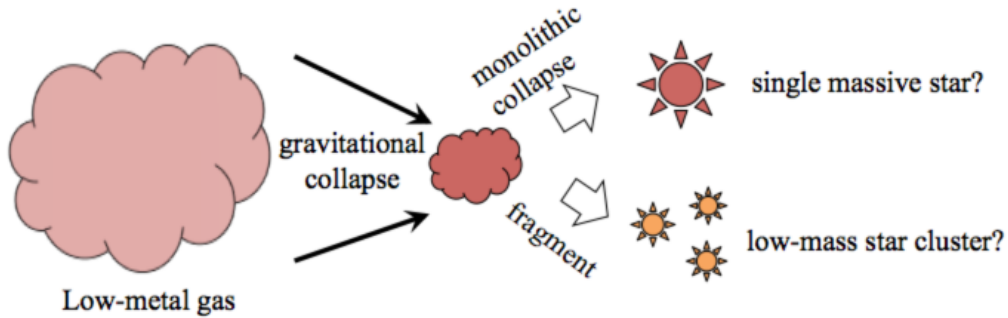


Figure 1.9: Schematic image of the fate of the low-metallicity collapsing cloud.

suppress gas elongation by their three-dimensional simulations for the polytropic gas mimicking the thermal evolution of the cloud. Finally, the authors demonstrate the gas collapse only for one cloud with each metallicity. [Hirano et al. \(2014\)](#) recently report that the thermal evolution of the clouds, which crucially affects the cloud fragmentation properties, would be varied even with a fixed metallicity ($Z = 0$ in their simulations). They first argue that the variation of the primordial stellar masses spreading ~ 10 – $1000 M_{\odot}$ according to the variation of the thermal evolution. They identify the collapse timescale as the another important parameter, which determine the thermal path of the cloud as well as the gas metallicity. In order to seek entire feature of the early clouds, it is required to investigate the various clouds with different collapse timescales.

1.4 Aims of the thesis

In this thesis, we aim to define the critical condition to the first low-mass star formation in the early Universe. We employ analytic calculations, semi-analytic one-zone models, and three-dimensional hydrodynamics simulations to follow the cloud collapse with extremely small metallicities. Because of the computational cost, we here focus on the early collapse phase of the star-forming clouds. The condition for the gas fragmentation into low-mass clumps are investigated (Figure 1.9).

1.4.1 Grain growth and the Pop III supernova models

To this aim, we begin with studying the necessary but so far overlooked thermal processes in the collapsing clouds with the one-zone simulations which is suitable to see the thermal evolution of the clouds. [Nozawa et al. \(2012\)](#) and [Chiaki et al. \(2013\)](#) predict the grain growth is important to enhance dust cooling rate with a simple model. We elaborate their calculations with the Pop III supernova metal and dust models as the realistic chemical abundance of the early prestellar clouds. Recently, several authors build the model of

nucleosynthesis in the main-sequence and the supernova explosion (Umeda and Nomoto 2002; Limongi and Chieffi 2012). Based on the metal yield, Nozawa et al. (2007) and Schneider et al. (2012a) employ the hydrodynamic model of expanding ejecta to follow the processes of metal condensation and dust sputtering and estimate the resulting dust content and size distributions. We perform one-zone calculations including the metal and dust models to see the effect on the cloud thermal evolution. Also, we explicitly see how grain growth can modify the fragmentation property of the gas.

Here, we focus on the formation of “ordinal” EMP star. A some fraction of EMP stars show the carbon-enhanced abundance feature ($[C/Fe] > 1$; Beers and Christlieb 2005), and are called carbon-enhanced extremely metal-poor (CEMP) stars. The fraction of CEMP stars increases with decreasing metallicities (Frebel and Norris 2013): the 28% of EMP stars so far observed are carbon-enhanced with $[Fe/H] < -3$, and three out of four stars have the carbon-enhanced abundance with $[Fe/H] \lesssim -5$ (SAGA database¹: Suda et al. 2008). The recently discovered star SMSS J0313 – 6708 for which no iron lines are detected and the upper limit is $[Fe/H] < -7.1$ has the carbon-enhanced feature ($[C/H] = -2.4$) (Keller et al. 2014). Even for the star, metallicity (mass fraction of total heavy elements) itself is moderate ($\sim 2.7 \times 10^{-3} Z_{\odot}$). It has been considered that the EMP stars with $[Fe/H] < -4$ generally have the carbon-enhanced feature relative to iron. However, recent observation of SDSS J102915 + 172927 with $[Fe/H] = -4.99$ reveals that abundance of not only iron but carbon is very small (Caffau et al. 2011). Carbon lines are not detected and the upper limit of the abundance is $[C/H] < -4.3$, corresponding the lowest metallicity $< 4.5 \times 10^{-5} Z_{\odot}$ ever observed. The explanation of existence of the both carbon- and iron-poor star is challenging topic due to a significant lack of coolant.

1.4.2 Three-dimensional simulations

To seek highly non-linear evolution of the collapsing clouds, we perform three-dimensional hydrodynamic simulations of low-metal clouds. First, we develop a novel zoom-in technique necessary to follow the cloud collapse from an interstellar medium to the protostellar core over the density of 20 orders of magnitude. Then, we apply this to the simulations of clouds with low metallicities. Finally, we attempt to identify the gas heating/cooling processes which determines the cloud fragmentation into low-mass protostellar cores.

1.4.2.1 Novel zoom-in simulation technique

In the collapse simulations, we are required to follow the gas evolution over 20 orders of magnitude. At that time, the mass (spacia)l resolution of the discretized fluid elements is restricted to be well less than the local Jeans mass (length) Truelove et al. (1997) (Jeans criterion). If the mass resolution is violate the criterion, the spurious fragmentation is reported to occur owing to the numerical noise. Besides, it is unrealistic that we start simulations with the sufficient mass resolution to follow the evolution of eventually

¹<http://sagadatabase.jp/>

formed protostellar cores. The cores are formed after the gas becomes optically thick at $n_{\text{H}} \sim 10^{15} \text{ cm}^{-3}$, where the Jeans mass is $M_{\text{J}} \sim 0.1 M_{\odot}$. When we impose the Jeans criterion of $m_{\text{p}} < 10^5 M_{\text{J}}$ (see Chapter 4), where m_{p} is the mass of a fluid element in the simulation, the required mass resolution is $\sim 10^{-6} M_{\odot}$. A typical molecular cloud with $n_{\text{H}} \sim 10^4 \text{ cm}^{-3}$ begins to collapse with the mass scale larger than the Jeans mass of $M_{\text{J}} \sim 10^2 M_{\odot}$. Therefore, the required number of the particles are $\sim 10^8$. Although such an expensive simulation is indeed possible with the machine power of the recent supercomputers, the performance of parameter studies should be limited.

To overcome the numerical difficulty, the particle splitting technique is often used in smoothed particle hydrodynamics (SPH) simulations. A coarse (parent) particle which is about to break the Jeans criterion as its density increases is replaced with a set of the finer (daughter) particles. In the course of the cloud collapse, the finer particles are generated toward the cloud center. It is based on the common idea with the adaptive mesh refinement (AMR) technique in Eulerian grid codes. While the distribution of refined grids can be almost uniquely determined according to the coordinate of the parent grid in the AMR codes, it is non-trivial how to distribute the daughter particles in the SPH simulations. Several authors have determined the distribution of the daughters in somewhat simple manners. [Kitsionas and Whitworth \(2002\)](#) put tens of daughters around the position of their parent on the lattice of the hexagonal closest packaging. [Mayer et al. \(2010\)](#) distribute the daughters on the vertices of the cube the half inter-particle distance on a side parallel to the coordinate of the simulation box. Although only the simple procedure is required in these methods, the global particle distribution should be affected by the symmetric distributions of daughters of each parent. We thus develop the novel particle splitting where daughter particles are distributed by the Voronoi diagrams created by the parent particles. We can expect that the particle distribution of the cloud is properly preserved with our method. The distribution of the particles are connected with the density structure of the clouds. The preservation of the density structure before particle splitting would lead us to more properly predict the cloud fragmentation which is affected by the gas density structure.

1.4.2.2 Necessary thermal processes

As discussed in Section 1.3.4, there are several thermal processes which crucially affect the cloud fragmentation but which have so far been overlooked. We propose that the two other processes are important as well as dust thermal emission: H_2 formation heating and $\text{OH}/\text{H}_2\text{O}$ molecular cooling. We summarize the expected effects of these three processes on the cloud elongation and fragmentation as follows:

- Dust cooling can trigger the gas elongation and the successive fragmentation into the low-mass pieces. Grain growth can further enhance the effect even in the cases where the metal condensation efficiency is initially small.
- Gas heating owing to hydrogen molecular formation can halt the gas elongation.

The heating might sufficiently make the cloud core round. Even though the dust cooling becomes efficient at higher density, it is possible that the timescale for the core elongation from such a round structure to a filamentary structure is larger than the gas dynamical timescale as presented by [Tsuribe and Omukai \(2008\)](#).

- Metal molecular cooling is possibly another important cooling agent as well as grains. Although this could not contribute to formation of low-mass clumps because these lines become optically thick at small densities $\sim 10^8 \text{ cm}^{-3}$ (see Chapter 2), it can even enhance the cloud elongation before the dust cooling becomes efficient.

1.4.2.3 Variation of collapse timescale

As [Hirano et al. \(2014\)](#) confirm by the simulations for more than 100 primordial clouds, the thermal evolution varies from cloud to cloud. Some of them undergo sufficient HD cooling because their compressional heating rate is smaller and the time during which the clouds are exposed to the radiative cooling is longer for the longer collapse timescale than the other clouds. These thermal properties generate the eventual mass of the formed Pop III stars. We in this thesis pick up the three minihalos which cover the entire diversity of the thermal properties of the cloud.

1.5 Structure of thesis

We have so far seen that the critical conditions for the first low-mass stars are highly unknown because of the several processes crucially affect the cloud evolution. We step-by-step disclose the effects of these factors. In Chapter 2, we begin with the list up the important chemical reactions and gas cooling/heating mechanisms which are included in our analytic, semi-analytic, and numerical models employed throughout this theses. Although we have already introduced some of them such as fine-structure cooling by oxygen and carbon and dust thermal emission, it is necessary to more closely understand the physical mechanisms. In Chapter 3, we investigate the effects of the Pop III supernova model and grain growth on the thermal evolution of metal-deficient clouds. To this aim, simple one-zone model is suitable.

We then move on the three-dimensional simulations to explicitly see the cloud fragmentation and to see the connection between the thermal evolution and the fragmentation property. We introduce our novel particle splitting method based on the Voronoi tessellation of SPH particles in Chapter 4, and apply it to our low-metal collapse simulations in Chapter 5. Finally, we present the concluding remarks in Chapter 6.

Chemical reactions and cooling rates

Contents

2.1	Cooling and heating processes	27
2.1.1	Radiative cooling	27
2.1.2	Chemical heating and cooling	36
2.1.3	Dust thermal emission	37
2.2	Chemical reactions	38
2.2.1	Gas-phase chemistry	39
2.2.2	Grain growth	45

2.1 Cooling and heating processes

2.1.1 Radiative cooling

The radiative cooling leads the gas temperature to decrease. The level of a species is excited by the collision with another ion, atom, or molecule. An electron usually contributes to the excitation as a carrier of the kinetic energy by its small mass, and a hydrogen atom or molecule is also important because of its large abundance. When the level is de-excited, the excessive energy is released in the form of radiation. The net effect is that the kinetic energy of gas is converted to the radiation energy. The rate of transition line cooling per unit volume can be written as the summation of the contributions of spontaneous radiation from the level i to j :

$$\Lambda = \sum_{i>j} h\nu_{ij} A_{ij} \beta_{ij} n_i \frac{S_{ij} - J_{\text{CMB},ij}}{S_{ij}}, \quad (2.1)$$

where ν_{ij} is the frequency corresponding to the energy difference between the levels i and j , A_{ij} is the coefficient of spontaneous emission from level i to $j < i$, and n_i is the population of the target molecule in the level i . The source function S_{ij} is written as

$$S_{ij} = \frac{A_{ij} n_i}{B_{ji} n_j - B_{ij} n_i} = \frac{2h\nu_{ij}^3}{c^2} \left(\frac{g_i n_j}{g_j n_i} - 1 \right)^{-1}, \quad (2.2)$$

where B_{ij} is the rate of the stimulated emission ($i < j$) or absorption ($i > j$), g_i and g_j is the statistical weights of the levels i and j , respectively. The intensity of the CMB photons at the frequency of the i - j transition is

$$J_{\text{CMB},ij} = \frac{2h\nu_{ij}^3}{c^2} \left[\exp\left(\frac{h\nu_{ij}}{kT_{\text{CMB}}}\right) - 1 \right]^{-1} \quad (2.3)$$

The rate of the photon reduction by the self-absorption of the molecules and dust is anisotropic. In the direction s of the line-of-sight, the escape probability can be written as

$$\beta_{ij}^s = \left(\frac{1 - e^{-\tau_{ij}^s}}{\tau_{ij}^s} \right) e^{-\tau_{\text{cont}}} \quad (2.4)$$

under the large velocity gradient (LVG) approximation (Takahashi et al. 1983; Omukai 2000). The optical depth τ_{ij}^s in the direction of a line-of-sight s is

$$\tau_{ij}^s = \frac{hc}{4\pi} \frac{B_{ji}n_j - B_{ij}n_i}{dv_s/ds} = \frac{c^3 A_{ij}}{8\pi\nu_{ij}} \left(\frac{g_i n_j}{g_j n_i} - 1 \right) \frac{n_i}{dv_s/ds}, \quad (2.5)$$

where dv_s/ds is the local velocity gradient. In the one-zone calculations (Chapter 3), we estimate the velocity gradient as

$$\frac{dv_s}{ds} = \frac{1}{3t_{\text{ff}}} \quad (2.6)$$

independent on the direction. Therefore, β_{ij} in Equation (2.1) equals to β_{ij}^s . In three-dimensional simulations (Chapter 5), the velocity gradient at the coordinate \mathbf{r} can be directly estimated by the SPH formula as

$$\frac{dv_s}{ds} = \sum_n \frac{m_n}{\rho} \frac{s - s_n}{|\mathbf{r} - \mathbf{r}_n|} (v_s - v_{s,n}) \nabla W(|\mathbf{r} - \mathbf{r}_n|, h), \quad (2.7)$$

where n is the index of a neighbor particle, and ∇W is the gradient of the kernel function (see Chapter 4). We estimate the velocity gradients in directions $s = x, y$, and z . Then, as in Hirano and Yoshida (2013), we estimate the escape probability as

$$\beta_{ij} = \frac{\beta_{ij}^x + \beta_{ij}^y + \beta_{ij}^z}{3}. \quad (2.8)$$

We estimate the population n_i from the balance equation between the transition rate from another level j to i and that from i to j as

$$n_i \sum_{i \neq j} \left[A_{ij} + B_{ij} J_{\text{CMB},ij} + \sum_k \gamma_{ij}^k n(k) \right] = \sum_{i \neq j} n_j \left[A_{ji} + B_{ji} J_{\text{CMB},ji} + \sum_k \gamma_{ji}^k n(k) \right], \quad (2.9)$$

where $A_{ij} = 0$ for $i < j$, γ_{ij}^k is the rate of the de-excitation ($i > j$) and excitation ($i < j$) by the impact, with molecules k , and $n(k)$ is the number density of the molecules k in the fluid. We neglect the self-absorption and stimulated emission by the line photons to save the computational cost. We still confirm the effect of the stimulated emission on the thermal evolution of the gas can be neglected by the semi-analytic calculations presented used in Chapter 3.

Table 2.1: Transition lines of HD molecules

$J \rightarrow J'$	${}^a\nu_{JJ'}$ [Hz]	${}^aA_{JJ'}$ [s^{-1}]	${}^b\gamma_{JJ'}^{\text{H}}$ [$\text{cm}^3 \text{s}^{-1}$]
$1 \rightarrow 0$	2.67×10^{12}	5.12×10^{-8}	$3.46 \times 10^{-12} + 2.83 \times 10^{-13}T^{0.77}$
$2 \rightarrow 1$	5.32×10^{12}	4.86×10^{-7}	$3.23 \times 10^{-12} + 1.57 \times 10^{-13}T^{0.92}$
$3 \rightarrow 2$	7.93×10^{12}	1.72×10^{-6}	$1.89 \times 10^{-12} + 6.85 \times 10^{-14}T^{1.03}$
$2 \rightarrow 0$	7.99×10^{12}	7.05×10^{-12}	$2.68 \times 10^{-13} + 8.66 \times 10^{-15}T^{1.12}$
$3 \rightarrow 1$	1.33×10^{13}	1.15×10^{-10}	$2.52 \times 10^{-13} + 1.02 \times 10^{-15}T^{1.47}$

Note — References: *a* [Abgrall et al. \(1982\)](#), *b* [Galli and Palla \(1998\)](#). In the last column, T is the gas temperature in the unit of K.

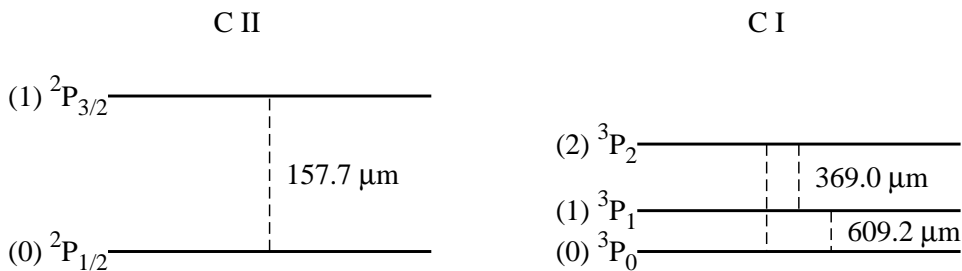


Figure 2.1: Transition levels of the species C II (left) and C I (right panel).

2.1.1.1 Molecular lines of primordial species

(a) H_2

H_2 molecules are the important cooling agent in the gas with $< 10^{-5} Z_{\odot}$, where the dust thermal emission is inefficient. We solve the cooling rate for the rotation energy levels $J = 0-19$, and the vibrational energy levels $v = 0, 1$, and 2. The spontaneous emission rate $A_{v,J;v',J'}$ for the ro-vibrational transition from (v, J) to (v', J') is taken from [Turner et al. \(1977\)](#). The rates γ_{ij}^k of the collisional excitation and de-excitation are taken from [Hollenbach and McKee \(1979\)](#) for $k = \text{H}$ and H_2 . The energy difference is calculated according to the formula of [Borysow et al. \(1989\)](#).

(b) HD

The radiative cooling by HD molecules becomes important in slowly collapsing clouds with large f_0 and with metallicities $\lesssim 10^{-6} Z_{\odot}$. The molecular cooling can serve as the variation of the thermal evolution of the hyper metal-poor clouds while the O I cooling is dominant in the slowly rotating clouds with $\gtrsim 10^{-5} Z_{\odot}$. We in this thesis consider the vibrational transitions $J = 0-3$. Table 2.1 shows the energy separation, A -coefficient, and collision rate of each transition which we here consider.

Table 2.2: Transition lines of metal ions and atoms

species	$i \rightarrow j$	ν_{ij} [Hz]	A_{ij} [s^{-1}]	γ_{ij}^e [$cm^3 s^{-1}$]	γ_{ij}^H [$cm^3 s^{-1}$]	$\gamma_{ij}^{H_2}$ [$cm^3 s^{-1}$]
C II	1 \rightarrow 0	1.9×10^{12}	2.4×10^{-6}	$2.8 \times 10^{-7}(T/100K)^{-0.5}$	$8.0 \times 10^{-10}(T/100K)^{0.07}$	
C I	1 \rightarrow 0	5.0×10^{11}	7.9×10^{-9}	3.0×10^{-9}	$1.6 \times 10^{-10}(T/100K)^{0.14}$	$0.05\gamma_{10}^H$
	2 \rightarrow 0	1.3×10^{12}	5.0×10^{-9}	5.0×10^{-9}	$9.2 \times 10^{-11}(T/100K)^{0.26}$	$0.5\gamma_{20}^H$
	2 \rightarrow 1	8.1×10^{11}	1.5×10^{-8}	1.5×10^{-8}	$2.9 \times 10^{-10}(T/100K)^{0.26}$	$0.5\gamma_{21}^H$
O I	1 \rightarrow 0	4.7×10^{12}	8.9×10^{-5}	1.4×10^{-8}	$9.2 \times 10^{-11}(T/100K)^{0.67}$	
	2 \rightarrow 0		1.0×10^{-10}	1.4×10^{-8}	$4.3 \times 10^{-11}(T/100K)^{0.80}$	
	2 \rightarrow 1	2.1×10^{12}	1.7×10^{-5}	5.0×10^{-9}	$1.1 \times 10^{-10}(T/100K)^{0.44}$	
	3 \rightarrow 0		6.3×10^{-3}	1.0×10^{-10}	1.0×10^{-12}	
	3 \rightarrow 1		2.1×10^{-3}	1.0×10^{-10}	1.0×10^{-12}	
	3 \rightarrow 2	4.7×10^{14}	7.3×10^{-7}	1.0×10^{-10}	1.0×10^{-12}	
	4 \rightarrow 0		2.9×10^{-4}	1.0×10^{-10}	1.0×10^{-12}	
	4 \rightarrow 1		7.3×10^{-2}	1.0×10^{-10}	1.0×10^{-12}	
	4 \rightarrow 2		0.0	1.0×10^{-10}	1.0×10^{-12}	
	4 \rightarrow 3	5.4×10^{14}	1.2	0.0	0.0	

References — Hollenbach and McKee (1989) and Osterbrock (1989).

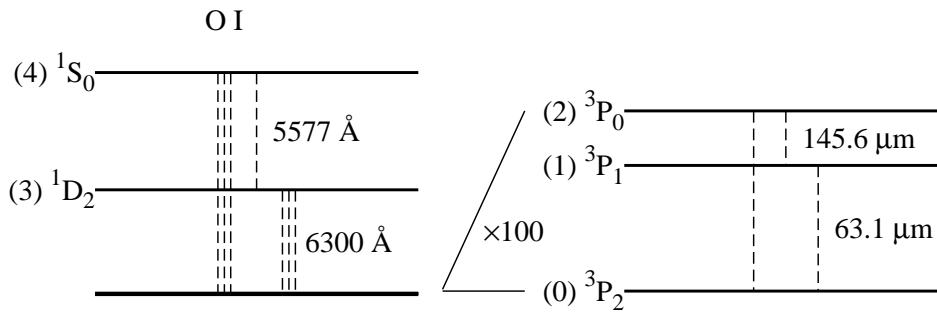


Figure 2.2: Transition levels of the species O I.

2.1.1.2 Forbidden line of metal ions and atoms

The metal ions and molecules emit photons by the forbidden line transition. Figures 2.1 and 2.2 show the levels of the species C II, C I, and O I. We confirm that the other abundant elements Si and Fe do not have significant effects on the gas thermal evolution by their line emission. Table 2.2 shows the A -coefficients and γ_{ij}^k ($k = e, \text{H}, \text{and H}_2$).

(a) C II

C^+ ions are not important during the cloud collapse even with the carbon-enhanced metal abundance because the ions are recombined immediately after we start the calculations. The cooling process is still worth reviewing because the well-known emission line at $158 \mu\text{m}$ can be used to observationally investigate the metal abundance and the star formation process in high redshift galaxies. Further, the simple two-level system is suitable to in detail see the process of the photon emission. The detailed balance equation (2.9) can be rewritten as

$$\sum_k \gamma_{01}^k n(k) n_0 = A_{10} n_1 + \sum_k \gamma_{10}^k n(k) n_1, \quad (2.10)$$

$$n(\text{C}^+) = n_0 + n_1 \quad (2.11)$$

for the two-level system, where $n(\text{C}^+)$ is the number density of carbon ions. We neglect the effect of the CMB radiation. At densities $n(\text{C}^+) < n_{\text{crit}} \equiv A_{10} / \sum \gamma_{10}^k y(k)$, the spontaneous emission is balanced with the collisional excitation as

$$\Lambda(\text{C}^+) = h\nu_{10} \sum_k \gamma_{01}^k n(k) n_0 \propto n_{\text{H}}^2. \quad (2.12)$$

Otherwise, the level population reaches the local thermal equilibrium (LTE), where

$$\frac{n_1}{n_0} = \frac{\sum \gamma_{01}^k n(k)}{\sum \gamma_{10}^k n(k)} \simeq \frac{g_1}{g_0} \exp\left(-\frac{h\nu_{10}}{kT}\right). \quad (2.13)$$

From Equations (2.10) and (2.11), the population of the level 1 can be obtained as

$$n_1 = \frac{\frac{g_1}{g_0} \exp\left(-\frac{h\nu_{10}}{kT}\right)}{1 + \frac{g_1}{g_0} \exp\left(-\frac{h\nu_{10}}{kT}\right)} n(\text{C}^+). \quad (2.14)$$

The cooling function is then

$$\Lambda(\text{C}^+) = h\nu_{10} A_{10} \frac{\frac{g_1}{g_0} \exp\left(-\frac{h\nu_{10}}{kT}\right)}{1 + \frac{g_1}{g_0} \exp\left(-\frac{h\nu_{10}}{kT}\right)} n(\text{C}^+) \propto n_{\text{H}} \quad (2.15)$$

if the abundance of carbon ions is constant. The density n_{crit} is called the critical density below which the cooling rate is proportional to n_{H}^2 and above which n_{H}^1 .

Figure 2.3 shows the cooling rate of C^+ and adiabatic heating rate as a function of the number density n_{H} of hydrogen nuclei. We fix the temperature to 300 K and

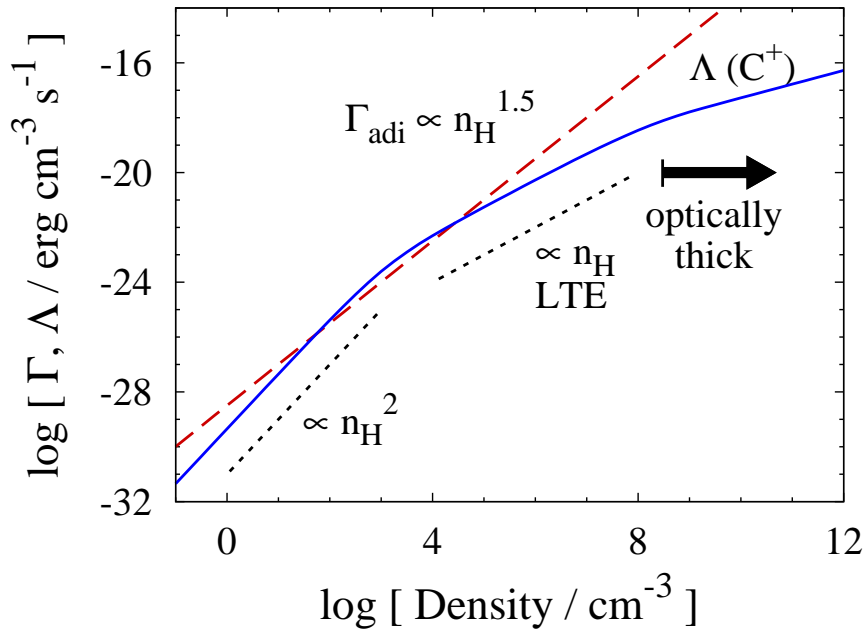


Figure 2.3: Cooling rate by C^+ ions $\Lambda(\text{C}^+)$ as a function of the gas density n_{H} (blue solid curve). We also plot the adiabatic heating rate Γ_{adi} (red dashed). These rates are calculated with a fixed temperature 300 K, and the number fraction of C^+ is 3.16×10^{-7} corresponding to the metallicity 10^{-3} . The abundances of the species e , H , and H_2 which induce collisional excitation are 10^{-6} , $\simeq 1$, and 10^{-4} , respectively.

the abundance of C^+ relative to hydrogen nuclei to 3.16×10^{-7} which is 10^{-3} times the solar abundance (Caffau et al. 2011). The fraction of electrons which collisionally induce the level excitation is 10^{-6} . In such a case, the collisional excitation by hydrogen atoms is dominant over electrons. The critical density is therefore $n_{\text{crit}} \simeq A_{10}/\gamma_{10}^{\text{H}}y(\text{H}) = 3 \times 10^3 \text{ cm}^{-3}$. We also plot the rate of gas compressional heating, which is the main heating mechanism. The rate of adiabatic compression per unit volume is

$$\Gamma_{\text{adi}} = \rho p \frac{d}{dt} \left(\frac{1}{\rho} \right) \sim \frac{p}{t_{\text{ff}}} \propto n_{\text{H}}^{1.5}. \quad (2.16)$$

The cooling can become dominant over the gas heating at density $\sim n_{\text{crit}}$ if the abundance is sufficiently large. At densities $> n_{\text{crit}}$, the cooling rate can never be larger than the compressional heating because, although the former even increases proportional to n_{H} , the latter increases more rapidly proportional to $n_{\text{H}}^{1.5}$. The increasing rate of the cooling efficiency is further quenched after the gas becomes optically thick at the transition frequency at $n_{\text{H}} \sim 10^8 \text{ cm}^{-3}$. Also, the ions are depleted into carbon atoms by the collisional recombination with electrons.

(b) C I

We consider the three-level system for carbon atoms. The cooling rate increases as $\propto n_{\text{H}}^2$ at $n_{\text{H}} < n_{\text{crit}}$ and as $\propto n_{\text{H}}$ at $n_{\text{H}} > n_{\text{crit}}$ also in the multi-level system. The level population becomes LTE at $n_{\text{crit}} \sim 10^3 \text{ cm}^{-3}$, where the difference of the rates $\Lambda(\text{C}) - \Gamma_{\text{adi}}$ marks the maximal value. When the gas metallicity is $\gtrsim 10^{-3} Z_{\odot}$, the cooling by C I becomes dominant before the atoms are oxidized onto CO molecules at $\sim 10^4 \text{ cm}^{-3}$. Especially, C I cooling becomes important for clouds with the abundances of the carbon-enhanced metal-poor star $[\text{C}/\text{Fe}] \gtrsim 1$ (Marassi et al. 2014).

(c) O I

With the carbon-normal abundances, oxygen is more abundant than carbon by a factor of 3–10 (Umeda and Nomoto 2002). In that case, O I cooling can be important only in the early stage of gas collapse at $< 10^4 \text{ cm}^{-3}$ with metallicities $\gtrsim 10^{-3} Z_{\odot}$. After the gas density reaches the quantity, the gas becomes optically thick and oxygen atoms are depleted onto OH molecules.

2.1.1.3 Metal molecular cooling

The effect of the transition line cooling owing to the metal molecules such as CO, OH, and H_2O on the thermal evolution of metal-poor gas have not so far been investigated in the context of the early star formation. The gas fragmentation is triggered when the gas cooling becomes inefficient and the temperature turns to increase as we have seen in Chapter 1. The line cooling by metal ions and atoms becomes ineffective at $\sim 10^3 \text{ cm}^{-3}$, where the level population reaches LTE and these atoms and ions begin to be depleted onto molecules. The Jeans mass at the density, which would be the typical scale of the

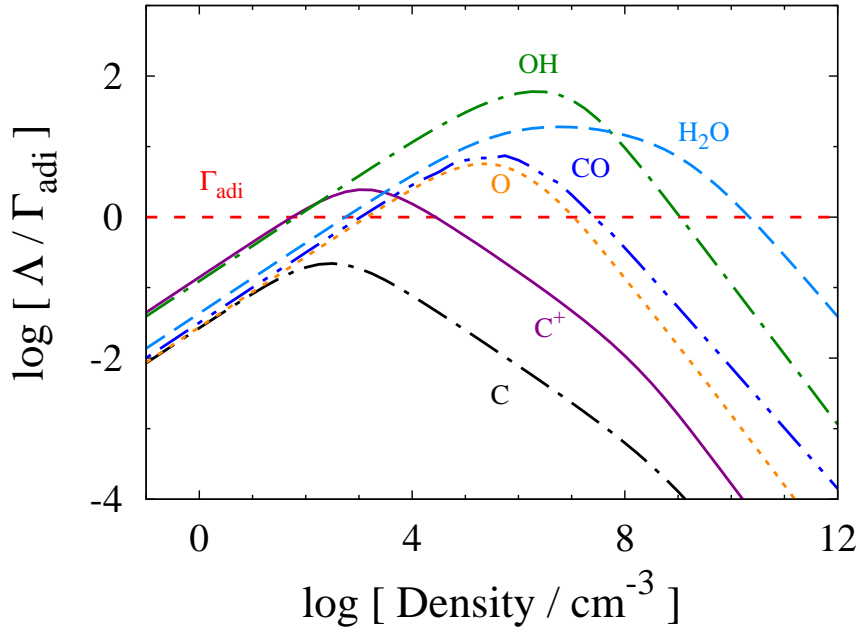


Figure 2.4: Ratio of cooling rates relative to the adiabatic heating rate for C II (purple solid), C I (black dot-dashed), O I (yellow dotted), CO (blue dot-dot-dashed), OH (green dot-dashed), and H₂O (cyan dashed) as a function of the density with a fixed temperature 300 K. The carbon and oxygen abundances relative to hydrogen nuclei are 3.16×10^{-7} and 5.75×10^{-7} , corresponding to the scaled solar abundance (Caffau et al. 2011) with a factor of 10^{-3} . We calculate the cooling rates in the case where all of the relevant elements are depleted onto each coolant.

mass of fragments formed by the metal ion and atomic cooling is

$$M_{\text{J,atom}} = 1.5 \times 10^4 M_{\odot} \left(\frac{\mu}{1.2}\right)^{-3/2} \left(\frac{n_{\text{H}}}{10^3 \text{ cm}^{-3}}\right)^{-1/2} \left(\frac{T}{300 \text{ K}}\right)^{3/2}. \quad (2.17)$$

The formation of the low-mass stars can not be explained by the gas fragmentation triggered by the ion and atomic cooling. Further, the cooling becomes efficient with metallicities $\gtrsim 10^{-3} Z_{\odot}$. The cooling could not explain the existence of the low-mass star with metallicity $\sim 10^{-5} Z_{\odot}$.

The molecules can continue to cool the gas after the ions and atoms are depleted. The molecular cooling turns to be ineffective at $\sim 10^8 \text{ cm}^{-3}$. Considering that the mass scale of the fragments is determined at that density, the Jeans mass is

$$M_{\text{J,molecule}} = 48 M_{\odot} \left(\frac{\mu}{1.2}\right)^{-3/2} \left(\frac{n_{\text{H}}}{10^8 \text{ cm}^{-3}}\right)^{-1/2} \left(\frac{T}{300 \text{ K}}\right)^{3/2} \quad (2.18)$$

with metallicities $\gtrsim 10^{-4} Z_{\odot}$. Although the only the molecular cooling can not explain the formation of the extremely metal-poor and low-mass stars, the molecular cooling, in particular OH and H₂O cooling play an important role in triggering gas elongation as we present in Chapter 5.

The molecular cooling rate can be estimated by the same procedure as presented in the previous section. However, we should treat spontaneous, radiative, and collisional transition of ~ 100 rotational transitions for each molecules. We here utilize the functional formula of the cooling L rate per molecule presented by [Neufeld and Kaufman \(1993\)](#) as

$$\frac{1}{L} = \frac{1}{L_0} + \frac{n(\text{H}_2)}{L_{\text{LTE}}} + \frac{1}{L_0} \left[\frac{n(\text{H}_2)}{n_{1/2}} \right]^{\alpha} \left(1 - \frac{n_{1/2} L_0}{L_{\text{LTE}}} \right), \quad (2.19)$$

where L_0 and L_{LTE} are the cooling rates per molecule at densities below and above the critical density, respectively. The collisional excitation and de-excitation with H₂ molecules are considered here. Only the transition from the first excited state to the ground state is taken into consideration in calculating L_0 while the populations of the relevant levels are LTE in calculating L_{LTE} . These functions are smoothly connected at density $n_{1/2}$ nearly according to the power law with the spectral index α . The cooling rate L_0 is the function of the gas temperature T . The other four quantities are the functions of a sort of column density $\tilde{N}(m)$ of molecule $m = \text{CO}$, OH, and H₂O, and the gas temperature T . The functional forms are given by [Omukai et al. \(2010\)](#) for CO and OH molecules, and by [Neufeld and Kaufman \(1993\)](#) and [Neufeld et al. \(1995\)](#) for H₂O at temperatures $T > 100 \text{ K}$ and $T < 100 \text{ K}$, respectively. The column density is defined as $\tilde{N}(m) = n(m)/|dv_s/ds|$ in the direction of the line-of-sight s under the LVG approximation. We estimate the cooling rates L in the directions x , y , and z , and then take the arithmetical average of these three quantities.

(a) CO

Table 2.3: Rate of energy released per H₂ molecule

Process	Reaction	Rate [eV s ⁻¹]
form. via H ⁻	3	3.53(1 + n _{cr} /n _H) ⁻¹
form. via three-body	5, 6	4.48(1 + n _{cr} /n _H) ⁻¹
diss. via three-body	4, 7	-4.48
form. on grains	8	0.2 + 4.2(1 + n _{cr} /n _H) ⁻¹

Note — In the second column, the reaction ID is the same as indicated in Table 2.4.

The energy rates shown here are taken from [Hollenbach and McKee \(1979\)](#).

It is well-known that the radiative cooling by CO molecules are important in the interstellar medium in our Galaxy. These molecules are second most abundant, following H₂ molecules. These heteronuclear diatomic molecules have the dipole moments and the excitation temperature is smaller than homonuclear molecules such as H₂. The CO molecular cooling is however not so important in the metal-poor gas especially in the Pop III supernova models, which generally predicts the large carbon abundance than oxygen.

(b) OH

In the Pop III supernova models, OH and H₂O molecules become the important coolants after their association at densities $\sim 10^4$ and 10^8 cm⁻³, respectively, with $10^{-3} Z_{\odot}$. Figure 2.4 shows the ratio of the cooling rates of metal ions, atoms, and molecules to the adiabatic heating rate for the scaled solar abundance with metallicity $10^{-3} Z_{\odot}$. If all oxygen nuclei are depleted onto OH molecules throughout the gas collapse, the cooling rate increases proportional to n_{H}^2 until $n_{\text{H}} \sim 10^7$ cm⁻³, where the gas becomes optically thick. Even though the oxygen atoms are depleted onto OH molecules at 10^4 cm⁻³, the gas continues to be cooled by the emission from OH molecules.

(b) H₂O

After H₂O molecules are formed from OH molecules, the cooling by the rotational transition of H₂O becomes the dominant cooling process in the gas. We calculate the H₂O with the ratio between ortho- and para-H₂O as 3:1. The molecules are formed at $\sim 10^8$ cm⁻³. After that, the gas heating by the H₂ molecular formation via three-body reactions (see below) becomes dominant and stabilizes the cloud. H₂O cooling is expected to overcome the stabilizing effect.

2.1.2 Chemical heating and cooling

Hydrogen molecules are formed via several reactions. When the atoms are associated, the binding energy of the molecule is released and converted to the gas thermal energy. The energy per molecule formed is listed in Table 2.3. In the list, the critical density n_{cr} is estimated as

$$n_{\text{cr}} = \frac{10^6 T^{-1/2}}{1.6y(\text{H}) \exp[-(400/T)^2] + 1.4y(\text{H}_2) \exp[-12000/(T + 1200)]}, \quad (2.20)$$

where the unit of the temperature T is kelvin. In particular, the gas heating by the hydrogen molecular formation via three-body reaction 5 has the significant effects on the gas thermal evolution. The chemical heating rate is

$$\begin{aligned}\Gamma_{3b} &= 4.48(1 + n_{\text{cr}}/n_{\text{H}})^{-1}k_5n(\text{H})^3 \text{ eV cm}^{-3} \text{ s}^{-1} \\ &= 1.3 \times 10^{-18}(1 + n_{\text{cr}}/n_{\text{H}})^{-1} \left(\frac{T}{300 \text{ K}}\right)^{-1} \left(\frac{y(\text{H})n_{\text{H}}}{10^8 \text{ cm}^{-3}}\right)^3 \text{ erg cm}^{-3} \text{ s}^{-1}\end{aligned}\quad (2.21)$$

while the adiabatic heating is

$$\Gamma_{\text{adi}} = 9.5 \times 10^{-18} \left(\frac{\mu}{1.2}\right)^{-1} \left(\frac{n_{\text{H}}}{10^8 \text{ cm}^{-3}}\right)^{3/2} \left(\frac{T}{300 \text{ K}}\right) \text{ erg cm}^{-3} \text{ s}^{-1}.\quad (2.22)$$

H_2 formation heating becomes dominant over the adiabatic heating at 10^8 – 10^9 cm^{-3} . The rapid heating stabilizes the gas against the growth of the deformation perturbations as [Tsuribe and Omukai \(2008\)](#) indicate by their simulations in the polytropic cloud model mimicking the evolution of the metal-poor clouds.

2.1.3 Dust thermal emission

The gas is cooled by the heat exchange with cold dust grains. The rate at which grains obtain the thermal energy per grain of species i with the radius r is

$$\mathcal{G}_i(r) = \sigma_{\text{d}} \langle nv(k) \rangle [2kT - 2kT_i(r)],\quad (2.23)$$

where $\sigma_{\text{d}} = \pi r^2$ is the geometrical cross-section of the grain and $\langle nv(k) \rangle = \sum n(k) (8kT/\pi\mu(k))^{1/2}$ is the average velocity multiplied by the number density of the gas-phase species k which collides with the grain. The grains release their energy by emitting photons at a rate

$$\mathcal{L}_i(r) = 4\sigma_{\text{B}}T_i(r) \langle Q_i^{\nu}(r) \rangle \sigma_{\text{d}}\beta_{\text{cont}},\quad (2.24)$$

where σ_{B} is the Stephan-Boltzmann constant, $\langle Q_i^{\nu}(r) \rangle \sigma_{\text{d}}$ is the average absorption cross-section weighted by the Planck distribution.

The escape probability β_{cont} of the continuum emission can be estimated as

$$\beta_{\text{cont}} = \min\{1, \tau_{\text{cont}}^{-2}\}\quad (2.25)$$

under the diffusion approximation, where τ_{cont} is the continuum opacity of the fluid consisting on gas and grains as

$$\tau_{\text{cont}} = \kappa_{\text{g}}\rho_{\text{g}} + \sum_i \int \langle Q_i^{\nu}(r) \rangle \sigma_{\text{d}}n_i\varphi_i(r)dr,\quad (2.26)$$

where κ_{g} is the absorption cross-section per unit gas. where n_i is the number density of grains i , and $\varphi_i(r)$ is the distribution of the grain radii normalized as $\int \varphi_i(r)dr = 1$. The

dominant processes of the photon absorption are Thomson scattering, Rayleigh scattering, and H^- free-free, bound-free, and bound-bound absorptions. We here utilize the table presented by [Mayer and Duschl \(2005\)](#). We neglect the absorption by heavy elements in the simulations of metal-poor star formation. The mass density of the gas ρ_g almost equals to the total mass density of the fluid ρ because the mass fraction of the dust is too small $< 1 \times (Z/Z_\odot) \%$.

The grain temperature is determined from the equation of the thermal balance $\mathcal{G}_i(r) = \mathcal{L}_i(r)$ for each species and radius under the assumption that the thermal equilibrium is rapidly reached than the dynamical time of the collapsing gas. Then, the total emission rate and gas cooling rate per unit volume can be obtained as

$$\Lambda_d = \sum_i \int \mathcal{L}_i(r) n_i \varphi_i(r) dr, \quad (2.27)$$

The heat exchange between gas and dust becomes rapid at the large density. The dust cooling rate can be written as

$$\begin{aligned} \Lambda_d &= \left[\sum_i \int \sigma_d n_i \varphi_i(r) dr \right] \langle nv(k) \rangle 2kT \\ &= 1.8 \times 10^{-7} \left(\frac{n_H}{10^{14} \text{ cm}^{-3}} \right)^2 \left(\frac{T}{1000 \text{ K}} \right)^{3/2} \left(\frac{Z}{10^{-5} Z_\odot} \right) \text{ erg cm}^{-3} \text{ s}^{-1} \end{aligned} \quad (2.28)$$

in the Pop III dust model utilized in our simulations in Chapter 5. We assume $T \gg T_i(r)$ well before the thermal coupling. On the other hand, the adiabatic heating rate is

$$\Gamma_{\text{adi}} = 3.7 \times 10^{-7} \left(\frac{\mu}{2.1} \right)^{-1} \left(\frac{n_H}{10^{14} \text{ cm}^{-3}} \right)^{3/2} \left(\frac{T}{1000 \text{ K}} \right) \text{ erg cm}^{-3} \text{ s}^{-1}. \quad (2.29)$$

It is the first point that the dust cooling can become effective at higher densities $n_H \sim 10^{11} - 10^{14} \text{ cm}^{-3}$ than the densities where the atomic and molecular cooling is important. At that time, the Jeans mass is

$$M_{J,\text{dust}} = 0.11 M_\odot \left(\frac{\mu}{2.3} \right)^{-3/2} \left(\frac{n_H}{10^{14} \text{ cm}^{-3}} \right)^{-1/2} \left(\frac{T}{1000 \text{ K}} \right)^{3/2}. \quad (2.30)$$

The cooling mechanism can explain the formation of the low-mass stars. The second point is that the dust cooling can become effective even with extremely low metallicities $\sim 10^{-5} Z_\odot$. Therefore, the dust cooling is considered to trigger the formation of the extremely metal-poor stars which have so far been observed in the Galactic halo (e.g. [Omukai 2000](#); [Schneider et al. 2003](#)).

2.2 Chemical reactions

The cooling rates depends not only on density and temperature but also on the abundance of the relevant species. The abundances evolve by the chemical reactions. Since the

Table 2.4: Chemical reactions of primordial species

No.	Reaction	Rate Coef.	Ref.
1	$\text{H}^+ + \text{e} \rightarrow \text{H} + \gamma$	$k_1 = \exp[-28.6130338 - 0.72411256(\ln(T(\text{eV})))$ $-2.02604473 \times 10^{-2}(\ln(T(\text{eV})))^2$ $-2.38086188 \times 10^{-3}(\ln(T(\text{eV})))^3$ $-3.21260521 \times 10^{-4}(\ln(T(\text{eV})))^4$ $-1.42150291 \times 10^{-5}(\ln(T(\text{eV})))^5$ $+4.98910892 \times 10^{-6}(\ln(T(\text{eV})))^6$ $+5.75561414 \times 10^{-7}(\ln(T(\text{eV})))^7$ $-1.85676704 \times 10^{-8}(\ln(T(\text{eV})))^8$ $-3.07113524 \times 10^{-9}(\ln(T(\text{eV})))^9]$	A97
2	$\text{H} + \text{e} \rightarrow \text{H}^- + \gamma$	$k_2 = 1.4 \times 10^{-18} T^{0.928} \exp(-T/1.62 \times 10^4)$	GP98
3	$\text{H}^- + \text{H} \rightarrow \text{H}_2 + \text{e}$	$k_3 = 4.0 \times 10^{-9} T^{-0.17} \quad (T > 300)$ $k_3 = 1.5 \times 10^{-9} \quad (T < 300)$	GP98
4	$\text{H}_2 + \text{H} \rightarrow 3\text{H}$	$k_4 = k_{\text{H}}^{1-a} k_{\text{L}}^a$ $k_{\text{L}} = 1.12 \times 10^{-10} \exp(-7.035 \times 10^4/T)$ $k_{\text{H}} = 6.5 \times 10^{-7} T^{-1/2} \exp(-5.2 \times 10^4/T) [1 - \exp(-6000/T)]$ $a = (1 + n/n_{\text{cr}})^{-1}$ $\log_{10}(n_{\text{cr}}) = 4.0 - 0.416 \log_{10}(T/10^4) - 0.327(\log_{10}(T/10^4))^2$	SK87
5	$3\text{H} \rightarrow \text{H}_2 + \text{H}$	$k_5 = 5.5 \times 10^{-29} T^{-1}$	PSS83
6	$2\text{H} + \text{H}_2 \rightarrow 2\text{H}_2$	$k_6 = k_5/8$	PSS83
7	$2\text{H}_2 \rightarrow 2\text{H} + \text{H}_2$	$k_7 = k_{\text{H}}^{1-a} k_{\text{L}}^a$ $k_{\text{L}} = 1.18 \times 10^{-10} \exp(-6.95 \times 10^4/T)$ $k_{\text{H}} = 8.125 \times 10^{-8} T^{-1/2} \exp(-5.2 \times 10^4/T) [1 - \exp(-6.0 \times 10^3/T)]$ $a = (1 + n/n_{\text{cr}})^{-1}$ $\log_{10}(n_{\text{cr}}) = 4.845 - 1.3 \log_{10}(T/10^4) + 1.62(\log_{10}(T/10^4))^2$	SK87 PSS83 (k_{H})
8	$2\text{H} + \text{grains} \rightarrow \text{H}_2 + \text{grains}$	see text	
9	$\text{D} + \text{H}^+ \rightarrow \text{D}^+ + \text{H}$	$k_9 = 3.7 \times 10^{-10} T^{0.28} \exp(-43/T)$	NU02
10	$\text{D}^+ + \text{H} \rightarrow \text{D} + \text{H}^+$	$k_{10} = 3.7 \times 10^{-10} T^{0.28}$	NU02
11	$\text{D} + \text{H}_2 \rightarrow \text{H} + \text{HD}$	$k_{11} = 9.0 \times 10^{-11} \exp(-3876/T)$	NU02
12	$\text{D}^+ + \text{H}_2 \rightarrow \text{H}^+ + \text{HD}$	$k_{12} = 2.1 \times 10^{-9}$	NU02
13	$\text{HD} + \text{H} \rightarrow \text{H}_2 + \text{D}$	$k_{13} = 3.2 \times 10^{-11} \exp(-3624/T)$	NU02
14	$\text{HD} + \text{H}^+ \rightarrow \text{H}_2 + \text{D}^+$	$k_{14} = 1.0 \times 10^{-9} \exp(-464/T)$	NU02

The unit of temperature T is K. The unit of all rate coefficients are $\text{cm}^3 \text{s}^{-1}$, but $\text{cm}^6 \text{s}^{-1}$ for three-body reactions 5 and 6. Ref.: A97; [Abel et al. \(1997\)](#), GP98; [Galli and Palla \(1998\)](#), SK87; [Shapiro and Kang \(1987\)](#), NU02; [Nakamura and Umemura \(2002\)](#), PSS83; [Palla et al. \(1983\)](#).

typical timescales of the reactions are comparable to the dynamical timescale of the collapsing gas, we should take the non-equilibrium chemistry into consideration in our simulations.

2.2.1 Gas-phase chemistry

2.2.1.1 Primordial species

As well as hydrogen molecules are the important coolant with metallicities $\lesssim 10^{-6} Z_{\odot}$, the thermal evolution at lower densities than 10^8 cm^{-3} is affected by the hydrogen molecular abundance enhanced by their formation on the grain surfaces in the present-day dust model ([Omukai et al. 2005](#)). Also, hydrogen deuteride (HD) can also be an important coolant in hyper metal-poor gas ($< 10^{-5} Z_{\odot}$) even without the background radiation against as found for the first time in our previous work ([Hirano et al. 2014](#)). We show

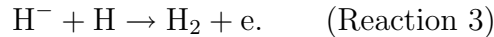
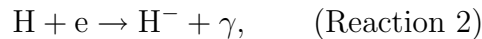
the chemical reaction rates of the primordial species included in our simulations in Table 2.4.

(a) Formation and dissociation of H_2 molecules

The homonuclear diatomic molecule H_2 does not have the dipole moment. To release the surplus energy which the molecules obtain in their formation, hydrogen molecules are formed more rapidly with catalysts than the formation process where two hydrogen atoms are directly associated with photon emission.

i) H^- process

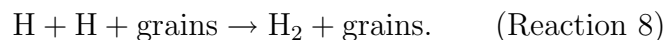
The molecules are formed via reactions



In the case, electron is the catalyst. The formation process is important at low densities $n_{\text{H}} \lesssim 10^8 \text{ cm}^{-3}$. The number fraction of hydrogen molecules slowly increases up to $\sim 3 \times 10^{-4}$ in the absence of the formation reaction on grain surfaces. Even with the small fraction, the H_2 cooling rate can exceed the adiabatic heating rate until the gas density reaches the critical density for the molecule. The gas is rapidly cooled at densities from $n_{\text{H}} \sim 1$ to $n_{\text{crit}} \sim 10^3 \text{ cm}^{-3}$. At $n_{\text{H}} > n_{\text{crit}}$, the gas temperature slowly increases with the balance between H_2 cooling and compressional heating.

ii) formation on grains

The reaction rate depends on the grain temperature. Dust grains promote the efficiency of the H_2 molecular formation via the reaction on the grain surfaces. Since H_2 molecules are major coolants in a low-metallicity gas, the thermal evolution of the collapsing gas is significantly affected especially in the early stages of collapse. At lower density $n_{\text{H}} \lesssim 10^8 \text{ cm}^{-3}$, the reaction on grain surfaces also contribute to the formation of hydrogen molecules. This can modify the efficiency of H_2 line cooling and the thermal evolution with intermediate metallicities $Z \gtrsim 10^{-3} Z_{\odot}$. Hydrogen atoms are absorbed on the surfaces of grains, move from a potential well to another well to form molecules as



The formation rate of hydrogen molecules per grain of species i with radius r is estimated as

$$\mathcal{R}_{\text{H}_2,i}(r) = \frac{1}{2}n(\text{H}_1)\langle v_{\text{H}}\rangle\pi r^2\varepsilon_{\text{H}_2}S_{\text{H}}, \quad (2.31)$$

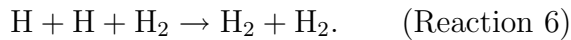
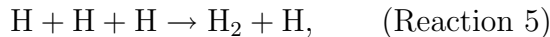
where $n(x)$ is the number density of gas-phase species x , $\langle v_{\text{H}}\rangle = (8kT/\pi m_{\text{H}})^{1/2}$ is the average velocity of hydrogen atoms, ε_{H_2} is the efficiency of H_2 recombination on grain surfaces, and S_{H} is the sticking efficiency of hydrogen atoms colliding with

the grain surfaces (Cazaux and Tielens 2002). The quantities of ε_{H_2} and S_{H} are functions of both gas and grain temperatures (see Schneider et al. 2006, for detailed formulations). We estimate $\mathcal{R}_{\text{H}_2,i}(r)$ for each grain species and radius. Then, the total formation rate of hydrogen molecules on grain surfaces per unit volume is described as

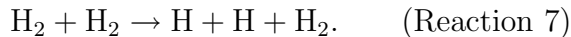
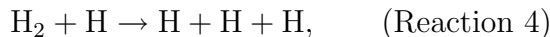
$$\left. \frac{dn_{\text{H}_2}}{dt} \right|_{\text{on grains}} = \sum_i \int \mathcal{R}_{\text{H}_2,i}(r) n_i \varphi_i(r) dr. \quad (2.32)$$

iii) three-body reactions

The third body can be hydrogen atoms at smaller densities or hydrogen molecules at larger densities. This is called three-body reactions and becomes important at $n_{\text{H}} \gtrsim 10^8 \text{ cm}^{-3}$. The importance of the reaction is first reported by Palla et al. (1983) in the context of the Pop III and II star formation. In the primordial gas, where the catalysts for hydrogen molecular formation is limited to the primordial species, the reactions are important to serve as the coolant (Abel et al. 2002; Yoshida et al. 2003). The reactions can be written as



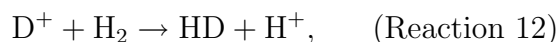
The inverse reactions, i.e., the collisional dissociation of hydrogen molecules



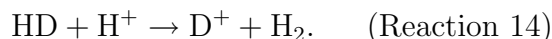
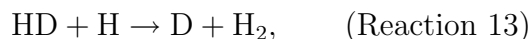
become important at densities $n_{\text{H}} \sim 10^{16}\text{--}10^{18} \text{ cm}^{-3}$. Since these are the endothermic reactions, the gas kinetic energy is absorbed to form hydrogen atoms. It is considered that the reactions becomes effective after the gas is optically thick to form the adiabatic core, and trigger the second collapse with sufficiently larger metallicities $\gtrsim 10^{-5} Z_{\odot}$ (Larson 1969; Omukai 2000).

(b) HD molecules

Hydrogen deuteride (HD) control the thermal evolution of the gas as well as H_2 molecules with metallicities $\lesssim 10^{-5} Z_{\odot}$. The molecules are formed via the reactions



balanced with the dissociation reactions



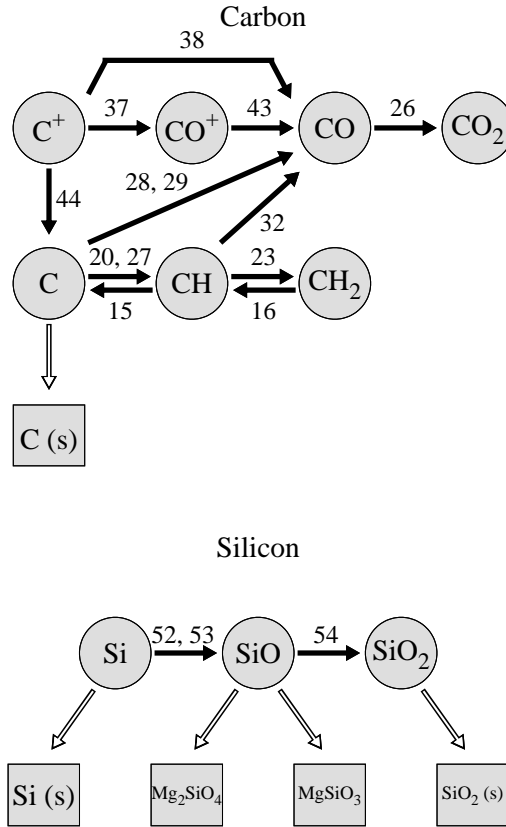


Figure 2.5: Chemical network of C-bearing (top) and Si-bearing (bottom) species. Circles and squares depict the gas- and solid-phase species, respectively. The index ‘(s)’ indicates the solid-phase species. The black arrows indicate the gas-phase reactions, and the white arrows indicate the accretion of gas-phase species onto grains. The numbers attached to the arrows are identical with the IDs in Table 2.5.

In the case where the gas temperature is above 100 K at $n_{\text{H}} \sim 10^4 \text{ cm}^{-3}$, the equilibrium between the formation reactions (Reactions 11 and 12) and the dissociation reactions (Reactions 13 and 14) is reached. The fraction of HD molecules relative to hydrogen nuclei is almost constant to $\sim 10^{-7}$. Whereas, if the gas temperature becomes below 100 K, the formation reaction rates slightly exceed the dissociation reaction rates. The increasing abundance of HD molecules leads the gas to be further cooled. Therefore, the difference of the temperature among clouds tend to be wider in the existence of HD molecules at densities $n_{\text{H}} \lesssim 10^8 \text{ cm}^{-3}$.

Table 2.5: Chemical reactions of metal

No.	Reaction	Rate Coef.	Ref.
15	$\text{H} + \text{CH} \rightarrow \text{C} + \text{H}_2$	$k_{15} = 4.98 \times 10^{-11}$	M97
16	$\text{H} + \text{CH}_2 \rightarrow \text{CH} + \text{H}_2$	$k_{16} = 2.70 \times 10^{-10}$	M97
17	$\text{H} + \text{OH} \rightarrow \text{H}_2 + \text{O}$	$k_{17} = 7.00 \times 10^{-14} (\text{T}/300)^{2.80} \exp(-1950/\text{T})$	M97
18	$\text{H} + \text{H}_2\text{O} \rightarrow \text{OH} + \text{H}_2$	$k_{18} = 6.83 \times 10^{-12} (\text{T}/300)^{1.60} \exp(-9720/\text{T})$	M97
19	$\text{H} + \text{O}_2 \rightarrow \text{OH} + \text{O}$	$k_{19} = 3.30 \times 10^{-10} \exp(-8460/\text{T})$	M97
20	$\text{C} + \text{H}_2 \rightarrow \text{CH} + \text{H}$	$k_{20} = 6.64 \times 10^{-10} \exp(-11700/\text{T})$	M97
21	$\text{O} + \text{H}_2 \rightarrow \text{OH} + \text{H}$	$k_{21} = 3.43 \times 10^{-13} (\text{T}/300)^{2.67} \exp(-3160/\text{T})$	M97
22	$\text{H}^+ + \text{O} \rightarrow \text{O}^+ + \text{H}$	$k_{22} = 7.00 \times 10^{-10} \exp(-232/\text{T})$	M97
23	$\text{H}_2 + \text{CH} \rightarrow \text{CH}_2 + \text{H}$	$k_{23} = 2.38 \times 10^{-10} \exp(-1760/\text{T})$	M97
24	$\text{H}_2 + \text{OH} \rightarrow \text{H}_2\text{O} + \text{H}$	$k_{24} = 1.55 \times 10^{-12} (\text{T}/300)^{1.60} \exp(-1660/\text{T})$	M97
25	$2\text{OH} \rightarrow \text{H}_2\text{O} + \text{O}$	$k_{25} = 1.65 \times 10^{-12} (\text{T}/300)^{1.14} \exp(-50/\text{T})$	M97
26	$\text{OH} + \text{CO} \rightarrow \text{CO}_2 + \text{H}$	$k_{26} = 1.00 \times 10^{-13}$	M97
27	$\text{C} + \text{H} \rightarrow \text{CH} + \gamma$	$k_{27} = 1.00 \times 10^{-17}$	M97
28	$\text{C} + \text{OH} \rightarrow \text{CO} + \text{H}$	$k_{28} = 1.10 \times 10^{-10} (\text{T}/300)^{0.50}$	M97
29	$\text{C} + \text{O}_2 \rightarrow \text{CO} + \text{O}$	$k_{29} = 3.30 \times 10^{-11}$	M97
30	$\text{O} + \text{H} \rightarrow \text{OH} + \gamma$	$k_{30} = 9.90 \times 10^{-19} (\text{T}/300)^{-0.38}$	M97
31	$2\text{O} \rightarrow \text{O}_2 + \gamma$	$k_{31} = 4.90 \times 10^{-20} (\text{T}/300)^{1.58}$	M97
32	$\text{O} + \text{CH} \rightarrow \text{CO} + \text{H}$	$k_{32} = 6.60 \times 10^{-11}$	M97
33	$\text{O} + \text{OH} \rightarrow \text{O}_2 + \text{H}$	$k_{33} = 4.34 \times 10^{-11} (\text{T}/300)^{-0.50} \exp(-30/\text{T})$	M97
34	$\text{H}^+ + \text{OH} \rightarrow \text{OH}^+ + \text{H}$	$k_{34} = 2.10 \times 10^{-9}$	M97
35	$\text{H}^+ + \text{H}_2\text{O} \rightarrow \text{H}_2\text{O}^+ + \text{H}$	$k_{35} = 6.90 \times 10^{-9}$	M97
36	$\text{H}^+ + \text{O}_2 \rightarrow \text{O}_2^+ + \text{H}$	$k_{36} = 2.00 \times 10^{-9}$	M97
37	$\text{C}^+ + \text{OH} \rightarrow \text{CO}^+ + \text{H}$	$k_{37} = 7.70 \times 10^{-10}$	M97
38	$\text{C}^+ + \text{O}_2 \rightarrow \text{O}^+ + \text{CO}$	$k_{38} = 6.20 \times 10^{-10}$	M97
39	$\text{O}^+ + \text{H} \rightarrow \text{H}^+ + \text{O}$	$k_{39} = 6.80 \times 10^{-10}$	M97
40	$\text{O}^+ + \text{H}_2 \rightarrow \text{OH}^+ + \text{H}$	$k_{40} = 1.70 \times 10^{-9}$	M97
41	$\text{OH}^+ + \text{H}_2 \rightarrow \text{H}_2\text{O}^+ + \text{H}$	$k_{41} = 1.01 \times 10^{-9}$	M97
42	$\text{H}_2\text{O}^+ + \text{H}_2 \rightarrow \text{H}_3\text{O}^+ + \text{H}$	$k_{42} = 8.30 \times 10^{-10}$	M97
43	$\text{CO}^+ + \text{H} \rightarrow \text{H}^+ + \text{CO}$	$k_{43} = 7.50 \times 10^{-10}$	M97
44	$\text{C}^+ + \text{e} \rightarrow \text{C} + \gamma$	$k_{44} = 4.40 \times 10^{-12} (\text{T}/300)^{-0.61}$	M97
45	$\text{OH}^+ + \text{e} \rightarrow \text{O} + \text{H}$	$k_{45} = 3.75 \times 10^{-8} (\text{T}/300)^{-0.50}$	M97
46	$\text{H}_2\text{O}^+ + \text{e} \rightarrow \text{OH} + \text{H}$	$k_{46} = 1.60 \times 10^{-7} (\text{T}/300)^{-0.50}$	M97
47	$\text{H}_2\text{O}^+ + \text{e} \rightarrow \text{O} + \text{H}_2$	$k_{47} = 2.00 \times 10^{-7} (\text{T}/300)^{-0.50}$	M97
48	$\text{H}_3\text{O}^+ + \text{e} \rightarrow \text{H}_2\text{O} + \text{H}$	$k_{48} = 3.50 \times 10^{-7} (\text{T}/300)^{-0.50}$	M97
49	$\text{H}_3\text{O}^+ + \text{e} \rightarrow \text{OH} + 2\text{H}$	$k_{49} = 6.50 \times 10^{-7} (\text{T}/300)^{-0.50}$	M97
50	$\text{O}_2^+ + \text{e} \rightarrow 2\text{O}$	$k_{50} = 1.95 \times 10^{-7} (\text{T}/300)^{-0.70}$	M97
51	$\text{H}_2 + \text{C} \rightarrow \text{CH}_2 + \gamma$	$k_{51} = 1.00 \times 10^{-17}$	M97
52	$\text{Si} + \text{OH} \rightarrow \text{SiO} + \text{H}$	$k_{52} = 3 \times 10^{-11}$	H80
53	$\text{Si} + \text{O}_2 \rightarrow \text{SiO} + \text{O}$	$k_{53} = 1.3 \times 10^{-11} \exp(-111/\text{T})$	LG90
54	$\text{SiO} + \text{OH} \rightarrow \text{SiO}_2 + \text{H}$	$k_{54} = 2 \times 10^{-13}$	H80

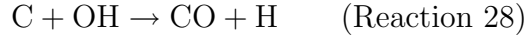
The units of temperature T and rate coefficients are K and $\text{cm}^3 \text{s}^{-1}$, respectively. Ref.: M97; Millar et al. (1997), H80; Hartquist et al. (1980), LG90; Langer and Glassgold (1990).

2.2.1.2 Metal species

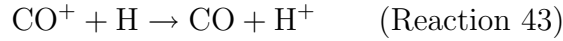
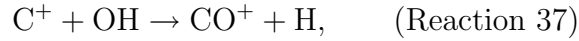
The important chemical reaction networks of carbon- and silicon-bearing species are described in Figure 2.5. Especially, CO molecules are important as the gas coolant with metallicities $Z > 10^{-3} Z_{\odot}$, and otherwise OH, and H₂O are. Table 2.5 shows the reaction rates of the metal species.

(a) C-bearing species

Carbon atoms formed most efficiently via the reaction



at densities $n_{\text{H}} \sim 1\text{--}10^8 \text{ cm}^{-3}$, followed by



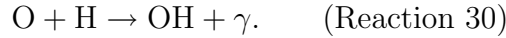
until $n_{\text{H}} \sim 10^5 \text{ cm}^{-3}$ and



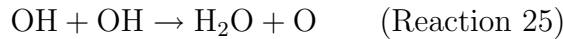
from $n_{\text{H}} \sim 10^5 \text{ cm}^{-3}$ with metallicity $10^{-4} Z_{\odot}$. Since the carbon atoms are depleted into CO molecules at $n_{\text{H}} \sim 10^5 \text{ cm}^{-3}$, the amorphous carbon grains can not accrete the atoms to grow.

(b) O-bearing species

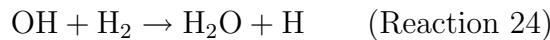
Oxygen atoms are reduced to OH and H₂O molecules. First, OH molecules are formed mainly via the reaction



Part of oxygen nuclei is depleted on OH molecules at $n_{\text{H}} \sim 10^5 \text{ cm}^{-3}$. The reaction



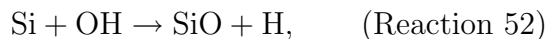
rapidly proceeds to form H₂O molecules until the OH molecules are dominant at $\lesssim 10^8 \text{ cm}^{-3}$. The main formation reaction of H₂O turns to be



after the hydrogen molecules becomes dominant by three-body reactions and after most of OH molecules are converted to H₂O molecules.

(c) Si-bearing species

Silicon atoms are oxidized into SiO and SiO₂ molecules. At $n_{\text{H}} \sim 10^5 \text{ cm}^{-3}$, SiO molecules are formed via



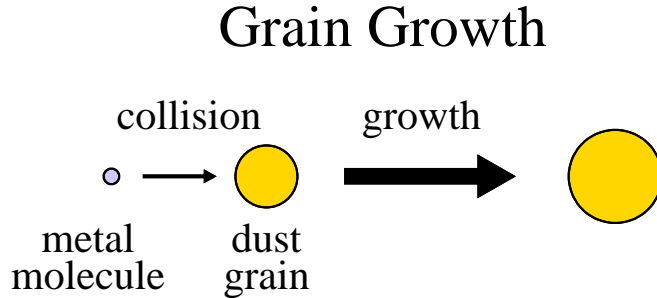
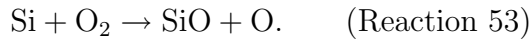
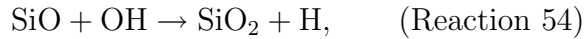


Figure 2.6: Conceptual image of grain growth. A metal atom or molecule (indicated by the blue circle) collides and sticks to a dust grain (left smaller yellow circle). As a result, the mass and the size of the dust grain increase (right larger yellow circle).



Although the SiO_2 molecules are rapidly formed at $n_{\text{H}} \gtrsim 10^8 \text{ cm}^{-3}$ via the reaction



the abundance of the molecules is comparable to the fraction of SiO. SiO and SiO_2 molecules are accreted onto silicate grains as we revisit below to contribute to the gas cooling efficiency.

2.2.2 Grain growth

Grain growth is the accretion process of the gas-phase metal molecules onto grains. This can enhance the cooling efficiency by the dust thermal emission. Figure 2.6 shows the conceptual image of the grain growth. A metal atom or molecule collides to a grain particle. It sticks to the grain at some rate (set 1 in our simulations), and as a result, the mass of the grain m_i increases by the mass of the molecule m_j . If the bulk density of the grain is not changed, the grain size increases by a factor of $[(m_i + m_j)/m_i]^{1/3}$. Hereafter, we use the indices i and j to indicate the element and grain species, respectively.

In the neighbor dense molecular cloud cores, the evidences of the grain growth are discovered by the recent observations (e.g. Chapman et al. 2009; Steinacker et al. 2010). The mid-infrared observations by the *Spitzer* telescope reveal that the scattered light by micron-size grains are detected in the cloud core. This can be the evidence of the growth of dust grains whose size is usually sub-micron in the interstellar medium. Also in the early Universe, it is expected that the grains, which has been partly destroyed by the effect of the reverse shock when they are released from Pop III supernovae, again accrete the gas-phase metal during the succeeding cloud collapse as the gas density increases so that the timescale of the growth is smaller than the dynamical time of the gas even with the small dust-to-gas mass ratio.

Table 2.6: Properties of grain growth reactions

Grains	Key species	Chemical Reaction	μ_{ij}	$a_{ij,0}$ (Å)
Si(s)	Si(g)	Si(g) → Si(s)	28.0	1.684
Fe(s)	Fe(g)	Fe(g) → Fe(s)	56.0	1.411
MgSiO ₃ (s)	Mg(g)	2Mg(g) + SiO(g) + 3H ₂ O(g) → MgSiO ₃ (s) + 3H ₂ (g)	70.0	2.055
	SiO(g)	2Mg(g) + SiO(g) + 3H ₂ O(g) → MgSiO ₃ (s) + 3H ₂ (g)	140.0	2.589
Mg ₂ SiO ₄ (s)	Mg(g), SiO(g)	Mg(g) + SiO(g) + 2H ₂ O(g) → Mg ₂ SiO ₄ (s) + 2H ₂ (g)	100.0	2.319
Fe ₃ O ₄ (s)	Fe(g)	3Fe(g) + 4H ₂ O(g) → Fe ₃ O ₄ (s) + 4H ₂ (g)	77.3	1.805
C(s)	C(g)	C(g) → C(s)	12.0	1.281
SiO ₂ (s)	SiO ₂ (g)	SiO ₂ (g) → SiO ₂ (s)	60.0	2.080
MgO(s)	Mg(g)	Mg(g) + H ₂ O(g) → MgO(s) + H ₂ (g)	40.0	1.646
FeS(s)	Fe(g), S(g)	Fe(g) + S(g) → FeS(s)	88.0	1.932
Al ₂ O ₃ (s)	Al(g)	2Al(g) + 3H ₂ O(g) → Al ₂ O ₃ (s) + 3H ₂ (g)	51.0	1.718

The subscripts “(s)” and “(g)” depict solid- and gas-phase species, respectively. μ_{ij} and $a_{ij,0}$ are the molecular weight and the hypothetical radius of a monomer of grain species i per nuclei of the key element j .

We introduce the condensation efficiency f_{ij} as the number fraction of nuclei of metal j locked into grain species i to indicate the amount of grains. The initial condensation efficiency $f_{ij,0}$ and grain size distribution $\varphi_{i,0}(r)$ for the relevant grain species i are given for each Pop III supernova model where dust formation and destruction in the expanding ejecta are computed. These values are made use of as the initial condition of dust properties in our simulations of low-metallicity gas collapse. From the mass conservation law, the temporal evolution of the condensation efficiency is determined as

$$f_{ij}(t) = f_{ij,0} \frac{\int r^3 \varphi_i(r, t) dr}{\int r^3 \varphi_{i,0}(r) dr}. \quad (2.33)$$

The temporarily increasing size of each grain can be obtained by the time integration of the growth rate:

$$\left(\frac{dr}{dt} \right)_i = \alpha_i \left(\frac{4\pi}{3} a_{ij,0}^3 \right) \left(\frac{kT}{2\pi m_{i1}} \right)^{1/2} n_{i1}(t), \quad (2.34)$$

where α_i is the sticking efficiency for species i , or the ratio of the monomers locked into the grains relative to the ones colliding with the grains. $a_{ij,0} = (3\mu_{ij}m_{\text{H}}/4\pi\varsigma_i)^{1/3}$ is the hypothetical radius of the grain monomer per nuclei of element j , and ς_i is the bulk density of the grain as a solid. $n_{i1}(t)$ is the number density of the gas-phase species which carries the element j from the gas-phase to the grains such as SiO molecule for the forsterite grains.

For simplicity, we assume that the growth rate of the size is controlled by a gas phase species which least frequently hits the grains. The species is hereafter called the *key species*. The frequency of the impact of species x_j which carries the element j can be written as $\nu_{ix_j} = \alpha_i \pi a_{ij,0}^2 (kT/2\pi m_{ix_j})^{1/2} n_{ix_j}(t)$. For a grain species with two carriers $x_j = 1$ and 2, if $\nu_{i1} < \nu_{i2}$, the species 1 becomes the key species. For example, when an SiO molecule is stucked into a forsterite (Mg₂SiO₄) grain at the least frequency $\nu_{\text{Mg}_2\text{SiO}_4, \text{SiO}}$, an Mg atom and two water molecules are stucked at the same rate under the key species approximation. Table 2.6 shows the reactions from the gas phase (g) to the solid-phase (s) considered in this Thesis and the quantities of μ_{ij} and $a_{ij,0}$.

Grain growth and its effect on cloud fragmentation

Contents

3.1	Overview	47
3.2	Dust models in the early Universe	48
3.2.1	Pop III supernova model	48
3.2.2	Difference of two models	51
3.2.3	Dust property	53
3.2.4	Setup	54
3.3	Overall thermal evolution of clouds	54
3.3.1	Important chemical and thermal processes	54
3.3.2	Effect of grain growth	58
3.4	Conditions for cloud fragmentation	59
3.4.1	Critical dust-to-gas mass ratio without grain growth	59
3.4.2	Critical metallicity	60
3.5	Implication for the observed primitive stars	63
3.6	Chapter summary	65

3.1 Overview

Dust grains in the early Universe play a crucial role in the transition of the typical stellar mass scale. It is considered that, even with a trace amount, they promote the gas fragmentation into low-mass clumps and determine the critical condition for the first low-mass star formation. Therefore, we should take care about the properties of dust grains. In previous works, the properties of dust grains in the solar neighborhood are often applied to the studies about the metal-poor star formation for simplicity. In the present-day, all refractory elements are condensed into dust grains. Whereas, it has been revealed that the dust-to-metal mass ratio in high-redshift objects is considerably smaller by the recent

observations. In the early star-formation site, the metal and dust are supplied mainly by Pop III supernovae. In the expanding ejecta, the dust destruction is also effective by the reverse shocks. By the impact with energetic gas particles, the materials in grains are released into the gas-phase. Therefore, it is expected that the the cloud polluted by the supernova-originated dust has smaller metal condensation efficiencies than in the present-day. Also, the earlier studies assume that the metal condensation efficiency onto grains are constant during gas contraction. The accretion of gas-phase metal onto grain (grain growth) might be important to enhance the grain cooling efficiency and promote the cloud fragmentation with smaller metallicities. It is worth estimating how grain growth affect the thermal evolution of metal-poor clouds.

In this Chapter, in order to define the condition for dust cooling to trigger the cloud fragmentation into low-mass cores, we perform a one-zone semi-analytic model of the thermal evolution of a collapsing cloud. We here employ the dust properties (the condensation efficiency of metal onto grains, abundance of grain species, and dust size distribution) consistently calculated with dust formation/destruction in early supernovae as the initial conditions of our collapse calculations. We also consider grain growth into our calculations self-consistently with cloud thermal evolution. In Section 3.2, we introduce the realistic dust model in the early Universe: Pop III dust models and discuss the features of them. Next, in Section 3.3, we pick up a dust model to see the resulting thermal evolution of the gas. Then, we attempt to define the critical conditions for the dust-induced gas fragmentation in Section 3.4, and apply the criterion for formation of the extremely metal-poor stars so far observed in Section 3.5.

The content in this Chapter has been already published in Monthly Notices of the Royal Astronomical Society, Volume 446, Issue 3, p.2659-2672 (Chiaki et al. 2015)

3.2 Dust models in the early Universe

3.2.1 Pop III supernova model

The dust properties (metal condensation efficiency, abundance of chemical species, and dust size distribution) is calculated by the two leading studies independently. Nozawa et al. (2007) and Schneider et al. (2012a) first calculate the self-consistently the hydrodynamic model of the expanding ejecta and dust formation/destruction therein. We hereafter call these models as N07 and S12, respectively. They treat the dust formation in the expanding supernova ejecta via nucleation and then accretion of ambient gas-phase metal onto embryo grains. The formation mechanisms occur efficiently after several 100 yr, when the temperature of the medium in the ejecta adiabatically decrease below the order of dust sublimation temperature of each grain species. They study a wide range of the progenitor masses with $M_{\text{pr}} = 13, 20, 25, \text{ and } 30 M_{\odot}$ (hereafter called M13, M20, M25, and M30 models, respectively) for the core-collapse supernova (CCSN). N07 explore also in the case of the pair-instability supernova (PISN) with $M_{\text{pr}} = 170$ (M170)

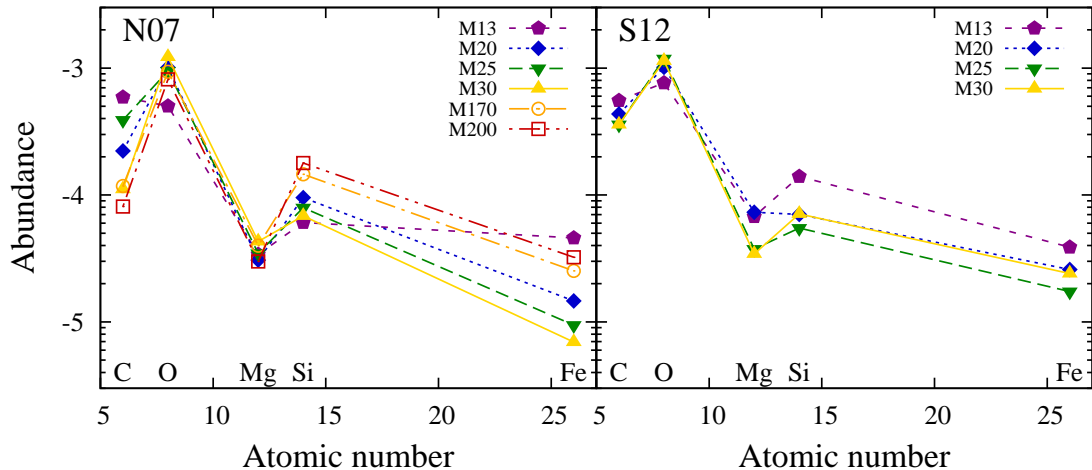


Figure 3.1: Number abundance A_j of heavy element j relative to hydrogen nuclei for our Pop III models N07 (left) and S12 (right). Since the values shown here is with $Z = Z_\odot$, the abundance in the cloud with metallicity Z is calculated as $A_j(Z/Z_\odot)$.

and $200 M_\odot$ (M200).

For each progenitor mass, dust destruction occurs $\sim 10^4$ yr after the explosion. At that time, the blast waves interact with the circumstellar medium. When the ejecta sweep up the ambient gas with the same mass, the reverse shocks are generated. When the grains are enclosed into the dense region between forward and reverse shocks, they undergo sputtering by the impact with the high energy gas particles. Then, the part of their materials are stripped away and the dust-to-metal mass ratio (condensation efficiency) in the gas becomes smaller. The destruction efficiency of grains is dependent on the strength of the reverse shocks. It can be parametrized by the ambient gas density. N07 investigate the grain destruction for the number densities of the ambient gas $n_{\text{amb}} = 0.1, 1,$ and 10 cm^{-3} (n0.1, n1, and n10, respectively). S12 investigate for the mass densities of the ambient gas $\rho_{\text{amb}} = 10^{-25}, 10^{-24},$ and $10^{-23} \text{ g cm}^{-3}$ (rev1, rev2, and rev3, respectively).

The Pop III dust models are the initial condition for the Pop II star-forming gas cloud. From metal mass created by nucleosynthesis in the progenitor star, we can obtain the abundance of heavy element j as

$$A_j = \frac{Z}{\mu_j X_{\text{H}}} \frac{M_j}{M_{\text{metal}}}, \quad (3.1)$$

where μ_j is the molecular weight of nucleus j relative to hydrogen, and $X_{\text{H}} = 1 - Y_{\text{He}}$ is the hydrogen mass fraction ($Y_{\text{He}} = 0.75$). Figure 3.1 shows the metal abundances with every progenitor mass in N07 and S12 models. These models also give the mass M_i of the grain species i released to the interstellar matter avoiding the destruction effect of the

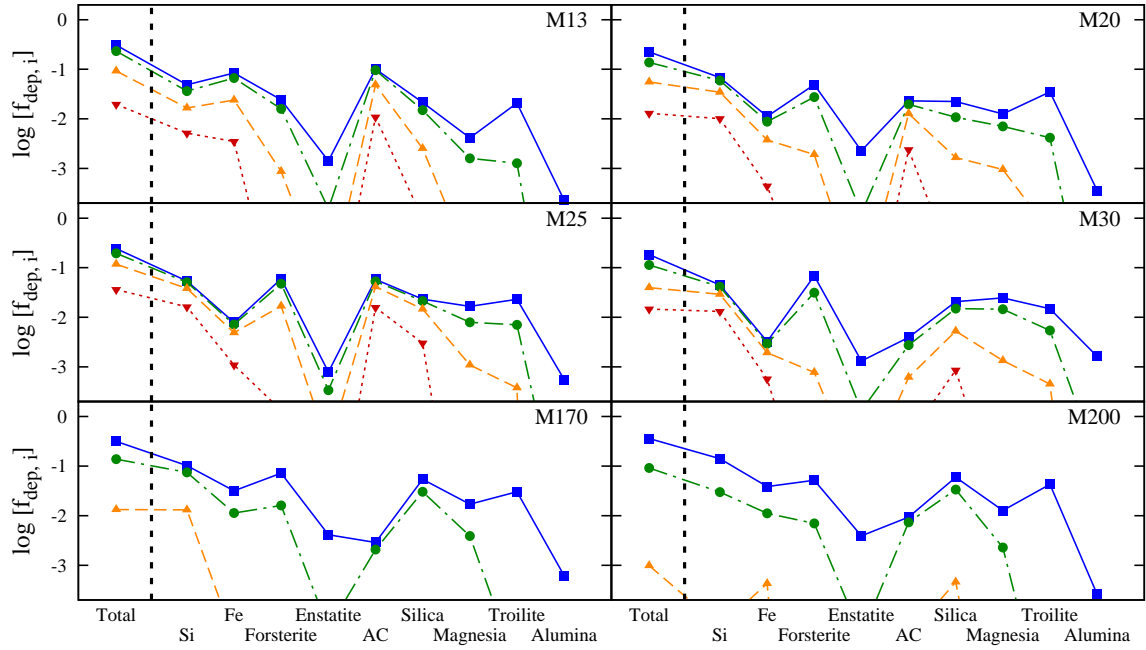


Figure 3.2: Initial depletion efficiency $f_{\text{dep},i,0}$ of metal onto grain species i in Pop III dust model N07. We show the quantities for the grains created in the expanding ejecta of Pop III supernova (n0: blue lines). The flesh dust is then partly destroyed by the reverse shocks. We show the three reverse shock models n0.1, n1, and n10 with larger destruction effects from top to bottom (green, yellow, and red lines, respectively). “AC” denotes the amorphous carbon.

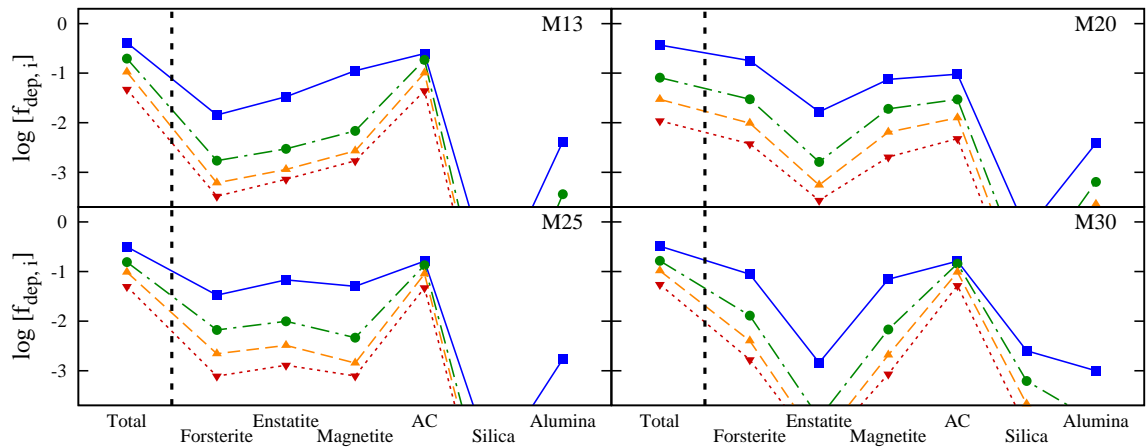


Figure 3.3: Same as Figure 3.2 but for S12 model.

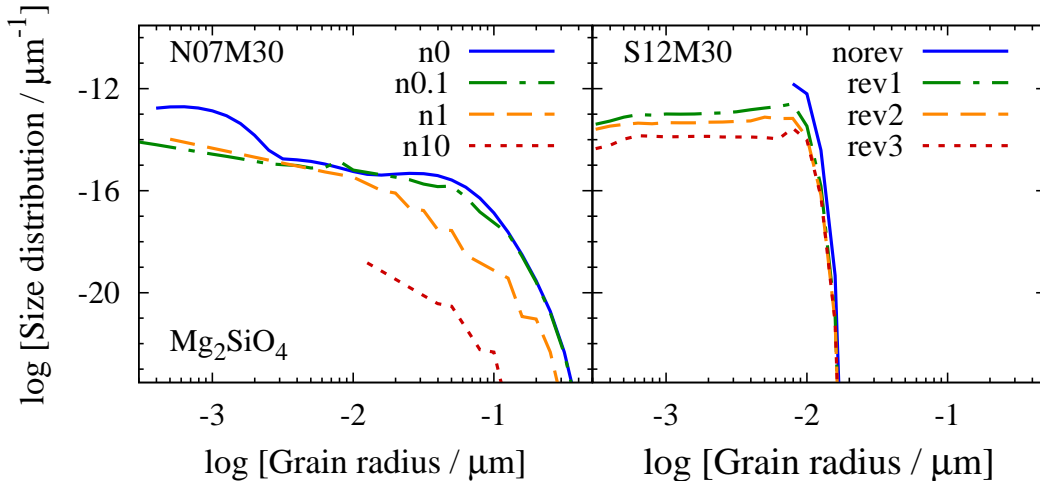


Figure 3.4: Initial size distribution of Forsterite grains for N07 (left) and S12 (right) models with progenitor mass $M_{\text{pr}} = 30 M_{\odot}$. We show four dust destruction models n0, n0.1, n1, and n10 for N07 and norev, rev1, rev2, rev3 for S12 from top to bottom.

reverse shocks. We compute the depletion efficiency of the total metal onto grain species i as $f_{\text{dep},i} = M_i/M_{\text{metal}}$ as shown in Figures 3.2 and 3.3 for N07 and S12, respectively. The fourth and sixth columns of Table 3.1 show the initial depletion efficiencies for carbon and silicate, respectively. As expected, the dust mass decreases with the increasing ambient gas density. The initial condensation efficiency of the collapsing cloud is estimated as

$$f_{ij,0} = \frac{M_i/\mu_{ij}}{M_j/\mu_j}. \quad (3.2)$$

3.2.2 Difference of two models

3.2.2.1 Metal abundance

The elemental abundance resulting from the nucleosynthesis of progenitor star affects the properties of grains formed. While S12 can predict the abundances less sensitive to the progenitor mass, N07 presents the various patterns. Both N07 and S12 perform the calculation in the core-collapse supernova (CCSN) models. The study by N07 is based on the stellar evolution and supernova calculations by Umeda and Nomoto (2002). They employ the standard parameters to calculate the nucleosynthesis. S12 fit the three parameters of the mass cut, for each SN model by the abundance pattern of the most primitive star SDSS J1029+1729 (Caffau et al. 2011) based on the procedure of Limongi and Chieffi (2012). All the progenitor models predict the moderate excesses of the lighter elements than Fe from the solar values by ~ 0.5 dex. Especially, N07M13 models predict

$C > O$, which would lead the carbon grains to grow by accretion of the gas-phase carbon atoms free from depletion onto CO molecules. Although the relationship between the progenitor mass and the metal abundances are not linear, we can see the trend that heavier elements such as Si and Fe increases with the increasing progenitor mass. This is due to the nucleosynthesis becomes more efficient in the more massive stars. Note that these elemental abundance are for C-normal extremely metal-poor (EMP) stars. For carbon-enhanced EMP (CEMP) star, see [Marassi et al. \(2014\)](#).

3.2.2.2 Grain composition

By the difference of their procedures, N07 and S12 models predict the different grain compositions, which is expected to affect the dust cooling efficiency and the gas thermal evolution. We here discuss one-by-one below:

- The mass fraction of carbon grains is generally larger for S12 model than N07. Carbon grains are formed by condensation of carbon atoms that are not depleted into CO molecules in the supernova ejecta. S12 consider the destruction of the molecules by the impact with high-energy electrons from decaying ^{56}Co ([Todini and Ferrara 2001](#)). N07 do not include the molecule dissociation, i.e., the carbon nuclei are kept to be depleted onto CO molecules. Although the carbon-rich layer is outer than oxygen-rich layer, the CO molecules are efficiently formed in the large overlapped region. That is why the formation of carbon grains is mitigated in N07 model.
- Magnetite grains are formed in S12 model but not in N07 model. This is due to the different treatment of fluid mixing in the ejecta between the two models. N07 calculate in the both cases: for the fully mixed and for no-mixed ejecta. We here take the latter case in this work. In this no-mixing model, the ejecta is considered to remain stratified, where the original onion-like structure is maintained during the explosions. Since the oxygen-rich layer does not overlap with the iron-rich layer settling in the innermost region of the ejecta, Fe_3O_4 grains are not formed. On the other hand, S12 consider mixed ejecta, where the composition of heavy elements is uniform, magnetite grains can be formed.

3.2.2.3 Size distribution

N07 and S12 models can also predict different size distribution. Figure 3.4 shows the size distributions of Mg_2SiO_4 grains formed and destroyed in the ejecta.

- The different features of size distribution are already appear before the grains are destroyed (see blue curves). The dust properties are determined mainly by the density, temperature, and concentration of refractory gas species in the site of the grain formation.

- For the dust model by S12, where the uniform density, temperature, and elemental composition in the ejecta are assumed. Considering that the grains are formed rapidly just after the temperature in formation site decreases down to the order of the grain sublimation temperatures, the size distribution of newly formed grains has the peaky log-normal form.
- On the other hand, N07 consider the radial distribution of physical quantities in the ejecta. Dust grains are formed with each characteristic radii in the layers with the different elemental compositions at the different epoch. By summing up the all contributions of grains formed in the different formation environments, the resulting size distribution spreads in a wider range of radius than S12 model.
- The succeeding dust destruction has additional effects on the size distribution of surviving grains (see green, yellow, and red curves in Figure 3.4).
 - S12 assume that the grains are kept to be trapped in the high-temperature region confined by the reverse and forward shocks. The dust radius continues to decrease by the sputtering effect until the ejecta cools down sufficiently. Consequently, the size distribution of surviving grain has a flat tail at the smaller radii than the original log-normal distributions. The amount of these grains becomes smaller with the increasing ambient gas density linearly.
 - The dynamics of dust grains is determined by the different equation of motion from the gas. They are decelerated by the drag force from the gas until the relative velocity between gas and dust is relaxed. N07 take this effect into consideration in their one-dimensional fluid model of ejecta expansion. The relaxation time is longer with larger grain radii because the geometrical cross-section per unit mass becomes smaller. They are more likely to escape from the high temperature region between the forward and reverse shocks, where grains are efficiently sputtered by the high energy ions. Whereas, the smaller grains continue to stay in the region and to be eroded. Consequently, we can see that the size distribution is truncated at the characteristic radius as indicated in the left panel of Figure 3.4.

In N07 model, the average size of grain processed by reverse shock is larger than in S12 model. With the larger grain size, the efficiency of gas cooling becomes smaller because the total grain cross-section becomes smaller with the fixed dust mass.

3.2.3 Dust property

In this study, at most ten dust species are considered: metallic silicon (Si), metallic iron (Fe), forsterite (Mg_2SiO_4), enstatite (MgSiO_3), magnetite (Fe_3O_4), amorphous carbon (C), silica (SiO_2), magnesia (MgO), troilite (FeS), and alumina (Al_2O_3). In some supernova models employed here, some species are not efficiently formed in ejecta, or are

(almost) totally destroyed by the reverse shocks. The amount of each grain species is quantified by the condensation efficiency f_{ij} defined as the number fraction of nuclei of element j condensed into dust species i . The mass density of dust species i per fluid mass is written as $\rho_i = f_{ij} A_j n_{\text{H}} \mu_{ij} m_{\text{H}}$, where μ_{ij} is the molecular weight of the grain species i per nucleus of element j (see Chapter 2). In this study, the differential size distribution function $\varphi_i(r)$ is used for grain species i , normalized as $\int \varphi_i(r) dr = 1$. The number of dust grains i per unit volume can be written as

$$n_i = \frac{\rho_i}{(4\pi/3)\varsigma_i \int r^3 \varphi_i(r) dr}, \quad (3.3)$$

where ς_i is the material density of species i as $\varsigma_i = 3\mu_{ij}m_{\text{H}}/4\pi a_{ij,0}^3$, and the quantities of molecular weight μ_{ij} and monomer radius $a_{ij,0}$ can be seen in Chapter 2. The number density of grains with radii between r and $r + dr$ is $n_i \varphi_i(r) dr$. Then, we calculate the grain temperature, cooling efficiency, and H_2 formation rate on the grain surfaces for each size bin and species as shown in Chapter 2.

3.2.4 Setup

Hereafter, we define the critical condition for the dust-induced fragmentation with each progenitor mass and ambient gas density by assumption that a target star-forming cloud is polluted by a single neighboring supernova. We consider the dust models without destruction (n0 and norev), and three reverse shock models for each progenitor mass. We follow the thermal evolution of the polluted cloud by performing one-zone semi-analytic calculations (see Chapter 1) During the collapse, we also consider the grain growth along with the procedure as described in Chapter 1. In addition to the model with grain growth, we see also in the case without grain growth as a controlled calculation. For a given supernova dust model, the dust-to-metal mass ratio (condensation efficiency) is determined. Therefore, we obtain the absolute amount of dust with a fixed metallicity. In order to determine the critical dust amount, we calculate with a range of metallicity between $Z = 10^{-7}$ – $10^{-2} Z_{\odot}$, where $Z_{\odot} = 0.02$ is the solar metallicity.

3.3 Overall thermal evolution of clouds

3.3.1 Important chemical and thermal processes

In this section, we discuss the thermal evolution of clouds for a dust model N07M30n1. Before determining the critical metallicity (dust amount), we perform one-zone calculations with various metallicities. Figure 3.5, we show the temperature evolutions with metallicities 10^{-6} (Z6), 10^{-5} (Z5), and $10^{-4} Z_{\odot}$ (Z4). We enumerate the important thermal processes during the collapse as follows:

- H_2 molecular formation on grains
At the density $n_{\text{H}} \sim 10^5 \text{ cm}^{-3}$, the variation of the temperature with different

Table 3.1: Initial dust properties and critical conditions without grain growth

Model	M_{pr}	rev.	$f_{\text{dep},\text{C},0}$	$S_{\text{C},0}$	$f_{\text{dep},\text{Sil},0}$	$S_{\text{Sil},0}$	$f_{\text{dep},0}$	\mathcal{D}_0	$\mathcal{D}_{\text{cr}}^{(\text{ng})}$	$[Z_{\text{cr}}^{(\text{ng})}]$
N07M13n0	13	n0	0.101	2.65	0.024	3.83	0.305	6.106	3.060	-5.3
N07M13n0.1		n0.1	0.096	2.64	0.016	2.77	0.233	4.659	2.335	-5.3
N07M13n1		n1	0.049	2.50	< 0.001	3.76	0.093	1.851	2.330	-4.9
N07M13n10		n10	0.011	3.88	< 0.001	7.77	0.020	0.392	1.966	-4.3
N07M20n0	20	n0	0.023	4.51	0.049	4.22	0.220	4.402	2.777	-5.2
N07M20n0.1		n0.1	0.020	3.46	0.028	2.96	0.137	2.750	3.462	-4.9
N07M20n1		n1	0.013	1.96	0.002	3.61	0.055	1.110	5.563	-4.3
N07M20n10		n10	0.002	2.24	< 0.001	4.87	0.013	0.259	8.199	-3.5
N07M2513n0	25	n0	0.058	2.42	0.060	3.53	0.240	4.797	3.810	-5.1
N07M25n0.1		n0.1	0.053	1.91	0.048	1.42	0.195	3.907	3.907	-5.0
N07M25n1		n1	0.041	1.12	0.017	1.35	0.118	2.351	4.692	-4.7
N07M25n10		n10	0.016	0.83	< 0.001	3.05	0.036	0.726	4.578	-4.2
N07M30n0	30	n0	0.004	6.85	0.068	3.99	0.184	3.671	2.916	-5.1
N07M30n0.1		n0.1	0.003	7.14	0.031	4.04	0.113	2.265	3.590	-4.8
N07M30n1		n1	< 0.001	10.27	< 0.001	8.57	0.040	0.791	6.280	-4.1
N07M30n10		n10	< 0.001	7.52	< 0.001	7.17	0.015	0.292	11.639	-3.4
N07M170n0	170	n0	0.003	4.66	0.072	6.62	0.315	6.297	3.156	-5.3
N07M170n0.1		n0.1	0.002	4.88	0.016	4.76	0.138	2.761	4.377	-4.8
N07M170n1		n1	< 0.001	10.03	< 0.001	1.27	0.013	0.266	16.796	-3.2
N07M170n10		n10	< 0.001	12.31	0.000	—	< 0.001	0.001	1.488	> -2.0
N07M200n0	200	n0	0.009	5.39	0.052	9.29	0.359	7.189	3.603	-5.3
N07M200n0.1		n0.1	0.007	5.20	0.007	4.94	0.091	1.824	2.892	-4.8
N07M200n1		n1	< 0.001	15.37	< 0.001	1.60	< 0.001	0.020	4.935	-2.6
N07M200n10		n10	< 0.001	18.02	0.000	—	< 0.001	< 0.001	< 0.001	> -2.0
S12M13norev	13	norev	0.249	4.59	0.033	45.76	0.413	8.260	0.826	-6.0
S12M13rev1		rev1	0.185	3.35	0.003	53.73	0.197	3.947	1.571	-5.4
S12M13rev2		rev2	0.101	3.22	0.001	52.36	0.106	2.117	1.336	-5.2
S12M13rev3		rev3	0.044	3.28	< 0.001	47.14	0.047	0.943	1.494	-4.8
S12M20norev	20	norev	0.095	37.56	0.179	14.68	0.369	7.384	0.738	-6.0
S12M20rev1		rev1	0.030	32.77	0.030	18.12	0.081	1.618	0.811	-5.3
S12M20rev2		rev2	0.013	27.85	0.010	18.22	0.030	0.591	0.937	-4.8
S12M20rev3		rev3	0.005	23.72	0.004	17.00	0.011	0.219	1.098	-4.3
S12M25norev	25	norev	0.162	11.51	0.068	29.42	0.315	6.293	0.997	-5.8
S12M25rev1		rev1	0.134	3.49	0.010	34.48	0.155	3.106	2.467	-5.1
S12M25rev2		rev2	0.090	2.32	0.003	34.39	0.097	1.934	2.435	-4.9
S12M25rev3		rev3	0.047	2.04	0.001	33.17	0.050	1.000	2.512	-4.6
S12M30norev	30	norev	0.161	1.44	0.088	26.22	0.324	6.485	1.629	-5.6
S12M30rev1		rev1	0.144	1.12	0.013	31.72	0.164	3.285	2.609	-5.1
S12M30rev2		rev2	0.097	1.15	0.004	32.36	0.104	2.071	2.607	-4.9
S12M30rev3		rev3	0.052	1.18	0.002	28.84	0.055	1.094	2.182	-4.7

Note — 1st column: models which we employ here. 2nd: progenitor mass M_{pr} (M_{\odot}). 3rd: reverse shock model (see text). 4–7th: initial mass fraction $f_{\text{dep},i,0}$ relative to the total metal mass and the initial geometrical cross-section $S_{i,0}$ ($\times 10^4 \text{ cm}^2 \text{ g}^{-1}$) per unit dust mass for grain species $i = \text{C}$ (amorphous carbon) and Sil (Silicates). For silicate grains, we show the values for the dominant species: MgSiO_3 for S12M13 and S12M25 models, and Mg_2SiO_4 for the other models. We write $f_{\text{dep},i,0}$ and $S_{i,0}$ in bold style when they are dominant coolants. 8th: the initial mass fraction of grains $f_{\text{dep},0}$ relative to metal. 9th: the dust-to-gas mass ratio \mathcal{D}_0 ($\times 10^{-8}$) for our $Z = 10^{-5} Z_{\odot}$ calculations. 10, 11th: critical dust-to-gas mass ratio $\mathcal{D}_{\text{cr}}^{(\text{ng})}$ and metallicity $Z_{\text{cr}}^{(\text{ng})}$ which we determine by one-zone calculations without grain growth ($[Z_{\text{cr}}^{(\text{ng})}] = \log[Z_{\text{cr}}^{(\text{ng})}/Z_{\odot}]$). To search the critical metallicity, we vary the metallicity from 10^{-7} to $10^{-2} Z_{\odot}$ every 0.1 dex. For example, $[Z_{\text{cr}}^{(\text{ng})}] = -5.3$ indicates that fragmentation condition is satisfied in one-zone model with $[Z_{\text{cr}}^{(\text{ng})}] \geq -5.3$, but not with $[Z_{\text{cr}}^{(\text{ng})}] \leq -5.4$.

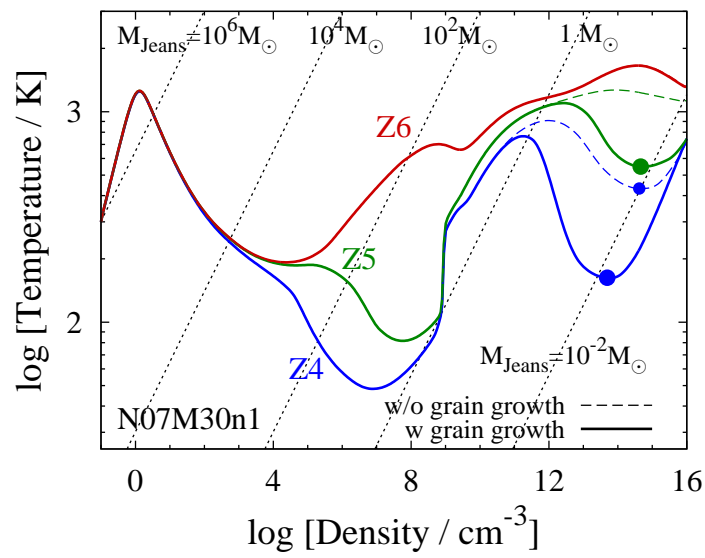


Figure 3.5: Temperature as a function of the increasing density in the course of time. We plot for the N07M30n1 model with $Z = 10^{-6} Z_{\odot}$ (red: Z6), $10^{-5} Z_{\odot}$ (green: Z5), and $10^{-4} Z_{\odot}$ (blue: Z4), respectively. The solid and dashed curves with each metallicity represent the trajectories with and without grain growth, respectively. The circle symbol indicates the density and temperature where the fragmentation criterion (see Chapter 1) is satisfied.

Table 3.2: Parameter for grain growth and resulting critical condition

Model	M_{pr}	rev.	$r_{\text{Sil}}^{\text{grow}}$	$\log(n_{\text{H,Sil}}^{\text{grow}})$	$f_{\text{dep,Sil,*}}$	$S_{\text{Sil,*}}$	$f_{\text{dep,*}}$	$\mathcal{D}_{\text{cr}}^{(\text{gg})}$	$[Z_{\text{cr}}^{(\text{gg})}]$
N07M13n0	13	n0	0.0060	no	0.024	3.83	0.351	0.769	-5.9
N07M13n0.1		n0.1	0.0444	no	0.017	2.78	0.270	1.473	-5.5
N07M13n1		n1	0.0331	15.2	0.001	3.95	0.128	0.928	-5.3
N07M13n10		n10	0.0147	15.9	< 0.001	8.45	0.043	0.312	-5.1
N07M20n0	20	n0	0.0074	*	0.051	5.22	0.224	2.777	-5.2
N07M20n0.1		n0.1	0.0342	12.8	0.034	3.12	0.146	2.184	-5.1
N07M20n1		n1	0.0313	14.0	0.003	4.00	0.057	1.397	-4.9
N07M20n10		n10	0.0228	15.6	< 0.001	5.25	0.013	0.820	-4.5
N07M2513n0	25	n0	0.0044	*	0.060	4.24	0.241	3.810	-5.1
N07M25n0.1		n0.1	0.0615	*	0.051	1.44	0.200	3.103	-5.1
N07M25n1		n1	0.0754	13.8	0.020	1.39	0.121	2.351	-5.0
N07M25n10		n10	0.0511	15.0	< 0.001	2.93	0.036	1.448	-4.7
N07M30n0	30	n0	0.0221	*	0.069	3.99	0.184	2.916	-5.1
N07M30n0.1		n0.1	0.0339	12.7	0.044	4.01	0.128	2.265	-5.0
N07M30n1		n1	0.0120	13.2	0.006	8.80	0.045	0.628	-5.1
N07M30n10		n10	0.0246	15.9	< 0.001	5.43	0.015	0.734	-4.6
N07M170n0	170	n0	0.0078	*	0.072	6.62	0.317	3.156	-5.3
N07M170n0.1		n0.1	0.0439	13.1	0.029	4.07	0.154	2.194	-5.1
N07M170n1		n1	0.1813	no	< 0.001	1.17	0.013	2.662	-4.0
N07M170n10		n10	—	—	0.000	—	< 0.001	1.488	> -2.0
N07M200n0	200	n0	0.0045	*	0.053	9.68	0.364	3.603	-5.3
N07M200n0.1		n0.1	0.0452	13.8	0.012	4.19	0.098	1.824	-5.0
N07M200n1		n1	0.1440	no	< 0.001	1.48	0.001	0.031	-4.8
N07M200n10		n10	—	—	0.000	—	< 0.001	< 0.001	-3.2
S12M13n0rev	13	n0rev	0.0051	10.4	0.200	25.28	0.602	0.826	-6.0
S12M13rev1		rev1	0.0039	11.2	0.203	14.62	0.476	0.497	-5.9
S12M13rev2		rev2	0.0040	11.6	0.178	10.90	0.333	0.336	-5.8
S12M13rev3		rev3	0.0047	12.4	0.069	10.79	0.164	0.188	-5.7
S12M20n0rev	20	n0rev	0.0159	*	0.179	14.68	0.370	0.466	-6.2
S12M20rev1		rev1	0.0115	11.1	0.141	11.56	0.242	0.204	-5.9
S12M20rev2		rev2	0.0109	11.8	0.107	9.24	0.172	0.118	-5.7
S12M20rev3		rev3	0.0118	12.4	0.064	7.43	0.105	0.069	-5.5
S12M25n0rev	25	n0rev	0.0080	9.1	0.086	27.19	0.337	0.997	-5.8
S12M25rev1		rev1	0.0061	11.5	0.093	17.77	0.259	0.982	-5.5
S12M25rev2		rev2	0.0060	12.0	0.074	13.58	0.181	0.770	-5.4
S12M25rev3		rev3	0.0061	12.3	0.049	11.21	0.105	0.501	-5.3
S12M30n0rev	30	n0rev	0.0088	*	0.088	26.22	0.325	1.629	-5.6
S12M30rev1		rev1	0.0065	11.3	0.068	19.56	0.240	1.039	-5.5
S12M30rev2		rev2	0.0062	12.0	0.045	16.09	0.157	0.825	-5.4
S12M30rev3		rev3	0.0071	12.5	0.024	13.24	0.084	0.548	-5.3

Note — 4th: average radius r_i^{grow} (μm) of grain species i . 5th: density $n_{\text{H},i}^{\text{grow}}$ (cm^{-3}) where the condensation efficiency of grain species i becomes above 0.5 by grain growth for $Z = 10^{-5} Z_{\odot}$ runs. “*” and “no” depict the models where the condensation efficiency is initially above 0.5 or where the condensation efficiency does not reach 0.5 until $n_{\text{H}} = 10^{16} \text{cm}^{-3}$, respectively. 6–8th: subscript “*” denotes the value for $Z = 10^{-5} Z_{\odot}$ at density $n_{\text{H}} = 10^{12} \text{cm}^{-3}$. 9–10th: critical dust-to-gas mass ratio $\mathcal{D}_{\text{cr}}^{(\text{gg})}$ and metallicity $Z_{\text{cr}}^{(\text{gg})}$ determined by our one-zone calculations with grain growth.

metallicity has already been seen. This is due to the H_2 molecular cooling enhanced by the efficient molecular formation on grain surfaces, which becomes important with increasing metallicity.

- OH cooling

While cooling by metal molecules such as OH and H_2O is not important in the present-day dust model, the enhancement of oxygen in our Pop III model leads such cooling to be important for 10^{-5} – $10^{-4} Z_\odot$. The cooling becomes dominant over gas compressional heating. We can see the rapid temperature decrease at $n_{\text{H}} \sim 10^5$ – 10^7 cm^{-3} .

- H_2 formation heating

With the metallicities $Z \gtrsim 10^{-5} Z_\odot$, we see the rapid increase of the temperature. This is due to the gas heating by the endothermic reaction of H_2 molecular formation. In this density regime, three-body reactions are important process for the molecular formation. The heating is relaxed when the sufficient molecules are formed and the H_2O cooling can operate in this regime. The moderate gas heating continues until the density reaches $\sim 10^{11} \text{ cm}^{-3}$.

- Dust cooling

Finally, cooling by dust thermal emission becomes dominant at highest density $n_{\text{H}} \sim 10^{12}$ – 10^{14} cm^{-3} , where the frequency of the heat exchange between gas and dust becomes sufficiently large. If the cooling becomes dominant, we can expect the dust-induced fragmentation into low-mass cores.

3.3.2 Effect of grain growth

Even in the very metal-poor environment, grain growth becomes important to enhance the gas cooling efficiency to reduce the temperature. The green curve in Figure 3.5 (N07M30n1Z5) shows that the temperature dip appears at $\sim 10^{14} \text{ cm}^{-3}$ if we consider grain growth. Especially Mg_2SiO_4 grains rapidly grow at density $n_{\text{H}} \sim 10^{13} \text{ cm}^{-3}$. For Z4 case (blue), the temperature dip becomes deeper, indicating that the dust cooling efficiency increases due to grain growth. Also with the metallicity, Mg_2SiO_4 grains becomes dominant after their growth at $n_{\text{H}} \sim 10^{11} \text{ cm}^{-3}$.

Further, grain growth is crucial to determine the critical metallicity in some cases including this N07M30n1 model. With $10^{-6} Z_\odot$, the both trajectories with and without grain growth do not satisfy the fragmentation criterion. With $10^{-4} Z_\odot$, the both trajectories satisfy because the amount of grain is enough even without the help of grain growth. In the case with $10^{-5} Z_\odot$, while the fragmentation condition are not satisfied without grain growth, the fragmentation is judged to occur only with grain growth. In this model, the critical metallicity decreases from $10^{-4.1}$ to $10^{-5.1} Z_\odot$ (see Tables 3.1 and 3.2), which corresponds to the decrease of the critical dust-to-gas mass ratio \mathcal{D}_{cr} from 6.3×10^{-8} to 0.63×10^{-8} . That is, the dust amount required to cool the gas becomes smaller by an

order of magnitude. Therefore, we can expect that grain growth can reduce the critical threshold metallicity for the cloud fragmentation. In the next section, we integrate the all results given by our calculations for wider range of parameters.

3.4 Conditions for cloud fragmentation

3.4.1 Critical dust-to-gas mass ratio without grain growth

In this section, we discuss the critical condition for cloud fragmentation for all Pop III dust models. We can obtain the critical metallicity Z_{cr} above which the dust cooling is efficient by our sequence of one-zone calculations for each Pop III model. Then, the critical metallicity is translated into the critical dust-to-gas mass ratio \mathcal{D}_{cr} as $\mathcal{D}_{\text{cr}} = f_{\text{dep},0} Z_{\text{cr}}$. We begin with discussion in the case without grain growth, where the dust amount is fixed during the cloud collapse. In this case, the initial dust-to-gas mass ratio is the important parameter to define the critical condition (see also S12). The critical dust-to-gas mass ratio $\mathcal{D}_{\text{cr}}^{(\text{ng})}$ in the case without grain growth is shown in the last second column of Table 3.1. The predicted critical dust amount is scattered. Then, we estimate the one-sigma range of $\mathcal{D}_{\text{cr}}^{(\text{ng})}$ as $[2.0\text{--}2.5] \times 10^{-8}$.¹ The origin of the scatter is largely due to the difference of the dust models between N07 and S12.

Difference between N07 and S12

Next, we discuss the variation of $\mathcal{D}_{\text{cr}}^{(\text{ng})}$ between the two models N07 and S12. The average value of $\mathcal{D}_{\text{cr}}^{(\text{ng})}$ is 3.4×10^{-8} for N07 and 1.3×10^{-8} for S12. N07 model predicts the larger $\mathcal{D}_{\text{cr}}^{(\text{ng})}$ than in S12 model by about a factor of 3. This stems from the overall difference of grain composition and size distribution between the two model as discussed above and briefly as follows:

- N07 predict larger grain sizes because of the ejecta model and the grain destruction model as seen in the discussion around Figure 3.4. The one-dimensional ejecta model of N07 predict the wider range of dust size distribution than the one-zone model of S12 just after the grains are formed, which predict the narrower log-normal distribution around the characteristic radius determined by the nature of each grain species. At the succeeding grain destruction phase, for N07 model, the larger grains are likely to escape from the destruction site while the small grains remaining in the region are eroded by the sputtering. The average size increases with the increasing destruction efficiency. On the other hand, in S12 model, the grains with intermediate size slowly depleted, and the flat tail is formed at the

¹Here, we neglect n1 and n10 models in the PISN case. Although n1 and n10 reverse shock models predict the large $\mathcal{D}_{\text{cr}}^{(\text{ng})}$ due to the significantly small initial \mathcal{D}_0 , the ambient gas of these star is expected to be less dense ($\sim 0.1\text{--}1 \text{ cm}^{-3}$) because they emit strong ionizing photons during their main-sequence (Kitayama et al. 2004; Whalen et al. 2004).

smaller radii. This leads the cross-section of thermal exchange between gas and dust per unit dust mass to be smaller.

- In N07 model, the supernova is predicted to release the small amount of carbon grains and not to create magnetite grains. Since the dissociation of CO molecular formation owing to electrons from ^{56}Co decay is not included, carbon grains do not accrete free available carbon atoms even though the gas density is still sufficiently large in the ejecta. Also, the feature of the unmixed ejecta reflects to the lack of magnetite grains. Both of them have large contribution to gas cooling in S12. As a result, the critical dust-to-gas mass ratio tends to be smaller for S12 model than for N07 model.

3.4.2 Critical metallicity

3.4.2.1 Without grain growth

We can translate the critical dust-to-gas mass ratio into the critical metallicity. These two values are connected with the relation via the initial depletion factor $f_{\text{dep},0}$ as

$$\mathcal{D}_{\text{cr}}^{(\text{ng})} = f_{\text{dep},0} Z_{\text{cr}}^{(\text{ng})}. \quad (3.4)$$

The critical metallicity can be written simply $Z_{\text{cr}}^{(\text{ng})} = 3.4 \times 10^{-8} f_{\text{dep},0}^{-1}$ for N07 and $1.3 \times 10^{-8} f_{\text{dep},0}^{-1}$ for S12. The reciprocal dependency on $f_{\text{dep},0}$ simply indicates that the smaller the dust cooling efficiency (larger $Z_{\text{cr}}^{(\text{ng})}$) with the smaller initial depletion efficiency.

3.4.2.2 With grain growth

If grain growth efficiently occurs and all refractory elements (Mg, Si, and Fe) are eventually depleted onto grains as in the present-day model (Pollack et al. 1994), the information of the initial depletion factor would be washed out. The critical condition for the efficient dust cooling can be written solely by the metallicity Z . In fact, a fraction of refractory elements is left to be depleted onto grains especially in the case with the small $f_{\text{dep},0}$.

In the last column in Table 3.2, we present the critical metallicity $Z_{\text{cr}}^{(\text{gg})}$ in the case with grain growth. We plot the critical condition for every model on the $f_{\text{dep},0}$ - Z plane in Figure 3.6. We can apparently see that the critical metallicity is reduced by the effect of grain growth especially in the case with small $f_{\text{dep},0}$. In the lowest $f_{\text{dep},0}$, the metallicity is reduced over a order of magnitude.

In the case without grain growth, where the critical condition is determined solely by the dust-to-gas mass ratio, $Z_{\text{cr}}^{(\text{ng})}$ is reciprocally proportional to $f_{\text{dep},0}$. In the extreme case where the all relevant elements are eventually accreted onto grains, the relationship between $Z_{\text{cr}}^{(\text{gg})}$ and $f_{\text{dep},0}$ is horizontal. Our model predicts the intermediate dependency between the two extreme cases. In quantitative manner, the spectral index of $Z_{\text{cr}}^{(\text{gg})}$ as a function of $f_{\text{dep},0}$ (called *growth index* hereafter) indicates how the refractory elements

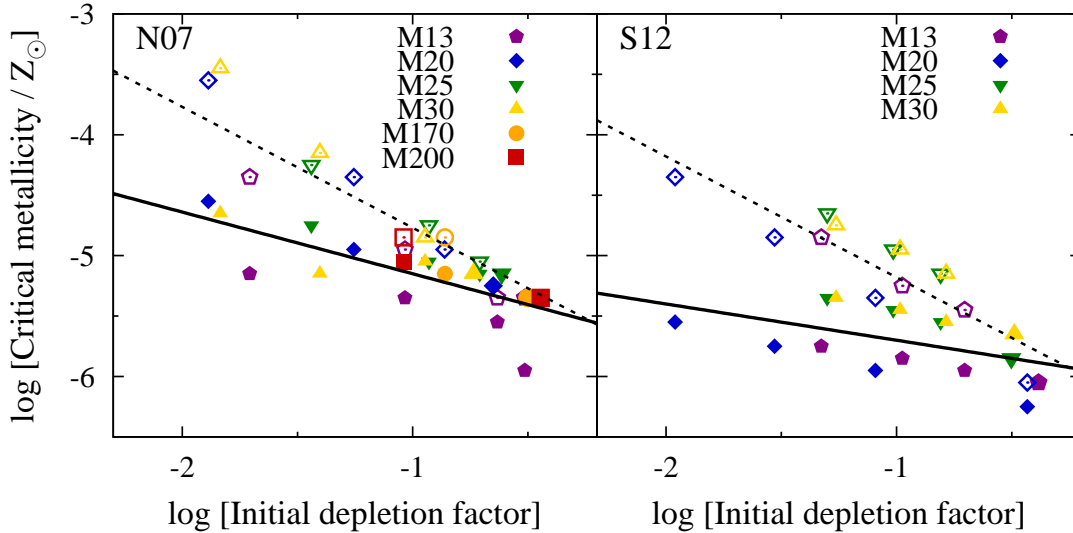


Figure 3.6: We plot the critical conditions for the dust-induced fragmentation on the $f_{\text{dep},0}$ - Z_{cr} plane determined by our one-zone calculations with (closed symbols) and without (open symbols) grain growth. We employ the Pop III supernova dust models of N07 (left) and S12 (right). The different symbols depict the different progenitor mass models. With each M_{pr} , the results of four dust destruction models are plotted for n0, n0.1, n1, and n10 (N07) and norev, rev1, rev2, and rev3 (S12) from right to left. We also plot the fitting function estimated by the Z_{cr} and $f_{\text{dep},0}$ for the Pop III dust models with (solid) and without (dashed) grain growth.

remain in the gas-phase. By the least squares method, we perform power-law fit of the dependency of $Z_{\text{cr}}^{(\text{gg})}$ and $f_{\text{dep},0}$ in both N07 and S12 models as:

$$\left(\frac{Z_{\text{cr}}^{(\text{gg})}}{10^{-5.5} Z_{\odot}} \right) = \left(\frac{f_{\text{dep},0}}{0.18} \right)^{-0.44 \pm 0.21}. \quad (3.5)$$

The critical metallicity still depends on the initial depletion factor. We will discuss it in the next Section.

Remaining dependency of $Z_{\text{cr}}^{(\text{gg})}$ on $f_{\text{dep},0}$

Difference between N07 and S12

The dependencies of $Z_{\text{cr}}^{(\text{gg})}$ on $f_{\text{dep},0}$ are $(Z_{\text{cr}}^{(\text{gg})}/10^{-5.5} Z_{\odot}) = (f_{\text{dep},0}/0.50)^{-0.51}$ and $(Z_{\text{cr}}^{(\text{gg})}/10^{-5.5} Z_{\odot}) = (f_{\text{dep},0}/0.022)^{-0.30}$ in N07 and S12 models, respectively (drawn in Figure 3.6 as solid lines). As explicitly shown in Figure 3.6, grains in S12 model have

the larger growth index than in N07. As we have discussed above, this results from the dust composition and size distribution predicted in these models. We find that the grain growth more efficiently occurs in S12 model. Table 3.2 shows that the density $n_{\text{H},i}^{\text{grow}}$ where the depletion efficiency f_{ij} exceeds 0.5, i.e. the grain growth is considered to occur sufficiently. We can see that $n_{\text{H},i}^{\text{grow}} \lesssim 10^{12} \text{ cm}^{-3}$ in S12 model while $n_{\text{H},i}^{\text{grow}} \gtrsim 10^{12} \text{ cm}^{-3}$ in N07 model. This indicates that, in S12 model, grain growth occurs well before the density reaches the regime where dust cooling is dominant. Therefore, dust cooling efficiency is apparently modified in the case S12.

Grain growth occurs more rapid in S12 than in N07 because of the difference of dust properties. In more quantitative manner, $n_{\text{H},i}^{\text{grow}}$ can be written as

$$n_{\text{H},i}^{\text{grow}} = 1.0 \times 10^{12} \text{ cm}^{-3} \left(\frac{A_j}{7.1 \times 10^{-10}} \right)^{-2} \left(\frac{f_{ij,0}}{0.1} \right)^{-0.8} \left(\frac{r_{i,0}^{\text{grow}}}{0.01 \mu\text{m}} \right)^2 \left(\frac{a_{i,0}}{1 \text{ \AA}} \right)^{-6} \left(\frac{m_{i1}}{m_{\text{H}}} \right),$$

from the balance between the grain growth timescale and gas dynamic timescale. The dependency on $f_{ij,0}$ is determined by fitting (valid for $f_{ij,0} < 0.5$). There, $r_{i,0}^{\text{grow}}$ is the cross-section-weighted average radius, $r_{i,0}^{\text{grow}} = \langle r^3 \rangle_{i,0}^{1/3}$.² The radius is the indicator of the contribution of the size distribution to grain growth. Table 3.2 shows that the value of $r_{i,0}^{\text{grow}}$ predicted by N07 is larger. That is why the dust in N07 model accretes the materials in the gas-phase more slowly.

Dependence of $Z_{\text{cr}}^{(\text{gg})}$ on M_{pr}

Among the progenitor mass models, the critical condition have a scatter. This is because both the abundance of grain species and size distribution affect the dust thermal properties. We attempt to quantify the contributions of dust composition and size distribution of each grain species to the dust cooling efficiency. Assuming $T \gg T_i(r)$, we rewrite the rate of dust cooling as

$$\Lambda_{\text{d}} = \sum_i \int \pi r^2 \langle n v(k) \rangle [2kT - 2kT_i(r)] n_i \varphi_i(r) dr, \quad (3.6)$$

$$\propto \sum_i f_{\text{dep},i} S_i, \quad (3.7)$$

where,

$$f_{\text{dep},i} = \frac{\rho_i}{\rho_{\text{metal}}} \quad (3.8)$$

is the indicator of the contribution of grain composition to cooling, and

$$S_i = \frac{\pi \langle r^2 \rangle_i}{(4\pi/3) \zeta_i \langle r^3 \rangle_i} = \frac{3}{4\zeta_i r_i^{\text{cool}}}, \quad (3.9)$$

is the cross-section of species i per unit dust mass indicating the contribution of grain size distribution to cooling. Here, the another type of average dust radius $r_i^{\text{cool}} = \langle r^3 \rangle_i / \langle r^2 \rangle_i$

² $\langle x \rangle_i$ is the size distribution-weighted average of a quantity x as $\int x \varphi_i(r) dr$.

is introduced to characterize dust cooling rate. We here discuss the difference among the progenitor mass models separately in N07 and S12 models.

- **N07**

M13 model predicts the abundance pattern of $A_C > A_O$. For such an abundance pattern, carbon grains can grow because even if CO molecules are formed rapidly in the collapse phase, free carbon atoms available to be accreted are left. It can be seen in Tables 3.1 and 3.2: abundance of carbon grain $f_{C,C}$ increases from 0.04–0.38 to 0.13–0.55. Carbon grains can contribute to the cooling efficiency if they can grow. This is because the carbon is generally more abundant than Si or Mg by an order of magnitude. By comparison between the product of $f_{\text{dep},i} S_i$ becomes eventually larger for carbon grain than silicate grains. Therefore, the progenitor model predicts the larger cooling efficiency than in the other cases, where carbon grain can not grow to contribute the cooling efficiency because of $A_C < A_O$. This leads the smallest $Z_{\text{cr}}^{(\text{gg})}$ for M13 model. Especially, for M13n0, since MgO grain can also contribute, the cooling efficiency is significantly large (even $Z_{\text{cr}}^{(\text{gg})} \sim 10^{-6} Z_{\odot}$).

- **S12**

- M13 vs. M30

For both models, growth of not only silicate but also Fe_3O_4 is important, and the contribution of silicate is slightly larger for M13 than M30. The resulting $Z_{\text{cr}}^{(\text{gg})}$ becomes smaller for M13.

- M20

For all four progenitor mass models, the dominant coolant changes from carbon to silicates by grain growth. For M20, since carbon grains can still contribute to the cooling efficiency, the model predicts smallest value of $Z_{\text{cr}}^{(\text{gg})}$.

3.5 Implication for the observed primitive stars

Recent observations have revealed the nature of the primitive stars. They indicate that there are two types of stars in the extremely metal-poor (EMP) stars (see e.g. [Beers and Christlieb 2005](#)):

- *Carbon-normal extremely metal-poor star*

The stars have the metallicity $[\text{Fe}/\text{H}] < -3.0$ without large enhancement of carbon ($[\text{C}/\text{Fe}] \lesssim 1$). The abundance pattern in our model can explain that of these stars.

- *Carbon-enhanced extremely metal-poor (CEMP) star*

The stars are categorized as the EMP star ($[\text{Fe}/\text{H}] < -3.0$) but show the significant enhancement of carbon ($[\text{C}/\text{Fe}] \gtrsim 1$).

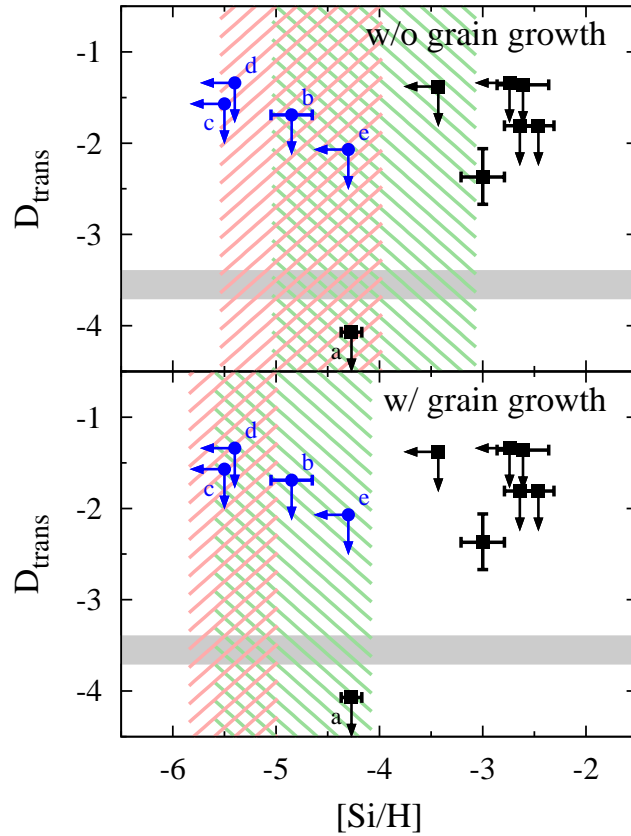


Figure 3.7: On the $D_{\text{trans}}\text{-}[\text{Si}/\text{H}]$ plane, the critical conditions for the dust-induced fragmentation obtained by our one-zone calculations are plotted as the green- and red-hatched region for N07 and S12, respectively. The condition is mitigated by the grain growth, which leads the critical Si abundance with grain growth (bottom) to be smaller than without grain growth (top). The critical condition under which the C/O fine-structure cooling triggers the cloud fragmentation is indicated by the grey-shaded region ($D_{\text{trans}} = -3.5 \pm 0.2$; Frebel et al. 2007; Frebel and Norris 2013). We compare our criteria with the C, O, and Si abundances of the extremely metal-poor stars so far observed. Black squares and blue circles indicate the abundances of C-normal EMP and CEMP stars, respectively. We show the abundances of recently discovered primitive star SDSS J1029+1729 (a: Caffau et al. 2011), and most iron-poor CEMP stars HE0557-4840 (b: Norris et al. 2007), HE0107-5240 (c: Christlieb et al. 2004), HE 1327-2326 (d: Frebel et al. 2008), and SMSS J0313-6708 (e: Keller et al. 2014). The other symbols indicate the abundances of C-normal main sequence stars with intermediate metallicities. These data are retrieved from the SAGA database (Suda et al. 2008).

Although what determines the difference of abundance pattern is still unclear, we in this section attempt to apply our criterion to explain their origins.

Recently, [Ji et al. \(2014\)](#) present that two criteria are required to explain the origin of EMP and CEMP stars.

- D_{trans}

As we have reviewed in Chapter 1, the critical discriminant D_{trans} is available to explain the origin of CEMP stars. However, the star SDSS J1029 + 1729 with $D_{\text{trans}} < -4.4$ ([Caffau et al. 2011](#)), has the lack of C and O, and the D_{trans} criterion is failed.

- $[\text{Si}/\text{H}]_{\text{cr}}$

[Ji et al. \(2014\)](#) consider that dust grains can also induce the gas cooling. They calculate the cooling efficiency of Si-bearing grains and define the critical silicon abundance ($[\text{Si}/\text{H}]_{\text{cr}}$). Here, they do not include carbon grains for simplicity. The formation of SDSS J1029 + 1729 can be explained by this strategy. However, the abundance of some CEMP stars lack of Si and Fe rules out the hypothesis that these stars are formed by this dust cooling scenario.

If it is true that the parent cloud of these stars do not have the dust cooling efficiency and resort only to fine-structure cooling, there would be problems as we have discussed in Chapter 1. The fine-structure cooling becomes inefficient at small densities ($n_{\text{H}} \sim 10^4 \text{ cm}^{-3}$), where the predicted fragment mass is large $\sim 10^4 M_{\odot}$. We reexamine whether grain growth overcomes the problem.

We plot the abundances observed so far on the $[\text{Si}/\text{H}]$ vs. D_{trans} plane in Figure 3.7. The green- and red-shaded areas show the critical Si abundance predicted by N07 and S12 models, respectively. We just derive the critical value as $A_{\text{Si}}Z_{\text{cr}}$. Without grain growth, the Si abundances of the CEMP stars c and d is smaller than $[\text{Si}/\text{H}]_{\text{cr}}$ predicted by any progenitor models in N07. This means that N07 model fails to explain the origin of these stars. However, with grain growth, some progenitor models in N07 become to predict the smaller $[\text{Si}/\text{H}]_{\text{cr}}$ than the Si abundances of the stars c and d. This means that the dust cooling scenario is not excluded by the observations so far.

3.6 Chapter summary

In this Chapter, we investigate the effect of the realistic dust models in the early Universe and grain growth on the thermal evolution and fragmentation properties of the clouds with extremely small metallicities. We employ the recent models of dust grains which have been released from Pop III stars. Comparison with the present-day dust model where all refractory elements are all depleted onto dust, in this model, the condensation efficiency of metal onto dust is smaller because of the efficient dust destruction process by the reverse shocks. Earlier studies with the present-day dust model have defined the critical

metallicity above which the dust cooling is efficient as between 10^{-6} and $10^{-5} Z_{\odot}$. If the dust destruction can be neglected, our models (N07n0 and S12norev) predict the same order of the critical metallicity. However, in the models with the most significant effect of the dust destruction (N07n10 and S12rev3), the critical metallicity becomes larger by a order of magnitude. In the PISN cases, the effect is much more severe because of their energetic feature which lead the dust destruction to strongly occur.

Grain growth can (partly) mitigate the dependency of the critical metallicity on the dust destruction effect. While $Z_{\text{cr}}^{(\text{ng})}$ depends on $f_{\text{dep},0}$ reciprocally as $Z_{\text{cr}}^{(\text{ng})} = 2.3 \times 10^{-8} f_{\text{dep},0}^{-1}$ without grain growth, the dependency is mitigated into $(Z_{\text{cr}}^{(\text{gg})}/10^{-5.5} Z_{\odot}) = (f_{\text{dep},0}/0.18)^{-0.44}$. In N07n10 and S12rev3 cases, the critical metallicity is reduced at most over an order of magnitude. We can conclude that the grain growth is necessary process to determine the fragmentation condition for low-mass star formation. Further, we apply our dust model to the abundances of the observed EMP and CEMP stars. Without grain growth, all progenitor models of N07 model fail to explain the origin of some CEMP stars with small Si abundances. If we include the effect of grain growth, the critical Si abundance in some of N07 model becomes smaller than that of the stars.

Zoom-in simulation scheme based on the Voronoi diagrams

Contents

4.1	Overview	67
4.2	Basics of the particle splitting	68
4.3	Strategy	69
4.3.1	Algorithm of Voronoi tessellation	71
4.3.2	Distribution of daughters	71
4.4	Bodenheimer test	81
4.4.1	Setup	81
4.4.2	Results	81
4.5	Collapse simulations of primordial gas cloud	84
4.5.1	Setup	84
4.5.2	Resulting density structures	85
4.6	Discussion	88
4.6.1	Implication for the gas fragmentation	88
4.6.2	Computational time	89
4.6.3	Resolution test	89
4.7	Chapter summary	90

4.1 Overview

As we have seen in the previous Chapter, dust thermal emission is crucial to form low-mass and low-metallicity star formation. In order to explicitly see the effect, hydrodynamic simulation is the useful tool because the dust cooling induces gas elongation and fragmentation (Chapter 1), which are both highly inhomogeneous phenomena. The difficulty in the cloud collapse simulation is that we should follow the fluid motion from an interstellar medium to protostellar cores with the density range over 20 orders of magnitude with

a sufficient resolution (so-called Jeans criterion; Truelove et al. 1997). If the criterion is not satisfied, the spurious fragmentation occurs because of the numerical noise. Since the aim of Thesis is to properly follow the cloud fragmentation, we should take care about it.

To save the computational cost, zoom-in techniques are often used. In the smoothed particle hydrodynamics (SPH) simulations, the coarse (parent) particles are replaced with the set of smaller mass (daughter) particles. Such a technique is called *particle splitting*, and corresponds to the adaptive mesh refinement (AMR) implemented in a part of Eulerian grid codes. While the way to split the coarse grid is almost uniquely determined in the AMR scheme, the distribution of daughter particles in SPH is not trivial. Previous studies such as Kitsionas and Whitworth (2002, hereafter, KW02) and Martel et al. (2006) present the simple methods of particle splitting: the daughters are distributed uniformly on the sphere and cube centered at their parent. Although their methods are very simple to be implemented, the symmetric distribution of the daughters is expected to smooth out the aspherical structure of the fluid.

In order to follow the aspherical structure such as sheet and filament, we develop the method as the daughters are distributed within the Voronoi cell tessellated by their parents. The Voronoi cells flexibly capture the distribution of the particles. In this Chapter, we introduce our novel particle splitting method based on the Voronoi diagrams and perform several test simulations. In Section 4.2, we briefly review the zoom-in simulation and resolution criterion. In Section 4.3, we introduce our particle splitting method. Then, the validity of our method is checked in Section 4.4 by the well-known Bodenheimer collapse test. There, we perform high-resolution simulation without particle splitting and lower-resolution simulation with previous and our splitting methods. In Section 4.5, we finally perform the simulation for the primordial gas cloud cut out from a cosmological simulation to compare the previous and our methods. Finally, we discuss the possibility that the difference splitting methods affect the cloud evolution including the fragmentation property and other issues in Section 4.6, and then summarize this Chapter in Section 4.7.

The content in this Chapter has been already published in Monthly Notices of the Royal Astronomical Society, Volume 451, Issue 4, p.3955–3963 (Chiaki and Yoshida 2015)

4.2 Basics of the particle splitting

In this Section, we briefly review the general feature of the particle splitting. Truelove et al. (1997) originally present the criterion for the AMR scheme in the Eulerian grid code. The parent coarse grid is split into the set of the finer grids in the scheme. They present the criterion for the grid refinement: the coarse grid is required to be split when the grid size is less than the factor of Jeans length $\lambda_J \sim c_T/\sqrt{G\rho}$, where c_T is the local sound speed (Jeans criterion). They confirm that the spurious fragmentation occurs in the case with the lack of resolution.

In the SPH simulations, the Jeans criterion is written by the Jeans mass $M_J \sim$

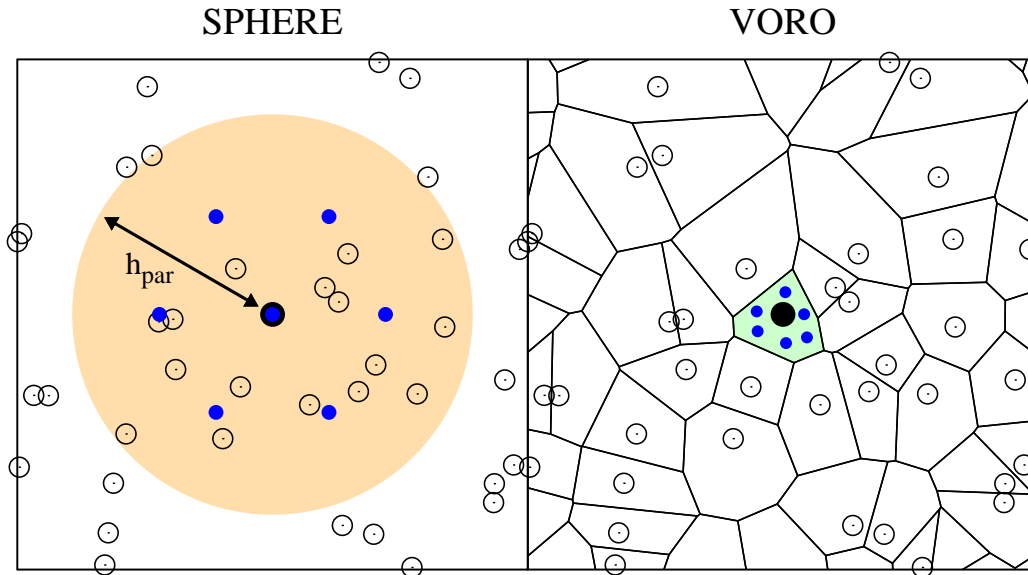


Figure 4.1: We compare the splitting methods of previous (left) and this work (right) in the two-dimensional manner. The central black particle represents the target parent particle. In the left panel, the daughters (blue dots) are distributed in the orange-shaded area with radius of h_{par} , or the smoothing length of the parent particle. The daughters are distributed to form the hexagonal closed packing. In the right panel, green-shaded area is the Voronoi cell of the parent. Its daughters are generated within the cell.

$(4\pi/3)\rho\lambda_J^3 \sim c_1^3 G^{-3/2} \rho^{-1/2}$. For a simulation with the number N_{ngb} of neighbor particles and particle mass m_{par} , the minimal mass $M_{\text{min}} = N_{\text{ngb}} m_{\text{par}}$ resolved by the SPH particles should satisfy

$$M_{\text{min}} < M_J / \mathcal{R}_{\text{cr}}, \quad (4.1)$$

where \mathcal{R}_{cr} is the mass fraction of the Jeans mass to M_{min} . This corresponds to the numbers of particles within the Jeans length. The quantity \mathcal{R}_{cr} is an indicator of the simulation resolution.

4.3 Strategy

In this section, we begin with comparing the idea of the previous studies and ours. We here focus on the particle splitting method presented by KW02. In their method, a daughter is located at the same coordinate its parent, and twelve are distributed to create the hexagonal closed packing. The angle of the distribution is randomly determined, and the distance l_{dau} of the twelve particles from the parent is $l_{\text{dau}} = 1.5h_{\text{par}}/13^{1/3}$, where h_{par} is the smoothing length of the parent particle. The length $h_{\text{par}}/13^{1/3}$ is the

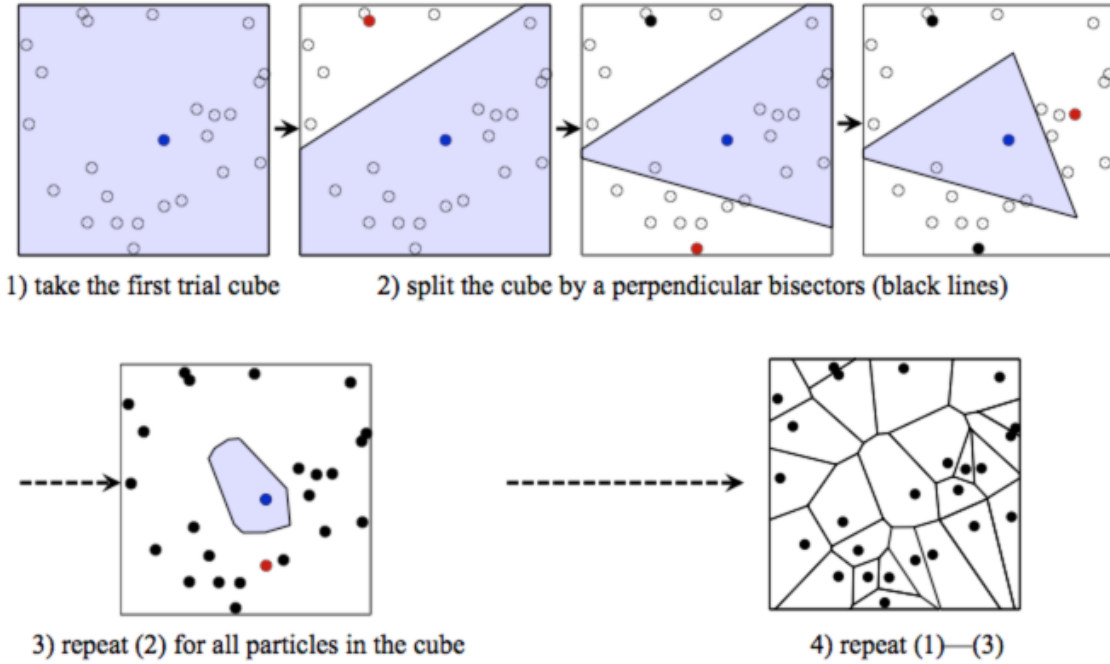


Figure 4.2: Two-dimensional illustration of our algorithm for the Voronoi tessellation. The blue shaded region represents the trial (in panels 1, 2) or final (3) Voronoi cell of the central blue particle (see text for the detailed description of the algorithm).

expected smoothing length of the daughters. We show the two-dimensional image of the distribution in the left panel of Figure 4.1. As one can see, some daughters leak into the upper originally sparse region. The density in this region will be overestimated after the splitting. This means that the anisotropic density structure would be smoothed out by the isotropic distribution of the daughters.

We in this Thesis develop the particle splitting technique by introducing the Voronoi tessellation, defined as space division into the group of points (Voronoi cell) whose distance from a corresponding generator is smallest. As we present in the right panel of Figure 4.1, the simulation box is divided by the Voronoi edges (black lines) as perpendicular bisectors between adjacent SPH particles. For a target particle (parent; black dots), the refined particles (daughters; blue dots) are distributed according to the geometrical structure of the Voronoi cell. The strong point of the particle splitting based on the Voronoi diagram is that the shape of the Voronoi cell traces the distribution of the parent particles. By distributing daughter particles uniformly in the Voronoi cell, we can preserve the original particle distributions created by the parent particles as shown in the blue dots in Figure 4.1.

4.3.1 Algorithm of Voronoi tessellation

In this Section, we introduce the scheme of the Voronoi tessellation. The scheme is implemented into the parallelized N -body/SPH code, GADGET-2 (Springel 2005). Figure 4.2 shows the two-dimensional image of our scheme of the Voronoi tessellation.

- 1) We first put the cube of a size $2l_{\text{cube}}$ centered at a parent particle (blue dot). The cube corresponds to the first trial Voronoi cell (blue-shaded region).
- 2) Then, we split the cube by the perpendicular bisector (black line) of a line segment between the parent and another particle (red dot) in the trial cube.
- 3) We repeat the procedure 2) for all particles in the cube. Then, we obtain the Voronoi cell for the central parent particle.

So far, particles outside the initial cube but closer to the parent particle than $2l_{\text{max}}$ can potentially modify the final shape of the Voronoi cell, where l_{max} is the maximal distance between the central particle and the vertices of the trial Voronoi cell constructed so far. If $l_{\text{max}} > l_{\text{cube}}/2$, we enlarge the initial cube and go back to 1).

- 4) After repeating 1)–3) for all particles, we obtain the Voronoi diagram in the simulation box.

In practice, we create the Voronoi cell only for the parcels which is about to break the Jeans criterion to save the computational cost. This algorithm scales as $\mathcal{O}(N_{\text{sp}} \log N_{\text{sp}})$ – $\mathcal{O}(N_{\text{sp}}^2)$ for the number of split particles N_{sp} . If the parent particles are uniformly distributed originally, we need not enlarge the initial cube size after the procedure 3), and thus the algorithm scales only as $\mathcal{O}(N_{\text{sp}} \log N_{\text{sp}})$. If the distribution of the particles are significantly inhomogeneous, the iteration of procedures 1)–3) will takes a cost.

4.3.2 Distribution of daughters

4.3.2.1 Setup for the selection

We then put daughter particles of a target parent particle according to the structure of the Voronoi cell. We first split the Voronoi cell into smaller units (“subcells”), along with the geometry of the cell, and then daughters are distributed, corresponding to each subcell. Although the distribution of the daughters is not uniquely determined, the daughters are required to be put as uniformly in the Voronoi cell as possible because the density of particles too close/distant to each other is over/underestimated. We try some patterns of particle distribution, and choose the one that best reproduces the original density distribution of the parent particles. The density ρ_i of SPH particle i is defined by the

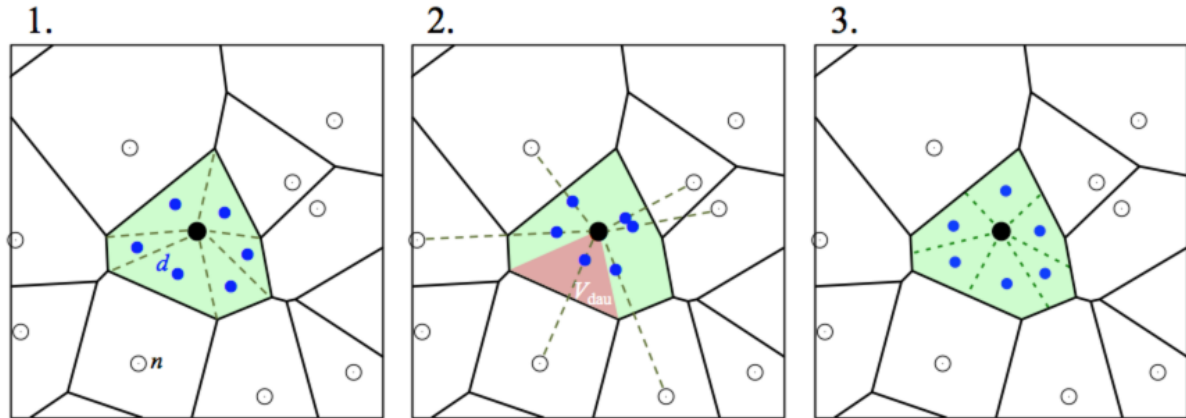


Figure 4.3: Two-dimensional images of three patterns of the daughter particle distributions. The daughters (blue dots) are distributed according to the structure of Voronoi cell cut out around a parent particle (black) and the distribution of the neighbor particle (open circles). 1: A daughter d is distributed on the center-of-mass of its corresponding subcell which is divided by the dashed lines connecting the parent and vertices of the Voronoi cell. 2: d is located on the internally dividing point of line segment (dashed line) between the particle and the neighbor particle n as shown in Figure 4.4. 3: d is on the center-of-mass of the subcell defined by the dashed line between the parent and the middle point of each corresponding edge. For the patterns 1 and 2, a Voronoi edge is defined to be the perpendicular bisector by $m_{\text{par}}^{1/3} : m_{\text{ngb}}^{1/3}$ of the parent p and the neighbor particle n , but for pattern 3, by 1 : 1.

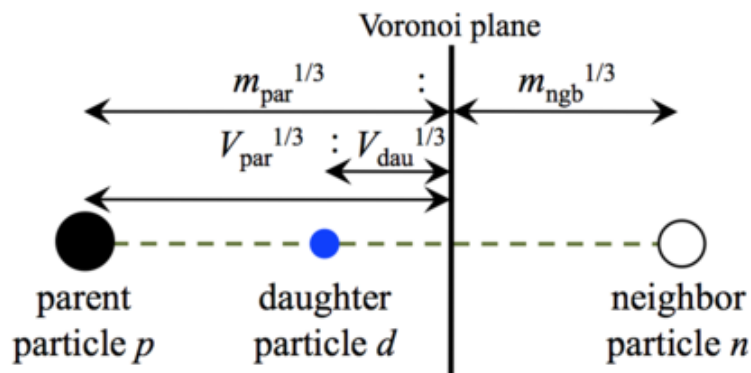


Figure 4.4: Location of a daughter d (blue dot) generated around parent p (black dot) in the case with VORO splitting of pattern 2. The daughter corresponds to the neighbor particle n (open circle).

standard SPH formulation as the statistical average of the neighbor particles:

$$\rho_i = \sum_{j=1}^{N_{\text{ngb}}} m_j W(r_{ij}, h_i), \quad (4.2)$$

where N_{ngb} is the number of neighbor particles, m_j is the mass of the neighbor particle j , and $W(r_{ij}, h_i)$ is the smoothing kernel as

$$W(r_{ij}, h_i) = \frac{8}{\pi h_i^3} \begin{cases} 1 - 6 \left(\frac{r_{ij}}{h_i}\right)^2 + 6 \left(\frac{r_{ij}}{h_i}\right)^3, & \left(0 \leq \frac{r_{ij}}{h_i} \leq 0.5\right) \\ 2 \left(1 - \frac{r_{ij}}{h_i}\right)^3, & \left(0.5 < \frac{r_{ij}}{h_i} \leq 1\right) \\ 0. & \left(1 < \frac{r_{ij}}{h_i}\right) \end{cases} \quad (4.3)$$

The smoothing length h_i of the particle i is iteratively estimated to be

$$\frac{4\pi}{3} \rho_i h_i^3 = N_{\text{ngb}} \bar{m}, \quad (4.4)$$

where \bar{m} is the mean particle mass. We compare the maximal and minimal densities ρ_{max} and ρ_{min} , respectively, among the SPH particles. We also see the particle-mean and standard deviation of the density $\bar{\rho}$ and σ_ρ , respectively, just after the particle splitting.

We first prepare a randomly generated locations of 16^3 parent particles in a simulation box with length of 1 code unit on a side. The particle mass is $m_{\text{par}} = 1/16^3$ so that the volume-averaged mass density is unity. At the initial state, ρ_{max} and ρ_{min} are significantly deviated from unity (6.16 and 0.46, respectively), and $\bar{\rho}$ and σ_ρ is large (1.34 and 0.49, respectively) by the random noise. We thus begin with performing the simulation without particle splitting for the time $10t_{\text{sc}}$ so that the density perturbation is relaxed by the gas pressure. Here, we define the sound crossing time t_{sc} as h_{par}^-/c_T , where $h_{\text{par}}^- = (3N_{\text{ngb}}/4\pi)^{1/3}/16$ is the average smoothing length, and c_T is the isothermal sound speed defined so that t_{sc} is the code unit. We consider that the typical scale of the density perturbation is the order of h_{par}^- . The perturbation is partly smoothed out by the gas pressure, and at the time $10t_{\text{sc}}$, ρ_{max} and ρ_{min} approach unity (1.08 and 0.92, respectively), and $\bar{\rho}$ and σ_ρ reduce down to 0.998 and 0.026, respectively. In this test simulations, we fix the number N_{ngb} of the neighbor particles 50 ± 1 , and the gas evolves isothermally without self-gravity. Since we impose the periodic boundary box, the gas is not dissipated beyond the boundaries. All the control parameters are the default of GADGET-2.0.7.

We then split the all particles in the simulation box, mimicking the cloud core, where the all particles have been refined. We here compare the three patterns of daughter particle distributions as follows. Figure 4.3 shows the schematic two-dimensional image of these patterns.

- 1: A daughter particle d is distributed on the center-of-mass of its corresponding sub-cell which is divided by the dashed lines connecting the parent and vertices of the Voronoi cell. In this case, the daughter corresponds to the neighbor particle n .

2: d is located on the internally dividing point of line segment (dashed line) between the particle and the neighbor particle. While we here consider that the parent particles have a uniform mass, the mass of the neighbor particles is sometimes different from that of the parent in practical collapse simulations. In the pattern 2, the Voronoi cell is defined by the plane which internally divide the particle p and its neighbor n by $m_{\text{par}}^{1/3} : m_{\text{ngb}}^{1/3}$.¹ When the parent particles are replaced with a daughter particle d , its location is shifted so that the distance from the Voronoi plane becomes closer by the factor of $(V_{\text{dau}}/V_{\text{par}})^{1/3}$ as shown in Figure 4.4, where V_{dau} and V_{par} are the volumes of the corresponding subcell (red-shaded region in Figure 4.3) and the whole Voronoi cell (green), respectively. The implementation of 2 is most simple among the three patterns because the only value that we should know is the coordinates of the neighbor particles.

3: d is on the center-of-mass of the subcell defined by the dashed line between the parent and the middle point of each corresponding edge. In Figure 4.3 shows the two-dimensional image. We describe the way to split the Voronoi cell into subcells and to distribute the daughters in three-dimensional manner in the Section 4.3.2.3. In this case, a daughter corresponds to each Voronoi vertex.

We then consider the particle mass assigned to daughters and a mass threshold m_{th} , which is the minimal mass of the daughters. If we give the daughter with mass of $(V_{\text{dau}}/V_{\text{par}})m_{\text{par}}$, the mass difference between adjacent particles can be too large. When particles with significantly different masses are mixed, the uncertainty of the smoothing length and density becomes large because we fix the number N_{ngb} of the neighbor particles in estimating the particle density as Equations (4.2) and (4.4). By the SPH formulation (Equation 4.2), the smoothing length is the radii of sphere who contains the fixed number N_{ngb} of neighbor particles. When the mass of neighbor particles is large relative to the target particle, the smoothing length h is underestimated. Since the kernel function is proportional to h^{-3} , the density is estimated to be small. To avoid this, we impose the lower limit of daughter particle mass. It is also considerable to give an equal mass to daughters although a daughter located in a subcell with small volume (size) tends to close to the adjacent daughters and its density will be overestimated. We here test three different ways to assign the daughter mass as follows:

A: The mass of a daughter is assigned to be $(V_{\text{dau}}/V_{\text{par}})m_{\text{par}}$, and the mass threshold is $m_{\text{th}} = m_{\text{par}}/1000$. The trial daughters with mass $m_{\text{dau}} < m_{\text{th}}$ are removed, and the total mass of these particles are added to the other daughters, proportional to V_{dau} , so that the total mass is conserved.

B: Same as A but $m_{\text{th}} = m_{\text{par}}/30$.

¹Strictly speaking, it does not satisfy the definition of the Voronoi tessellation, but it would be desirable that the typical size of the cell of the particle increases proportional to $m_{\text{par}}^{1/3}$.

Table 4.1: Trial coordinate and mass of daughters in Voronoi particle splitting

Model	$N_{\text{p,fin}}$	ρ_{max}	ρ_{min}	$\bar{\rho}$	σ_{ρ}
SPHERE	53 248	4.03	0.72	1.17	0.22
1A	57 514	3.79	0.30	1.05	0.19
1B	47 747	5.28	0.51	1.12	0.28
2A	57 514	2.80	0.23	1.20	0.28
2B	47 747	2.62	0.60	1.19	0.20
2C	40 960	2.63	0.77	1.31	0.16
3C	40 960	1.83	0.67	1.06	0.14

Note — $N_{\text{p,fin}}$ is the number of particles after splitting. ρ_{max} , ρ_{min} , $\bar{\rho}$, and σ_{ρ} depict the maximum, minimum, particle-averaged, and standard deviation of the densities of SPH particles just after the splitting.

C: After we put trial daughters on the center-of-mass of subcells, we merge the subcells whose corresponding daughters are closest. We then put the new (merged) daughter on the center-of-mass of the merged subcell. This procedure is repeated until the number of subcells becomes down to N_{dau} . In this way, we can realize the uniform distribution of the daughters. To conserve the uniformity of the distribution of the daughters, N_{dau} is desired to be large. Besides, to prevent the mass difference between parent and daughter particles, which can be adjacent to each other in practical zoom-in simulations, from becoming too large, and to save the computational cost, we set $N_{\text{dau}} = 10$.

We test six combinations (1A, 1B, 2A, 2B, 2C, and 3C) of the coordinate (1–3) and mass (A–C) of the daughters to compare ρ_{max} , ρ_{min} , $\bar{\rho}$ and σ_{ρ} between just before and after the particle splitting.

4.3.2.2 Results for the trial simulations

The tried models and the results are summarized in Table 4.1. We compare the results for the splitting method of this work with the previous method of KW02 (called SPHERE). After the particle splitting, we terminate our simulations at $t = 20t_{\text{sc}}$. Figures 4.5 and 4.6 show the time evolution of ρ_{max} , ρ_{min} and σ_{ρ} , respectively. After we randomly generate the distribution of the parent particles, the amplitude of density perturbation is dumped and approaches unity, oscillating due to the gas pressure (black dot-dashed curves). The period of oscillation is roughly $\sim t_{\text{sc}}$. Then, at $t = 10t_{\text{sc}}$, the maximal/minimal densities abruptly increases/decreases because the particle splitting adds the perturbation to the density distribution (green and red curves). For SPHERE splitting, the number of particles becomes $13 \times 16^3 = 53\,248$, and ρ_{max} and ρ_{min} become 4.03 and 0.72, respectively. The particle-averaged density for the daughters is 1.17, which is larger than the volume-averaged density of 1. This means that the number of particles whose density is

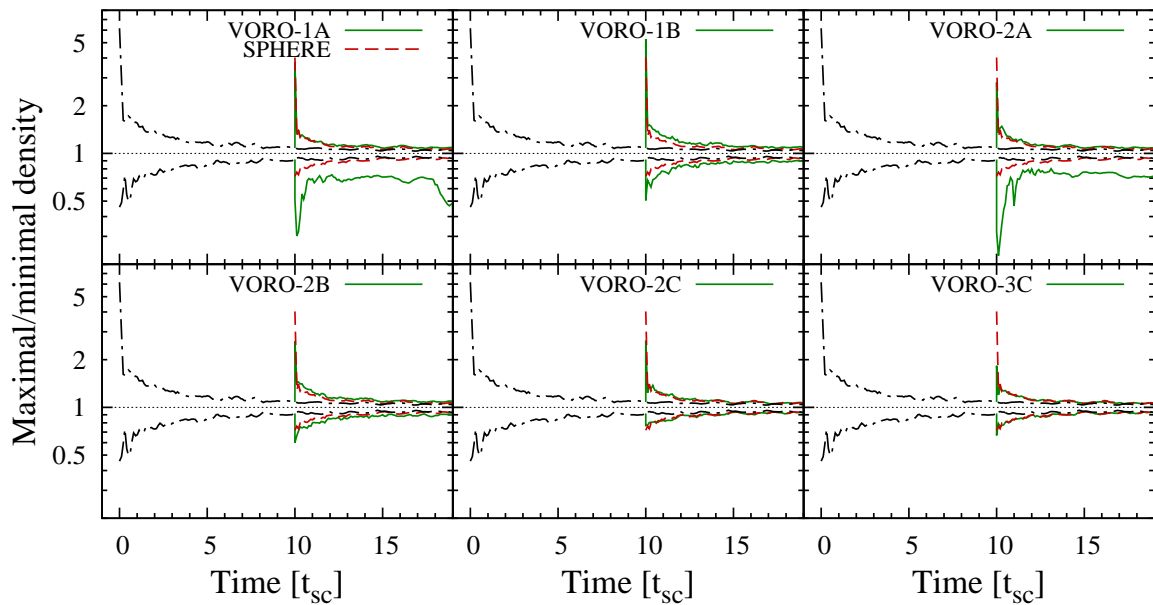


Figure 4.5: Temporal evolutions of the maximal and minimal densities among SPH particles. We begin with distributing 16^3 parent particles in a periodic simulation box at $t = 0t_{sc}$, and then split all particles at $t = 10t_{sc}$. Black dot-dashed curves represent the densities in the case without particle splitting, red dashed curves with SPHERE splitting, and the green solid curves with VORO splitting for the six patterns of daughter particle distributions: 1A (left-top), 1B (middle-top), 2A (right-top), 2B (left-bottom), 2C (middle-bottom), and 3C (right-bottom).

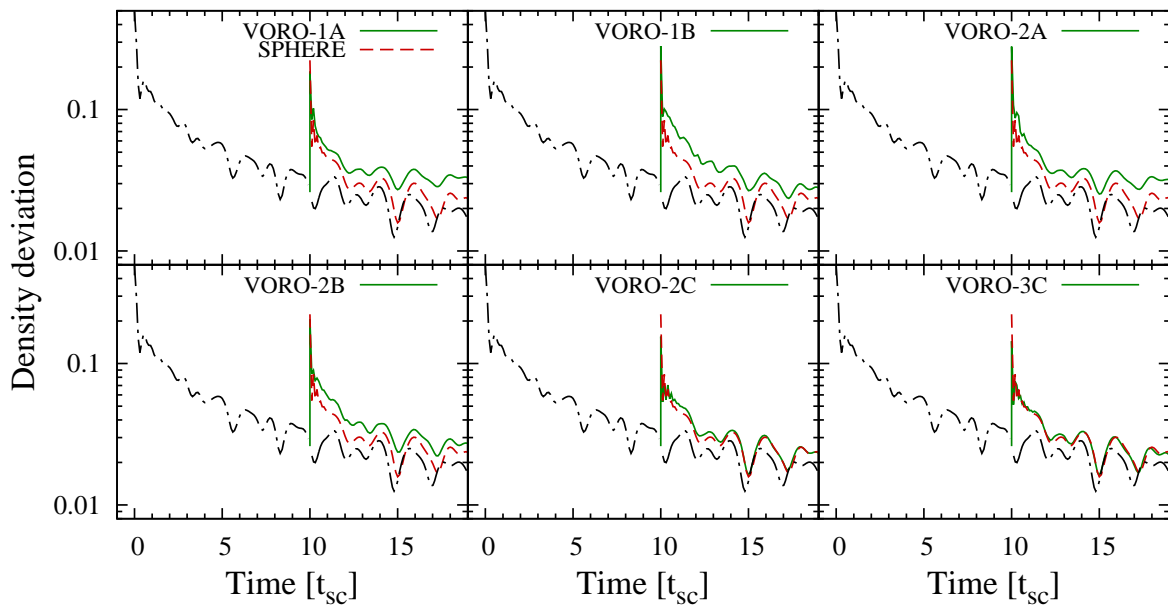


Figure 4.6: Same as Figure 4.5 but for the deviation of density.

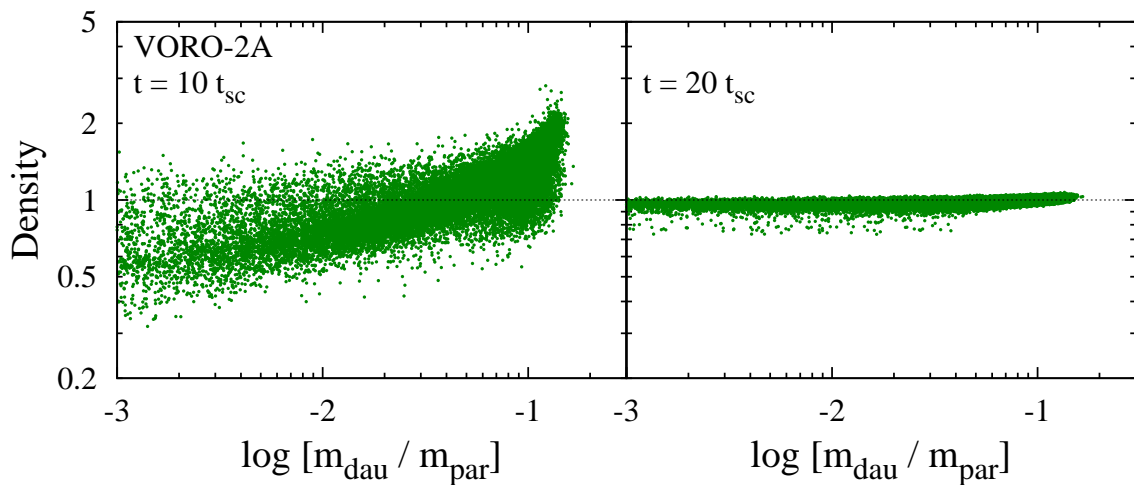


Figure 4.7: Density assigned to SPH particles (Equation 4.2) in our model 2A, where the mass of daughters are proportional to the volume of the subcell, as a function of the particle mass just after splitting (left) and when the simulation is terminated (right).

overestimated is larger than the ones whose density is underestimated. As shown in the left panel of Figure 4.1, some daughters are likely to be too close to others by the nature of SPHERE splitting that the angle of the hexagonal closed packing array, on which the daughters are distributed, is randomly determined. The standard deviation of particle density σ_ρ increases from 0.022 to 0.22 just after the particle splitting. After that, the maximal/minimal density decreases/increases, approaching the original value 1, and σ_ρ is dumped by the gas pressure.

For the pattern of particle distribution 1, $(\rho_{\max}, \rho_{\min}) = (3.79, 0.30)$ and $(5.28, 0.51)$ for the mass threshold of $m_{\text{th}} = m_{\text{par}}/1000$ (A) and $m_{\text{par}}/30$ (B), respectively. For the pattern 2, $(5.28, 0.51)$ and $(2.80, 0.23)$, respectively. In the model A, particles whose density is significantly underestimated appear. It is because the particles assigned the small mass tends to have small density. Figure 4.7 shows the relationship between the particle density and mass just after the particle splitting ($t = 10t_{\text{sc}}$) and when we terminate the simulation ($20t_{\text{sc}}$) in the model 2A. A positive correlation between these two quantities can be seen at $t = 10t_{\text{sc}}$ and some particles with $m_{\text{dau}} \lesssim m_{\text{par}}/30$ remain underdense at $20t_{\text{sc}}$. This suggests that the ideal mass threshold is $m_{\text{th}} > m_{\text{par}}/30$. On the other hand, the number of particles is desired to be as large as possible to reproduce the density structure originally created by the parent particles. Thus, the threshold $m_{\text{th}} = m_{\text{par}}/30$ would be valid when we assign the mass of daughter particle proportional to the volume of subcells. We can see that the density underestimation is overcome in both patterns 1B and 2B, enhancing the mass threshold although ρ_{\max} and $\bar{\rho}$ are larger for 1B than for 1A.

In the cases A and B, the deviation of density σ_ρ remains large, even larger than SPHERE splitting (see the left four panels of Figure 4.5). When the different mass particles are adjacent, the density is overestimated or underestimated as discussed above. This triggers the remaining density deviation in the cases A and B (Figure 4.6). We also test the case 2C, where the particle mass is assigned uniformly for the distribution pattern 2. The density deviation at $t > 10t_{\text{sc}}$ becomes smaller, down to the same level of the SPHERE splitting. However, the particle-averaged density $\bar{\rho}$ just after the splitting becomes larger (1.31) in the case 2C than in 2B. In the particle distribution pattern 2, two daughters can become close to each other (see Figure 4.3). While these particles are likely to have small mass in the cases A and B because of the small volume of their subcells, these particles are assigned larger mass $m_{\text{par}}/N_{\text{dau}}$ in the case of C. This leads the particle densities to be overestimated in the case 2C.

Moreover, in the distribution pattern 2, where a daughter d is located between its parent p and the neighbor n along the straight line, if the distance between p and n is close, d and n become closer to each other. Also in the pattern 1, the subcell becomes flattened if the parent and the corresponding neighbor is close. The daughter is located close to the neighbor, and their density is likely to be overestimated.

Finally, we perform the simulation in the case 3C, where daughters are distributed on the center-of-mass of the subcell corresponding to each Voronoi vertex, and its mass is uniformly given with $m_{\text{par}}/N_{\text{dau}}$. Since the daughters are no longer distributed between

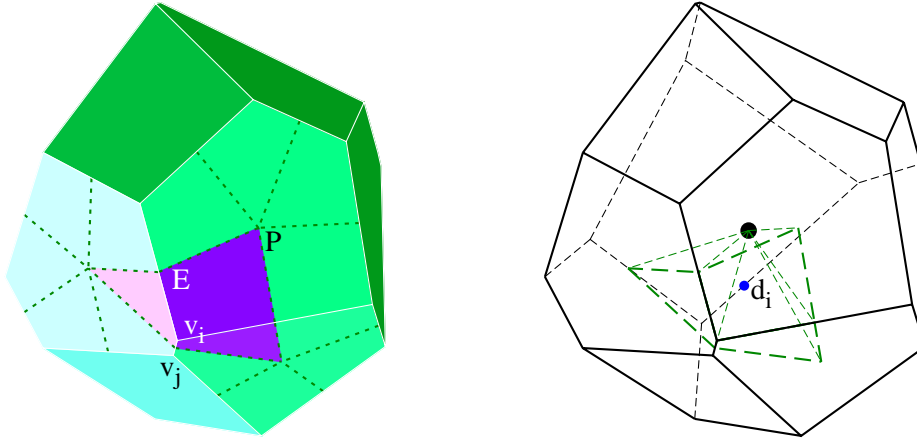


Figure 4.8: We plot the three-dimensional structure of the Voronoi cell of a parent particle (black dot). The daughter particle (blue dot; “ d_i ”) is located on the center-of-mass of the subcell defined by the green-dotted lines and the purple planes. The green dotted line connects between the center-of-mass of the planes (P) and the middle point of the edge (E). The daughter d_i corresponds to the vertex i . This will be merged with the adjacent daughter corresponding to the vertex v_j (see text).

their parent and the neighbor particles, the density overestimation is suppressed: the maximal density ρ_{\max} and density deviation σ_ρ just after the particle splitting are reduced down to 1.83 and 1.06, respectively. Although the minimal density ρ_{\min} becomes smaller (0.67) than 2C and SPHERE case, the particle-averaged density $\bar{\rho}$ becomes closer to unity (1.06). This suggests that the overestimation and underestimation of the density occur to the similar extent. We can conclude that the reproduction of the original density distribution is refined in 3C model with respect to the other cases. We in this Thesis determine the coordinate and mass of the daughters, utilizing 3C.

4.3.2.3 Detail description of pattern 3 in three-dimensional manner

Figure 4.3 schematically presents the way to locate the daughter particles in the Voronoi cell for the pattern 3 in the two-dimensional manner. The test simulations are performed three-dimensionally. In this Section, we present the method to distribute daughter for the pattern 3 in the three-dimensional manner. Figure 4.8 shows the three-dimensional description of the configuration of the subcell and the daughter particles. As described in the left panel of Figure 4.8, planes of the subcell (indicated by the purple-shaded region) are defined by the dotted line segments, which connect the center-of-mass of the Voronoi plane (P) and the middle point of the Voronoi edges (E). Then, we cut out the polyhedron (subcell) defined by the edges connecting each vertex of the the planes with the parent

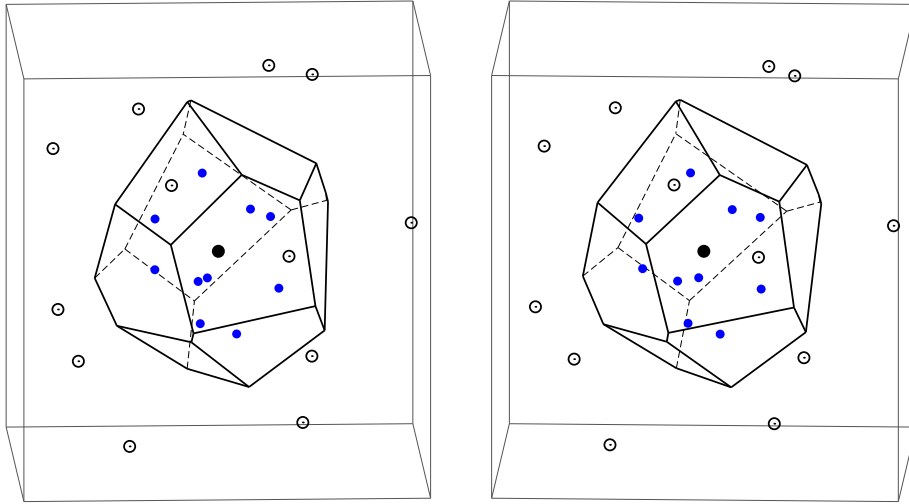


Figure 4.9: Stereograph of the particle distribution. The ten daughters (blue dots) can be seen within the Voronoi cell defined by the black lines around the parent (black dot). The Voronoi cell is defined by the distribution of the neighbor particles (open circles).

as shown in the right panel of Figure 4.8. A daughter d_i is located at the center-of-mass of the subcell corresponding to the Voronoi vertex v_i .

The typical number of the vertices per Voronoi cell is 20–30. We then perform the merger process as presented above. In the case where the adjacent subcells are closest, we merge the subcells. The vertex v_i is actually close to the adjacent vertex v_j , and the daughter d_i is also close to the next daughter corresponding to v_j . Such a close pair of the daughters are merged. We merge such a close pair of daughters until the number N_{dau} of the daughters becomes 10 if the number of vertices are above this. We show the stereograph of the final distribution of the daughters in Figure 4.9. We redistribute the mass of the parent m_{par} to the daughters equally $m_{\text{dau}} = m_{\text{par}}/N_{\text{dau}}$.

4.3.2.4 Physical quantities assigned to daughters

SPH particles have the quantities of position, mass, velocity, temperature, and chemical composition. Once the position and mass are given by the above procedure, its density is determined by Equation (4.2). Just after splitting, we give the same temperature as the parent to its daughters as a trial value. After the one computational timestep, the temperature is recalculated according to the change of particle density with entropy conserved. We reassign the same velocity as the parent to its daughters so that the kinetic energy and momentum are strictly conserved. The chemical compositions of the daughters are also assigned to the same quantities as the parent particle.

Table 4.2: Setup for BB79 tests

Quantity	Symbol	Value
Cloud mass	M_{ini}	$1 M_{\odot}$
Cloud radius	R_{ini}	0.02 pc
Sound speed	c_{T}	0.17 cm s^{-1}
Rotation rate	Ω_{ini}	$7.2 \times 10^{-13} \text{ s}^{-1}$
Pert. amplitude	$A_{m=2,\text{ini}}$	0.1

4.4 Bodenheimer test

4.4.1 Setup

In this section, we discuss the results of the so-called Bodenheimer test (Boss and Bodenheimer 1979). We hereafter call the set of runs as BB79. We prepare the isothermal uniform gas sphere with rotation and bar-mode ($m = 2$) perturbation. The parameters for the simulations are shown in Table 4.2. The initial mass and cloud radius gives the initial density of $n_{\text{H,ini}} = 2.0 \times 10^{-18} \text{ g cm}^{-3}$. The initial sound speed corresponds to the temperature of 8 K for the fully isothermal gas, and the ratio of the thermal energy to the gravitational energy as $\alpha_{\text{ini}} = 5c_{\text{T}}^2 R_{\text{ini}}/2GM_{\text{ini}} = 0.32$. The initial rotation rate are given, corresponding to the initial ratio of the rotational energy to the gravitational energy as $\beta_{\text{ini}} = \Omega_{\text{ini}}^2 R_{\text{ini}}^3/3GM_{\text{ini}} = 0.28$. We assign the particle mass as $m_{\text{p,ini}} = \bar{m}_{\text{p,ini}}(1 + A_{m=2,\text{ini}} \cos 2\phi/2)$ at the angle ϕ , where $\bar{m}_{\text{p,ini}} = M_{\text{ini}}/N_{\text{p}}$ is the average particle mass.

We perform the simulations in the case without particle splitting (NOSP) and with the previous KW02 and our methods (SPHERE and VORO, respectively). In NOSP simulation, we set the number of SPH particles $\sim 10^8$ in order to satisfy the Jeans criterion $\mathcal{R}_{\text{cr}} \sim 100$ at density $\sim 5 \times 10^{-12} \text{ g cm}^{-3}$, where the gas becomes optically thick and we terminate our simulations. In the case with splitting, we distribute $N_{\text{p}} \sim 4 \times 10^6$ of particles. In these runs, the particles are on-the-fly split into daughters at the corresponding densities where the Jeans criterion for $\mathcal{R}_{\text{cr}} = 100$ is about to broken.

4.4.2 Results

4.4.2.1 Overall feature of density structure

In Figure 4.10, we show the density slice obtained by our simulations when the maximal density among the SPH particles reaches $5 \times 10^{-12} \text{ g cm}^{-3}$. Among all of three models (NOSP, SPHERE, and VORO), the density structure is not significantly changed. Filamentary structure is maintained without fragmentation with slight blobs appearing at the both ends of the filament. We further see the density profiles in the three cases as a function of the distance at the center of one of the two blobs in Figure 4.11. The density

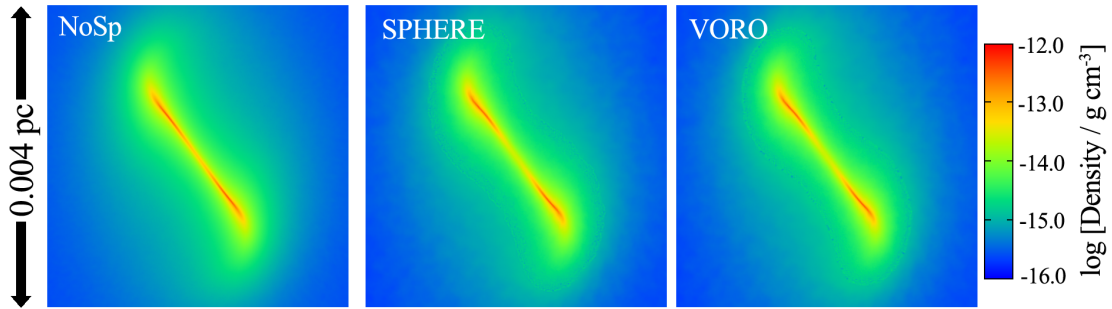


Figure 4.10: Density slice on the plane perpendicular to the rotational axis for the Bodenheimer test simulations (BB79) without particle splitting (NOSP; left) and with the particle splitting of the previous work (SPHERE; middle) and the present work (VORO; right) at the peak density $\sim 5 \times 10^{-12} \text{ g cm}^{-3}$.

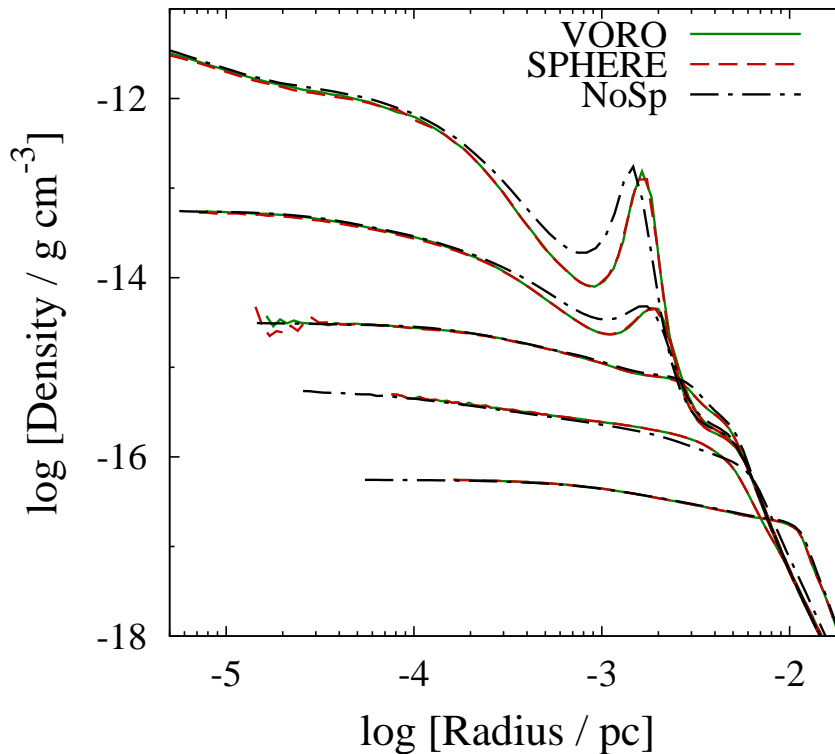


Figure 4.11: Density as a function of the distance from the most dense region (one of the two blobs shown in Figure 4.10). in the BB79 simulations for NOSP (black dot-dashed), SPHERE (red dashed) and VORO (green). Note that the red and green curves closely overlap with each other.

profiles also have the almost same feature in the three simulations although the density between the two blobs at distance 10^{-3} pc is slightly smaller for SPHERE and VORO than for NOSP by a factor of 3. We can conclude that the particle splitting does not affect the density structures.

4.4.2.2 Comparison with the semi-analytic studies

In this section, we compare our results with the semi-analytic and numerical studies previously presented by Tsuribe and Inutsuka (1999a,b). They follow the evolution of the rotating isothermal clouds with various α and β parameters to seek the fragmentation conditions. They conclude that the fragmentation condition is sensitive dominantly to the α parameter. The case with $\alpha = 0.32$ and $\beta = 0.28$, where we investigate here, is the marginal case (Tsuribe and Inutsuka 1999b), and they confirm that the fragmentation occurs when the initial perturbation amplitude is larger than 0.15 by their simulations (Tsuribe and Inutsuka 1999a). Our perturbation amplitude is 0.1, and thus our simulation results is consistent with their studies.

When we further continue the simulation for NOSP, the density in the central filament increases and breaks the Jeans criterion. The several spherical clumps appear along the filament. From the semi-analytic approaches, we can say that this is due to the spurious fragmentation presented by Truelove et al. (1997). The length resolution becomes comparable to the typical length of the density structure, and then the numerical noise becomes important to create random distribution of the SPH particles. This triggers the spurious fluctuations of the gravitational potentials.

4.4.2.3 Comparison between two splitting methods

In this BB79 test, we can not see the difference of the density structure between the previous and this work. As seen in Figure 4.1, if the length-scale of the density structure is smaller than the length-scale over which the daughters are distributed, the anisotropic structure in SPHERE can be smoothed out by the uniform distribution of the daughter particles. The length scale of the density structure can be measured by $l_\rho = \rho/|\nabla \cdot \rho|$, and the scale of the daughter particle distribution is $\sim h_{\text{par}} \sim c_{\text{T}} \mathcal{R}_{\text{cr}}^{-1/3} (G\rho)^{-1/2}$. We compare these scales on the iso-density surface where the particle splitting occurs. By the gas rotation, the disk structure is formed. The fluid elements on the equatorial plane have a smaller infall velocity relative to the fluids contract along the rotational axis because of the support by the centrifugal force. Therefore, the upper and lower sides of the disk, the density gradient becomes largest. At the density $\sim 5 \times 10^{-13}$ g cm $^{-3}$, the particle splitting occurs for the second time. On the iso-density surface, l_ρ marks the minimal value on the poles, 4×10^{-6} pc. The value is still larger than $h_{\text{par}} \sim 3 \times 10^{-6}$ pc. In the simulations with very small sound speed ($c_{\text{T}} = 0.1$ km s $^{-1}$), h_{par} tends to be sufficiently small. In that case, the splitting method SPHERE can work very well to preserve the density structure of the gas. However, in the warm gas such as the primordial gas, this

Table 4.3: Setup and result for MH tests

run	N_{ngb}	\mathcal{R}_{cr}	$N_{\text{p,ini}}$	$N_{\text{p,fin}}$	Comp. time
MH-SPHERE	64 ± 8	1000	169 511	314 867	48 315 s
MH-VORO	64 ± 8	1000	169 511	318 148	81 320 s
MH-SPHERE-H	64 ± 8	4000	169 511	1 283 284	323 309 s

Note — In the last column we show the computational time from $n_{\text{H,peak}} = 10 \text{ cm}^{-3}$ to $n_{\text{H,peak}} = 1 \times 10^{12} \text{ cm}^{-3}$.

is not the case.

4.5 Collapse simulations of primordial gas cloud

4.5.1 Setup

4.5.1.1 Target cloud

Then, we perform the simulation in the primordial minihalo case. We hereafter call the set of runs as MH. The data of the dark matter minihalo with the gas trapped by the halo is taken from the cosmological simulation of [Hirano et al. \(2014\)](#). We cut out the $\sim 1 \text{ kpc}$ region centered at the isolated minihalo with the halo mass $M_{\text{h}} = 4.8 \times 10^5 M_{\odot}$ at the redshift $z = 15$. The halo is categorized into a subclass where the less-massive Pop III stars are formed ($\sim 10\text{--}100 M_{\odot}$) because in the course of collapse, HD, which is another important coolant in the primordial gas, is efficiently formed. We start the collapse simulation of the hosted gas cloud from the peak density $n_{\text{H}} = 10 \text{ cm}^{-3}$. The included chemical reactions, cooling rates and the treatment in the optically thick regimes are shown in Chapter 2. Here, we do not include the chemistry and cooling by metal and dust.

4.5.1.2 Numerical scheme

We show in Table 4.3 the numerical setup for the simulations with the particle splitting methods by previous (SPHERE) and present works (VORO). Initially the simulation data contains 169 511 gas particles. The number increases in the course of collapse by the particle splitting. Here, we set the fiducial value of $\mathcal{R}_{\text{cr}} = 1000$. In the central region of the gas, some particles are already split once, and the mass of these once split particles is $m_{\text{p}}^{(1)} = 5/13 M_{\odot}$. We follow the collapse until the central density reaches $n_{\text{H}} = 1 \times 10^{12} \text{ cm}^{-3}$. At that time, the SPH particles are split four times. By the n 'th splitting, the particle mass becomes $m_{\text{p}}^{(n)} = m_{\text{p}}^{(1)}/13^{n-1}$ for SPHERE or $m_{\text{p}}^{(n)} = m_{\text{p}}^{(1)}/10^{n-1}$ for VORO. Therefore, the particles are split when the local Jeans mass (as a function of the particle density and temperature) is reduced down to $M_{\text{J}} = \mathcal{R}_{\text{cr}} N_{\text{ngb}} m_{\text{p}}^{(n-1)}$. The series

of simulations is carried out on Cray XC30,² using 128 cores.

4.5.2 Resulting density structures

Figure 4.12 shows the results of the collapse simulations with the particle splitting methods of SPHERE and VORO when the maximal density $n_{\text{H,peak}}$ among the SPH particles reaches 10^{12} cm^{-3} . At $n_{\text{H}} \sim 10^3 \text{ cm}^{-3}$, HD cooling becomes efficient. The cloud core is elongated and wound by the rotation, and then the disk and spiral structure form. This trend lasts until the gas density becomes $n_{\text{H}} \sim 10^6\text{--}10^7 \text{ cm}^{-3}$, where HD lines become optically thick. In the middle panel of the Figure 4.12, we can see the spiral arms triggered by HD cooling. One can see that the structure of disk and the spiral arms are remarkably difference between the two splitting methods. While the diffused spiral arms are around the less dense smooth spheroidal disk in SPHERE, the dense and thin spiral arms are seen around the ellipsoidal core.

After the gas density exceeds $\sim 10^6\text{--}10^7 \text{ cm}^{-3}$, the gas becomes optically thick for HD transition lines. The cloud collapse is partly halted and the density gradient becomes steep.³ Figure 4.13 shows that the density profile for our MH simulations. At the density $\sim 10^6\text{--}10^7 \text{ cm}^{-3}$ (length $\sim 0.1 \text{ pc}$), the profile becomes very steep almost proportional to r^{-4} , and the fourth step of particle splitting is operated.

Let us again compare the two length scales: one for the density gradient, and one for the distribution of the daughter particles. The length scale l_ρ of the density gradient is reduced down to $\sim 0.01 \text{ pc}$. The scale over which the daughters are distributed is

- SPHERE: the order of the smoothing length h_{par} of the parent particles
 $\sim h_{\text{par}} \sim (N_{\text{ngb}} m_{\text{par}} / \rho)^{1/3} \sim c_{\text{T}} \mathcal{R}_{\text{cr}}^{-1/3} (G\rho)^{-1/2} \sim 0.01 \text{ pc}$.
- VORO: the order of the inter-particle length λ_{p} of the parent particles
 $\sim \lambda_{\text{p}} \sim (m_{\text{par}} / \rho)^{1/3} \sim 0.004 \text{ pc}$

For SPHERE, h_{par} is comparable to l_ρ , which means that the distribution of the daughters can only marginally follow the density structure. Whereas, for VORO, the distribution of the daughters can well capture the steep density gradient.

In the simulations for the primordial gas, we can see the remarkable difference between the two splitting methods SPHERE and VORO while they show the almost the same result in BB79. This stems from the gas temperature. In BB79 case, the gas is cold ($c_{\text{T}} \sim 0.1 \text{ km s}^{-1}$), corresponding to $T \simeq 8 \text{ K}$. In the warm primordial gas with $T \sim 100 \text{ K}$, since h_{par} becomes larger according to $h_{\text{par}} \propto T^{1/2}$, daughter particles have a lack of ability to capture the steep density structures.

²Center for Computational Astrophysics, National Astronomical Observatory of Japan.

³This trend can be seen also at $n_{\text{H}} \sim 10^8 \text{ cm}^{-3}$, where the gas heating by the exothermic reactions to form H_2 molecules are dominant.

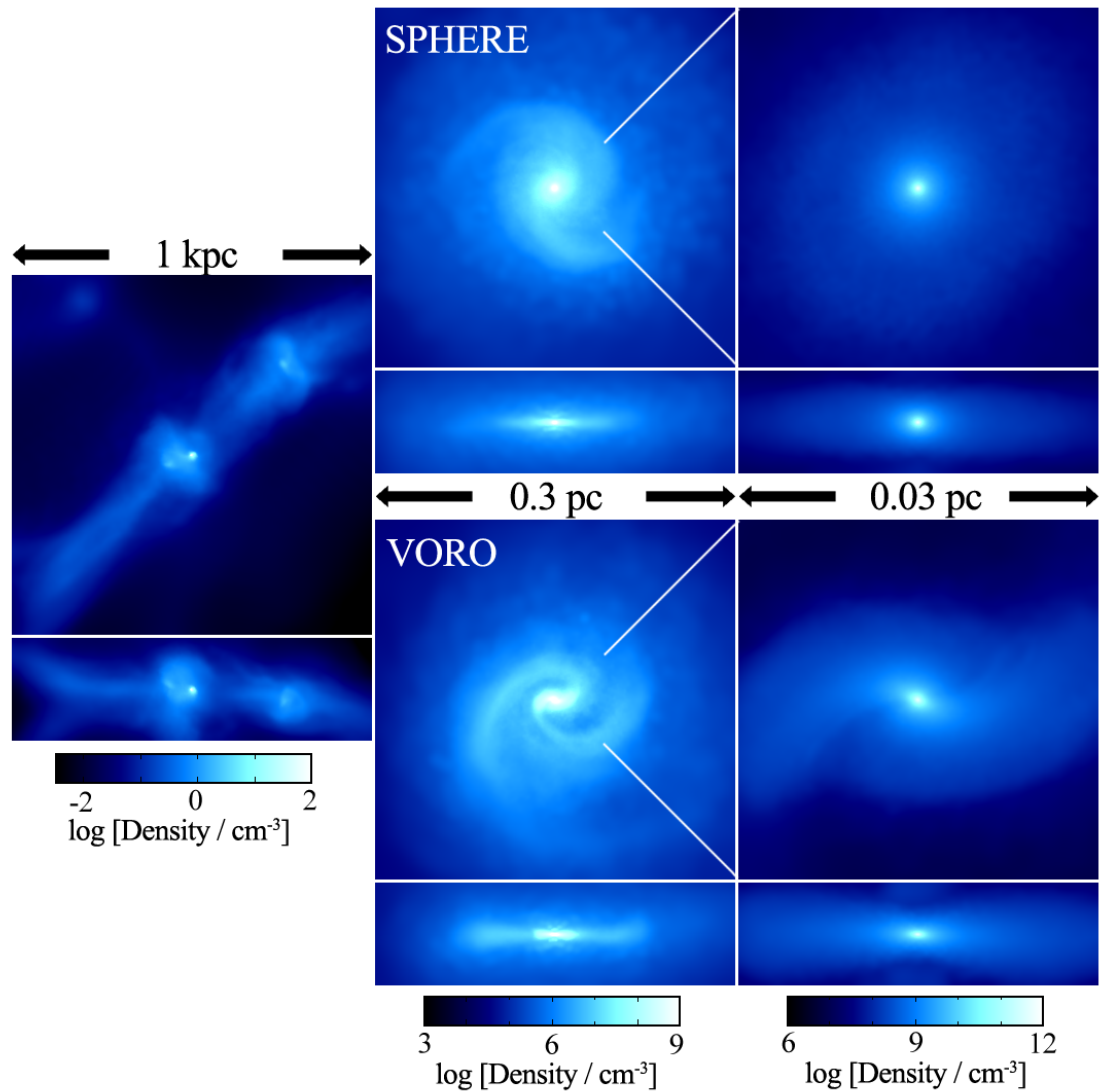


Figure 4.12: Density-weighted density projection of the primordial clouds in our MH simulations from the face-on and edge-on views of the disk when the peak density reaches $n_{\text{H,peak}} = 10^{12} \text{ cm}^{-3}$. We show the results obtained with the particle splitting methods of SPHERE (top) and VORO (bottom) from the same initial condition.

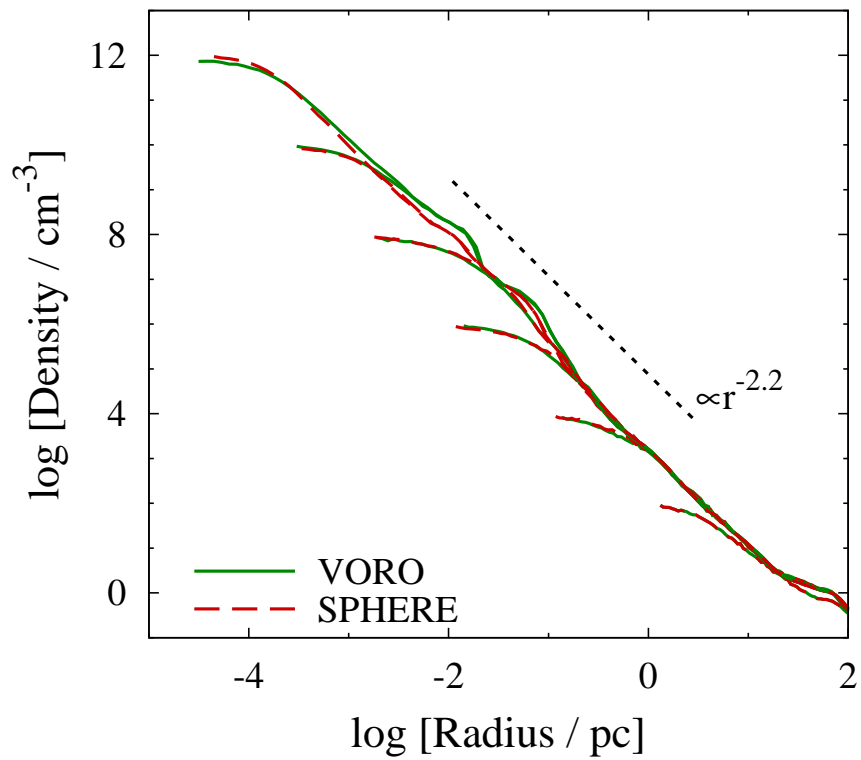


Figure 4.13: Density as a function of the distance from the cloud center in our simulations for the minihalo (MH) with the splitting methods of SPHERE (red dashed) and VORO (green solid). We also plot the density gradient of $\propto r^{-2.2}$, which typical primordial clouds are along (black-dotted line).

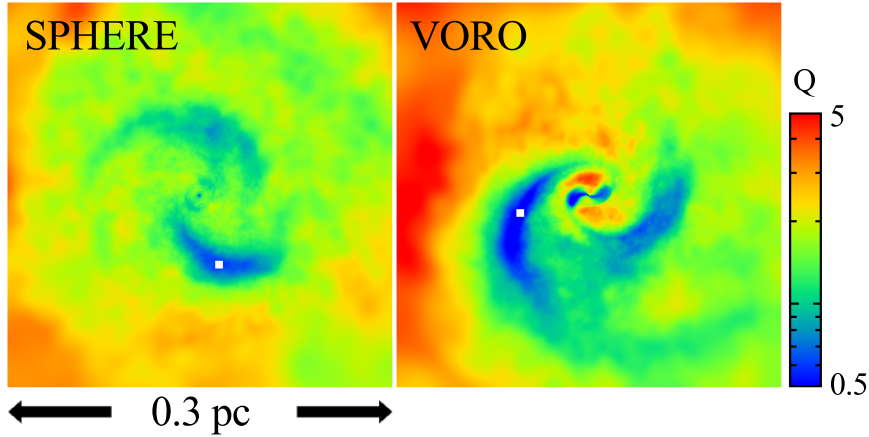


Figure 4.14: Color contour map of Toomre Q -parameter, which spreads from 0.5 (blue) to 5 (red) in the plotted region for SPHERE (left) and VORO (right). The white squares indicate the point where the Q -parameter marks the smallest value.

4.6 Discussion

4.6.1 Implication for the gas fragmentation

We have so far seen that the particle splitting methods can affect the global structure of the gas cloud. For VORO case, the dense and apparent spiral arms are formed with respect to the SPHERE case. Such the difference might also change the gravitational feature of the disk. It is reported that the dense massive spiral arms on the disk fragment by self-gravity (Turk et al. 2009). Although we can not follow the further evolution of the arms, we here utilize the Toomre Q -parameter to see whether the spiral arms in our simulations fragment by self-gravity or not. The parameter is defined as $Q = 2\Omega c_T / \pi G \Sigma$, where Σ is the column density integrated in the direction parallel to the rotational axis.

Figure 4.14 shows the distribution of the Q -parameter in our simulations. We can see that the parameter is small along the dense spiral arms (see 4.12). The blue-colored region, where $Q < 1$, more widely spreads for VORO than for SPHERE. This should reflect the feature of our splitting method that the anisotropic structure is captured by the elaborated distribution of the daughter particles. Recently, Takahashi (2015) present the critical condition for fragmentation of the dense spiral arms. They present that, when $Q < 1$, it does not immediately indicate the fragmentation on the disk. Instead, they confirm that the spiral arms appear if the disk satisfies the criterion by their simulations. By their linear analysis of the instability of gas ring, an analogue of the spiral arm, it is suggested that the arms with $Q \lesssim Q_{\text{cr}}$ becomes unstable to fragment. The critical value Q_{cr} depends on the selection of the gravitational potentials. In the case with the incompressible fluid, $Q_{\text{cr}} = 0.6$, and $1/\pi$ for the three-dimensional potentials. This model predicts that, If even a part of the spiral arms satisfies the criterion, such a region

becomes unstable to fragment. We measure the minimum values of Q in the spiral arms, and compare with the critical value. As a result, we obtain $Q_{\min} = 0.59$ for SPHERE and $Q_{\min} = 0.41$ for VORO. As one can expect, the apparent thin filament appearing in the simulation with our splitting method predicts the smaller Q -value than with the previous method. This reflects the nature of both splitting methods. The concentrated gas is more likely to be unstable by its self-gravity in the former case. Meanwhile, in the former case, the symmetric distribution of the daughter particle is imposed, and the resulting diffused density structure may suppress the effect of the self-gravity. The minimal Q -value is slightly larger than the critical value in both cases, i.e., the spiral arms are marginally stable against the fragmentation. Still, the global structure of the spiral arms is considered to have an effect on the evolution of the central embryo stars (also see Greif et al. 2012; Vorobyov et al. 2013). We also comment that the criterion of the fragmentation of spiral arms on the disk is still under the debate. The critical value depends on the selection of the gravitational potentials. In order to investigate it by simulations, it is required to fully resolve the spiral arm structures for a long time.

4.6.2 Computational time

The construction of the Voronoi diagram is indeed costly with current algorithm introduced in Section 4.3.1. In the primordial cloud collapse simulations, the computational time is 48 315 and 81 320 seconds respectively for SPHERE and VORO (Table 4.3) with the splitting criterion $\mathcal{R}_{\text{cr}} = 1000$ to follow the cloud evolution from $n_{\text{H,peak}} = 10$ to 10^{12} cm^{-3} , using 128 cores. Especially, the procedure of the Voronoi tessellation accounts for the half of the total computational time. It is expected that we can shorten the computational time for the Voronoi tessellation, introducing the incremental construction scheme scaling as $\mathcal{O}(N_{\text{sp}} \log N_{\text{sp}})$ (Sugihara and Iri 1994) and the more efficient parallelization scheme scaling as $\mathcal{O}(N_{\text{sp}})$ (Chiaki, Yoshikawa & Yoshida, in preparation).

4.6.3 Resolution test

Through the series of our simulations, it is indicated that the length resolution in the case with VORO particle splitting is effectively higher than SPHERE by a factor of $\sim \lambda_{\text{p}}/h_{\text{par}} \sim N_{\text{ngb}}^{-1/3}$. In our method, the Voronoi cell flexibly capture the density distribution created by the set of parent particles, and preserve the anisotropic density structure while such the structure is spherically smoothed out in SPHERE simulations. In utilizing the method SPHERE, we recommend to impose another criterion for splitting than the Jeans criterion so that the length scale l_{ρ} of density gradient is resolved by the smoothing length h_{par} . In principle, the results of the simulations of SPHERE and VORO will converge with the infinite resolution. We run the another simulation for SPHERE with substantially high resolution criterion $\mathcal{R}_{\text{cr}} = 4000$ (SPHERE-H). Figure 4.15 shows the resulting snapshots for SPHERE, VORO and SPHERE-H. This high-resolution run shows the dens spiral arms and the ellipsoidal core. We can see that the VORO splitting reproduces qualitatively

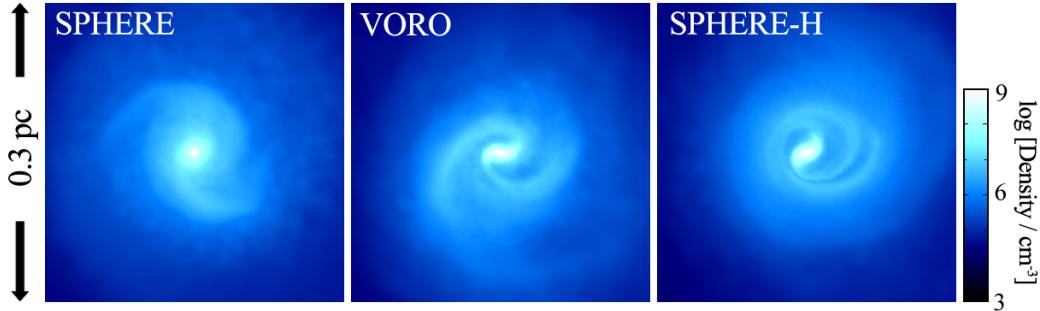


Figure 4.15: Density map of the collapsing primordial cloud at the peak density $n_{\text{H,peak}} = 10^{12} \text{ cm}^{-3}$ for SPHERE (left), VORO (middle) with the splitting criterion $\mathcal{R}_{\text{cr}} = 1000$ and SPHERE-H with $\mathcal{R}_{\text{cr}} = 4000$ (right). The right and middle panels are identical to the middle panels of Figure 4.12.

similar structure.

This test also serves as the convergence check of the simulations. It is ideal to compare the result of the sufficiently high-resolution run without particle splitting with that of the simulation with splitting. For the set of runs BB79, we compare the NOSP and SPHERE/VORO runs and see the results are qualitatively the same. On the other hand, the run MH, and the part of collapse simulations for the metal-poor gas clouds (presented in Chapter 5), the target gas clouds are taken from the cosmological simulation in the larger simulation box ($1 h^{-1} \text{ Mpc}$ comoving length on a side). In that case, we resort to the comparison between the simulations with the different splitting criteria \mathcal{R}_{cr} to check the convergence. Although the thinner and denser spiral arms winding about one round appear around the central blob in the run SPHERE-H than for VORO, the computational time for SPHERE-H (323 309 s) is by a factor of about four longer than VORO (81 320 s). In Chapter 5, we perform the collapse simulations for metal-poor gas clouds ($Z = 10^{-6} - 10^{-3} Z_{\odot}$). In addition to the primordial chemistry in MH case, we compute the chemistry of another 19 metal species, the equilibrium grain temperature (thermal emission rate) for 20–35 size bins of 9 grain species (total 253 size bins), and the further evolution until the central density reaches $n_{\text{H, cen}} > 10^{16} \text{ cm}^{-3}$ to follow the dust-induced fragmentation which occurs at high densities typically $n_{\text{H}} \sim 10^{12} - 10^{14} \text{ cm}^{-3}$ (see Chapter 1) in the metal-poor cloud simulations. Let us set the splitting criterion $\mathcal{R}_{\text{cr}} = 1000$ in this Thesis.

4.7 Chapter summary

In this Chapter, we present the newly-developed method of the particle splitting. While the daughter particles are distributed in the symmetric manner around the parent particles, the locations of the daughters are determined based on the Voronoi diagram created

by the distribution of the parent particles. In the former case, it is liable that the anisotropic fluid structure with the steep density gradient might not be captured. We perform two sets of the simulations: so-called Bodenheimer test (BB79) and the collapse simulations of a primordial gas cloud hosted by a cosmological minihalo (MH). In these simulations, our splitting method (VORO) is compared with the previously presented method by which the daughter particles are distributed on the sphere with radius h_{par} centered at the parent particles (SPHERE).

- In BB79, we test the collapse of an uniform, isothermal, and rotating cloud in the three cases without particle splitting (NOSP) and with the splitting method of SPHERE and VORO. Consequently, all of three give the consistent density structures: the filamentary structure with slight blobs are formed. In this set of simulations, we can confirm that the both of the particle splitting methods are valid to properly follow the evolution of the collapsing cloud. These results are also consistent with the previous semi-analytic and numerical works.
- In MH, we follow the cloud contraction in a cosmological minihalo with SPHERE and VORO. In this case, we can confirm that the structure of the apparent spiral arms and the ellipsoidal core is preserved for VORO, while the less dense, diffused spiral arms and spheroidal core appear for SPHERE. This reflects the feature of the both methods. The daughter particles distributed within the Voronoi cell can flexibly follow the original density structure generated by their parents. Whereas, if the daughters are distributed isotropically, this fails to capture the density structure with the density gradient appearing in a certain direction. Further, we estimate the Q -parameter, the indicator of the instability in the disk. Although Q is slightly larger than the critical value in VORO, the difference of the density structures should affect the evolution of the central protostellar core.

As above, the density structure is similar for SPHERE and VORO in the BB79 test while different in MH. This is because of the temperature of the two cloud. In BB79, the cloud temperature is low, corresponding to $c_T \sim 0.1 \text{ km s}^{-1}$. Whereas, the primordial cloud is warm $T \simeq 100 \text{ K}$ ($c_T \sim 1 \text{ km s}^{-1}$) because of the lack of important coolant (metal and dust). In warmer cloud, the separation between newly located daughters and their parents becomes longer ($\sim h_{\text{par}} \propto c_T$). Accordingly, the length scale at which the daughters smooth out the density structure becomes larger. We can conclude that our novel method of particle splitting should be utilized in the collapse simulation with warmer gas especially in the metal-free or metal-deficient cases in order to capture the anisotropic fluid structures including cloud fragmentation.

Fragmentation properties of metal deficient clouds

Contents

5.1	Overview	93
5.2	Numerical method	94
5.2.1	Hydrodynamics and particle splitting	94
5.2.2	Chemistry and cooling in collapse phase	95
5.2.3	Accretion phase	95
5.2.4	Initial conditions	96
5.3	Evolution of uniform clouds	102
5.4	Cloud fragmentation	104
5.4.1	Overall features	104
5.4.2	Filament fragmentation	106
5.4.3	Disk fragmentation	125
5.5	Gas accretion onto protostars	125
5.5.1	Overall features	125
5.5.2	Detail cloud evolution	126
5.6	Discussion	130
5.7	Chapter Summary	132

5.1 Overview

We have so far discussed that the cloud fragmentation in the metal-poor environment is dependent on the initial dust model and grain growth. Also, we see that the numerical zoom-in technique also would have an effect on the density structure of the cloud, which is crucial to determine the fragmentation condition. In this Chapter, we perform the simulations for the metal-deficient cloud collapse. In our model, grain growth, molecular

cooling, and gas heating owing to hydrogen molecular formation are for the first time self-consistently included as well as the non-equilibrium chemistry and fine-structure cooling. The initial abundance of heavy element and grain species and dust size distribution are given by the Pop III supernova model introduced in Chapter 3.

Employing the state-of-the-art particle splitting method based on the Voronoi tessellation described in Chapter 4, the central mass resolution is eventually refined into $\sim 10^{-5} M_{\odot}$ (10 earth masses). Further, as Hirano et al. (2014) recently indicated, the different clouds hosted by minihalos undergo the different thermal evolutions. We here perform simulations for the several pre-stellar clouds, and see that the different properties of these clouds have effect on the thermal properties of cloud, and the fragmentation condition. In Section 5.2, we introduce our numerical method, and follow the necessary chemical reactions and cooling/heating processes in the metal-deficient cloud collapse by using the results for the uniform gas sphere in Section 5.3. Then, we see whether each cloud fragments or not, and derive the critical conditions for the cloud fragmentation in Section 5.4. In Section 5.5, we discuss the numerical results for the succeeding phase of gas accretion onto the protostars. Finally, we discuss some issues in Section 5.6.

The content in this Chapter has been submitted to Monthly Notices of the Royal Astronomical Society.

5.2 Numerical method

5.2.1 Hydrodynamics and particle splitting

In this Chapter, we continuously use the parallel N -body/SPH simulation code GADGET-2 (Springel 2005) to seek the evolution of three-dimensional structure of the metal-poor gas clouds. The cloud collapse is a phenomenon whose dynamic range of density (length scale) is very wide, over 20 (10) order of magnitude. We initially follow the fluid dynamics over the ~ 1 kpc. To resolve the length scale of ~ 0.1 AU over which eventually the protostars lie, we resort to the zoom-in technique. We in Chapter 4 develop the novel particle splitting method based on the Voronoi tessellation. In this method, we distribute the finer daughter particles around the coarse parent particle according to the geometry of the Voronoi cell created by the parent particle distribution. By the nature of the Voronoi cells which well capture the original distribution of the parent particles, the even global anisotropic density structure can be reproduced in the cloud collapse simulations. Here, the mass of the SPH particles are refined so that always they resolve the Jeans mass M_J divided by the factor of \mathcal{R}_{cr} (Chapter 4) to avoid the spurious fragmentation (Jeans criterion: Truelove et al. 1997, 1998) as $\mathcal{R}_{\text{cr}} N_{\text{ngb}} m_{\text{par}} = M_J$. Here, the number of neighbor particle is $N_{\text{ngb}} = 64 \pm 8$. We set $\mathcal{R}_{\text{cr}} = 1000$ according to Hirano et al. (2014).

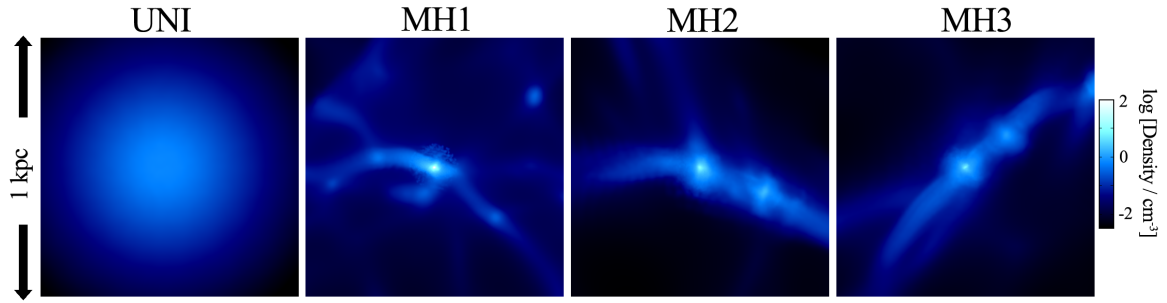


Figure 5.1: Density-weighted density projection of our clouds UNI, MH1, MH2, and MH3 from left to right just after the simulations are started.

5.2.2 Chemistry and cooling in collapse phase

The cooling processes considered here are fine-structure line cooling of C II, C I, and O I, and transition line cooling by H₂ and by HD molecules. We for the first time implement the molecular cooling by CO, OH, and H₂O into the simulation. Since the formation reaction of hydrogen molecules is the exothermic one, the binding energy is released to heat the gas when the molecules are formed. They are mainly formed via three-body reactions at the densities $n_{\text{H}} \sim 10^8\text{--}10^{11} \text{ cm}^{-3}$. Such the gas heating effect can halt the cloud elongation preceding to its fragmentation as reported by the simulation of [Tsuribe and Omukai \(2008\)](#) for the polytropic analog of low-metallicity gas. Then, we should examine whether it affects the cloud fragmentation or not also in our simulations. In order to determine the cooling efficiencies of gas, the non-equilibrium chemical networks for 27 species (H⁺, e⁻, H, H⁻, H₂, D⁺, D, HD, C⁺, C, CH, CH₂, CO⁺, CO, CO₂, O⁺, O, OH⁺, OH, H₂O⁺, H₂O, H₃O⁺, O₂⁺, O₂, Si, SiO, and SiO₂) are implicitly solved. Also in this simulation, we consider the accretion of gas-phase metal onto dust grains (grain growth) during the cloud collapse. The reactions and their rates are shown in Chapter 2.

5.2.3 Accretion phase

After the core becomes optically thick, it no longer collapses. The simulation timestep is limited to the Courant condition to follow the dynamical time of the gas in the core ($\sim 1 \text{ yr}$). The accretion process of the ambient gas lasting for the longer timescale ($\sim 10^5 \text{ yr}$) is difficult to follow. Several authors employ a sink particle technique to overcome this difficulty. The fluid elements within a given radius (accretion radius) centered at the density peak are replaced with the Lagrangian particles ([Dopcke et al. 2013](#); [Safranek-Shrader et al. 2014b](#); [Smith et al. 2015](#)). One can save the computational cost by masking the central dense region whose dynamical time is significantly small. Yet, the boundary condition of the sink particles might have artificial effects on the accreting gas just outside

Table 5.1: Initial condition for UNI cloud

Quantity	Symbol	Value
Cloud mass	M_{ini}	$2.3 \times 10^6 M_{\odot}$
Cloud radius	R_{ini}	551 pc
Temperature	T_{ini}	300 K
Rotation rate	Ω_{ini}	$1.4 \times 10^{-17} \text{ s}^{-1}$
Pert. amplitude	$\sigma_{\rho, \text{ini}}$	0.1

Table 5.2: Initial condition for minihalos MH1–3

Cloud	z_{form}	M_{h}^{DM}	M_{h}^{b}	R_{h}	M_{PopIII}
MH1	20.46	1.5×10^5	2.2×10^4	26.5	283.9
MH2	16.20	2.2×10^5	4.0×10^4	46.8	751.3
MH3	15.15	1.1×10^5	1.4×10^4	37.5	60.5

Note — These simulations are cut out from a cosmological simulation box with $1h^{-1}$ comoving Mpc on a side (Hirano et al. 2014). The cosmological parameters presented by Komatsu et al. (2011) are applied. We show the formation redshifts z_{form} in the second column. The dark matter and baryon components of the halo mass M_{h}^{DM} (third) and M_{h}^{b} (fourth), respectively, in units of M_{\odot} at the Virial radius R_{h} (fifth column in units of pc), within which the average density of the halo is 200 times that of the average density in the Universe at z_{form} . M_{PopIII} (M_{\odot}) is the final stellar mass of the Pop III star obtained by simulations without metal.

the particle. It may enhance the rate of the ejection of sinks by the N -body effect. Also, the accretion radius has effect on the separation of fragments (Machida and Doi 2013; Greif et al. 2012). Instead, we in this work impose the stiff equation of state within an opaque core. The hydrostatic core is artificially formed, and the contraction of the gas is partly stopped. We set the adiabatic index 1.4 in the region with densities $> 10^{16} \text{ cm}^{-3}$, where even the primordial gas becomes optically thick. Thanks to this, we can follow the accretion process on the protostars and the cloud fragmentation even for a limited time (several ten years).

5.2.4 Initial conditions

5.2.4.1 Cloud models

The two sets of clouds are employed as the initial conditions in this work; one spherical cloud as a controlled simulation, and three clouds hosted by less-massive dark matter halos (minihalos) with mass $M_{\text{h}} \sim 10^5\text{--}10^6 M_{\odot}$ formed in the early Universe (redshift $z \sim 20\text{--}15$), and selected from cosmological simulations. The detailed properties of these clouds are described as follows:

- **Uniform sphere (UNI)**

We create the initial condition with a uniform density $n_{\text{H,ini}} = 0.1 \text{ cm}^{-3}$ and a random density fluctuation by 10%. We call this cloud as UNI, hereafter. The

Table 5.3: Metal abundances

X	C	O	Mg	Al	Si	S	Fe
A_X	1.08×10^{-4}	1.19×10^{-3}	4.19×10^{-5}	8.29×10^{-7}	6.67×10^{-5}	3.01×10^{-5}	6.76×10^{-6}
$[X/Fe]$	0.22	1.01	0.77	0.14	0.99	1.01	0.00

Note — Metal abundance with progenitor Pop III mass $M_{\text{pr}} = 30 M_{\odot}$ and an ambient gas density $n_{\text{amb}} = 1 \text{ cm}^{-3}$ (Nozawa et al. 2007). A_X is the number abundance of element X measured with $Z = Z_{\odot}$.

other parameters are shown in Table 5.1. The cloud mass M_{ini} and radius R_{ini} correspond respectively to the Jeans mass and length for the density $n_{\text{H,ini}}/f_{\text{enh}}$ and temperature T_{ini} , where f_{enh} is the enhancement factor introduced for the cloud to collapse. Here, we set $f_{\text{enh}} = 1.8$ (Matsumoto and Hanawa 2003).¹ Also, the initial angular momentum Ω_{ini} corresponds to $\beta_{\text{ini}} = \Omega_{\text{ini}}^2 R_{\text{ini}}^3 / 3GM_{\text{ini}}$ is 10^{-3} . The initial deuterium and helium abundances are $A_{\text{D}} = 5.3 \times 10^{-5}$ and $A_{\text{He}} = 0.079$, respectively.

- **Three cosmological minihalos** (MH1, MH2, and MH3)

We assume that the second generation stars are born in the clouds with the similar density configurations as for the Pop III stars. We cut out the ~ 1 kpc region (physical) from a cosmological simulation of Hirano et al. (2014) with a large simulation box of $1 h^{-1}$ comoving Mpc on a side. The regions are centered at the three dark matter minihalos, named MH1, MH2, and MH3. Table 5.2 shows the formation redshift z_{form} , halo mass (M_{h}^{DM} and M_{h}^{b} for the dark matter and baryon components, respectively), and radius R_{h} of these halos. They are formed at redshifts $z_{\text{form}} = 15\text{--}20$, and with halo masses of $M_{\text{h}} \sim 10^5 M_{\odot}$ in the range of several tens of parsecs. Recently, Hirano et al. (2014) find that the primordial minihalos undergo different thermal evolution during collapse even with the same metallicity ($Z = 0$), and eventually the difference affects the final stellar mass. In their simulations, the final stellar masses of the stars in MH1, MH2, and MH3 are 283.9, 751.3, and 60.5 M_{\odot} , respectively, which cover the range of 110 Pop III stellar mass of $10\text{--}1000 M_{\odot}$.

Figure 5.1 shows the projection maps of these four clouds. For minihalo models (MH1, MH2, and MH3), clouds are formed in the connecting point of the cosmological large scale structures.

5.2.4.2 Metal and dust models

In this study, we first consider the realistic dust properties in the low-metallicity cloud simulations. We uniformly add the metal and dust in our simulation clouds introduced above. Here, we consider that the target clouds are pre-enriched by Pop III supernova

¹The enhancement factor f_{enh} indicates the excess of the gravitational force to the pressure gradient. The corresponding α -parameter is $\alpha_{\text{ini}} = f_{\text{enh}}^{-2/3} = 0.68$.

Table 5.4: Dust properties

i	Silicon	Iron	Forsterite	Enstatite	Carbon	Silica	Magnesia	Troilite	Alumina	Total
$f_{\text{dep},i,0} [\times 10^{-3}]$	29.14	1.93	0.77	< 0.01	0.62	5.27	1.34	0.45	< 0.01	39.53
$r_{i,0}^{\text{grow}} [\times 10^{-2} \mu\text{m}]$	38.67	28.30	1.20	1.38	1.97	5.76	5.31	3.53	0.11	

Note — Initial factor $f_{\text{dep},i,0}$ of metal depleted onto grain species i and the characteristic radius $r_{i,0}^{\text{grow}} = \langle r^3 \rangle_i / \langle r^2 \rangle_i$ of grain species i are shown.

with progenitor mass $M_{\text{pr}} = 30 M_{\odot}$ and with the ambient gas density $n_{\text{amb}} = 1 \text{ cm}^{-3}$ as a characteristic model. (N07M30n1 model in Chapter 3). The metal abundances and dust properties are shown in Tables 5.3 and 5.4, respectively. In this model, the remarkable features are:

- **O-enhancement**

Pop III stars create metal with the elemental abundance showing oxygen and α -element excesses. Especially, this model predicts large O abundance ($[\text{O}/\text{Fe}] \simeq 1$; see Table 5.3). The efficiency of O I, OH, and H₂O line cooling will be enhanced relative to the present-day model.

- **Small dust-to-metal mass ratio**

As a general feature of the Pop III supernova, the initial dust-to-metal ratio $f_{\text{dep},0}$ is small (4%; Table 5.4) relative to present day ($\sim 50\%$). Still, since most of metal is in the gas-phase, grains will grow during the cloud collapse. We also comment that the rate of H₂ formation reactions on grain surfaces is smaller than in the present-day because dust amount is small.

The amount of metal and dust becomes smaller in the course of expansion of the polluted region, containing their relative abundances. We can set the metallicity, defined as the total mass fraction of all heavy elements relative to the gas, as a dilution efficiency. The recent simulations show that the region polluted by a single supernova will have the metallicities with a wide range (Ritter et al. 2012; Smith et al. 2015). Here, in order to define the critical metallicity (expected to lie at $\sim 10^{-5} Z_{\odot}$; see Chapter 3), we study the range of 10^{-6} – $10^{-3} Z_{\odot}$, where $Z_{\odot} = 0.02$. We call the models with 10^{-6} , 10^{-5} , 10^{-4} , and $10^{-3} Z_{\odot}$ as z6, z5, z4, and z3, respectively. Initially all of C nuclei are assumed to be in the form of C⁺, and all of O and Si nuclei are assumed to be in neutral atoms.

Initially, the number of SPH particles is 455 641 for UNI. In the minihalo models, the number of SPH (dark matter) particles is 464 670 (498 254), 995 908 (1 021 693), and 169 511 (182 388) for MH1, MH2, and MH3 models, respectively. The simulations for MH1 and the others are carried out on Cray XC30² and COMA,³ respectively. We use 256 and 128 cores for MH2 and the other clouds, and the computational time is 18 and 13 days on average, respectively.

²Center for Computational Astrophysics, National Astronomical Observatory of Japan.

³Center for Computational Sciences in University of Tsukuba.

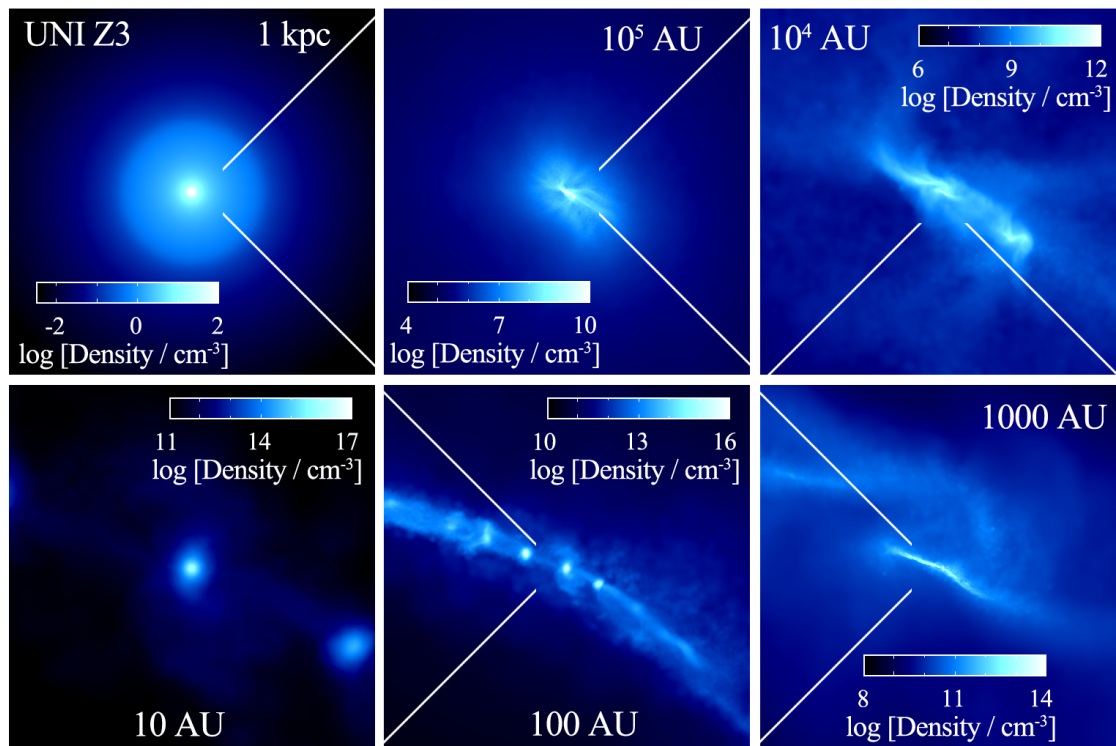


Figure 5.2: Density-weighted density map of the cloud UNI-Z3 from a snapshot output 36.4 yr after the first protostellar core appears. The length scale of the boxes becomes smaller clockwise from the scales of the initial cloud radius (1 kpc) to the protostars (10 AU) as written in each panel.

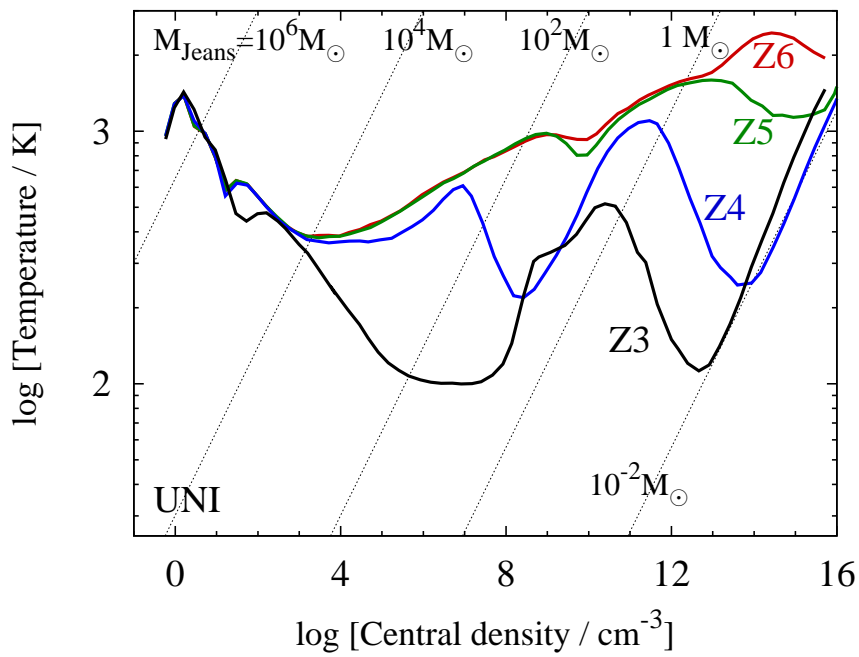


Figure 5.3: Evolution of temperature at the cloud center as a function of the average density for UNI for metallicity cases z3, z4, z5, and z6 from bottom to top.

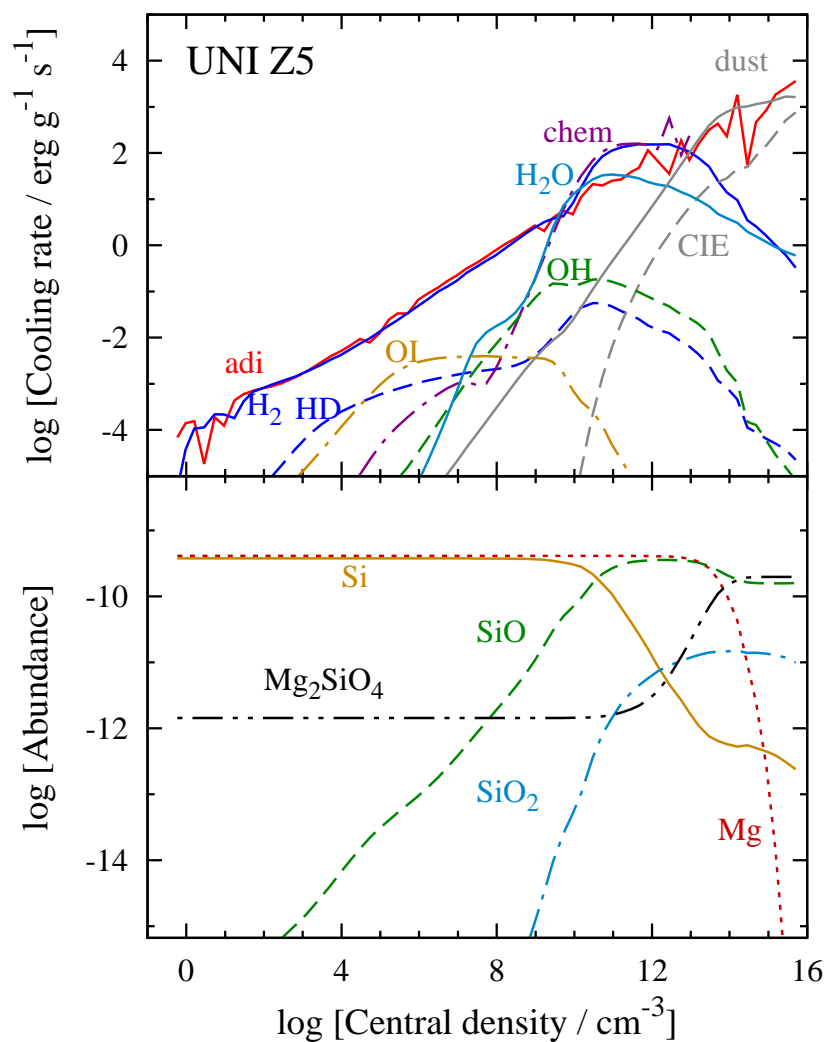


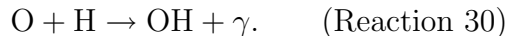
Figure 5.4: *Top*: cooling functions as a function of central density for UNI-Z5. The labels “adi” and “chem” depict adiabatic compressional heating, and heating owing to H₂ molecule formation, respectively. *Bottom*: colored curves show the number abundances of Si- and Mg- bearing gas-phase species relative to hydrogen nuclei. Black dot-dot-dashed curve shows the abundance of Si nuclei locked up into forsterite grains.

5.3 Evolution of uniform clouds

We in this section briefly see the chemical and thermal evolutions of the initially uniform, and spherical cloud UNI. Figure 5.2 shows the density maps of the cloud UNI-z3 plotted from a single snapshot dumped at 36.4 yr after the first protostellar core formation (see below). Thanks to our novel method of the particle splitting, we can follow the entire cloud collapse history from the diffuse gas ($n_{\text{H}} = 0.1 \text{ cm}^{-3}$) to protostellar cores ($\gtrsim 10^{16} \text{ cm}^{-3}$). The mass resolution $M_{\text{min}} = N_{\text{ngb}} m_{\text{par}}$ of the SPH particle is progressively refined from $320 M_{\odot}$ to $3.2 \times 10^{-5} M_{\odot}$ (10 earth mass) after the seven-times splitting. In the initially spherical cloud, the cloud shape in the central region is distorted by the initially given density fluctuations. Strikingly, the cloud fragments in the two-step at length scale 10^4 AU (top-right panel of Figure 5.2) and at 100 AU (bottom-middle). The former is triggered by OH cooling, and the latter is by dust cooling. We revisit to closely see the process of fragmentation below.

Next, we see the thermal and chemical evolutions of the cloud center to identify the important cooling and heating processes. Figure 5.3 shows the evolution of the temperature in the cloud core as a function of the density for UNI-z3, z4, z5, and z6.⁴ The gas cooling/heating rates and the chemical evolutions for the Si-bearing gas-phase and solid species are plotted in Figure 5.4 for UNI-z5. We review the transition of the important thermal processes in the course of time.

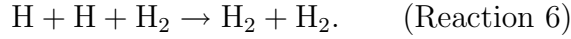
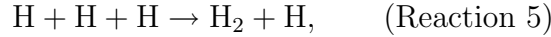
- For all metallicities, adiabatic compressional heating is dominant over gas cooling with $\lesssim 1 \text{ cm}^{-3}$.
- Then, ro-vibrational transition line cooling by H_2 becomes important. The cooling efficiency becomes weak after the level populations of the lines reach the local thermal equilibrium (LTE) at $n_{\text{H}} \sim 10^3 \text{ cm}^{-3}$. After that, the gas temperature slowly increases as in a Pop III star forming clouds with extremely metal-deficient cases z4–6.
- For z3, efficient fine-structure line cooling by O I leads to the temperature to decrease. Then, O atoms are depleted into OH molecules via the neutral-neutral radiative attachment reaction



For z3, by efficient transition line cooling owing to OH molecules at $\sim 10^4\text{--}10^8 \text{ cm}^{-3}$, the gas becomes unstable to fragment two intermediate-mass clumps (top-right panel of Figure 5.2). For z4, OH cooling becomes important at $\sim 10^6\text{--}10^8 \text{ cm}^{-3}$.

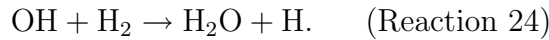
⁴Hereafter, the quantities in the cloud core is estimated as the mass-weighted average over the gas particles with densities $n_{\text{H}} > n_{\text{H,peak}}/3$, where $n_{\text{H,peak}}$ is the density of the densest SPH particle in each snapshot.

- Then, the remarkable gas heating occurs at $\sim 10^8 \text{ cm}^{-3}$ for z3. This is owing to the heating mechanism along with the hydrogen molecular formation via three-body reactions as



At that time, the gas becomes stabilized to form the pressure-supported spherical core because the specific heat ratio exceeds the critical value $4/3$ for the contraction. A hydrostatic core defined by accretion shocks is formed. By the further accretion onto the core, the gas density can continue to increase for z3.

- After $\sim 10^8 \text{ cm}^{-3}$, the temperature keeps slowly increasing. H_2 formation heating is slightly dominant over H_2 and H_2O line cooling. The H_2O molecules are formed by reduction of OH molecules as



For z5, H_2O cooling becomes dominant during the short time at $\sim 10^{10} \text{ cm}^{-3}$. The cyan solid curve in the top panel of Figure 5.4 becomes dominant only for a moment. This creates the slight temperature dip on $n_{\text{H}}-T$ plane.

- Forsterite grains undergo rapid metal accretion until the magnesium atoms in the gas phase are totally depleted as in the present-day (the bottom panel of Figure 5.4) at $n_{\text{H}} \sim 10^{10}$, 10^{12} , and 10^{14} cm^{-3} for z3, z4, and z5, respectively.
- Dust thermal emission is effective at 10^{11} – 10^{13} cm^{-3} for z3 and 10^{12} – 10^{14} cm^{-3} for z4. For z5, the dust cooling marginally processes to form slight temperature dip. In our simulation, we can not see the fragmentation. Whereas, the second fragmentation occurs for z3 case (bottom-middle panel of Figure 5.2). The filamentary structure induced by dust cooling appears, and density fluctuations grow to form several cores along the filament.

When the thermal coupling between gas and dust is reached, dust cooling efficiency becomes smaller. Just after that, the gas becomes optically thick for continuum cooling, and starts to create a hot hydrostatic core surrounded by the accretion shock. This occurs at 1×10^{13} , 3×10^{14} , 3×10^{15} , and $1 \times 10^{16} \text{ cm}^{-3}$ for z3, z4, z5, and z6, respectively. At this time, the core has the irregular shapes, and a disk supported by the rotation is formed just inside the core. At the center of the disk, a spherical region supported by isotropic thermal pressure appears. In this Thesis, we call the spherical region as a “protostar”. During or after the first protostar appears, the gas fragmentation occurs in some cases, and the protostars continue to accrete the ambient gas. Then, we follow the process of the cloud fragmentation and mass accretion onto the cores.

Definition of protostar

Here, we introduce our definition of “protostar”. First, we find the density peak, and the gas particles with $> n_{\text{H,peak}}/10^3$ around the peak is logarithmically divided into 100 density bins. We then measure the ellipticity $\mathcal{E} = a/b - 1$ of each bin, where a and b are the major- and minor-axes, respectively. Fitting the particle distribution in each bin by an ellipsoid with a and b gives us the ellipticity. The surface of the protostar is then defined as the iso-density surface with $\mathcal{E} < \mathcal{E}_*$ and most distant from the peak. Here, \mathcal{E}_* is the threshold ellipticity. We here set $\mathcal{E}_* = 0.3$.⁵

5.4 Cloud fragmentation

5.4.1 Overall features

5.4.1.1 Fragmentation process

We continue the simulations to see whether our clouds fragment or not after the opaque core appears. Without sink technique, we can follow the evolution of the gas over several tens of years from the first protostar formation. Even at the time, the gas fragmentation is already seen in some models. The results of our 16 simulations for four clouds with four metallicity models 10^6 – $10^{-3} Z_{\odot}$ are shown in Figure 5.5. We find these two remarkable points:

1. Even with efficient dust cooling with $\gtrsim 10^{-5} Z_{\odot}$, the clouds do not necessarily fragment for all models contrary to the accepted notion. For instance, fragmentation does not occur even 50 years after the first protostar formation for MH1-Z3 while the multiple clumps are already formed before the first protostar is formed for MH1-Z4. For MH3-Z3, although the central blob does not still satisfy our criterion for a protostar (see above), the fragmentation is unlikely to occur in the diffused filament. Consequently, only one out of four clouds undergoes fragmentation with each metallicity (UNI for Z3, MH1 for Z4, and MH1 also for Z5).
2. Even though dust cooling is not efficient with $10^{-6} Z_{\odot}$, the cloud fragmentation can be seen for MH1-Z6. Still, the fragments appear in the spiral arms on the accretion disk not by dust cooling but by the self-gravity. Such a configuration of fragments is different from that for the other cases with fragmentation (UNI-Z3, MH1-Z4, and MH1-Z5), where the fragments appear along a almost straight filamentary structure created by dust cooling (see Chapter 1).

5.4.1.2 Filament fragmentation vs. disk fragmentation

First of all, let us focus on the four cases where fragmentation occurs (UNI-Z3, MH1-Z4, MH1-Z5, and MH1-Z6). It is an important point that the cloud fragments also with a very small metallicity of $10^{-6} Z_{\odot}$. For MH1-Z6, the perturbations grow in the spiral arms,

⁵The protostellar mass is estimated to be only 20% smaller with a threshold of $\mathcal{E}_* = 0.2$.

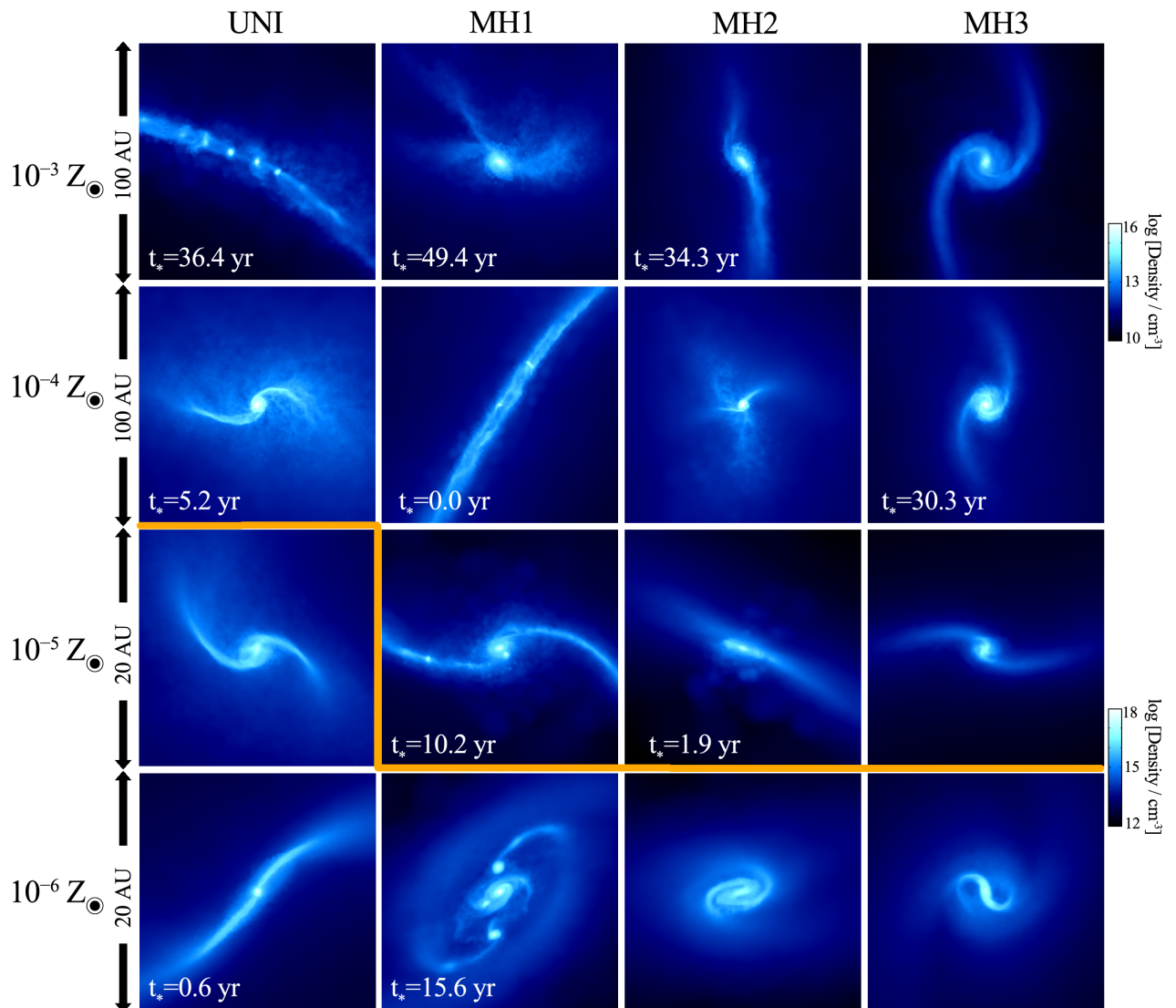


Figure 5.5: Color contour map of the density distribution of the clouds UNI, MH1, MH2, and MH3 from left to right with metallicities 10^{-6} , 10^{-5} , 10^{-4} , and $10^{-3} Z_{\odot}$ from bottom to top. The output time t_* of each snapshot is written in the bottom-left corner of the panel as the elapsed time from the formation of the first protostar in each cloud. Above the orange line, dust cooling is effective (see text).

and occasionally the growth rate is enhanced by the interactions between the arms. This happens in an accretion disk with a small size of ~ 10 AU. Such configuration is seen also in the other simulations of [Clark et al. \(2011\)](#) and [Greif et al. \(2012\)](#) for metal-free clouds. In their and our cases, the fragmentation is not induced by dust cooling. Meanwhile, with the intermediate metallicities 10^{-5} – $10^{-3} Z_{\odot}$, the fragments appear in a thin and dense filament at almost even intervals (UNI-z3, MH1-z4, and MH1-z5). Such a peculiar configuration is due to the instability triggered by dust cooling. The length scale of the filament is ~ 20 – 100 AU, comparable with or larger than the disk in MH1-z6.

We distinguish the two types of fragmentation and call the former as *disk fragmentation* and the latter as *filament fragmentation*. Especially, the disk fragmentation has been discussed analytically ([Toomre 1964](#); [Gammie 2001](#)) and numerically by [Clark et al. \(2011\)](#) and [Greif et al. \(2012\)](#). We here closely discuss the filament fragmentation, which has rarely investigated by numerical studies (see also [Tsuribe and Omukai 2006](#)), in the next section. We then briefly revisit the disk fragmentation in Section 5.4.3.

5.4.2 Filament fragmentation

5.4.2.1 Collapse timescale and thermal evolution

In this Section, we discuss the condition for the filament fragmentation. As seen above, the condition depends not solely on the gas metallicity. In other words, the cloud thermal evolution, which critically affects the fragmentation condition, is not uniquely determined by the gas metallicity. The top panels of Figure 5.6 shows the temperature of the cloud core as a function of the density for our clouds with z4 and z5. One can see that the evolutionary trajectories spreads widely even with a fixed metallicity. The variation would generate the different fragmentation properties for our clouds.

We find that the different thermal evolution among the clouds can be explained by the variation of the collapse timescale t_{col} , i.e. the timescale for the central density to increase due to the contraction as

$$t_{\text{col}} = \frac{\rho}{d\rho/dt}. \quad (5.1)$$

In a slowly collapsing cloud, the adiabatic compressional heating rate per unit volume decreases according to

$$\Gamma_{\text{adi}} = -\rho p \frac{d}{dt} \left(\frac{1}{\rho} \right) = \frac{p}{t_{\text{col}}}. \quad (5.2)$$

Since this is the dominant heating in the most course of collapse, the evolutionary track on the $n_{\text{H}}-T$ plane (Figure 5.6) tends to pass in a lower temperature region.

The time interval over which the peak density increases from $n_{\text{H,peak}} = 10^2 \text{ cm}^{-3}$ to 10^{16} cm^{-3} is measured to be 3, 4, 11, and 19 Myr for UNI, MH1, MH2, and MH3, respectively. It shows that the cloud UNI contracts most rapidly while MH3 most slowly. The resulting evolutionary trajectories in Figure 5.6 roughly reflect the trend as the temperature of UNI keeps highest almost throughout the collapse while the temperature

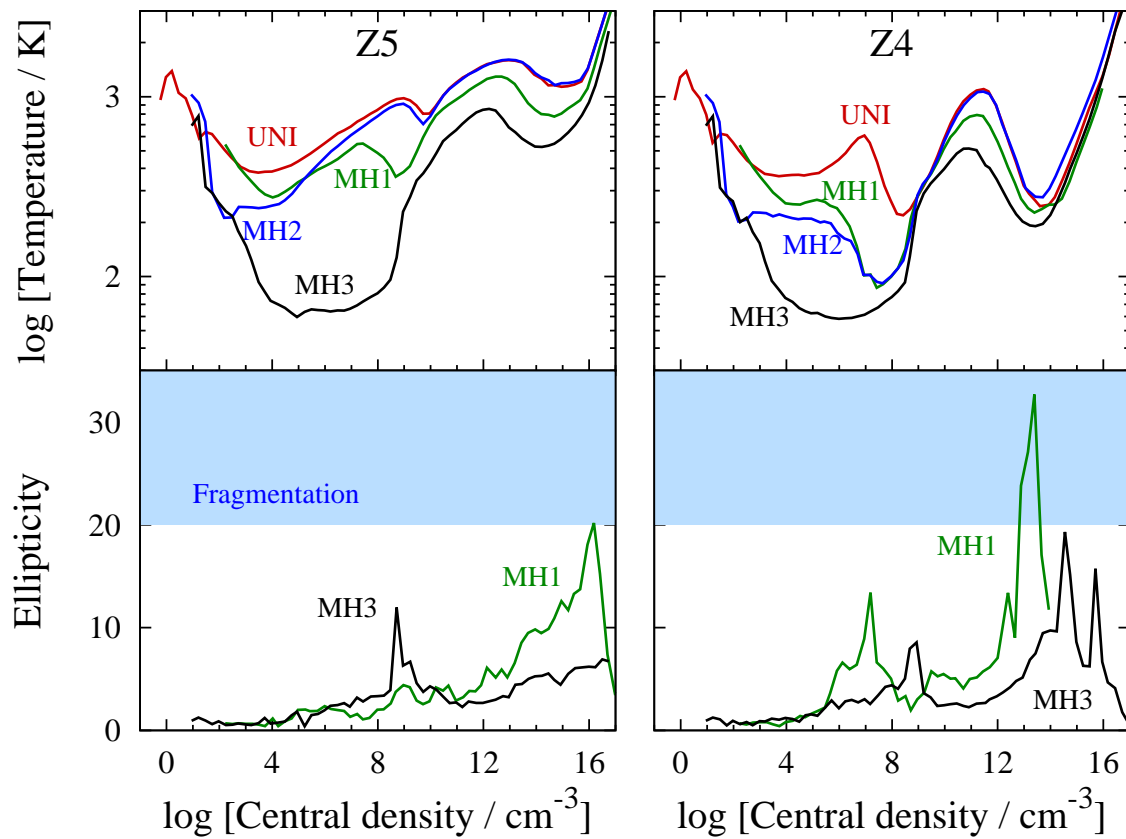


Figure 5.6: Temperature (top) and ellipticity (bottom) of the cloud core as a function of the density of the clouds UNI (red), MH1 (green), MH2 (blue), and MH3 (black) for the two metallicity cases Z5 (left) and Z4 (right). We show the ellipticities only for MH1 and MH3 cases to make them easy to see. In the blue shaded region ($\mathcal{E} > 20$), the gas is sufficiently elongated to fragment.

of MH3 keeps lowest among the four clouds, even reaches the CMB floor (~ 50 K) during $n_{\text{H}} \sim 10^4\text{--}10^8 \text{ cm}^{-3}$. The collapse timescale depends on the halo mass and radius (Table 5.2). We in more detail see the dependence in Section 5.6.

Naively, we expect that the cooler cloud with a large collapse timescale is more likely to fragment. This is, however, not the case. In the cloud MH3, which collapses most slowly, the fragmentation does not occur in all metallicity cases (see the left-most column in Figure 5.5). The overall evolution of the clouds does not necessarily determine the fragmentation properties of the gas.

Figure 5.6 shows that the different cooling/heating processes become dominant at the corresponding density and temperature. For example, MH1-Z5 and MH3-Z5 enter the density regime where dust cooling is efficient ($n_{\text{H}} \sim 10^{12}\text{--}10^{14} \text{ cm}^{-3}$) while UNI-Z5 and MH2-Z5 do not. In addition to dust thermal emission, we identify the other two cooling/heating processes responsible to the cloud fragmentation: H_2 formation heating and OH cooling. We hereafter discuss these three processes one-by-one.

5.4.2.2 Important thermal processes

A. Dust cooling

Dust cooling is the important cooling process to induce the cloud fragmentation into low-mass clumps because it sets in at the high density regime $n_{\text{H}} \sim 10^{12}\text{--}10^{14} \text{ cm}^{-3}$, where the corresponding Jeans mass is small $\sim 0.1 M_{\odot}$. Figures 5.5 and 5.6 clearly show that the dust cooling promote the fragmentation e.g. for MH1-Z4 and MH1-Z5. This occurs only when the gas ellipticity is sufficiently large to form the thin filament as we can see in Figure 5.5. The bottom panel of Figure 5.6 shows the evolution of core ellipticity \mathcal{E} .⁶ We can see that the dust cooling promotes the bar-mode instability, and leads the ellipticity to increase. From our simulations, the filament fragmentation occurs if its ellipticity becomes above 20–30, which is consistent with the results of [Tsuribe and Omukai \(2006\)](#). We call the threshold value of the ellipticity as the “critical ellipticity” \mathcal{E}_* .

For UNI-Z5 and MH2-Z5, the dust cooling efficiency is too small to enhance the cloud ellipticity up to \mathcal{E}_* even though the slight dip is seen in Figure 5.6. The ellipticity increases to only at most 11 and 12 for UNI-Z5 and MH2-Z5, respectively. Figure 5.5 shows the filament which is short and does not host fragments.

We stress that grain growth enhances the dust cooling rate to promote the gas elongation and succeeding fragmentation. As shown in Figure 5.4, especially forsterite grains grow until the gas-phase magnesium atoms are consumed at $n_{\text{H}} \sim 10^{14} \text{ cm}^{-3}$ in our Pop III dust model ($M_{\text{pr}} = 30 M_{\odot}$, $n_{\text{amb}} = 1 \text{ cm}^{-3}$). In Figure 5.7 (a), we compare the results of the simulations with (top) and without (bottom) grain growth for MH1-Z5 case at the same epoch $t_* = 4.6$ yr after the first protostar formation. The several protostellar cores

⁶Fitting the distribution of the SPH particles with $n_{\text{H}} > n_{\text{H,peak}}/3$ by an ellipsoid with major- and minor-axes a and b , we obtain the core ellipticity $\mathcal{E} = a/b - 1$.

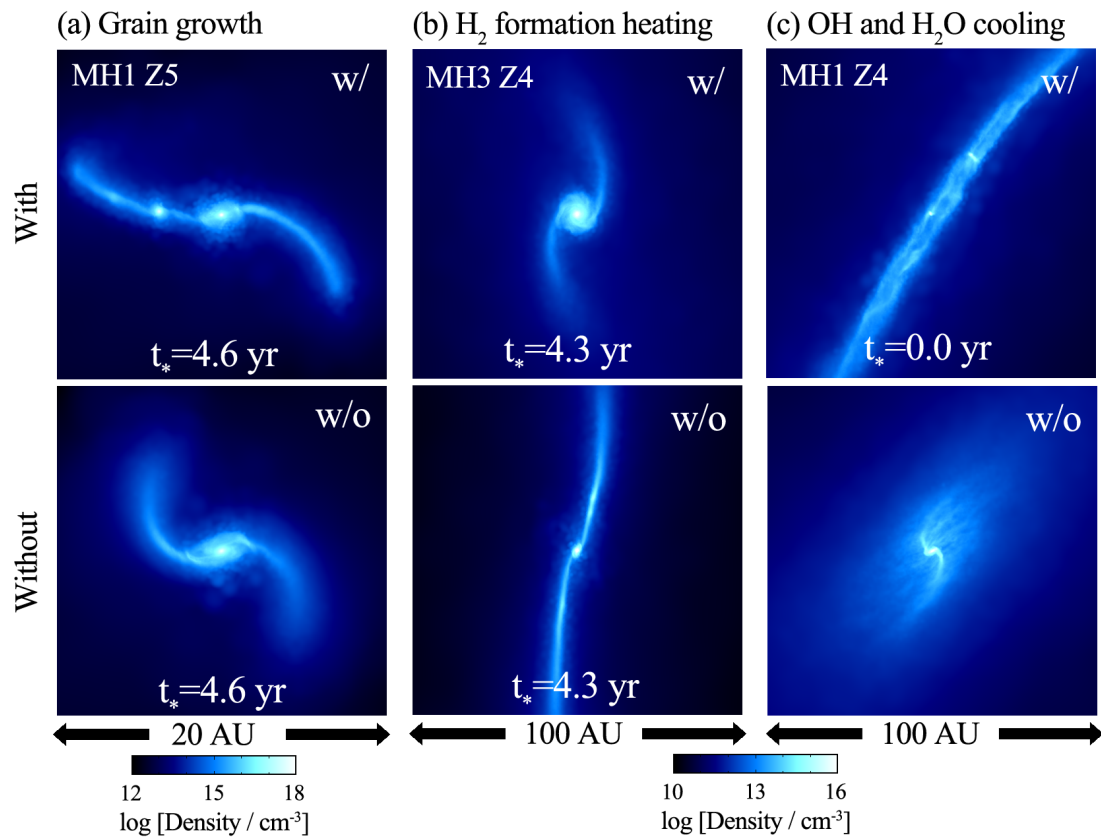


Figure 5.7: We compare the cloud fragmentation in the fiducial simulations (top) and the test case (bottom) at the same epoch t_* after the first protostar formation. All the relevant chemo-thermal processes are included in the former, while, in the latter simulations, (a) grain growth, (b) H_2 formation heating, and (c) OH and H_2O cooling are not included.

are formed in a filament in the case with grain growth, the fragmentation does not occur in the less diffused and short filament if we do not include grain growth.

B. H_2 formation heating

In most of the cases, the fragmentation does not occur even though dust cooling is efficient. We find that chemical heating owing to the exothermic H_2 formation prevents the fragmentation. For example, in MH3-z5, gas heating owing to H_2 formation via three-body reactions makes the temperature rapidly rise from 130 K at $5 \times 10^8 \text{ cm}^{-3}$ to 700 K at $2 \times 10^{11} \text{ cm}^{-3}$, corresponding to the specific heat ratio 1.7, which is sufficient to stabilize the gas and make it rounder. Accordingly, the core ellipticity rapidly decreases from 12 to 2 (the bottom of Figure 5.6).

For such a small ellipticity, even though dust cooling enhances the cloud elongation at the higher densities 10^{12} – 10^{14} cm^{-3} , the ellipticity does not increase up to the critical value. In that case, the timescale for which dust cooling raises the ellipticity from a small value to the critical ellipticity becomes to exceed the dynamical timescale of the cloud. In the clouds UNI, MH1, and MH2 with metallicities 10^{-4} – $10^{-3} Z_\odot$ and in MH3 with 10^{-6} – $10^{-3} Z_\odot$, H_2 formation heating suppresses the gas ellipticity.

Tsuribe and Omukai (2008) show that the metallicity range where a cloud elongation is prevented by H_2 formation heating and the succeeding fragmentation is halted is 10^{-5} – $10^{-4} Z_\odot$. Our model predicts the metallicity range by an order of magnitude larger than in their simulations. This is because the authors employ the present-day dust model, where the rate of H_2 formation on grain surfaces is 30 times larger than in our Pop III supernova dust model. In the present-day dust model, with metallicity $10^{-3} Z_\odot$, hydrogen atoms are exhausted into the molecular form by the efficient molecular formation on grains before three-body reactions rapidly process to heat the gas. Meanwhile, in our simulations, the molecular formation via three-body reactions are enhanced by the abundant hydrogen atoms remaining by the poor efficiency of the grain surface reactions even with $\sim 10^{-3} Z_\odot$. Therefore, the associated gas heating makes the cloud rounder with 10^{-4} – $10^{-3} Z_\odot$.

We again perform a controlled simulation without the H_2 formation heating in order to clarify the effect of the heating mechanism on the cloud fragmentation properties. Figure 5.7 (b) shows the density map in the central 100 AU region of the cloud MH3-z4 with (top) and without (bottom) H_2 formation heating. In the former case, the core ellipticity \mathcal{E} is reduced down to around 3 because of the effective H_2 formation heating at $\sim 10^9 \text{ cm}^{-3}$. In the latter case, OH cooling, instead of H_2 formation heating, enhances the gas ellipticity up to 15 at $\sim 10^9 \text{ cm}^{-3}$, and then \mathcal{E} further increases to ~ 30 by dust cooling. The formed filament fragments into several protostellar cores as in Figure 5.7 (b).

C. OH/ H_2O cooling

For MH1-z4, although H_2 formation heating is effective, the cloud is elongated to form

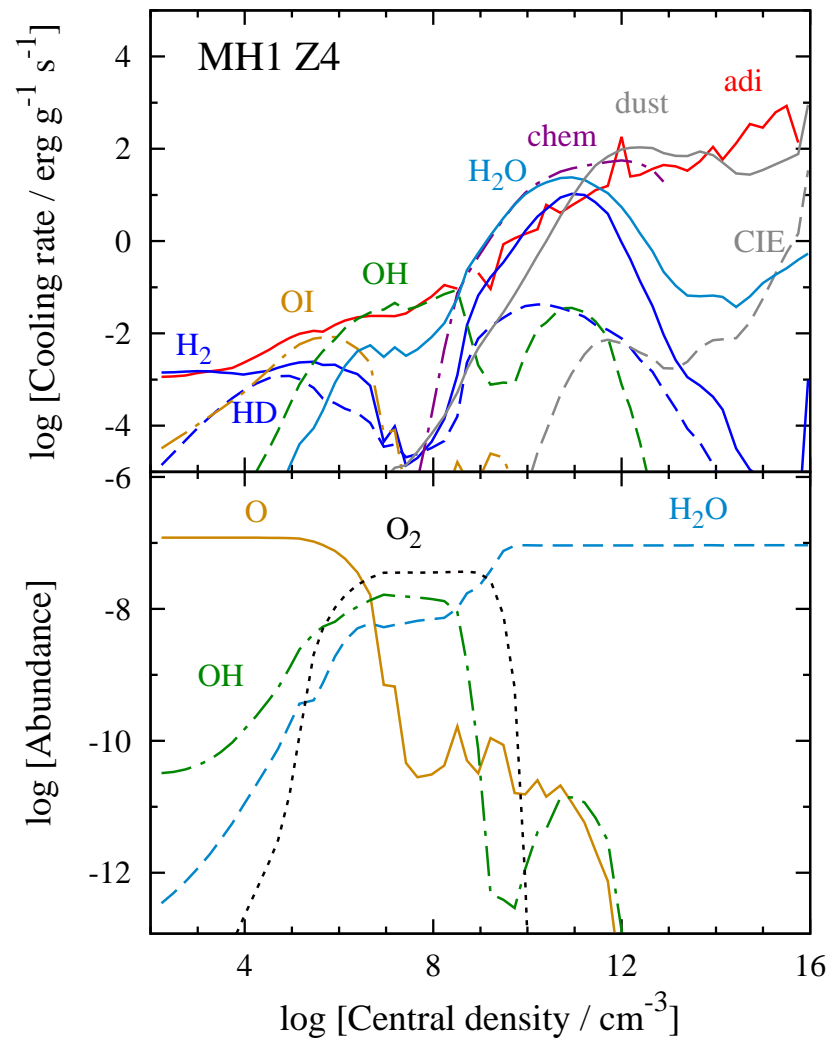


Figure 5.8: Cooling/heating rates (top) and the abundances of the O-bearing species (bottom) as a function of the central density for MH1-Z4.

a thin filament, which fragments into a few clumps. In this case, OH and H₂O cooling is found to be important. Figure 5.8 shows the temporal evolution of the heating and cooling rates as a function of density for the cloud. At $n_{\text{H}} = 10^6\text{--}10^8 \text{ cm}^{-3}$, a large fraction of OH molecules are formed, and its cooling efficiency even exceeds the adiabatic compressional heating rate (red solid). The thin filament created by OH cooling confines the adiabatic core due to rapid H₂ formation heating, and the timescale for the stabilization becomes longer than the dynamical timescale. At $n_{\text{H}} \sim 10^{11} \text{ cm}^{-3}$, where the chemical heating ceases, the ellipticity \mathcal{E} is largest for MH1 among the four clouds for z4 thanks to efficient OH cooling. In that case, the succeeding dust cooling can enhance \mathcal{E} up to the critical value within the cloud dynamical time. The ellipticity eventually increases up to 33, and then, the fragmentation occurs (see Figure 5.6). Although OH cooling is indeed effective for MH2-z4 at $10^6\text{--}10^8 \text{ cm}^{-3}$, it is marginal to compensate the stabilization by H₂ formation.

The test simulation where the effects of OH and H₂O cooling is neglected for MH1-z4. (Figure 5.7 (c)) reveals that the core ellipticity is significantly reduced by the chemical heating. Eventually, a single protostar is formed without fragmentation. We can see that the efficient OH and H₂O cooling drives the formation of a long filament, which is the seed of the bar-mode perturbation with a large initial amplitude.

We for the first time demonstrate that OH/H₂O cooling plays a crucial role to determine whether the cloud fragments or not, by employing the Pop III supernova model with the excess of α -element oxygen. During the collapse, the abundant oxygen yields the O-bearing molecules, which can significantly contribute to gas cooling in some cases. We here investigate this only for a model ($M_{\text{pr}} = 30 M_{\odot}$, $n_{\text{amb}} = 1 \text{ cm}^{-3}$), but the oxygen excess is general trend for the Pop III supernovae (see Figure 3.1). The metal-poor stars with $[\text{Fe}/\text{H}] \lesssim -3.0$ also show the feature of the oxygen-excess (Cayrel et al. 2004; Suda et al. 2008). Although we see the rapid OH cooling in one (MH1) out of four clouds with z4, the element might be a key to form the first low-mass stars even for a small number of clouds undergo the rapid OH cooling.

Criteria for filament fragmentation

We summarize the criteria for filament fragmentation of low-metallicity clouds as

- (i) dust cooling is efficient to induce the cloud elongation with the ellipticity up to $\mathcal{E}_* = 20$ for clouds to fragment into low-mass clumps, and
 - (ii-a) H₂ formation heating is not effective to dump the bar-mode perturbation as a precursor of the further cloud elongation by dust cooling, or
 - (ii-b) OH cooling is efficient to enhance the cloud elongation even though H₂ formation heating is effective.

The overall thermal evolution of the cloud is related to its collapse time, and the different trajectories pass the density-temperature regimes where different thermal processes including the above three become dominant.

5.4.2.3 Simplified model for cloud thermal evolution

In this Section, we employ a simplified model to in more detail see the relationship between the thermal evolution of the cloud with different collapse time and the conditions for the filament fragmentation. To this aim, we perform the one-zone semi-analytic collapse model used in Chapter 3. First, we introduce a parameter which characterizes the cloud collapse timescale t_{col} . We then discuss the results of the one-zone calculations, and present the region of (t_{col}, Z) favored to the filament fragmentation in the realm of the simplified model.

Indicator of collapse time

It is difficult to use t_{col} itself as a model parameter because it varies during the collapse even for a given cloud: cooling/heating processes quicken/slower the collapse. We therefore introduce a parameter f_0 as an indicator of the collapse timescale characterizing an individual cloud. The parameter is defined as the excess of the collapse time to the self-similar solution for the polytropic gas cloud with the specific heat ratio γ :

$$f_0 = \frac{t_{\text{col}}}{t_{\text{col}}^{\text{s}}(\gamma)}, \quad (5.3)$$

where $t_{\text{col}}^{\text{s}}(\gamma)$ is a part of t_{col} which depends on γ , the indicator of the gas cooling/heating, as

$$t_{\text{col}}^{\text{s}}(\gamma) = \frac{1}{\sqrt{1 - f_{\nabla p}(\gamma)}} t_{\text{col}}^0, \quad (5.4)$$

where the factor $1/\sqrt{1 - f_{\nabla p}}$ represents the ratio of the collapse time against that for the pressure-less homogeneous collapse (so-called dust collapse) t_{col}^0 , written by the ratio $f_{\nabla p}$ between the pressure gradient and gravitational force (Larson 1969). The self-similar solutions for the isothermal gas (so-called Larson-Penston solution) is reported by Penston (1969) and Larson (1969). Yahil (1983) and Lai (2000) give the solution in the case with more general polytropic index ($\gamma > 1$). We here use the fitting formula presented by Omukai et al. (2005) as

$$f_{\nabla p}(\gamma) = \begin{cases} 0 & (\gamma < 0.83) \\ 0.6 + 2.5(\gamma - 1) - 6.0(\gamma - 1)^2 & (0.83 < \gamma < 1) \\ 1.0 + 0.2(\gamma - 4/3) - 2.9(\gamma - 4/3)^2 & (\gamma > 1) \end{cases} \quad (5.5)$$

(same as Equation 1.20). The collapse time for the dust collapse t_{col}^0 is $(2/3\pi)t_{\text{ff}} = 0.212t_{\text{ff}}$ asymptotically (Penston 1969), where $t_{\text{ff}} = (3\pi/32G\rho_{\text{cen}})^{1/2}$ is the free-fall time and ρ_{cen} is the central mass density.⁷ In the isothermal case ($\gamma = 1$), the collapse time $t_{\text{col}}^{\text{s}} = 0.34 t_{\text{ff}}$ agrees with the Larson-Penston type solution. The time $t_{\text{col}}^{\text{s}}(\gamma)$ increases with the increasing γ , and diverges as $\gamma \rightarrow 4/3$.

⁷In the one-zone calculations of Omukai et al. (2005), they set the collapse timescale as $t_{\text{col}}^{\text{s}} = (1/\sqrt{1 - f_{\nabla p}})t_{\text{ff}}$, which corresponds to $f_0 = 4.7$.

One-zone semi-analytic collapse model

We modify our one-zone code to solve the evolution of clouds with various f_0 . There, the density is imposed to increase as

$$\frac{d\rho}{dt} = \frac{\rho}{t_{\text{col}}} = \frac{\rho}{f_0 t_{\text{col}}^s(\gamma)}. \quad (5.6)$$

For $\gamma \gtrsim 4/3$, the collapse time t_{col} diverges, which means our assumption of the self-similar collapse fails. In the real simulations, the collapse continues by the accretion of the gas. To resemble this, we set the upper limit of $t_{\text{col}}^s(\gamma) = 5 t_{\text{ff}}$. In the early stage of the collapse ($n_{\text{H}} < 100 \text{ cm}^{-3}$), we assume that the gas infall as free-fall collapse ($t_{\text{col}}^s(\gamma) = t_{\text{col}}^0$). For a given density, temperature, and chemical compositions, the code solves exactly the same chemical reactions, grain growth rates, and heating/cooling rates as in our three-dimensional simulations. By integrating the cooling and heating functions, we obtain the temperature at an arbitrary time. Here, the CMB temperature is set 50 K, which creates the temperature floor. In the ideal case where the cloud evolves spherically and self-similarly, the parameter f_0 is constant. We in this model impose a constant f_0 . The calculations are performed with a range of $f_0 = 1-10$ every 0.05 dex and $Z = 10^{-6}-10^{-3} Z_{\odot}$ every 0.1 dex to cover the parameter range of the clouds in our simulations.

We show the resulting evolutionary tracks in Figure 5.9 for $f_0 = 1-10$. These trajectories show the qualitatively similar trend to the results of the simulations. We can see that the temperature is small for a slowly collapsing cloud (large f_0). As in the simulations, the trajectories enter the regimes where the different thermal processes is dominant:

- The dust thermal emission induce sufficient gas cooling (criterion (i)) only at larger f_0 for z5 as the simulations predict. Since the adiabatic gas heating becomes smaller with increasing f_0 , the dust amount required to compensate this becomes smaller. The one-zone model predicts $f_0 > 3.5$ (0.55 dex) for z5. Here, we decide that the dust cooling becomes important when the minimal value of γ becomes below a threshold value $\gamma_{\text{th}} = 0.8$. The value is determined by our simulations: the minimum γ at $n_{\text{H}} = 10^{12}-10^{14} \text{ cm}^{-3}$ is 0.84 and 0.85 for respectively UNI-z5 and MH2-z5 without fragmentation while 0.78 for MH1-z5 with fragmentation.
- Further, H_2 formation heating becomes important for all clouds with $f_0 > 1$ if the metallicity is $10^{-4}-10^{-3} Z_{\odot}$, and for clouds with $f_0 > 3.2$ (0.50 dex) if the metallicity is $10^{-5} Z_{\odot}$. The threshold γ_{th} for (ii-b) is here defined to be 1.1. Although the γ reaches 1.3 in our simulation for MH1-z5, the accuracy of the one-zone model is limited to sufficiently small γ .
- Transition line cooling owing to OH molecules becomes important in a range of f_0 with z4 as indicated by the simulation. Our one-zone model predicts that the range of the f_0 is 2.5 (0.40 dex)–4.5 (0.65 dex). For the cloud MH1-z4, γ reaches below 0.5 by the OH cooling. However, even for $\gamma_{\text{th}} = 0.6$, the region of f_0 favorable to

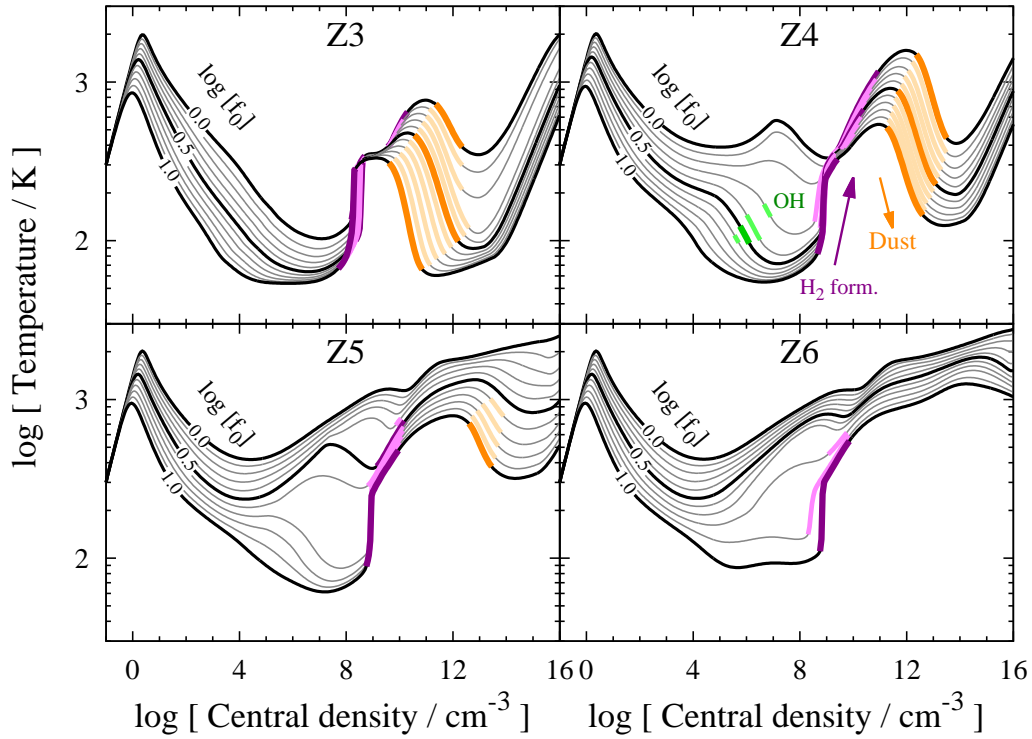


Figure 5.9: Temporal evolution of the temperature as a function of the density in a cloud core obtained by our one-zone calculations for metallicities z3, z4, z5, and z6. We show the results for the collapse timescales f_0 from 1 to 10 every 0.1 dex (black curves) and for the metallicity $10^{-4} Z_{\odot}$. We also over-plot thick segments in the regimes where $\gamma < 0.8$ by dust emission (orange) where $\gamma > 1.1$ by H₂ formation heating (purple), and where $\gamma < 0.7$ by OH and H₂O cooling (green).

Table 5.5: Collapse timescale f_0 .

Z	UNI	MH1	MH2	MH3
z3	1.1 ± 0.4	1.7 ± 0.6	2.4 ± 2.0	3.6 ± 2.1
z4	1.1 ± 0.4	2.2 ± 0.9	2.4 ± 1.6	5.4 ± 3.4
z5	1.0 ± 0.3	2.1 ± 0.6	2.0 ± 1.8	6.2 ± 3.2
z6	1.0 ± 0.2	2.0 ± 0.5	2.1 ± 1.8	6.4 ± 3.4

Note — To compute f_0 , we estimate the collapse time and the specific heat ratio as $t_{\text{col}} = \rho/(\Delta\rho/\Delta t)$ and $\gamma = (\Delta T/T)/(\Delta\rho/\rho) + 1$, respectively from every snapshot, where Δx is the interval of x between a snapshot and its previous one. We output the data every 0.25 dex $n_{\text{H,peak}}$. We show the arithmetic mean and the standard deviation of f_0 measured at each output time with $n_{\text{H,peak}} < 10^8 \text{ cm}^{-3}$.

OH cooling does not appear in the one-zone case. We then ease the criterion and search the region with $\gamma_{\text{th}} = 0.65$ and 0.7.

Figure 5.10 shows the results obtained by the one-zone calculations for all f_0 and Z . Above the orange line, dust cooling is efficient to reduce γ below 0.8. H_2 formation heating is dominant and γ becomes above 1.1 in the upper region than the purple line. OH cooling is efficient within the region surrounded by the green lines. We here draw critical lines for $\gamma_{\text{th}} = 0.65$ (around the darker green region) and 0.7 (around the lighter green region). Since the former is the severer criterion, the region favorable to $\gamma_{\text{th}} = 0.65$ is smaller than the latter. We linearly interpolate the results of one-zone calculations to draw these boundaries. The parameter regions for the fragmentation obtained by the one-zone calculations are indicated by the orange- and green-shaded regions. They are determined as follows:

- (i) Above the orange line, dust cooling is efficient to promote the eventual cloud elongation and fragmentation. The line corresponds to the one in Figure 5.5.
- (ii-a) Below the purple line, the cloud avoids the significant stabilization by H_2 formation heating. This ruled out the most of the region where the criterion (i) is favored. Therefore, the orange region remains to satisfy the fragmentation criteria.
- (ii-b) Within the green line, OH cooling is efficient to enhance the cloud elongation. Even though the H_2 formation heating is efficient, this effect leads the cloud to fragment by the succeeding dust cooling.

Comparison between the results of one-zone model and simulations

We estimate the value f_0 from the results of our simulation. Table 5.5 shows the average and standard deviation of f_0 measured from our simulations during the early

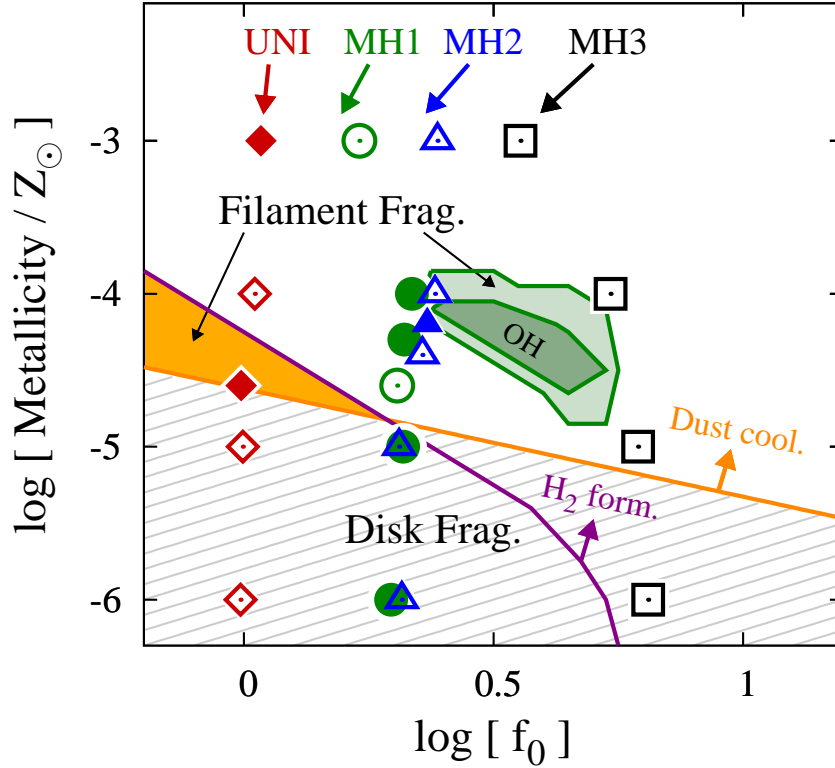


Figure 5.10: Regions favorable for the filament fragmentation (orange- and green- shaded regions) and the disk fragmentation (grey-hatched area) obtained by the one-zone semi-analytic calculations for clouds with the collapse timescale f_0 and metallicity Z . Above the orange (“Dust cool.”) line, dust cooling is efficient to reduce the adiabatic heat ratio γ below 0.8, and, above purple (“H₂ form.”) line, chemical heating are efficient to enhance γ above 1.1. In the light and dark green-colored region, OH cooling is efficient (“OH”) to reduce γ below 0.7 and 0.65, respectively. We draw these lines by linearly interpolating the results of the one-zone calculations. We also plot at the values (f_0, Z) of the simulation clouds UNI (red diamonds), MH1 (green circles), MH2 (blue triangles), and MH3 (black squares). Close and open symbols are plotted for the simulations with and without fragmentation, respectively.

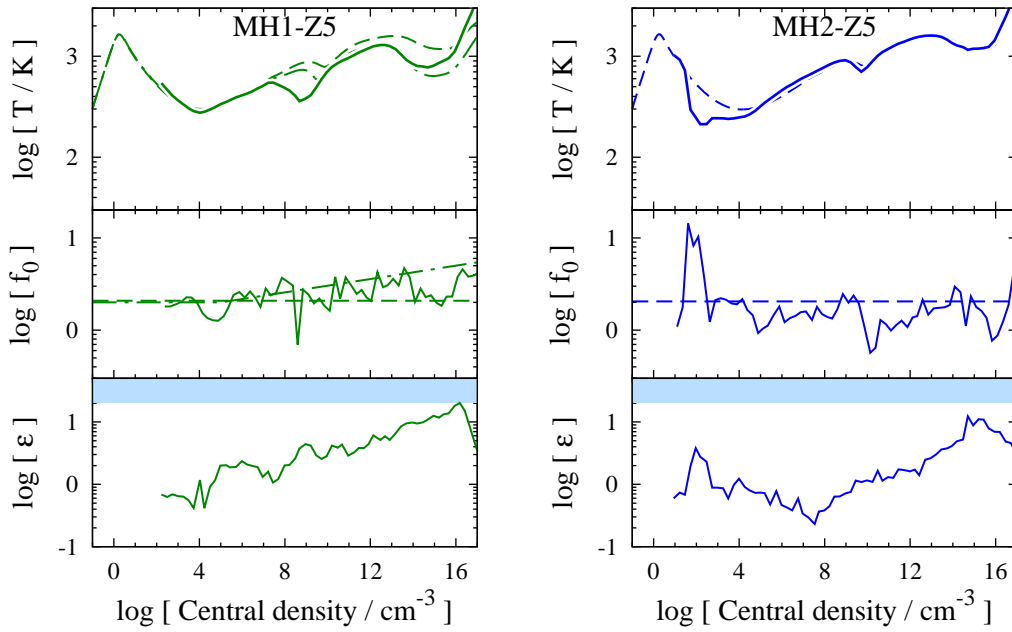


Figure 5.11: Temporal evolution of temperature T (top), the collapse time f_0 (middle), and cloud ellipticity \mathcal{E} (bottom) as a function of the central density for MH1-z5 (left) and MH2-z5 (right). The blue-shaded region is the ellipticity with which a formed filament fragments ($\mathcal{E} > 20$). The solid and dashed curves represent the results of the simulation and one-zone calculation with constant $f_0 = 2.1$ and 2.0 for MH1-z5 and MH2-z5, respectively. For MH1-z5, dot-dashed curve represents the result of one-zone calculation with modified evolution of f_0 as shown by the dot-dashed curve in the middle panel.

stage of collapse ($n_{\text{H,peak}} < 10^8 \text{ cm}^{-3}$). Even with the deviation, the average value of f_0 increases roughly from UNI to MH3.

In Figure 5.10, we over-plot the (f_0, Z) of the simulated clouds (see Table 5.5 for the values and errors of f_0). The filled (open) symbols are plotted for the clouds with (without) fragmentation. We explicitly perform the additional simulations for the other metallicities and plot the symbols for them. For UNI-Z3, the discrepancy may be due to the limitation of our one-zone model to reproduce the non-linear evolution of the hydrostatic core created by H_2 formation heating, where t_{col} reaches the significantly large value. For MH1-z6, the criterion should not be applied in the disk fragmentation regime, which is not triggered by the thermal processes during the cloud collapse.

With metallicities 10^{-5} – $10^{-4} Z_{\odot}$, the simulation results are *qualitatively* followed by the one-zone calculations: In the region of $f_0 \lesssim 2$ and $Z = 10^{-5}$ – $10^{-4.5} Z_{\odot}$, the fragmentation is favored by efficient dust cooling but inefficient chemical heating. This can be seen in the simulations for UNI with $Z = 10^{-4.6} Z_{\odot}$. Also, the isolated region for OH cooling on (f_0, Z) plane is predicted as the simulation results.

The parameter region of (f_0, Z) is quantitatively different between the two approaches. Hereafter, we discuss in more detail the discrepancy appearing for the individual models.

- MH1-z5

For this model, the average value of f_0 is 2.1 at $n_{\text{H}} < 10^8 \text{ cm}^{-3}$. In that case, the one-zone model predicts that the cloud does not enter the fragmentation regime. Figure 5.11 shows that f_0 deviates from the average value, roughly monotonically increases as the central density increases. This is considered to be because the cloud ellipticity increases, and the cloud departs from the self-similar solution based on which the one-zone model is established. For an elongated cloud, since gravitational force in the radial direction is suppressed relative to the spherical cloud (Tsuribe and Inutsuka 1999b), the collapse speed becomes slower. At density $n_{\text{H}} = 2 \times 10^{16} \text{ cm}^{-3}$, \mathcal{E} increases up to 18 and f_0 reaches 4.5. We impose the modified evolution of f_0 so that $f_0 = 2.0$ for $n_{\text{H}} < 10^5 \text{ cm}^{-3}$ and f_0 increases up to 5 at $n_{\text{H}} = 10^{16} \text{ cm}^{-3}$ linearly in the logarithmic manner (dot-dashed line). The result of one-zone calculation recovers the evolution of the three-dimensional simulation although the discrepancy remains at $n_{\text{H}} = 10^9 \text{ cm}^{-3}$ and 10^{14} – 10^{16} cm^{-3} . If f_0 continues to be 2, as MH2-z5, the dust cooling is inefficient to induce fragmentation. Besides, if f_0 is 5 from the initial state, the effect of H_2 formation heating becomes important. In the earlier stage of collapse ($n_{\text{H}} < 10^8$), the cloud can avoid to enter the regime ($f_0 > 3.2$) where H_2 formation heating is effective. Then, the cloud undergoes the regime ($f_0 > 3.5$) where the dust cooling is efficient at $n_{\text{H}} \sim 10^{13}$ – 10^{14} cm^{-3} .

- MH1-z4 and MH2-z4

The results of the one-zone model do not agree with the simulation for the clouds MH1-z4 and MH2-z4. Figure 5.12 shows that the overall temperature evolution with

the constant f_0 is consistent with the simulations. Still, the temperature is lower than predicted with the one-zone model at $n_{\text{H}} \sim 100 \text{ cm}^{-3}$ for MH2-Z4. The trend lasts until $n_{\text{H}} \sim 10^6 \text{ cm}^{-3}$, and OH cooling is less effective than for MH1-Z4 because the temperature is still low. At the time, the central density of the gas cloud exceeds that of the hosting dark matter halo. The left panel of Figure 5.13 shows the radial profile of the density of the gas and dark matter components. It is expected that the excess of the density due to the halo makes the gravitational potential shallower after the central gas density becomes over the dark matter density, and the gas infall rate becomes slower.

We measure the gravitational potential at the radius r_{cloud} within which the gas is unstable to collapse. Such the radius can be estimated as the one where the ratio of the enclosed mass $M(r)$ to the Bonnor-Ebert mass M_{BE} becomes maximum (Abel et al. 2002; Hirano et al. 2014). There, M_{BE} is the characteristic mass scale of the self-gravitating cloud as

$$M_{\text{BE}} = \frac{1.18c_{\text{T}}^4}{G^{3/2}P(r)}, \quad (5.7)$$

where c_{T} is the sound speed and $P(r)$ is the pressure at a radius r (Ebert 1955; Bonnor 1956). The right panel of Figure 5.13 shows $M(r)/M_{\text{BE}}$, and the dots are plotted at the peak. The right panel of Figure 5.14 shows the time evolution of the gravitational potential $\Phi = GM(r)/r$ at the radius r_{cloud} . Since the gravitational potential near the cloud center is negligible, the smaller Φ indicates the shallower potential. Figure 5.14 shows that, at $n_{\text{H}} = 100 \text{ cm}^{-3}$, the potential becomes smaller.

For MH1-Z4, the gas exceeds the dark matter density at $n_{\text{H}} \sim 10^4 \text{ cm}^{-3}$. The similar trend that the temperature slightly increases after the density can be seen. This effect is smaller than MH2-Z4 as shown in the left panel of Figure 5.14 because of the smaller mass of the dark matter halo (Table 5.2). The trajectory enters the regime where OH cooling is effective at higher temperature than MH2-Z4, and the efficiency of the cooling becomes larger.

We have so far seen that the deviation of cloud evolution in the simulations from that in the one-zone calculation with a constant f_0 is important to determine the fragmentation properties. The deviation can be explained by the departure of the cloud shape from the self-similar solution such as the cloud elongation and the additional gravitational potential created by dark matter halo. And especially, whether OH cooling becomes important or not is very sensitive to the deviation as Figure 5.9 indicate that the iso- f_0 curves are separated widely in the regime of OH cooling at $n_{\text{H}} \sim 10^6 \text{ cm}^{-3}$ for 10^{-5} and $10^{-4} Z_{\odot}$.

Analytic formulae of boundaries

Although it is difficult to describe the thermal evolution of the cloud by a simple constant f_0 model, it is important to know the relationship between f_0 and Z where the relevant thermal processes (dust cooling, chemical heating, OH/H₂O cooling) become

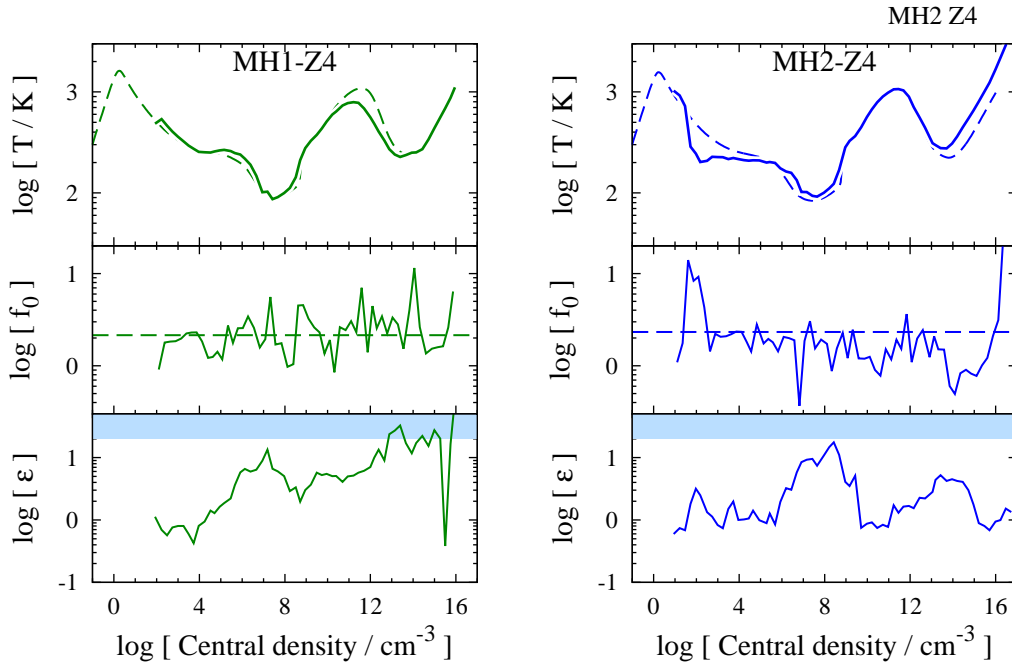


Figure 5.12: Same as Figure 5.11 but for MH1-z4 (left) and MH2-z4 (right). The dashed curves represent the one-zone model with constant $f_0 = 2.2$ (MH1-z4) and 2.4 (MH2-z4).

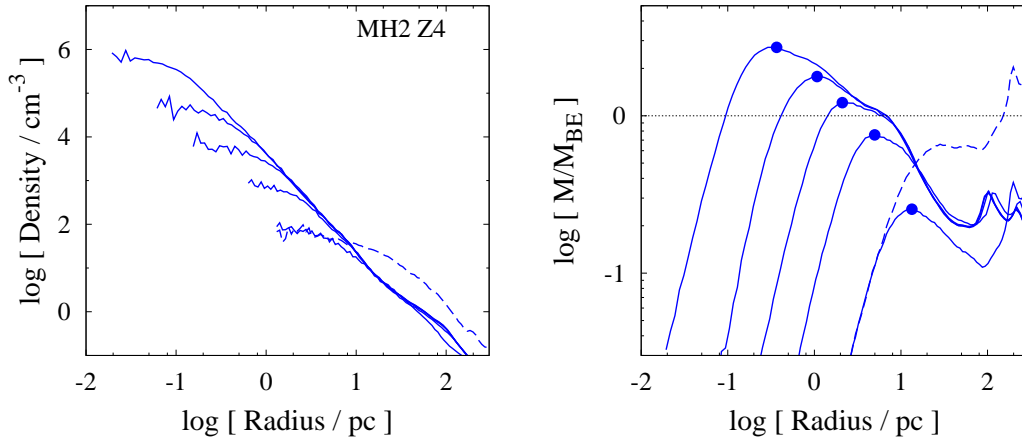


Figure 5.13: Profile of density (left) and the ratio of the enclosed mass $M(r)$ to the Bonnor-Ebert mass M_{BE} (right) as a function of radius r for MH2-z4. We plot the profiles of gas (solid) at the time when $n_{\text{H,peak}} = 10^2, 10^3, 10^4, 10^5$ and 10^6 cm^{-3} from right to left, and the dark matter (dashed) at $n_{\text{H,peak}} = 10^2 \text{ cm}^{-3}$ respectively. The density of dark matter halo is converted to the corresponding hydrogen number density. The dots represent the position where $M(r)/M_{\text{BE}}$ reaches the maximum value.

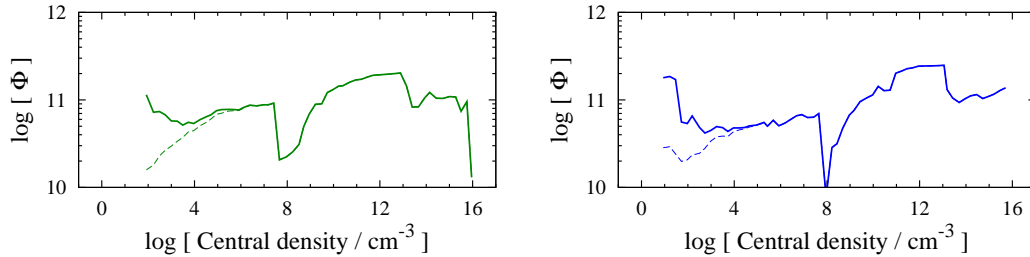


Figure 5.14: Temporal evolution of the gravitational potential $\Phi = GM(r)/r$ in units of erg g^{-1} at the radius where $M(r)/M_{\text{BE}}$ reaches the maximum value for MH1-Z4 (left) and MH2-Z4 (right). The dashed curve represents the contribution of baryon only, and the solid represents the total of baryon and dark matter.

important. The boundaries shown in Figure 5.10 can be described by analytic formulae. In this part, we define the conditions where the three thermal processes become effective at the corresponding density.

A. Dust cooling

The critical condition where dust cooling becomes dominant (Orange line in Figure 5.10) is determined by the balance between the adiabatic compressional heating rate and the cooling rate by dust. From Equation (5.2), the compressional heating per unit volume is

$$\Gamma_{\text{adi}} = 5.0 \times 10^{-7} f_0^{-1} \text{ erg cm}^{-3} \text{ s}^{-1}$$

at $n_{\text{H}} = 10^{14} \text{ cm}^{-3}$ and $T = 1000 \text{ K}$ with $t_{\text{col}}^s(0.8) = 0.21t_{\text{ff}}$. In our Pop III dust model, the dust cooling rate is

$$\Lambda_{\text{d}} = 1.8 \times 10^{-7} \left(\frac{Z}{10^{-5} Z_{\odot}} \right) \text{ erg cm}^{-3} \text{ s}^{-1}$$

when the all of magnesium nuclei are locked up into forsterite grains. Equating these formulae yields the relationship between f_0 and Z as

$$Z > 2.8 \times 10^{-5} f_0^{-1} Z_{\odot}. \quad (5.8)$$

The equation is well consistent with the orange line in Figure 5.10. This formula indicates that, with slower collapse (larger f_0), the gas compressional heating is less efficient, and thus only a small amount of dust is required to overcome the gas heating.

B. H_2 formation heating

The condition for the efficient H_2 formation heating is that the equilibrium temperature T_{eq} at $n_{\text{H}} < 10^8 \text{ cm}^{-3}$ is smaller than one at $> 10^8 \text{ cm}^{-3}$. At $n_{\text{H}} = 10^{11} \text{ cm}^{-3}$, the

temperature is largely determined by the thermal balance between H₂ formation heating and H₂ line cooling. This yields $T_{\text{eq}} = 870$ K. At $n_{\text{H}} = 10^7$ cm⁻³, while adiabatic compressional heating is the major heating process, H₂ line cooling ($Z \lesssim 10^{-5} Z_{\odot}$) or H₂O line cooling ($\gtrsim 10^{-5} Z_{\odot}$) is the dominant cooling process. The condition where $T_{\text{eq}} < 870$ K at $n_{\text{H}} = 10^7$ cm⁻³ is $\Gamma_{\text{adi}} < \Lambda_{\text{H}_2} + \Lambda_{\text{H}_2\text{O}}$, where Λ_x is the cooling function of species x per unit volume. These cooling/heating rates are written as

$$\begin{aligned}\Gamma_{\text{adi}} &= 2.6 \times 10^{-17} f_0^{-1} \text{ erg cm}^{-3} \text{ s}^{-1}, \\ \Lambda_{\text{H}_2} &= 3.7 \times 10^{-18} \text{ erg cm}^{-3} \text{ s}^{-1}, \\ \Lambda_{\text{H}_2\text{O}} &= 7.9 \times 10^{-18} \left(\frac{Z}{10^{-5} Z_{\odot}} \right) \text{ erg cm}^{-3} \text{ s}^{-1}\end{aligned}$$

at 10^7 cm⁻³ and $T = 870$ K with $t_{\text{col}}^{\text{s}}(1.0) = 0.34 t_{\text{ff}}$. Then, we obtain the condition as

$$Z > (3.4 f_0^{-1} - 0.47) \times 10^{-5} Z_{\odot}. \quad (5.9)$$

The equation is almost consistent with the purple line in Figure 5.10.

For the clouds plotted above the both orange and purple line, the fragmentation is unlikely to occur because of the stabilizing effect of H₂ chemical heating. On the other hand, the orange region is favored for the fragmentation (criteria (i) and (ii)-a). We see that the cloud MH1-z5 which lies near the boundary undergo the fragmentation. We explicitly confirm the validity of the criterion by performing the simulations for UNI ($f_0 \sim 1$) with $Z = 10^{-4.6} Z_{\odot}$. As a result, the fragmentation occurs in this cloud.

C. OH/H₂O cooling

The region within the green line represents the regime where OH cooling is effective at $n_{\text{H}} \sim 10^7$ cm⁻³. OH molecules are formed and contribute to the gas cooling (see Figure 5.8). The major heating source is adiabatic compressional heating. At 10^7 cm⁻³ and 200 K with $t_{\text{col}}^{\text{s}}(\gamma = 0.6-0.7) = 0.21 t_{\text{ff}}$,

$$\begin{aligned}\Gamma_{\text{adi}} &= 1.0 \times 10^{-17} f_0^{-1} \text{ erg cm}^{-3} \text{ s}^{-1}, \\ \Lambda_{\text{OH}} &= 3.2 \times 10^{-19} \left(\frac{y(\text{OH})}{0.1 A_{\text{O}}} \right) \left(\frac{Z}{10^{-5} Z_{\odot}} \right) \text{ erg cm}^{-3} \text{ s}^{-1},\end{aligned}$$

where $y(\text{OH})$ is the abundance of OH molecules relative to hydrogen nuclei, and A_{O} is the elemental abundance of oxygen. The equation $\Gamma_{\text{adi}} = \Lambda_{\text{OH}}$ yields

$$Z = 3.1 \times 10^{-4} f_0^{-1} Z_{\odot}. \quad (5.10)$$

The part of the equation is consistent with the green region in Figure 5.10. For large f_0 and Z , OH molecules are already formed at $n_{\text{H}} < 10^7$ cm⁻³. The gas evolves nearly isothermally by the balance between Γ_{adi} and Λ_{OH} , without the rapid cooling ($\gamma \lesssim 0.7$).

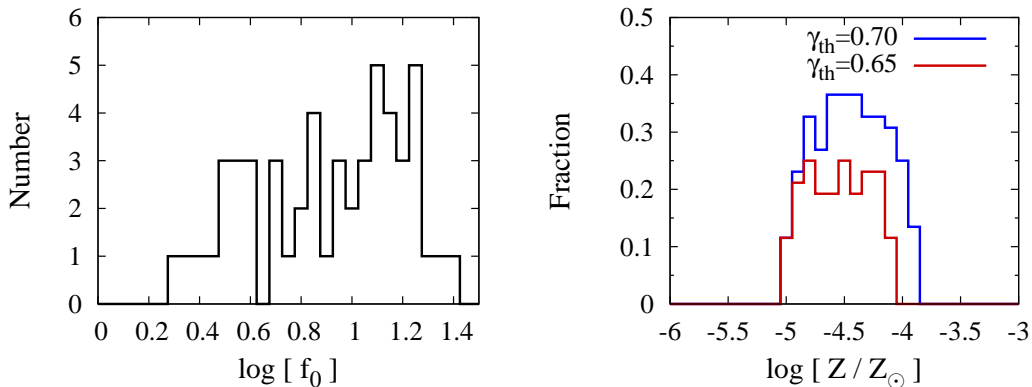


Figure 5.15: Left: number distribution of the 52 Pop III star-forming clouds as a function of f_0 , the indicator of the collapse timescale. These clouds are taken from the cosmological simulations of Hirano et al. (2014) and reanalyzed in this work. Right: number fraction of Pop II star-forming clouds which satisfy the fragmentation criteria written in Section 5.4.2.2, obtained by the one-zone model with constant f_0 . We consider that the criteria (*ii-b*) is satisfied when the specific heat ratio γ becomes below 0.65 (red) and 0.7 (blue).

The criterion (*ii-b*) is thus satisfied in the narrow region on the f_0 - Z plane. The green shaded region with the label “OH” indicates the regimes where OH cooling promotes the gas elongation. The cloud eventually fragments by dust cooling even though the H_2 formation heating intends to stabilize the gas (criteria (*i*) and (*ii-b*)). As seen above, MH1-Z4 undergoes the efficient cooling by OH molecules. The values of f_0 and Z for this cloud is properly plotted on the green-shaded region in Figure 5.10. Also for MH2 with $10^{-4.2} Z_\odot$, the effect of OH cooling promotes the cloud elongation and eventually fragmentation occurs.

Fraction of clouds with fragmentation

We further estimate the fraction of the clouds which undergo the fragmentation. In order to know this, we need a distribution of f_0 of extremely low-metallicity gas clouds. Unfortunately, we have not so far had the way to directly obtain the information. Instead, one of the clues may be the distribution of the collapse timescales of a bulk of primordial clouds obtained by the cosmological simulations of Hirano et al. (2014). We reanalysis 52 of the primordial clouds to get the distribution of f_0 as shown in the left panel of Figure 5.15. Summing up the number of clouds which satisfy the fragmentation criteria, we obtain the fraction of the clouds for the filament fragmentation in the low-metallicity regime for the two γ_{th} below which OH cooling is considered to induce the cloud elongation. The number fraction is 20–25% for $\gamma_{\text{th}} = 0.65$ (severer criterion), and 30–35% for $\gamma_{\text{th}} = 0.7$ with the metallicity $\sim 10^{-5}$ – $10^{-4} Z_\odot$.

5.4.3 Disk fragmentation

In this section, we discuss the disk fragmentation seen for MH1-Z6. Several authors have discussed that the fragmentation occurs on the accretion disks even in the metal-free cases, and argued that the metal-free and low-mass stars are likely to be formed (Clark et al. 2011; Greif et al. 2012; Susa et al. 2014). The fragmentation in their simulations can be categorized as the disk fragmentation. In the regime

$$Z < 2.8 \times 10^{-5} f_0^{-1} Z_{\odot}, \quad (5.11)$$

where dust cooling is inefficient (see Equation 5.8), we can not apply the criterion for the filament fragmentation in principle. In that case, not gas cooling but the self-gravity triggers the cloud fragmentation (e.g. Vorobyov and Basu 2010). In our simulations, the cloud fragmentation can be seen only for one (MH1-Z6) out of five clouds (UNI-Z5 and four Z6 clouds; below the orange line in Figure 5.5), which satisfy Equation (5.11). The peculiar density structure of the MH1 cloud might drive the fragmentation, or it might be just because the disk evolution for the cloud can be followed for the longest time (16 years) among the five clouds. The fragmentation might be seen also for other clouds if we could extend the simulations. Here, we present the maximal region where the disk fragmentation is likely to occur as Equation (5.11) indicated by the grey-hatched area on the f_0 - Z plane (Figure 5.10).

For MH1-Z6, until the simulation is terminated, we find that five gas clumps are formed and immediately migrate into the central protostar within several years. If their formation and migration continue until the end of the accretion process, the mass of the central protostar would further increase. Besides, with the dynamical ejection of some clumps due to the N -body gravitational interaction among the clumps, they would avoid the merger with the central protostar and no longer accrete the gas from the dense circumstellar disk (Zhu et al. 2012; Susa et al. 2014), which would indicate the low-mass star formation even with very low metallicities $Z \lesssim 10^{-5} Z_{\odot}$.

5.5 Gas accretion onto protostars

5.5.1 Overall features

We have so far discussed the criteria for the fragmentation in low-metallicity clouds. It should be noted that the gas fragmentation does not directly mean the low-mass star formation. The protostar acquires the mass by the gas accretion after the fragmentation. The mass of the eventually formed stars is determined after the entire process of the gas accretion (typically for 10^5 yr). Since we do not employ the sink-particle technique here, we follow the gas accretion phase for a limited time (several tens of years). However, we can accurately follow the gas accretion process and even merger of protostellar cores with the central core. Figure 5.16 shows the evolution of the mass fed by the accretion process

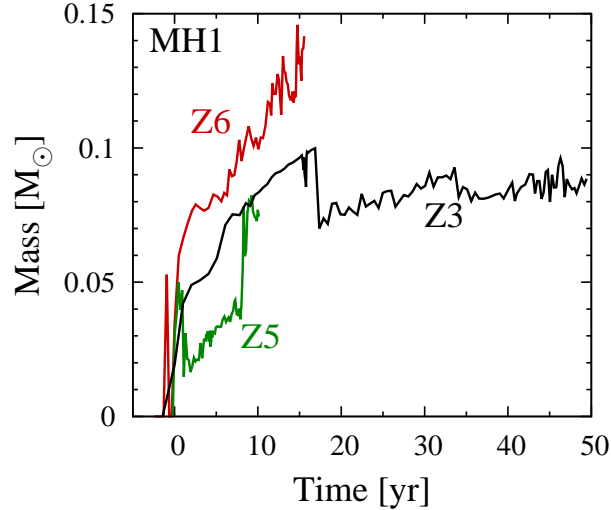


Figure 5.16: Mass of the protostar first formed in the cloud MH1 for z3 (black), z5 (green), and z6 (red) as a function of the time after the first protostar appears.

of the central protostar for MH1. We find that the growth rate of the protostellar mass increases with decreasing metallicity because the gas temperature increases.

5.5.2 Detail cloud evolution

Next, we present the accretion history of the cores including the secondary ones. For UNI-Z3, the cloud fragments in the two stage: first by OH cooling and second by dust cooling as we have seen in Figure 5.2. For MH1-Z5 and MH1-Z6, the secondary protostars fall into the central core.

Two-stage fragmentation for UNI-Z3

For the cloud UNI-Z3, the fragmentation in the two stages are observed. Figure 5.17 shows the zoom-in snapshot of the cloud. The cloud in the first step fragments into two clumps (referred to as Clump A and B from left to right) by OH cooling at $n_{\text{H}} \sim 10^9 \text{ cm}^{-3}$. The separation between the two clumps is $2 \times 10^3 \text{ AU}$, and the masses of the clumps A and B are 15 and $8 M_{\odot}$, respectively. These intermediate-mass clumps further fragment at $n_{\text{H}} \sim 10^{13} \text{ cm}^{-3}$ by dust cooling. In Clump A, the density perturbations at the same interval grow to form three protostars labeled as A1, A2, and A3, in the order of their formation epoch. Whereas, Clump B monolithically collapses to form a single protostar B1. The bottom panel of Figure 5.17 shows the mass growth rates of the protostars.

As discussed above, we confirm that the transition line cooling can also induce the gas fragmentation as predicted by the several authors (Bromm and Loeb 2003; Frebel et al. 2005; Ji et al. 2014). Here, the relevant cooling agent is OH molecules, rather than ions

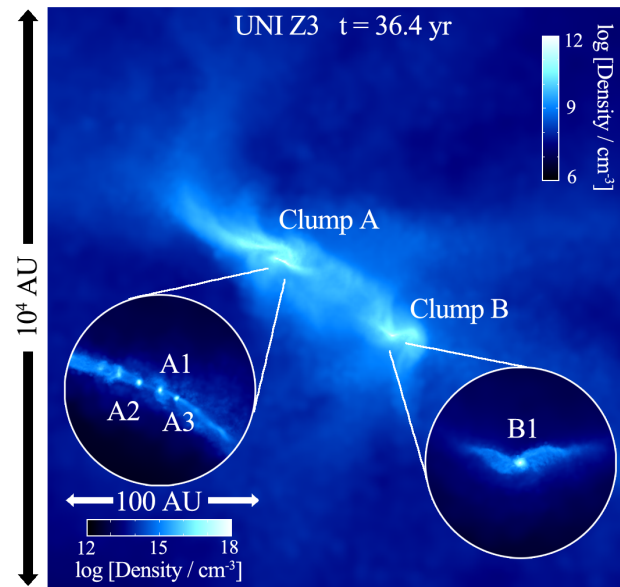


Figure 5.17: Snapshots of the cloud UNI-Z3 at 36.4 years after the first protostar appears. First, the spherical cloud fragments into two clumps by OH molecular cooling, called Clumps A and B. The density structures of Clump A (left) and B (right) are shown in the insets. The former further fragments into three protostars A1–A3 by dust cooling, while the latter collapses monolithically to one protostar called B1.

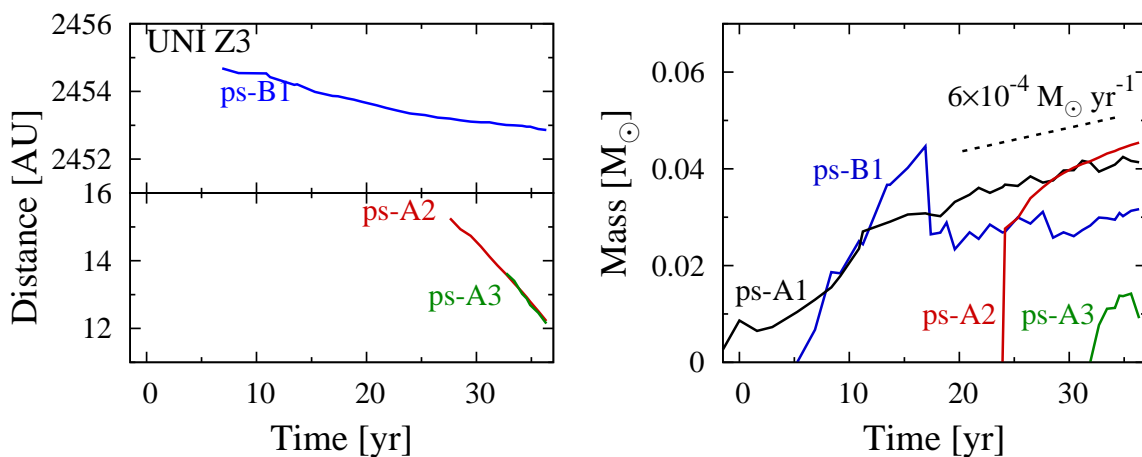


Figure 5.18: Evolution of the distance of the secondary protostars A2, A3 and B1 from the central first protostar A1 (left) and the protostellar mass (right) for UNI-Z3.

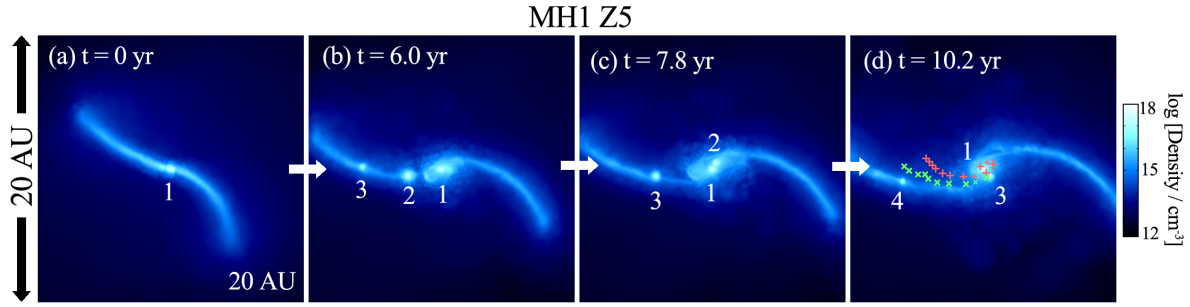


Figure 5.19: Snapshot of the cloud MH1-z5 at the epochs $t_* = 0$ yr (a), 6.0 yr (b), 7.8 yr (c), and 10.2 yr (d) from the first protostar formation. We number the four protostars “1”, “2”, “3”, and “4” in the order of their formation epoch. In the panel (d), we plot the orbits of the protostars 2 (red plus) and 3 (green cross) with large symbols at every 0.5 yr and small symbols at every 0.25 yr. These symbols are plotted at the same time as plotted in the left panel of Figure 5.20.

or atoms that the previous studies conclude to be important. Although O I cooling is dominant until the level populations reach LTE at $\sim 10^4 \text{ cm}^{-3}$, the gas temperature does not turn to increase. Instead, the gas temperature keeps dropping by cooling of newly formed OH molecules. The cloud continues to be elongated without fragmentation. Only after the OH lines become optically thick and H_2 formation heating becomes efficient, the cloud fragments at $n_{\text{H}} \sim 10^8 \text{ cm}^{-3}$, where the Jeans mass is $\sim 10 M_{\odot}$. Although the mass is still large and the formed star is unlikely to survive until the present-day, the transition line cooling is important to trigger the first-step of the fragmentation.

Clump A enters the second step of the fragmentation at density $n_{\text{H}} \sim 10^{13} \text{ cm}^{-3}$ where the dust cooling works. Along the thin dense filament, five blobs appear at a similar interval. Three of the five blobs sufficiently grow to satisfy our criterion of a protostar (see above). The left panel of Figure 5.18 shows the separations of the protostars from A1. When the protostars A2 and A3 appear, they are at a characteristic distance ~ 15 AU from A1. The linear analysis of an isothermal filament shows that the wave length of the perturbations which most rapidly grow is $\lambda_{\text{max}} = 2\pi H$, where $H = (2c_{\text{T}}^2/\pi G\rho_{\text{cen}})^{1/2}$ is the scale-height of the filament (Nagasawa 1987; Inutsuka and Miyama 1997). The length is estimated to be 17 AU for the filament with the mean density 10^{13} cm^{-3} and temperature 100 K. The value is comparable to the initial interval of the protostars. The mass growth rate of the protostars approaches the common value of $6 \times 10^{-4} M_{\odot} \text{ yr}^{-1}$ as indicated by black-dotted line in Figure 5.18.

Merger of protostars for MH1-z5

For MH1-z5, the secondary protostars migrate into and eventually merge with the

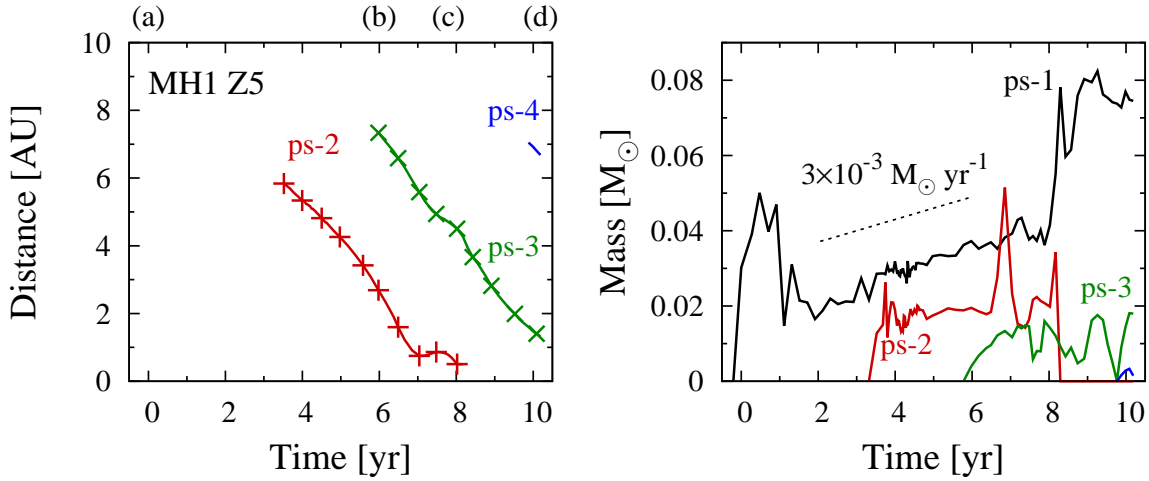


Figure 5.20: Same as Figure 5.18 but for MH1-Z5.

central core. Figure 5.19 shows the projected position, and the left panel of Figure 5.20 shows the distance of the protostars 2 and 3 from the central most massive core 1. The protostars 2–4 are born at a distance of ~ 7 AU, comparable to λ_{max} for the filament with $n_{\text{H}} = 10^{15} \text{ cm}^{-3}$ and $T = 1000$ K. The protostars approach to the center for an order of the free-fall time. During the infall of a protostar, the next protostar is formed at the similar distance (left panel of Figure 5.20). Here, the protostar 2 eventually merges with the protostar 1, and a large mass is supplied with the protostar 1. Although the growth rate of the protostar 1 is on average $3 \times 10^{-3} M_{\odot} \text{ yr}^{-1}$, it abruptly increases when protostar 2 merges with 1 just after epoch (c).

Disk fragmentation for MH1-Z6

The disk fragmentation is witnessed in several thick spiral arms only for MH1-z6. The temporal evolution of the spiral arms and the disk is shown in Figure 5.21. We here enumerate the different points to distinguish the disk fragmentation from the filament fragmentation.

1. In MH1-z6, five blobs appear at various distances to the core. Especially, blob 2 is formed by the interaction between the spiral arms. Whereas, in the regime of the filament fragmentation, the formation sites of protostars are separated at a distance $\sim \lambda_{\text{max}}$.
2. In the disk fragmentation regime, the blobs have the rotational velocity dominant over the radial velocity. The blobs slowly infall with rotating around the center.

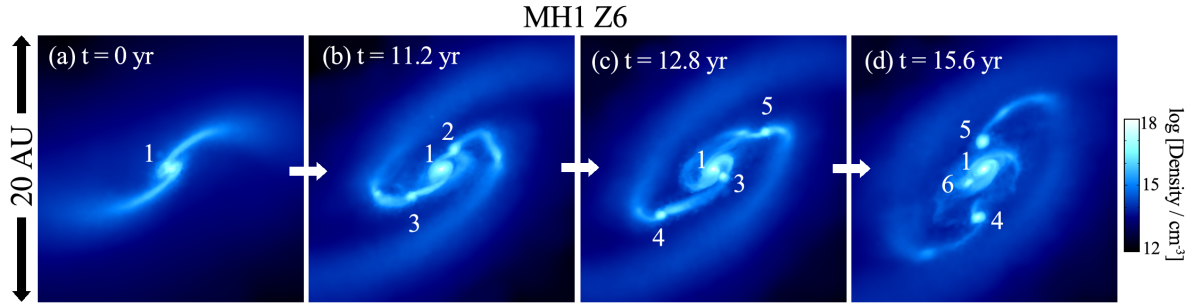


Figure 5.21: Same as Figure 5.19 but for MH1-z6 at the epochs $t_* = 0$ yr (a), 11.2 yr (b), 12.8 yr (c), and 15.6 yr (d) from the first protostar formation.

Whereas, in the filament fragmentation regime, the radial velocity (along the filament) is larger than the rotational velocity at their birth.

3. Interestingly, none of the secondary blobs satisfy our criterion for a protostar, where we require the sphericity of the object. The clumps around the central core are diffused and have oblate shapes, while most of the protostars in the filament fragmentation regime have the spherical shape.

5.6 Discussion

Our three-dimensional hydrodynamics simulations reveal that the cloud thermal evolution and fragmentation *mode* can be determined not only by the gas metallicity Z but also the cloud collapse timescale f_0 . We confirm that the thermal evolution is important to determine the cloud fragmentation as follows:

- The dust thermal emission is crucial to induce gas elongation and fragmentation into low-mass clumps $\sim 0.1 M_\odot$ by its nature that the thermal exchange between gas and dust is efficient at high density $n_H \sim 10^{12}-10^{14} \text{ cm}^{-3}$, corresponding to small Jeans mass.
- Gas heating owing to the exothermic H_2 formation reactions stabilizes the gas at $n_H \sim 10^8 \text{ cm}^{-3}$ before dust cooling becomes efficient. In that case, the timescale for the succeeding gas deformation by dust cooling exceeds the dynamical time of the cloud, and the fragmentation fails to occur. In Pop III dust model, this happens in most cases with metallicities $10^{-4}-10^{-3} Z_\odot$.
- In some cases, OH line cooling enhances the cloud elongation in advance to the stabilization by H_2 formation heating. Eventually dust-induced gas elongation and fragmentation occurs.

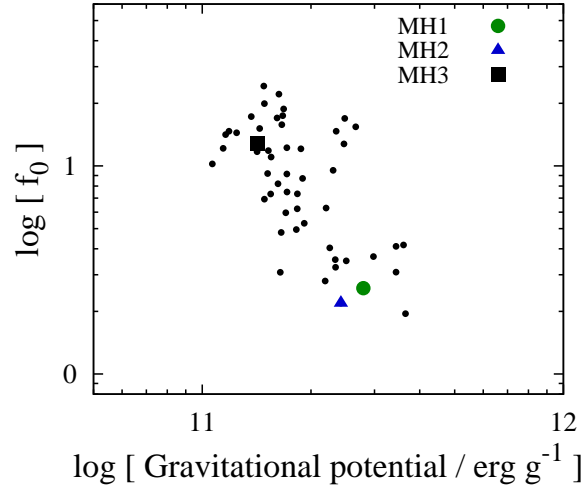


Figure 5.22: Relationship between the collapse timescale f_0 and the initial halo potential $\Phi = GM_h/R_h$ for 52 primordial clouds simulated by Hirano et al. (2014) including MH1 (green circle), MH2 (blue triangle), and MH3 (black square).

The collapse timescale t_{col} , or f_0 is determined by the properties of the dark matter halo: their mass and radius. These quantities are characterized by M_h and R_h which are determined when the matter density turns to increase against the cosmic expansion (shown in Table 5.2 for our MH1, MH2, and MH3 models). We in the simulations estimate R_h to be the filtering scale within which the average density is 200 times the average in the whole Universe (e.g. Peebles 1980), and M_h is the enclosed mass of both dark matter and baryon within R_h . We compare the halo potential $\Phi = GM_h/R_h$ with f_0 of 52 primordial clouds used in the discussion around Figure 5.15. Figure 5.22 shows that, the deeper potential becomes (the larger Φ), the faster the cloud collapses (the smaller f_0 becomes).

We should note that the cloud fragmentation into low-mass cores does not necessarily mean the low-mass star formation. The stellar mass is finally determined by the entire gas accretion process onto the protostellar cores (Shu 1977; Shu et al. 1987; Omukai and Palla 2003; Hosokawa et al. 2011, 2012). Since the dynamical timescale of the system is limited to the one of the central dense core, we can follow the gas accretion processes for only limited time (several tens years) without employing the other techniques such as sink particle. During the accretion process, several physical phenomena may modify the mass accretion rate of the protostar and the resulting final stellar mass: First, the accretion rate might be suppressed if some of the protostellar cores are ejected dynamically by the N -body interactions among the multiple cores. These core escaped from the dense filament or circumstellar disk (Clark et al. 2011; Greif et al. 2012; Susa et al. 2014). Also, the radiative feedback from the protostar becomes important to halt the gas accretion after

its mass exceeds $\sim 10 M_{\odot}$ (Hosokawa et al. 2012). The accretion rate can also be affected by the magnetic field (Machida and Doi 2013). Still, we show that the mass accretion rate decreases with increasing metallicity, which indicates that the typical stellar mass decreases in the course of metal enrichment of the Universe.

In the realistic case, the enrichment process of the cloud by Pop III supernovae are accompanied by the turbulence driven by the propagation of the blast wave. The turbulent motion would affect the thermal evolution of the gas and the fragmentation properties, suppressing the instability in the gas or even inducing the cloud fragmentation (Dopcke et al. 2011, 2013; Smith et al. 2015). The numerical simulations of Dopcke et al. (2013) reveal that the small mass fragments, or sink particles, are formed by a turbulent motion of the gas with a wide metallicity range $Z = 0-10^{-4} Z_{\odot}$. Smith et al. (2015) directly follow the enrichment and second-generation star-formation processes, and find that the cloud polluted with $2 \times 10^{-5} Z_{\odot}$ fragments with the length scale of ~ 1 AU, which is consistent with the scale of the velocity fluctuation driven by the supernova shock. We will study the effects of turbulence on the fragmentation in the entire cosmological setup as a future work.

In this numerical model, we first employ a Pop III supernova model of metal abundance, condensation efficiency of metal onto grains, abundance of grain species, and dust size distribution. This model is consistently calculated with the hydrodynamic evolution of the expanding supernova ejecta, where dust production and destruction proceed (Nozawa et al. 2007). We should note that the supernova dust model reproduces the observed Pop II star with a “normal” abundance pattern. The observations of long-lived metal-poor star in the Galactic halo show that there are two types of metal-deficient stars with $[\text{Fe}/\text{H}] < -3$: carbon-enhanced ($[\text{C}/\text{Fe}] > 1$; Beers and Christlieb 2005) and carbon-normal stars. To reproduce the abundance pattern of the carbon-enhanced stars, we should consider additional processes, such as the metal enrichment by faint supernovae (Umeda and Nomoto 2003). The one-zone calculations performed by Marassi et al. (2014) indicate that, by the carbon-enhanced feature, the clouds polluted by such supernovae can indeed be cooled by carbon grains in most cases at around $n_{\text{H}} \sim 10^{12} \text{ cm}^{-3}$ although the growth of carbon grains is prohibited by the formation of CO molecules in the early stage ($n_{\text{H}} \sim 10^4 \text{ cm}^{-3}$). However, the clouds undergo the temperature decline below 100 K owing to significant C I and HD cooling at densities $n_{\text{H}} \lesssim 10^5 \text{ cm}^{-3}$. In this case, H₂ formation heating becomes dominant at $n_{\text{H}} = 10^8 \text{ cm}^{-3}$, and the fragmentation owing to dust cooling will be suppressed.

5.7 Chapter Summary

In this Chapter, we perform three-dimensional simulations for low-metallicity clouds. We for the first time consider the relevant processes as grain growth as well as non-equilibrium chemical reactions, radiative cooling including metal molecular cooling, chemical heating owing to hydrogen molecular formation in our code. As Hirano et al. (2014) recently

report, the thermal evolution of clouds and resulting stellar mass vary from cloud to cloud even with the fixed metallicity ($Z = 0$ in their case). In this Thesis, the thermal evolution of four gas clouds is followed. One of the clouds initially has the uniform density with rotation, and random density fluctuations. The other three are selected from the set of Pop III star-forming clouds formed in a cosmological simulation so that these three cover the entire range of mass spectrum of the eventually formed Pop III stars. These clouds undergo the different thermal trajectories as confirmed by Hirano et al. (2014). The variation is expected to appear also in the metal-poor case, and have effects on the fragmentation properties. We uniformly put a trace of metal and dust with metallicities 10^{-6} – 10^{-3} . The metal abundance and dust properties are calculated from the Pop III model. During the cloud collapse, we follow the cloud evolution from extremely low density ($\lesssim 0.1 \text{ cm}^{-3}$) to the density of the protostar $\gtrsim 10^{16} \text{ cm}^{-3}$, utilizing our Voronoi particle splitting method.

Consequently, we find that the cloud shape and fragmentation property diverges even with a given metallicity. On the contrary to the accepted knowledge that the cloud fragments when the dust cooling is effective with metallicities above $\sim 10^{-5} Z_{\odot}$, only one of four clouds undergoes fragmentation even though the dust cooling is effective for almost all clouds. The diversity of the cloud fragmentation properties stems from the variety of the thermal evolution. The variation is driven by the collapse timescale t_{col} which varies from cloud to cloud. In a slowly collapsing cloud, the gas compressional heating rate becomes small, and thus the temperature becomes lower throughout the collapse. The clouds with the different evolutionary paths undergo the regime where different cooling/heating processes are important. We identify the two important processes as well as dust thermal emission as follows:

The chemical heating owing to the hydrogen molecular formation via the exothermic reactions stabilizes the gas and prevents the cloud from deforming at the intermediate density $\sim 10^8 \text{ cm}^{-3}$. Actually, the cloud fragmentation via filamentary structure has a high threshold. This only occurs when the cloud ellipticity \mathcal{E} becomes above the large threshold value 20–30 (called the *critical ellipticity* hereafter). If rapid gas heating leads the cloud to be sufficiently round, the timescale for the ellipticity to grow from such a small value to the critical ellipticity becomes longer than the dynamical time of the cloud. In the most of the cloud, this H_2 formation heating halt the gas elongation as the precursor of the eventual fragmentation due to dust cooling. In some cases, the clouds fragment into low-mass clumps. We find that the rapid OH or H_2O cooling is effective at $n_{\text{H}} \sim 10^6$ – 10^8 cm^{-3} to compensate the stabilizing effect by chemical heating.

We further employ the one-zone semi-analytic collapse model to see the relationship between the collapse time and the thermal evolution of metal-poor clouds. We newly define the indicator f_0 as the ratio of the collapse timescale of the cloud to that of the self-similar solution. Compared with the simulation results, the simple model with constant f_0 fails to quantitatively reproduce the simulation results because the cloud shape departures from the self-similar one. Instead, the clouds are deformed by the dark matter potential and elongation by radiative cooling. In addition, the thermal processes

are sensitive to the change of f_0 during the collapse in the simulated clouds. This would mean that it is necessary to perform simulations to properly follow the fragmentation process of the metal-deficient clouds.

CHAPTER 6
Conclusion

Contents

6.1 Summary	135
6.2 Concluding remarks	139

6.1 Summary

It is under the debate how the extremely-metal poor stars recently discovered in the Galactic halo can acquire such the small mass that they can survive for the cosmic time. The star SDSS J102915 + 172927 is the most metal-poor ever observed with $Z = 4.5 \times 10^{-5} Z_{\odot}$ (Caffau et al. 2011). Their small metal content supports the idea that they are the very second-generation stars born from the cloud enriched by metal-free massive stars (Pop III stars). The Pop III stars are considered to be predominantly massive (from 20 to even $1000 M_{\odot}$) as suggested by the metal abundance of the observed Pop II stars (Caffau et al. 2011; Keller et al. 2014; Aoki et al. 2014). Some numerical studies also show that the first stars have large masses (Bromm et al. 1999; Abel et al. 2002; Hirano et al. 2014).

The additional cooling by metal and dust is considered to trigger the gas fragmentation into low-mass clumps during cloud collapse (Bromm et al. 2001). The linear analysis of the bar-mode perturbations on a spherical cloud shows that the cloud elongation is promoted/halted when the gas is cooled/heated (Hanawa and Matsumoto 2000; Lai 2000). When cooling is dominant, the gas is elongated to form a filamentary structure. After the amplitude of perturbations on the filament exceeds the density where the cooling becomes insufficient, the cores are stabilized to collapse spherically separately.

Recently, gas cooling by the dust thermal emission successfully explains the cloud fragmentation into low-mass prestellar core even in an extremely metal-poor environment (Omukai et al. 2005; Safranek-Shrader et al. 2014b). This cooling becomes effective only after the thermal coupling between gas and dust becomes efficient at $n_{\text{H}} \sim 10^{14} \text{ cm}^{-3}$, corresponding to the Jeans mass of $\sim 0.1 M_{\odot}$. Several authors present that the dust cooling is effective even with $> 10^{-5} Z_{\odot}$,

However, the critical metallicity is determined with the present-day dust model instead of the models realistic in the early Universe. The dust cooling efficiency might be

overestimated. The formation path of early grains is limited to Pop III supernovae (Dwek et al. 2007). The grain destruction by the reverse shocks also suppress the dust-to-metal mass ratio (Bianchi and Schneider 2007; Nozawa et al. 2007). Recent observations reveal that the dust-to-metal ratio is significantly smaller than in the present-day (Zafar et al. 2011).

First, we investigate the effect of the realistic dust models in the early Universe and grain growth. Here, we employ the semi-analytic one-zone model for contracting clouds pre-enriched by Pop III supernovae at the aim to focus on their thermal properties. In this model, the density increases at the rate of $\sim t_{\text{ff}}$, where t_{ff} is the free-fall time. We solve the chemical reactions to derive the cooling/heating rates which depends on the density, temperature, and chemical compositions in a time-dependent manner. As the metal and dust properties, we utilize the Pop III dust models. The metal content is obtained from the nucleosynthetic model of progenitor stars and their supernova explosion. The dust properties are then calculated with the hydrodynamic evolution of expanding ejecta, which is the formation site of grains. We consider a wide range of progenitor mass $M_{\text{pr}} = 13\text{--}30 M_{\odot}$ of core-collapse supernovae (CCSNe) and $170\text{--}200 M_{\odot}$ for pair-instability supernovae (PISNe). Finally, the dust destruction by reverse shocks propagating inward is treated. The destruction efficiency is determined by the ambient gas density n_{amb} around the supernovae. Our model covers a range of $n_{\text{amb}} = 0.1\text{--}10 \text{ cm}^{-3}$. We utilize the Pop III model as the initial condition of the succeeding one-zone collapse calculations. Since here assume that a cloud is polluted by a progenitor, the model parameters are M_{pr} and n_{amb} . We perform one-zone calculations with various metallicities to define the critical metallicity Z_{cr} above which dust cooling becomes effective in each Pop III model.

In some cases, grain growth occurs efficiently before the gas becomes optically thick. The dust cooling efficiency is enhanced, and consequently Z_{cr} becomes smaller, i.e., the smaller metal (dust) is enough to induce fragmentation than in the case without grain growth. This can be seen especially in the model with small fractions $f_{\text{dep},0}$ of metal depleted onto grains initially. It tends to mitigate the effect of initial depletion factor $f_{\text{dep},0}$ compared with the case without grain growth. Also, as we have expected, Z_{cr} is dependent on the Pop III models. We find that Z_{cr} is almost linearly related to $f_{\text{dep},0}$, one of the quantities which characterizes the dust property of each Pop III model. While Z_{cr} depends on f_{dep} reciprocally as

$$Z_{\text{cr}}^{(\text{ng})} = 2.3 \times 10^{-8} f_{\text{dep},0}^{-1} \quad (6.1)$$

without grain growth, the dependency is mitigated into

$$\left(\frac{Z_{\text{cr}}^{(\text{gg})}}{10^{-5.5} Z_{\odot}} \right) = \left(\frac{f_{\text{dep},0}}{0.18} \right)^{-0.44}. \quad (6.2)$$

We can conclude that the grain growth is necessary process to determine the fragmentation condition for low-mass star formation. We also should note that the critical metallicity has the slight dependency on the Pop III model (spectral index of -0.44). This indicates that the critical condition can slightly vary for different clumps.

Dust thermal emission, even enhanced by the metal accretion phenomenon, is expected to enhance the cloud elongation and fragmentation. To confirm this explicitly, we perform three-dimensional hydrodynamic simulations. Before that, we elaborate the numerical technique used in collapse simulations. The cloud collapse is a phenomenon with a large dynamic range of the density over 20 orders of magnitude. Further, the mass (length) resolution should be sufficiently smaller than the local Jeans mass (length) to avoid the spurious fragmentation due to the numerical noise (Jeans criterion; [Trulove et al. 1997](#)). The strategy of particle splitting is frequently used: a coarse (parent) particle about to violate the Jeans criterion is replaced with the set of finer (daughter) particles. On the contrary to the adaptive mesh refinement (AMR) technique in a grid code, the distributions of daughter particles are not trivial in a Lagrangian smoothed particle hydrodynamics (SPH) code, which we in this theses utilize. The previous studies have developed simple and less-costly methods. [Kitsionas and Whitworth \(2002\)](#) distribute the daughters uniformly on a sphere centered at their parent. [Mayer et al. \(2010\)](#) put them on edges of a cube. With these symmetric distribution of daughters, one might fail to capture the highly anisotropic shape of clouds such as a thin filament formed by dust cooling.

We develop the method such that the daughters are distributed uniformly within the Voronoi cell tessellated by their parents. The Voronoi cells flexibly capture the distribution of the particles. The several test simulations show that the resulting cloud shape for the run with our splitting method (hereafter, VORO) is consistent with that without the particle splitting. We perform the simulation for the primordial gas cloud cut out from a cosmological simulation. As a result, the structures of spiral arms and spheroidal core are more clearly captured in the run VORO than in the other cases. With the other methods, one or both of the aspherical structures cannot reproduced. The structures become somewhat blurred, and approach to spherical shapes. This would affect also the fragmentation condition of early clouds.

We finally perform three-dimensional simulations for low-metallicity clouds. We for the first time consider grain growth as well as non-equilibrium chemical reactions, radiative cooling including metal molecular cooling, chemical heating owing to hydrogen molecular formation in our code. As [Hirano et al. \(2014\)](#) recently report, the thermal evolution of clouds and resulting stellar mass vary from cloud to cloud even with the fixed metallicity ($Z = 0$ in their case). In this thesis, the thermal evolution of four gas clouds is followed. One of the clouds initially has the uniform density of $n_{\text{H,ini}} = 0.1 \text{ cm}^{-3}$, rotation (the energy ratio of rotation to gravity 10^{-3}), and random density perturbation of 10%. The other three are selected from the Pop III star-forming clouds formed in a cosmological simulation so that they cover the different type of the clouds. We uniformly put a trace of metal and dust with metallicities 10^{-6} – 10^{-3} . The metal abundance and dust properties are calculated from the Pop III model. We pick up the model with $M_{\text{pr}} = 30 M_{\odot}$ and $n_{\text{amb}} = 1 \text{ cm}^{-3}$ as a characteristic parameters. During the cloud collapse, we follow the cloud evolution from extremely low density ($\lesssim 0.1 \text{ cm}^{-3}$) to the density of $\gtrsim 10^{16} \text{ cm}^{-3}$, utilizing our Voronoi particle splitting method.

The resultant fragmentation properties are rather complicated. We see the cloud fragmentation occurs only one out of four clouds with each of the four metallicities. With metallicities $\geq 10^{-5} Z_{\odot}$, the clouds of the majority undergo monolithically collapse without fragmentation even though the dust cooling is efficient in almost all the models. Also, we notice that the fragmentation occurs also with very low metallicity $10^{-6} Z_{\odot}$.

First, we focus on the cases with fragmentation. With $\geq 10^{-5} Z_{\odot}$, the multiple protostellar cores appear on a thin filamentary structure which is triggered by the dust cooling. We call the regime of fragmentation as *filament fragmentation*. The filament fragmentation is predicted analytically (Hanawa and Matsumoto 2000; Lai 2000) and by numerical simulations (Tsuribe and Omukai 2006) for a polytropic gas. We confirm this in our more elaborated simulations including all relevant chemical reactions and radiative cooling processes. With $10^{-6} Z_{\odot}$, the clumps are formed in spiral arms on an accretion disk. Let us call such a type of fragmentation as *disk fragmentation*. In the disk fragmentation regime, the fragmentation is not triggered by gas cooling but by the self-gravity of the disk. We consider that the disk fragmentation is the same fragmentation mode as reported by several authors (Clark et al. 2011; Greif et al. 2012) in their clouds without metal. We for the first time see that two fragmentation mode appear in a series of the simulations.

Next, we consider the mechanisms which induce the variation of fragment properties. Since the criterion for the disk fragmentation has been studied by earlier works such as Gammie (2001) and Takahashi (2015), we here focus on the necessary thermal processes triggering the filament fragmentation. The diversity of the cloud fragmentation properties stems from the variety of the thermal evolution. This variation can be explained the collapse timescale t_{col} which varies from cloud to cloud. In a slowly collapsing cloud, the gas compressional heating rate becomes small, and thus the temperature becomes lower throughout the collapse. The clouds with the different evolutionary paths undergo the regime where different cooling/heating processes are important. We identify the three important processes including dust thermal emission as follows:

- **dust cooling**

Dust thermal emission induces the cloud elongation and fragmentation into low-mass ($\lesssim 0.1 M_{\odot}$) clumps.

- **H₂ formation heating**

The chemical heating owing to the hydrogen molecular formation via the exothermic reactions stabilizes the gas and prevents the cloud from deforming at the intermediate density $\sim 10^8 \text{ cm}^{-3}$. Actually, the cloud fragmentation via filamentary structure has a high threshold. This only occurs when the cloud ellipticity \mathcal{E} becomes above the large threshold value 20–30 (called the *critical ellipticity* hereafter). If rapid gas heating leads the cloud to be sufficiently round, the timescale for the ellipticity to grow from such a small value to the critical ellipticity becomes longer than the dynamical time of the cloud. In the most of the cloud, this H₂ formation heating

halt the gas elongation as the precursor of the eventual fragmentation due to dust cooling.

- **OH/H₂O cooling**

In some cases, the clouds fragment into low-mass clumps. We find that the rapid OH or H₂O cooling is effective at $n_{\text{H}} \sim 10^6\text{--}10^8 \text{ cm}^{-3}$ to compensate the stabilizing effect by chemical heating.

Therefore, the fragmentation condition can be written as

Conditions for filament fragmentation

- (i) dust cooling is efficient to induce the cloud elongation with the ellipticity up to $\mathcal{E}_* = 20$ for clouds to fragment into low-mass clumps, and
- (ii-a) H₂ formation heating is not effective to dump the bar-mode perturbation as a precursor of the further cloud elongation by dust cooling, or
- (ii-b) OH cooling is efficient to enhance the cloud elongation even though H₂ formation heating is effective.

6.2 Concluding remarks

In this Thesis, we have step-by-step disclosed the nature of the evolution of the primitive clouds to seek the condition for the cloud fragmentation into low-mass cores which would be the precursor of the first low-mass star formation in the early Universe. The Pop III supernova model and grain growth can determine the critical condition for the sufficient dust cooling. However, our three-dimensional simulations reveal that the efficient dust cooling do not directly mean the gas fragmentation. Another thermal mechanism, H₂ formation heating, can halt the eventual dust-induced fragmentation in the most cases. Therefore, with a metallicity range $10^{-5}\text{--}10^{-3} Z_{\odot}$, the fraction of clouds which undergo filament fragmentation is very small: one out of four clouds in our simulation. Although disk fragmentation might contribute to create the low-mass and hyper metal-poor ($Z \lesssim 10^{-5} Z_{\odot}$) star, we could say that the very primitive low-mass star formation would be a “rare” event.

The recent observation of the Galactic halo stars find that the abundance of the objects with $[\text{Fe}/\text{H}] \sim -5\text{--}-4$ is very small. By the simple estimation of the metal enrichment process in the halo, the number of the stars decrease reciprocally with decreasing metallicity (Hartwick 1976). Such a trend is confirmed with $[\text{Fe}/\text{H}] \gtrsim -3.5$, but is failed for $[\text{Fe}/\text{H}] \lesssim -4$ (Norris 1999). Note that the “iron-poor” does not simply mean the small metallicity, which is defined as the mass fraction of “all” heavy element. These iron-poor stars often show the carbon-enhanced feature ($[\text{C}/\text{Fe}] \gtrsim 1$), and thus the metallicity itself is not so small. Rather, the star with the small amount of both carbon and iron is fur

less abundant. So far, only one star has been discovered (SDSS J1029 + 1729; Caffau et al. 2011). These observational facts might support our results.

There are still limitations of our current model. We here follow the evolution of collapsing cloud, employing the Pop III supernova model which predicts the metal abundance consistent with the carbon-normal extremely metal-poor (EMP) stars. To explain the formation process of another population, carbon-enhanced extremely metal-poor (CEMP) stars, it is required to consider additional process such as the mixing-fallback model in a faint supernova (Umeda and Nomoto 2003). Our numerical model, in which any abundances of metal elements and grain species and dust size distribution can be included, will be applied to the problem. Our further comprehensive studies for the CEMP stars as well as the present carbon-normal EMP star formation models reveal the entire formation process of the low-mass and low-metallicity stars.

Then, it is necessary to estimate the initial mass function of forming Pop II stars to clarify the succeeding chemical enrichment and star formation processes in the early Universe. In our simulation presented here, the process of the gas accretion onto the protostellar core is followed for several tens of years. It is required to follow the entire accretion history to estimate the final stellar mass when the core reaches the zero-age main-sequence, but challenging because the computational time is limited by the dynamical timescale of dense protostellar core. If the central protostellar core reaches $10 M_{\odot}$, the photoionization and photodissociation become important to halt the mass accretion (Hosokawa et al. 2011, 2012). Also, some researchers report that a part of cores are ejected by the dynamical interactions with other cores (Greif et al. 2012; Susa et al. 2014).

Finally, we employ simulations in the “quiescent” cloud with slight turbulent motion. Although this environment is suitable to seek the condition of fragmentation driven by thermal processes such as dust cooling, it is known that the turbulent motion triggered by the supernova explosion and merger of dark matter halos can enhance the cloud fragmentation into low-mass clumps (Dopcke et al. 2013; Safranek-Shrader et al. 2014b; Smith et al. 2015). The next target of this work is to explicitly follow the chemical and dynamical effects of stellar feedback and cosmological structure formation on the succeeding star formation and eventual first galaxy formation in the early Universe, applying our numerical procedures.

Bibliography

- T. Abel, P. Anninos, Y. Zhang, and M. L. Norman. Modeling primordial gas in numerical cosmology. *New A*, 2:181–207, August 1997. doi: 10.1016/S1384-1076(97)00010-9. (Cited on page 39.)
- T. Abel, G. L. Bryan, and M. L. Norman. The Formation and Fragmentation of Primordial Molecular Clouds. *ApJ*, 540:39–44, September 2000. doi: 10.1086/309295. (Cited on page 4.)
- T. Abel, G. L. Bryan, and M. L. Norman. The Formation of the First Star in the Universe. *Science*, 295:93–98, January 2002. doi: 10.1126/science.295.5552.93. (Cited on pages 4, 15, 41, 120 and 135.)
- H. Abgrall, E. Roueff, and Y. Viala. Vibration-rotation transition probabilities for the ground electronic $\chi_1^-/\sigma^+/\sigma^+$ state of HD. *A&AS*, 50:505–522, December 1982. (Cited on page 29.)
- W. Aoki, N. Tominaga, T. C. Beers, S. Honda, and Y. S. Lee. A chemical signature of first-generation very massive stars. *Science*, 345:912–915, August 2014. doi: 10.1126/science.1252633. (Cited on pages 4, 16 and 135.)
- J. Audouze and J. Silk. The First Generation of Stars: First Steps toward Chemical Evolution of Galaxies. *ApJ*, 451:L49, October 1995. doi: 10.1086/309687. (Cited on page 1.)
- T. C. Beers and N. Christlieb. The Discovery and Analysis of Very Metal-Poor Stars in the Galaxy. *ARA&A*, 43:531–580, September 2005. doi: 10.1146/annurev.astro.42.053102.134057. (Cited on pages 2, 16, 24, 63 and 132.)
- S. Bianchi and R. Schneider. Dust formation and survival in supernova ejecta. *MNRAS*, 378:973–982, July 2007. doi: 10.1111/j.1365-2966.2007.11829.x. (Cited on pages 17, 21 and 136.)
- W. B. Bonnor. Boyle’s Law and gravitational instability. *MNRAS*, 116:351, 1956. doi: 10.1093/mnras/116.3.351. (Cited on page 120.)
- A. Borysow, L. Frommhold, and M. Moraldi. Collision-induced infrared spectra of H₂-He pairs involving 0-1 vibrational transitions and temperatures from 18 to 7000 K. *ApJ*, 336:495–503, January 1989. doi: 10.1086/167027. (Cited on page 29.)
- A. P. Boss and P. Bodenheimer. Fragmentation in a rotating protostar - A comparison of two three-dimensional computer codes. *ApJ*, 234:289–295, November 1979. doi: 10.1086/157497. (Cited on page 81.)

- V. Bromm and A. Loeb. The formation of the first low-mass stars from gas with low carbon and oxygen abundances. *Nature*, 425:812–814, October 2003. doi: 10.1038/nature02071. (Cited on pages 10, 15 and 126.)
- V. Bromm, P. S. Coppi, and R. B. Larson. Forming the First Stars in the Universe: The Fragmentation of Primordial Gas. *ApJ*, 527:L5–L8, December 1999. doi: 10.1086/312385. (Cited on pages 4 and 135.)
- V. Bromm, A. Ferrara, P. S. Coppi, and R. B. Larson. The fragmentation of pre-enriched primordial objects. *MNRAS*, 328:969–976, December 2001. doi: 10.1046/j.1365-8711.2001.04915.x. (Cited on page 135.)
- V. Bromm, P. S. Coppi, and R. B. Larson. The Formation of the First Stars. I. The Primordial Star-forming Cloud. *ApJ*, 564:23–51, January 2002. doi: 10.1086/323947. (Cited on pages 4 and 15.)
- E. Caffau, P. Bonifacio, P. François, L. Sbordone, L. Monaco, M. Spite, F. Spite, H.-G. Ludwig, R. Cayrel, S. Zaggia, F. Hammer, S. Randich, P. Molaro, and V. Hill. An extremely primitive star in the Galactic halo. *Nature*, 477:67–69, September 2011. doi: 10.1038/nature10377. (Cited on pages 1, 16, 24, 33, 34, 51, 64, 65, 135 and 140.)
- E. Caffau, P. Bonifacio, P. François, M. Spite, F. Spite, S. Zaggia, H.-G. Ludwig, M. Steffen, L. Mashonkina, L. Monaco, L. Sbordone, P. Molaro, R. Cayrel, B. Plez, V. Hill, F. Hammer, and S. Randich. A primordial star in the heart of the Lion. *A&A*, 542:A51, June 2012. doi: 10.1051/0004-6361/201118744. (Cited on page 4.)
- R. Cayrel, E. Depagne, M. Spite, V. Hill, F. Spite, P. François, B. Plez, T. Beers, F. Primas, J. Andersen, B. Barbuy, P. Bonifacio, P. Molaro, and B. Nordström. First stars V - Abundance patterns from C to Zn and supernova yields in the early Galaxy. *A&A*, 416:1117–1138, March 2004. doi: 10.1051/0004-6361:20034074. (Cited on page 112.)
- S. Cazaux and A. G. G. M. Tielens. Molecular Hydrogen Formation in the Interstellar Medium. *ApJ*, 575:L29–L32, August 2002. doi: 10.1086/342607. (Cited on page 41.)
- N. L. Chapman, L. G. Mundy, S.-P. Lai, and N. J. Evans, II. The Mid-Infrared Extinction Law in the Ophiuchus, Perseus, and Serpens Molecular Clouds. *ApJ*, 690:496, January 2009. doi: 10.1088/0004-637X/690/1/496. (Cited on pages 18 and 45.)
- G. Chiaki and N. Yoshida. Particle splitting in smoothed particle hydrodynamics based on Voronoi diagram. *MNRAS*, 451:3955–3963, August 2015. doi: 10.1093/mnras/stv1227. (Cited on page 68.)
- G. Chiaki, T. Nozawa, and N. Yoshida. Growth of Dust Grains in a Low-metallicity Gas and Its Effect on the Cloud Fragmentation. *ApJ*, 765:L3, March 2013. doi: 10.1088/2041-8205/765/1/L3. (Cited on pages 19, 21 and 23.)

- G. Chiaki, S. Marassi, T. Nozawa, N. Yoshida, R. Schneider, K. Omukai, M. Limongi, and A. Chieffi. Supernova dust formation and the grain growth in the early universe: the critical metallicity for low-mass star formation. *MNRAS*, 446:2659–2672, January 2015. doi: 10.1093/mnras/stu2298. (Cited on page 48.)
- N. Christlieb, B. Gustafsson, A. J. Korn, P. S. Barklem, T. C. Beers, M. S. Bessell, T. Karlsson, and M. Mizuno-Wiedner. HE 0107-5240, a Chemically Ancient Star. I. A Detailed Abundance Analysis. *ApJ*, 603:708–728, March 2004. doi: 10.1086/381237. (Cited on pages 2 and 64.)
- P. C. Clark, S. C. O. Glover, R. S. Klessen, and V. Bromm. Gravitational Fragmentation in Turbulent Primordial Gas and the Initial Mass Function of Population III Stars. *ApJ*, 727:110, February 2011. doi: 10.1088/0004-637X/727/2/110. (Cited on pages 106, 125, 131 and 138.)
- G. Dopcke, S. C. O. Glover, P. C. Clark, and R. S. Klessen. The Effect of Dust Cooling on Low-metallicity Star-forming Clouds. *ApJ*, 729:L3, March 2011. doi: 10.1088/2041-8205/729/1/L3. (Cited on pages 21, 22 and 132.)
- G. Dopcke, S. C. O. Glover, P. C. Clark, and R. S. Klessen. On the Initial Mass Function of Low-metallicity Stars: The Importance of Dust Cooling. *ApJ*, 766:103, April 2013. doi: 10.1088/0004-637X/766/2/103. (Cited on pages 21, 22, 95, 132 and 140.)
- E. Dwek, F. Galliano, and A. P. Jones. The Evolution of Dust in the Early Universe with Applications to the Galaxy SDSS J1148+5251. *ApJ*, 662:927–939, June 2007. doi: 10.1086/518430. (Cited on pages 16, 17 and 136.)
- R. Ebert. Über die Verdichtung von H I-Gebieten. Mit 5 Textabbildungen. *ZAp*, 37:217, 1955. (Cited on page 120.)
- A. Ferrara. The Positive Feedback of Population III Objects on Galaxy Formation. *ApJ*, 499:L17, May 1998. doi: 10.1086/311344. (Cited on page 2.)
- A. Frebel and J. E. Norris. *Metal-Poor Stars and the Chemical Enrichment of the Universe*, page 55. 2013. doi: 10.1007/978-94-007-5612-0_3. (Cited on pages 24 and 64.)
- A. Frebel, W. Aoki, N. Christlieb, H. Ando, M. Asplund, P. S. Barklem, T. C. Beers, K. Eriksson, C. Fechner, M. Y. Fujimoto, S. Honda, T. Kajino, T. Minezaki, K. Nomoto, J. E. Norris, S. G. Ryan, M. Takada-Hidai, S. Tsangarides, and Y. Yoshii. Nucleosynthetic signatures of the first stars. *Nature*, 434:871–873, April 2005. doi: 10.1038/nature03455. (Cited on pages 10, 16 and 126.)
- A. Frebel, J. L. Johnson, and V. Bromm. Probing the formation of the first low-mass stars with stellar archaeology. *MNRAS*, 380:L40–L44, September 2007. doi: 10.1111/j.1745-3933.2007.00344.x. (Cited on pages 10 and 64.)

- A. Frebel, R. Collet, K. Eriksson, N. Christlieb, and W. Aoki. HE 1327-2326, an Unevolved Star with $[\text{Fe}/\text{H}] < -5.0$. II. New 3D-1D Corrected Abundances from a Very Large Telescope UVES Spectrum. *ApJ*, 684:588–602, September 2008. doi: 10.1086/590327. (Cited on pages 2 and 64.)
- D. Galli and F. Palla. The chemistry of the early Universe. *A&A*, 335:403–420, July 1998. (Cited on pages 29 and 39.)
- C. F. Gammie. Nonlinear Outcome of Gravitational Instability in Cooling, Gaseous Disks. *ApJ*, 553:174–183, May 2001. doi: 10.1086/320631. (Cited on pages 106 and 138.)
- M. Geha, T. M. Brown, J. Tumlinson, J. S. Kalirai, J. D. Simon, E. N. Kirby, D. A. VandenBerg, R. R. Muñoz, R. J. Avila, P. Guhathakurta, and H. C. Ferguson. The Stellar Initial Mass Function of Ultra-faint Dwarf Galaxies: Evidence for IMF Variations with Galactic Environment. *ApJ*, 771:29, July 2013. doi: 10.1088/0004-637X/771/1/29. (Cited on pages 4 and 22.)
- T. H. Greif, V. Bromm, P. C. Clark, S. C. O. Glover, R. J. Smith, R. S. Klessen, N. Yoshida, and V. Springel. Formation and evolution of primordial protostellar systems. *MNRAS*, 424:399–415, July 2012. doi: 10.1111/j.1365-2966.2012.21212.x. (Cited on pages 89, 96, 106, 125, 131, 138 and 140.)
- Z. Haiman and A. Loeb. Signatures of Stellar Reionization of the Universe. *ApJ*, 483:21–37, July 1997. (Cited on page 2.)
- Z. Haiman, M. J. Rees, and A. Loeb. Destruction of Molecular Hydrogen during Cosmological Reionization. *ApJ*, 476:458–463, February 1997. (Cited on page 2.)
- T. Hanawa and T. Matsumoto. Stability of a Dynamically Collapsing Gas Sphere. *PASJ*, 52:241, April 2000. (Cited on pages 5, 7, 135 and 138.)
- T. W. Hartquist, A. Dalgarno, and M. Oppenheimer. Molecular diagnostics of interstellar shocks. *ApJ*, 236:182–188, February 1980. doi: 10.1086/157731. (Cited on page 43.)
- F. D. A. Hartwick. The Chemical Evolution of the Galactic Halo. *ApJ*, 209:418–423, October 1976. doi: 10.1086/154735. (Cited on page 139.)
- T. Hartwig, V. Bromm, R. S. Klessen, and S. C. O. Glover. Constraining the primordial initial mass function with stellar archaeology. *MNRAS*, 447:3892–3908, March 2015. doi: 10.1093/mnras/stu2740. (Cited on page 3.)
- C. Hayashi and T. Nakano. Thermal and Dynamical Properties of a Protostar and Its Contraction to the Stage of Quasi-Static Equilibrium. *Progress of Theoretical Physics*, 34:754–775, November 1965. doi: 10.1143/PTP.34.754. (Cited on page 12.)

- S. Hirano and N. Yoshida. Radiative Cooling Implementations in Simulations of Primordial Star Formation. *ApJ*, 763:52, January 2013. doi: 10.1088/0004-637X/763/1/52. (Cited on page 28.)
- S. Hirano, T. Hosokawa, N. Yoshida, H. Umeda, K. Omukai, G. Chiaki, and H. W. Yorke. One Hundred First Stars: Protostellar Evolution and the Final Masses. *ApJ*, 781:60, February 2014. doi: 10.1088/0004-637X/781/2/60. (Cited on pages 4, 23, 26, 39, 84, 94, 96, 97, 120, 124, 131, 132, 133, 135 and 137.)
- D. Hollenbach and C. F. McKee. Molecule formation and infrared emission in fast interstellar shocks. I Physical processes. *ApJS*, 41:555–592, November 1979. doi: 10.1086/190631. (Cited on pages 29 and 36.)
- D. Hollenbach and C. F. McKee. Molecule formation and infrared emission in fast interstellar shocks. III - Results for J shocks in molecular clouds. *ApJ*, 342:306–336, July 1989. doi: 10.1086/167595. (Cited on page 30.)
- T. Hosokawa, K. Omukai, N. Yoshida, and H. W. Yorke. Protostellar Feedback Halts the Growth of the First Stars in the Universe. *Science*, 334:1250–, December 2011. doi: 10.1126/science.1207433. (Cited on pages 4, 131 and 140.)
- T. Hosokawa, K. Omukai, and H. W. Yorke. Rapidly Accreting Supergiant Protostars: Embryos of Supermassive Black Holes? *ApJ*, 756:93, September 2012. doi: 10.1088/0004-637X/756/1/93. (Cited on pages 131, 132 and 140.)
- S.-i. Inutsuka and S. M. Miyama. A Production Mechanism for Clusters of Dense Cores. *ApJ*, 480:681–693, May 1997. (Cited on page 128.)
- S.-I. Inutsuka and S. M. Miyama. Self-similar solutions and the stability of collapsing isothermal filaments. *ApJ*, 388:392–399, April 1992. doi: 10.1086/171162. (Cited on page 7.)
- A. P. Ji, A. Frebel, and V. Bromm. The Chemical Imprint of Silicate Dust on the Most Metal-poor Stars. *ApJ*, 782:95, February 2014. doi: 10.1088/0004-637X/782/2/95. (Cited on pages 11, 65 and 126.)
- C. C. Joggerst, S. E. Woosley, and A. Heger. Mixing in Zero- and Solar-Metallicity Supernovae. *ApJ*, 693:1780–1802, March 2009. doi: 10.1088/0004-637X/693/2/1780. (Cited on page 3.)
- S. C. Keller, M. S. Bessell, A. Frebel, A. R. Casey, M. Asplund, H. R. Jacobson, K. Lind, J. E. Norris, D. Yong, A. Heger, Z. Magic, G. S. da Costa, B. P. Schmidt, and P. Tisserand. A single low-energy, iron-poor supernova as the source of metals in the star SMSS J031300.36-670839.3. *Nature*, 506:463–466, February 2014. doi: 10.1038/nature12990. (Cited on pages 2, 16, 24, 64 and 135.)

- T. Kitayama, N. Yoshida, H. Susa, and M. Umemura. The Structure and Evolution of Early Cosmological H II Regions. *ApJ*, 613:631–645, October 2004. doi: 10.1086/423313. (Cited on page 59.)
- S. Kitsionas and A. P. Whitworth. Smoothed Particle Hydrodynamics with particle splitting, applied to self-gravitating collapse. *MNRAS*, 330:129–136, February 2002. doi: 10.1046/j.1365-8711.2002.05115.x. (Cited on pages 25, 68 and 137.)
- E. Komatsu, K. M. Smith, J. Dunkley, C. L. Bennett, B. Gold, G. Hinshaw, N. Jarosik, D. Larson, M. R. Nolta, L. Page, D. N. Spergel, M. Halpern, R. S. Hill, A. Kogut, M. Limon, S. S. Meyer, N. Odegard, G. S. Tucker, J. L. Weiland, E. Wollack, and E. L. Wright. Seven-year Wilkinson Microwave Anisotropy Probe (WMAP) Observations: Cosmological Interpretation. *ApJS*, 192:18, February 2011. doi: 10.1088/0067-0049/192/2/18. (Cited on page 96.)
- P. Kroupa. The Initial Mass Function of Stars: Evidence for Uniformity in Variable Systems. *Science*, 295:82–91, January 2002. doi: 10.1126/science.1067524. (Cited on page 4.)
- D. Lai. Global Nonradial Instabilities of Dynamically Collapsing Gas Spheres. *ApJ*, 540: 946–961, September 2000. doi: 10.1086/309361. (Cited on pages 7, 113, 135 and 138.)
- W. D. Langer and A. E. Glassgold. Silicon chemistry in interstellar clouds. *ApJ*, 352: 123–131, March 1990. doi: 10.1086/168519. (Cited on page 43.)
- R. B. Larson. Numerical calculations of the dynamics of collapsing proto-star. *MNRAS*, 145:271, 1969. (Cited on pages 5, 7, 12, 41 and 113.)
- Y. Li, R. S. Klessen, and M.-M. Mac Low. The Formation of Stellar Clusters in Turbulent Molecular Clouds: Effects of the Equation of State. *ApJ*, 592:975–985, August 2003. doi: 10.1086/375780. (Cited on page 15.)
- M. Limongi and A. Chieffi. Presupernova Evolution and Explosive Nucleosynthesis of Zero Metal Massive Stars. *ApJS*, 199:38, April 2012. doi: 10.1088/0067-0049/199/2/38. (Cited on pages 16, 22, 24 and 51.)
- K. Lodders, H. Palme, and H.-P. Gail. Abundances of the Elements in the Solar System. *Landolt Börnstein*, page 44, 2009. doi: 10.1007/978-3-540-88055-4_34. (Cited on page 19.)
- M. N. Machida and K. Doi. The formation of Population III stars in gas accretion stage: effects of magnetic fields. *MNRAS*, 435:3283–3305, November 2013. doi: 10.1093/mnras/stt1524. (Cited on pages 96 and 132.)

- U. Maio, K. Dolag, B. Ciardi, and L. Tornatore. Metal and molecule cooling in simulations of structure formation. *MNRAS*, 379:963–973, August 2007. doi: 10.1111/j.1365-2966.2007.12016.x. (Cited on page 10.)
- S. Marassi, G. Chiaki, R. Schneider, M. Limongi, K. Omukai, T. Nozawa, A. Chieffi, and N. Yoshida. The Origin of the Most Iron-poor Star. *ApJ*, 794:100, October 2014. doi: 10.1088/0004-637X/794/2/100. (Cited on pages 17, 33, 52 and 132.)
- H. Martel, N. J. Evans, II, and P. R. Shapiro. Fragmentation and Evolution of Molecular Clouds. I. Algorithm and First Results. *ApJS*, 163:122–144, March 2006. doi: 10.1086/500090. (Cited on page 68.)
- H. Masunaga and S.-i. Inutsuka. A Radiation Hydrodynamic Model for Protostellar Collapse. II. The Second Collapse and the Birth of a Protostar. *ApJ*, 531:350–365, March 2000. doi: 10.1086/308439. (Cited on page 7.)
- T. Matsumoto and T. Hanawa. Fragmentation of a Molecular Cloud Core versus Fragmentation of the Massive Protoplanetary Disk in the Main Accretion Phase. *ApJ*, 595:913–934, October 2003. doi: 10.1086/377367. (Cited on page 97.)
- L. Mayer, S. Kazantzidis, A. Escala, and S. Callegari. Direct formation of supermassive black holes via multi-scale gas inflows in galaxy mergers. *Nature*, 466:1082–1084, August 2010. doi: 10.1038/nature09294. (Cited on pages 25 and 137.)
- M. Mayer and W. J. Duschl. Rosseland and Planck mean opacities for primordial matter. *MNRAS*, 358:614–631, April 2005. doi: 10.1111/j.1365-2966.2005.08826.x. (Cited on page 38.)
- T. J. Millar, P. R. A. Farquhar, and K. Willacy. The UMIST Database for Astrochemistry 1995. *A&AS*, 121:139–185, January 1997. doi: 10.1051/aas:1997118. (Cited on page 43.)
- M. Nagasawa. Gravitational Instability of the Isothermal Gas Cylinder with an Axial magnetic Field. *Progress of Theoretical Physics*, 77:635–652, March 1987. doi: 10.1143/PTP.77.635. (Cited on page 128.)
- F. Nakamura and M. Umemura. The Stellar Initial Mass Function in Primordial Galaxies. *ApJ*, 569:549–557, April 2002. doi: 10.1086/339392. (Cited on page 39.)
- D. A. Neufeld and M. J. Kaufman. Radiative Cooling of Warm Molecular Gas. *ApJ*, 418:263, November 1993. doi: 10.1086/173388. (Cited on page 35.)
- D. A. Neufeld, S. Lepp, and G. J. Melnick. Thermal Balance in Dense Molecular Clouds: Radiative Cooling Rates and Emission-Line Luminosities. *ApJS*, 100:132, September 1995. doi: 10.1086/192211. (Cited on page 35.)

- J. E. Norris. The Chemical Abundance Structure of the Galactic Halo. In B. K. Gibson, R. S. Axelrod, and M. E. Putman, editors, *The Third Stromlo Symposium: The Galactic Halo*, volume 165 of *Astronomical Society of the Pacific Conference Series*, page 213, 1999. (Cited on page 139.)
- J. E. Norris, N. Christlieb, A. J. Korn, K. Eriksson, M. S. Bessell, T. C. Beers, L. Wisotzki, and D. Reimers. HE 0557-4840: Ultra-Metal-Poor and Carbon-Rich. *ApJ*, 670:774–788, November 2007. doi: 10.1086/521919. (Cited on pages 2 and 64.)
- T. Nozawa, T. Kozasa, H. Umeda, K. Maeda, and K. Nomoto. Dust in the Early Universe: Dust Formation in the Ejecta of Population III Supernovae. *ApJ*, 598:785–803, December 2003. doi: 10.1086/379011. (Cited on pages 17 and 19.)
- T. Nozawa, T. Kozasa, A. Habe, E. Dwek, H. Umeda, N. Tominaga, K. Maeda, and K. Nomoto. Evolution of Dust in Primordial Supernova Remnants: Can Dust Grains Formed in the Ejecta Survive and Be Injected into the Early Interstellar Medium? *ApJ*, 666:955–966, September 2007. doi: 10.1086/520621. (Cited on pages 17, 19, 24, 48, 97, 132 and 136.)
- T. Nozawa, T. Kozasa, and K. Nomoto. Can the Growth of Dust Grains in Low-metallicity Star-forming Clouds Affect the Formation of Metal-poor Low-mass Stars? *ApJ*, 756:L35, September 2012. doi: 10.1088/2041-8205/756/2/L35. (Cited on pages 19 and 23.)
- K. Omukai. Protostellar Collapse with Various Metallicities. *ApJ*, 534:809–824, May 2000. doi: 10.1086/308776. (Cited on pages 7, 10, 11, 12, 13, 17, 19, 22, 28, 38 and 41.)
- K. Omukai. Primordial Star Formation under Far-Ultraviolet Radiation. *ApJ*, 546:635–651, January 2001. doi: 10.1086/318296. (Cited on page 2.)
- K. Omukai and F. Palla. Formation of the First Stars by Accretion. *ApJ*, 589:677–687, June 2003. doi: 10.1086/374810. (Cited on page 131.)
- K. Omukai, T. Tsuribe, R. Schneider, and A. Ferrara. Thermal and Fragmentation Properties of Star-forming Clouds in Low-Metallicity Environments. *ApJ*, 626:627–643, June 2005. doi: 10.1086/429955. (Cited on pages 12, 39, 113 and 135.)
- K. Omukai, T. Hosokawa, and N. Yoshida. Low-metallicity Star Formation: Prestellar Collapse and Protostellar Accretion in the Spherical Symmetry. *ApJ*, 722:1793–1815, October 2010. doi: 10.1088/0004-637X/722/2/1793. (Cited on pages 13 and 35.)
- D. E. Osterbrock. *Astrophysics of gaseous nebulae and active galactic nuclei*. 1989. (Cited on page 30.)
- F. Palla, E. E. Salpeter, and S. W. Stahler. Primordial star formation - The role of molecular hydrogen. *ApJ*, 271:632–641, August 1983. doi: 10.1086/161231. (Cited on pages 39 and 41.)

- P. J. E. Peebles. *The large-scale structure of the universe*. 1980. (Cited on page 131.)
- M. V. Penston. Dynamics of self-gravitating gaseous spheres-III. Analytical results in the free-fall of isothermal cases. *MNRAS*, 144:425, 1969. doi: 10.1093/mnras/144.4.425. (Cited on page 113.)
- J. B. Pollack, D. Hollenbach, S. Beckwith, D. P. Simonelli, T. Roush, and W. Fong. Composition and radiative properties of grains in molecular clouds and accretion disks. *ApJ*, 421:615–639, February 1994. doi: 10.1086/173677. (Cited on pages 13 and 60.)
- C. M. Raiteri, M. Villata, and J. F. Navarro. Simulations of Galactic chemical evolution. I. O and Fe abundances in a simple collapse model. *A&A*, 315:105–115, November 1996. (Cited on pages 4 and 15.)
- J. S. Ritter, C. Safranek-Shrader, O. Gnat, M. Milosavljević, and V. Bromm. Confined Population III Enrichment and the Prospects for Prompt Second-generation Star Formation. *ApJ*, 761:56, December 2012. doi: 10.1088/0004-637X/761/1/56. (Cited on page 98.)
- C. Safranek-Shrader, M. Milosavljević, and V. Bromm. Star formation in the first galaxies - II. Clustered star formation and the influence of metal line cooling. *MNRAS*, 438:1669–1685, February 2014a. doi: 10.1093/mnras/stt2307. (Cited on page 22.)
- C. Safranek-Shrader, M. Milosavljević, and V. Bromm. Formation of the first low-mass stars from cosmological initial conditions. *MNRAS*, 440:L76–L80, May 2014b. doi: 10.1093/mnrasl/slu027. (Cited on pages 22, 95, 135 and 140.)
- E. E. Salpeter. The Luminosity Function and Stellar Evolution. *ApJ*, 121:161, January 1955. doi: 10.1086/145971. (Cited on page 4.)
- F. Santoro and J. M. Shull. Critical Metallicity and Fine-Structure Emission of Primordial Gas Enriched by the First Stars. *ApJ*, 643:26–37, May 2006. doi: 10.1086/501518. (Cited on page 10.)
- P. Schady, M. J. Page, S. R. Oates, M. Still, M. de Pasquale, T. Dwelly, N. P. M. Kuin, S. T. Holland, F. E. Marshall, and P. W. A. Roming. Dust and metal column densities in gamma-ray burst host galaxies. *MNRAS*, 401:2773–2792, February 2010. doi: 10.1111/j.1365-2966.2009.15861.x. (Cited on page 13.)
- R. Schneider and K. Omukai. Metals, dust and the cosmic microwave background: fragmentation of high-redshift star-forming clouds. *MNRAS*, 402:429–435, February 2010. doi: 10.1111/j.1365-2966.2009.15891.x. (Cited on page 15.)
- R. Schneider, A. Ferrara, R. Salvaterra, K. Omukai, and V. Bromm. Low-mass relics of early star formation. *Nature*, 422:869–871, April 2003. (Cited on page 38.)

- R. Schneider, K. Omukai, A. K. Inoue, and A. Ferrara. Fragmentation of star-forming clouds enriched with the first dust. *MNRAS*, 369:1437–1444, July 2006. doi: 10.1111/j.1365-2966.2006.10391.x. (Cited on page 41.)
- R. Schneider, K. Omukai, S. Bianchi, and R. Valiante. The first low-mass stars: critical metallicity or dust-to-gas ratio? *MNRAS*, 419:1566–1575, January 2012a. doi: 10.1111/j.1365-2966.2011.19818.x. (Cited on pages 17, 24 and 48.)
- R. Schneider, K. Omukai, M. Limongi, A. Ferrara, R. Salvaterra, A. Chieffi, and S. Bianchi. The formation of the extremely primitive star SDSS J102915+172927 relies on dust. *MNRAS*, 423:L60–L64, June 2012b. doi: 10.1111/j.1745-3933.2012.01257.x. (Cited on pages 3 and 18.)
- P. R. Shapiro and H. Kang. Hydrogen molecules and the radiative cooling of pregalactic shocks. *ApJ*, 318:32–65, July 1987. doi: 10.1086/165350. (Cited on page 39.)
- F. H. Shu. Self-similar collapse of isothermal spheres and star formation. *ApJ*, 214:488–497, June 1977. doi: 10.1086/155274. (Cited on pages 7 and 131.)
- F. H. Shu, F. C. Adams, and S. Lizano. Star formation in molecular clouds - Observation and theory. *ARA&A*, 25:23–81, 1987. doi: 10.1146/annurev.aa.25.090187.000323. (Cited on pages 7 and 131.)
- B. D. Smith, J. H. Wise, B. W. O’Shea, M. L. Norman, and S. Khochfar. The first Population II stars formed in externally enriched mini-haloes. *MNRAS*, 452:2822–2836, September 2015. doi: 10.1093/mnras/stv1509. (Cited on pages 22, 95, 98, 132 and 140.)
- L. Spitzer. *Physical processes in the interstellar medium*. 1978. (Cited on page 5.)
- V. Springel. The cosmological simulation code GADGET-2. *MNRAS*, 364:1105–1134, December 2005. doi: 10.1111/j.1365-2966.2005.09655.x. (Cited on pages 71 and 94.)
- J. Steinacker, L. Pagani, A. Bacmann, and S. Guieu. Direct evidence of dust growth in L183 from mid-infrared light scattering. *A&A*, 511:A9, February 2010. doi: 10.1051/0004-6361/200912835. (Cited on pages 18 and 45.)
- T. Suda, Y. Katsuta, S. Yamada, T. Suwa, C. Ishizuka, Y. Komiya, K. Sorai, M. Aikawa, and M. Y. Fujimoto. Stellar Abundances for the Galactic Archeology (SAGA) Database — Compilation of the Characteristics of Known Extremely Metal-Poor Stars. *PASJ*, 60:1159–, October 2008. doi: 10.1093/pasj/60.5.1159. (Cited on pages 24, 64 and 112.)
- K. Sugihara and M. Iri. A robust topology-oriented incremental algorithm for voronoi diagrams. *International Journal of Computational Geometry & Applications*, 04(02):179–228, 1994. doi: 10.1142/S0218195994000124. URL <http://www.worldscientific.com/doi/abs/10.1142/S0218195994000124>. (Cited on page 89.)

- H. Susa, K. Hasegawa, and N. Tominaga. The Mass Spectrum of the First Stars. *ApJ*, 792:32, September 2014. doi: 10.1088/0004-637X/792/1/32. (Cited on pages 125, 131 and 140.)
- S. Takahashi. *Formation and evolution of the protoplanetary disks*. PhD thesis, Kyoto University, 2015. (Cited on pages 88 and 138.)
- T. Takahashi, J. Silk, and D. J. Hollenbach. H₂O heating in molecular clouds - Line transfer and thermal balance in a warm dusty medium. *ApJ*, 275:145–162, December 1983. doi: 10.1086/161521. (Cited on page 28.)
- P. Todini and A. Ferrara. Dust formation in primordial Type II supernovae. *MNRAS*, 325:726–736, August 2001. doi: 10.1046/j.1365-8711.2001.04486.x. (Cited on pages 17 and 52.)
- N. Tominaga, N. Iwamoto, and K. Nomoto. Abundance Profiling of Extremely Metal-poor Stars and Supernova Properties in the Early Universe. *ApJ*, 785:98, April 2014. doi: 10.1088/0004-637X/785/2/98. (Cited on page 16.)
- A. Toomre. On the gravitational stability of a disk of stars. *ApJ*, 139:1217–1238, May 1964. doi: 10.1086/147861. (Cited on page 106.)
- J. K. Truelove, R. I. Klein, C. F. McKee, J. H. Holliman, II, L. H. Howell, and J. A. Greenough. The Jeans Condition: A New Constraint on Spatial Resolution in Simulations of Isothermal Self-gravitational Hydrodynamics. *ApJ*, 489:L179–L183, November 1997. doi: 10.1086/310975. (Cited on pages 24, 68, 83, 94 and 137.)
- J. K. Truelove, R. I. Klein, C. F. McKee, J. H. Holliman, II, L. H. Howell, J. A. Greenough, and D. T. Woods. Self-gravitational Hydrodynamics with Three-dimensional Adaptive Mesh Refinement: Methodology and Applications to Molecular Cloud Collapse and Fragmentation. *ApJ*, 495:821–852, March 1998. doi: 10.1086/305329. (Cited on page 94.)
- T. Tsuribe and S.-i. Inutsuka. Criteria for Fragmentation of Rotating Isothermal Clouds Revisited. *ApJ*, 523:L155–L158, October 1999a. doi: 10.1086/312267. (Cited on page 83.)
- T. Tsuribe and S.-i. Inutsuka. Criteria for Fragmentation of Rotating Isothermal Clouds. I. Semianalytic Approach. *ApJ*, 526:307–313, November 1999b. doi: 10.1086/307983. (Cited on pages 83 and 119.)
- T. Tsuribe and K. Omukai. Dust-cooling-induced Fragmentation of Low-Metallicity Clouds. *ApJ*, 642:L61–L64, May 2006. doi: 10.1086/504290. (Cited on pages 8, 15, 106, 108 and 138.)

- T. Tsuribe and K. Omukai. Physical Mechanism for the Intermediate Characteristic Stellar Mass in Extremely Metal Poor Environments. *ApJ*, 676:L45–L48, March 2008. doi: 10.1086/587035. (Cited on pages 22, 26, 37, 95 and 110.)
- M. J. Turk, T. Abel, and B. O’Shea. The Formation of Population III Binaries from Cosmological Initial Conditions. *Science*, 325:601–, July 2009. doi: 10.1126/science.1173540. (Cited on page 88.)
- J. Turner, K. Kirby-Docken, and A. Dalgarno. The Quadrupole Vibration-Rotation Transition Probabilities of Molecular Hydrogen. *ApJS*, 35:281, 1977. doi: 10.1086/190481. (Cited on page 29.)
- H. Umeda and K. Nomoto. Nucleosynthesis of Zinc and Iron Peak Elements in Population III Type II Supernovae: Comparison with Abundances of Very Metal Poor Halo Stars. *ApJ*, 565:385–404, January 2002. doi: 10.1086/323946. (Cited on pages 16, 22, 24, 33 and 51.)
- H. Umeda and K. Nomoto. First-generation black-hole-forming supernovae and the metal abundance pattern of a very iron-poor star. *Nature*, 422:871–873, April 2003. (Cited on pages 3, 132 and 140.)
- P. Ventura, F. Dell’Agli, R. Schneider, M. Di Criscienzo, C. Rossi, F. La Franca, S. Gallerani, and R. Valiante. Dust from asymptotic giant branch stars: relevant factors and modelling uncertainties. *MNRAS*, 439:977–989, March 2014. doi: 10.1093/mnras/stu028. (Cited on page 16.)
- E. I. Vorobyov and S. Basu. The Burst Mode of Accretion and Disk Fragmentation in the Early Embedded Stages of Star Formation. *ApJ*, 719:1896–1911, August 2010. doi: 10.1088/0004-637X/719/2/1896. (Cited on page 125.)
- E. I. Vorobyov, A. L. DeSouza, and S. Basu. The Burst Mode of Accretion in Primordial Protostars. *ApJ*, 768:131, May 2013. doi: 10.1088/0004-637X/768/2/131. (Cited on page 89.)
- D. Whalen, T. Abel, and M. L. Norman. Radiation Hydrodynamic Evolution of Primordial H II Regions. *ApJ*, 610:14–22, July 2004. doi: 10.1086/421548. (Cited on page 59.)
- A. Yahil. Self-similar stellar collapse. *ApJ*, 265:1047–1055, February 1983. doi: 10.1086/160746. (Cited on page 113.)
- T. Yoneyama. On the Fragmentation of a Contracting Hydrogen Cloud in an Expanding Universe. *PASJ*, 24:87, 1972. (Cited on page 5.)

- N. Yoshida, T. Abel, L. Hernquist, and N. Sugiyama. Simulations of Early Structure Formation: Primordial Gas Clouds. *ApJ*, 592:645–663, August 2003. doi: 10.1086/375810. (Cited on pages 4, 15 and 41.)
- T. Zafar, P. Møller, C. Ledoux, J. P. U. Fynbo, K. K. Nilsson, L. Christensen, S. D’Odorico, B. Milvang-Jensen, M. J. Michałowski, and D. D. M. Ferreira. A Ly α blob and $z_{\text{abs}} \simeq z_{\text{em}}$ damped Ly α absorber in the dark matter halo of the binary quasar Q 0151+048. *A&A*, 532:A51, August 2011. doi: 10.1051/0004-6361/201016332. (Cited on pages 13 and 136.)
- Z. Zhu, L. Hartmann, R. P. Nelson, and C. F. Gammie. Challenges in Forming Planets by Gravitational Instability: Disk Irradiation and Clump Migration, Accretion, and Tidal Destruction. *ApJ*, 746:110, February 2012. doi: 10.1088/0004-637X/746/1/110. (Cited on page 125.)